

# **Validation and Verification of the Atmospheric Radionuclide Transport Model (ARTM)**

Doctorate Thesis  
at the Meteorological Institute Munich  
of the Ludwig Maximilian University of Munich

submitted by  
Sebastian Hettrich  
born in Bad Aibling

Munich, 1<sup>st</sup> February 2017

Erstgutachter: Prof. Dr. Mark Wenig  
Zweitgutachter: Prof. Dr. George Craig  
Tag der Abgabe: 09. Februar 2017  
Tag der mündlichen Prüfung: 31. März 2017

# Zusammenfassung

Aufgrund der Tatsache, dass die Immissionen radioaktiver Nuklide, resultierend aus den Freisetzungen kerntechnischer Anlagen in Deutschland, im Vergleich zum natürlich vorkommenden radioaktiven Untergrund zu gering sind, um effizient in der Umgebung der Anlagen gemessen werden zu können, ist das Bundesamt für Strahlenschutz (BfS) zum Schutz der Bevölkerung dazu angehalten, deren Ausbreitung zu simulieren und die maximale Personendosis zu berechnen.

Während seit den 1970er Jahren Gauß-Fahnenmodelle in Gebrauch waren, hat die Entwicklung immer neuerer und schnellerer Rechenmaschinen Anreize zur Entwicklung des realistischeren Lagrange-Teilchenmodell gesetzt, welche in naher Zukunft für behördliche Zwecke zur Bewertung der Strahlenexposition durch radioaktive Emissionen zum Einsatz kommen sollen. Eines dieser Lagrange-Teilchenmodelle – entwickelt für Langzeitausbreitungen – ist das Atmosphärische-Radionuklid-Transport-Modell (ARTM).

In dieser Arbeit wird ARTM anhand realer und fiktiver Szenarien, in welchen das Programmverhalten und seine Simulationsergebnisse untersucht werden, verifiziert und validiert. Eine intensive Sensitivitätsanalyse einiger ausgewählter Modelleingabeparameter und deren Auswirkung auf die Ergebnisse wurde durchgeführt, um die programminternen mathematischen Algorithmen zu verifizieren. ARTM wurde auch zur Validierung und zur Evaluierung der Simulationsergebnisse auf zwei Szenarien angewendet, bei denen Immissionsmessdaten vorhanden waren. Diese Untersuchungen – zuzüglich eines Vergleichs mit dem Kurzzeitausbreitungsmodell LASAIR (Lagrange-Simulation der Ausbreitung und Inhalation von Radionukliden) – zeigen den Anwendungsbereich von ARTM auf und wo noch weitere Entwicklungen nötig sind.





# Abstract

Due to the fact that the immissions resulting from the release of radioactive nuclides from nuclear facilities in Germany are too small in comparison to the natural radioactive background to be efficiently measured in their vicinity, the German Federal Office for Radiation Protection (BfS) is obliged to simulate their distribution and calculate the maximum dose rates in order to protect the population.

While since the 1970's Gaussian plume models have been in use, the advent of fast modern computing machines has triggered the development towards the more realistic Lagrangian particle models which shall be used for regulatory purposes in order to assess the radiation exposure from radioactive emissions in the near future.

One of these Lagrangian models, developed for simulating long-term emissions, is the Atmospheric Radionuclide Transport Model (ARTM).

In this work, ARTM is verified and validated for several real and fictive scenarios, in which both the behaviour of the programme and its simulation results are studied. An intensive sensitivity study on a selection of model input parameters and their effect on results is performed in order to verify the programme-internal mathematical algorithms. ARTM is also applied to two scenarios where measurement data were available in order to validate and evaluate the simulation results. These studies, plus a comparison with the short-term model LASAIR (Lagrange Simulation of Dispersion and Inhalation of Radionuclides), demonstrate the range of usability for ARTM and where further development is needed.



# Acknowledgements

First of all I would like to thank Hans Wildermuth, Prof. Dr. Mark Wenig and Dr. Christopher Strobl for the scientific and academic supervision of this work, their valuable advice and their support in making this work happen.

I would like to also thank my colleagues Hartmut Walter and Gerhard Heinrich for providing me the opportunity to use the LASAIR model for my studies and supplying me with meteorological maps, as well as for their help and scientific support in specific issues related with LASAIR and dispersion simulations in general. Special thanks also to my colleague Michaela Kainz for her support with ARTM.

Furthermore I would like to thank Dr. Clemens Schlosser and Dr. Florian Gering for their inputs and the provision of complementary literature. Thanks also to Kathrin Arnold for providing additional tools and pre-studies, and Dr. Kathrin Folger for her help in specific questions regarding the PhD submission. Also, I have to thank Angelika Maier for helping me with many administrative things and for her support in organising meeting rooms and conference travels. My appreciation also goes to my international colleagues within the MODARIA Working Group 2, and here especially to Dr. Marija Zlata Boznar and Dr. Primož Mlakar for providing the Šoštanj scenario and their support for questions regarding the scenario, as well as to Dr. Kathleen Thiessen for organising the working group's efforts.

I also like to express my gratitude to Dr. Cornelia Richter and Harald Thielen of the GRS for their support with issues and detail questions regarding ARTM, and to Dr. Ulf Janicke and Dr. Lutz Janicke for their kind support and the provision of a patch for LASAIR.

Last but not least, I want to send a special thanks also to all proof-readers of my work!



# Table of contents

	Table of Abbreviations	11
	Table of Definitions	12
<b>1</b>	<b>Introduction</b>	<b>13</b>
1.1	Gaussian and Lagrangian dispersion models	13
1.1.1	Gaussian plume model	13
1.1.2	Lagrange-Particle-Model	17
1.1.3	Comparison between Gaussian plume model and Lagrange particle model	19
1.2	Atmospheric dispersion models used in this study	20
1.2.1	Atmospheric Radionuclide Transport Model (ARTM)	20
1.2.1.1	Operating Mode of ARTM	21
1.2.1.2	Limitations for global application	21
1.2.1.3	Limitations in the field of application	23
1.2.1.4	Necessary inputs for ARTM	23
1.2.2	Lagrange Simulation of Dispersion and Inhalation of Radionuclides (LASAIR)	24
1.2.2.1	Operating Mode of LASAIR	24
1.2.2.2	Limitations of LASAIR	27
1.2.2.3	Necessary inputs for LASAIR	28
1.3	Additional programmes	28
1.3.1	ARTM support programmes	28
1.3.1.1	Programmes for orography conversion	29
1.3.1.2	Conversion of Meteorological Data	38
1.3.1.3	Analysis of Simulation Results	38
1.3.2	LASAIR support programmes	39
1.4	Data sets descriptions	40
1.4.1	La Hague	40
1.4.2	Neckarwestheim	43
1.4.3	Šoštanj	44
1.4.4	Urban Buildings Scenario	47
1.5	Modelling Results	48
<b>2</b>	<b>Sensitivity Analysis of ARTM</b>	<b>49</b>
2.1	Sensitivity analysis with La Hague scenario	50
2.1.1	External input parameters	50
2.1.1.1	Emission strength	51
2.1.1.2	Source geometry	52
2.1.1.3	Terrain roughness	65
2.1.1.4	Dispersion Categories	69
2.1.1.5	Summary external parameters	75
2.1.2	Internal parameters	76
2.1.2.1	Random numbers	77
2.1.2.2	Particle quality	77
2.1.2.3	Grid size and Orography	81
2.1.2.4	Summary internal parameters	86
2.2	Sensitivity analysis with the Neckarwestheim-scenario	89
2.2.1	Random numbers	90
2.2.2	Particle quality	91

2.2.3	Points of maximum concentration	93
2.2.4	Summary	95
2.3	Conclusion of the ARTM sensitivity analysis	95
<b>3</b>	<b>Validation of ARTM with the La Hague scenario</b>	<b>96</b>
<b>4</b>	<b>The Šoštanj modelling exercise</b>	<b>101</b>
4.1	The first modelling attempts and their difficulties	101
4.1.1	Orography	102
4.1.2	Meteorology	103
4.1.3	Emissions	103
4.1.4	Other issues	105
4.2	Results of the Šoštanj Modelling Exercise	107
4.2.1	ARTM modelling results	107
4.2.2	LASAIR modelling results	111
4.3	Conclusion	118
<b>5</b>	<b>The urban building scenario</b>	<b>120</b>
5.1	The reference scenario – building scenario 1	120
5.2	One single building – building scenario 2	123
5.3	Building an approximated urban structure – building scenario 3a-d	127
5.4	Realistic urban scenario and its approximation – building scenario 4, 3b and 3b-a	134
5.4.1	Dispersion in complex urban structures	134
5.4.2	Approximation of complex urban structures	136
5.5	Conclusion of the urban building scenario	137
<b>6</b>	<b>Conclusion</b>	<b>139</b>
<b>7</b>	<b>References</b>	<b>142</b>
A	Wind Field Models	146
B	Version Information	155
C	Coordinate Systems	156
D	Synoptical Estimation of Dispersion Categories	159
E	Meteorological Data Files	170
F	Šoštanj TPP Buildings	176
G	ARTM Input Parameter	181

# Table of Abbreviations

ASC	ASCII (American Standard Code for Information Interchange) text file
ARTM	Atmospheric Radionuclide Transfer Model
AUSTAL2000	Dispersion modelling following the TA-Luft (German: Ausbreitungsrechnung nach TA-Luft)
AVV	General Instruction for Administration (German: Allgemeine Verwaltungsvorschrift)
BfS	German Federal Office for Radiation Protection (German: Bundesamt für Strahlenschutz)
CORINE	Coordination of Information on the Environment
DCC	Dispersion Class Calculator
DEM	Digital Elevation Model
DOS	Disk Operation System
GE	Grid Equaliser
GO-ARTM	Graphical user interface for ARTM (German: Graphische Oberfläche)
GK	Gauss-Krüger coordinate system
GMT	Greenwich Mean Time
GSC	Grid Size Calculator
GUI	Graphical User Interface
IAEA	International Atomic Energy Agency
IRSN	Institut de Radioprotection et de Sûreté Nucléaire
ISO	International Organisation for Standardisation
KTA	Nuclear Safety Standards Commission (German: Kerntechnischer Ausschuss)
LAR	Long-term Dispersion Calculation (German: Langzeitausbreitungsrechnung)
LASAIR	Lagrange Simulation of Dispersion and Inhalation of Radionuclides
LASAT	Lagrange Simulation of Aerosol Transport
LC	Location Calculator
MEIS	Modelling, Meteorology, Measurement Environmental Information Systems Engineering, Education, Informatics Consulting, Systems
MODARIA	Modelling and Data for Radiological Impact Assessments
SODAR	Sonic Detection And Ranging
SSK	Commission for Radiation Protection (German: Strahlenschutzkommission)
StrlSchV	Decree on radiation protection (German: Strahlenschutzverordnung)
TA Luft	Technical Instructions on Air Quality Control (German: Technische Anleitung zur Reinhaltung der Luft)
TALdia	Diagnostic wind field model following the TA Luft
TPP	Thermal Power Plant
UTC	Coordinated Universal Time
UTM	Universal-Trans-Mercator coordinate system (explanation see in Appendix C.2)
UP2-800	Plutonium factory (French: Usine Plutonium) 2-800
UP3	Plutonium factory (French: Usine Plutonium) 3
VDI	Association of German Engineers (German: Verein Deutscher Ingenieure)

# Table of Definitions

Deviation Range	The range between the lowest value minus its standard deviation and the highest value plus its standard deviation in a target grid. It shows the maximum variation that could be possible for the central measurement station, in case of slight spatial deviations.
Emission Strength	Denominates the emission rate in $Bq \cdot s^{-1}$ that is released through the stacks.
Geo-coordinates	In this work, the term ‘geo-coordinates’ refers to the geographic coordinate system used to describe locations on Earth. In this coordinate system, a location is defined by the longitude and latitude values in $^{\circ}$ , as opposed to the UTM system, where locations are determined by the distance in metres from the equator and the zero meridian.
Grid	The expression ‘grid’ is used in this work to describe a table of values, for example the altitude values or the immission values, that projects the map of the simulation area.
Immission	Defines here the amount of measured or simulated pollution at a given target location.
Orography	Defines the totality of all altitude values and is used to describe the altitude map of the simulation area.
Particle Quality	Refers to the amount of simulation particles used within ARTM. The basic particle quality level is qs0 with $6.3 \times 10^7$ simulation particles. Each increase in level increases the particle amount by a factor of 2. Details can be found in table 2.1.2.2 I.
Point of maximum concentration	Is the location within the simulation area, where the highest value of the activity concentration occurs for one of the simulated radio nuclides. Often, different radionuclides have slightly different points of maximum concentration.
Quality Level	Describes the quality of an input parameter into ARTM (see also ‘Particle Quality’)
Radiation Balance	Describes the difference of incoming and outgoing solar and infrared radiation. It is used to estimate the atmospheric turbulence, i.e. dispersion categories.
Standard Deviation	In this thesis/work ‘standard deviation’ always refers to the ‘unbiased estimation of the standard deviation’ (as described by Richard M. Brugger (1969); explained in section 1.3.1.3 iii), which is used due to its higher accuracy for small sample sizes.
Starting random number	Is a user input into ARTM, which starts a determined random number generator. For each chosen starting random number, the initial distribution of simulation particles will be different.
Surface Roughness	Is a parameter with unit [m] to describe the land coverage. The more obstacles, the higher this number. It is important to consider turbulence for the simulation.
Time Series	Is a chronological input or output file, containing the same kind of data for each time step.
Total concentration values	Describes the average concentration values for each grid cell in the entire simulation area over the entire simulation period.
Validation	Specifies the objective confirmation that the requirements for a special use case are fulfilled [DIN EN ISO 9000, 2015].
Verification	Refers to the objective confirmation that the product meets certain requirements and properties [DIN EN ISO 9000, 2015].



# 1. Introduction

In order to legally handle the peaceful use of nuclear energy and the protection against its dangers, Germany introduced in 1959 its first ‘Atomgesetz’ (nuclear law) and in 1976 the ‘Strahlenschutzverordnung’ (decree on radiation protection) was added [BfS, 2016]. Its aim was to study the exposure of the population to artificial and natural radiation, and to regulate the use of radioactive material and ionising radiation in order to protect humans and the environment [StrlSchV, 2001]. With this decree, the necessity was born to monitor the emissions of all nuclear facilities in Germany and to predict their risks for the population. The general instruction for administration according to § 47 of the StrlSchV, here just called AVV (‘Allgemeine Verwaltungsvorschrift’; 2012), describes and determines the methods allowed to be used in order to protect the population from airborne pollutions released by nuclear facilities. The exposure of the population has to be monitored, considering all thinkable contamination pathways, from the emission directly to the human body via the lungs or the skin, and the indirect ways through the food path, resulting from the deposition [AVV, 2012]. However, due to the containment and efficient filter systems, the emissions are in most cases so small, that the resulting immissions in the local area, after the dilution during the transport, are below the background radiation [LfU, 2016]. The AVV here describes the use of an atmospheric dispersion model based on the Gaussian plume model [AVV, 2012].

## 1.1 Gaussian and Lagrangian dispersion models

There exist several types of atmospheric dispersion models, common ones are Gaussian plume models, the Lagrangian particle models and fluid dynamic approaches [Mayall, 2003]. While the latter one still is too complex to run a simulation on a normal computer, the Gaussian plume model and the Lagrangian particle model find common use for regulatory purposes and for simulating the dispersion of emissions from accidental releases.

Here the basics of these two approaches are described.

### 1.1.1 Gaussian plume model

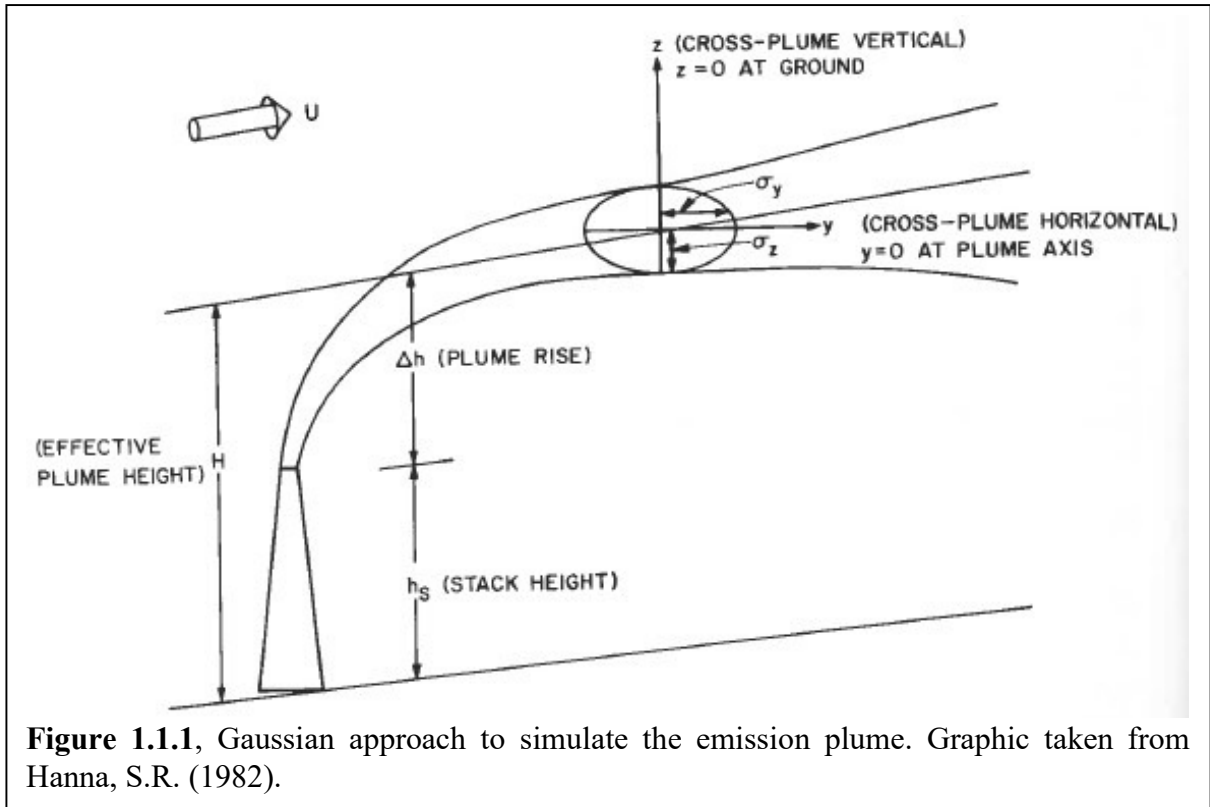
The Gaussian plume model provides a simplified approximation of the real emission plume, it is based on data and experiences gained from observations [Hanna, 1982]. Figure 1.1.1 shows a schematic of a Gaussian plume [Hanna, 1982]. For the calculation, a 2-dimensional Gaussian distribution is applied [AVV, 2012]. The concentration  $c$  at the location  $(x,y,z)$  can be calculated with equation (1.1.1 i) [Hanna, 1982; AVV, 2012].

$$c(x,y,z) = \frac{\dot{A}}{2\pi \cdot u \cdot \sigma_y(x) \cdot \sigma_z(x)} \cdot \exp\left(-\frac{y^2}{2\sigma_y^2(x)}\right) \cdot \left[ \exp\left(-\frac{(z-H)^2}{2\sigma_z^2(x)}\right) + \exp\left(-\frac{(z+H)^2}{2\sigma_z^2(x)}\right) \right] \quad (1.1.1 \text{ i})$$

The emission strength  $\dot{A}$  is the basic input component, and can, depending on the use case of the model for conventional releases or radioactive releases, have the unit  $g \cdot s^{-1}$  or  $Bq \cdot s^{-1}$ , accordingly the concentration  $c$  can show up in  $g \cdot m^{-3}$  or  $Bq \cdot m^{-3}$  [Hanna, 1982; AVV, 2012]. The values  $x$ ,  $y$ , and  $z$  are Cartesian coordinates with the origin at the bottom point of the

emission source [AVV, 2012].  $H$  is the effective emission altitude above ground in metres and  $u$  is the wind speed at the effective emission altitude, measured in  $m \cdot s^{-1}$  [Hanna, 1982; AVV, 2012].  $\sigma_y(x)$  and  $\sigma_z(x)$  respectively are the horizontal and vertical dispersion factors dependent of the distance to the source, dispersion category and effective emission height [AVV, 2012]. The second term in the square brackets represents the reflection of the particle from the ground [Hanna, 1982]. They can be determined by (1.1.1 ii) and the corresponding values for the dispersion and coefficients  $p_y$  and  $p_z$  the dispersion exponent  $q_y$  and  $q_z$ , which can be found in the AVV, appendix 7 [AVV, 2012].

$$\begin{aligned}\sigma_y &= p_y \cdot x^{q_y} \\ \sigma_z &= p_z \cdot x^{q_z}\end{aligned}\tag{1.1.1 ii}$$



The over-ground concentration distribution  $\hat{C}(x, y)$  on the lee side of the source is given by (1.1.1 iii) [AVV, 2012].

$$\hat{C}(x, y) = \frac{\dot{A}}{\pi \cdot u \cdot \sigma_y(x) \cdot \sigma_z(x)} \cdot \exp\left(-\frac{y^2}{2\sigma_y^2(x)}\right) \cdot \exp\left(-\frac{H^2}{2\sigma_z^2(x)}\right)\tag{1.1.1 iii}$$

This results in a short term dispersion factor  $\hat{X}(x, y)$  and a long term dispersion factor  $\hat{X}_i^r(x)$  as defined in (1.1.1 iv) and (1.1.1 v) [AVV, 2012].

$$\hat{X}(x, y) = \frac{\hat{C}(x, y)}{\dot{A}}\tag{1.1.1 iv}$$

$$\bar{X}_i^\tau(x) = \frac{\bar{C}_i^\tau(x)}{A} = \sqrt{\frac{2}{\pi}} \cdot \frac{N}{2 \cdot \pi \cdot x} \cdot \sum_{j=1}^6 \frac{\exp\left(-\frac{H^2}{2\sigma_{z,j}^2(x)}\right)}{\sigma_{z,j}(x)} \cdot \sum_{m=1}^M \frac{p_{i,j,m}^\tau}{u_{j,m}} \quad (1.1.1 \text{ v})$$

Here  $N$  is the amount of angular sectors, usually 12 sectors, each with  $30^\circ$  in width,  $p_{i,j,m}^\tau$  is the occurrence of wind with dispersion category  $j$ , wind speed  $m$  in sector  $i$  during the time period  $\tau$  (usually a full year),  $M$  is the amount of wind speed levels and  $u_{j,m}$  is the wind speed in effective emission height for the wind speed level  $m$  and dispersion category  $j$  [AVV, 2012].

The contamination resulting from fallout and washout are considered in specific fallout and washout factors given in (1.1.1 vi) and (1.1.1 vii), respectively [AVV, 2012].

$$\bar{F}_i^\tau(x) = v_g \cdot \bar{X}_i^\tau(x) \quad (1.1.1 \text{ vi})$$

$$\bar{W}_i^\tau(x) = \frac{\bar{B}_{w,i}^\tau(x)}{A} \quad (1.1.1 \text{ vii})$$

$v_g$  is the deposition velocity, which comes into play for the dry fallout [AVV, 2012]. The washout depends on  $\bar{B}_{w,i}^\tau(x)$ , the soil contamination for the wet deposition as given in (1.1.1 viii), and  $A$ , which is the emitted activity in Bq [AVV, 2012].

$$\bar{B}_{w,i}^\tau(x) = A \cdot \frac{N}{2 \cdot \pi \cdot x} \cdot \sum_{j,m,k} q_{i,j,m,k}^\tau \cdot \frac{\Lambda_k}{u_{j,m}} \quad (1.1.1 \text{ viii})$$

$q_{i,j,m,k}^\tau$  is the occurrence of precipitation with dispersion category  $j$ , wind speed  $m$  in sector  $i$  during the time period  $\tau$  for the precipitation intensity level  $k$  [AVV, 2012]. The washout coefficient  $\Lambda$  is a function of the precipitation intensity  $I$  in  $\text{mm} \cdot \text{h}^{-1}$ , the precipitation intensity  $I_0 = 1 \text{mm} \cdot \text{h}^{-1}$ , a specific washout coefficient  $\Lambda_0$  for  $I_0$  from empirical values as can be viewed in appendix 7 of the AVV, and an exponent  $\kappa$ , which distinguishes between aerosols and iodine ( $\kappa = 0.8$ ) and super heavy water ( $\kappa = 1.0$ ) [AVV, 2012].

$$\Lambda = \Lambda_0 \left( \frac{I}{I_0} \right)^\kappa \quad (1.1.1 \text{ ix})$$

Through fallout, washout and also radioactive decay, the amount of particles in the plume decreases [AVV, 2012]. This is accounted for via the factors  $f_A$  (fallout),  $f_R$  (washout), and  $f_{Z,r}$  (decay) [AVV, 2012].

$$f_A = \exp \left( - \frac{v_g}{u} \cdot \sqrt{\frac{2}{\pi}} \cdot \int_0^x \frac{\exp\left(-\frac{H^2}{2 \cdot \sigma_z^2(x')}\right)}{\sigma_z(x')} dx' \right) \quad (1.1.1 \text{ x})$$

$$f_R = \exp\left(-\frac{\Lambda \cdot x}{u}\right) \quad (1.1.1 \text{ xi})$$

$$f_{z,r} = \exp\left(-\frac{\lambda_r \cdot x}{u}\right) \quad (1.1.1 \text{ xii})$$

With  $\lambda_r$  being the decay constant.

Local influences can also be integrated into the Gaussian model up to a certain degree:

- The plume rise, resulting from exhaust with emission impulse and heat, needs to be calculated (for example using the equations given in chapter 4.1.4 following the VDI guidelines 3782 Part 3 (1985)) and then added to the stack height [AVV, 2012].
- If the buildings surrounding the emission source have double the height of the effective emission height, or higher, the AVV provides an approximation to consider these influences [AVV, 2012]. Here the building height is  $H_G$  and the width is  $b_G$ , and  $I_G$  is defined as the smaller value of these two [AVV, 2012]. If  $H < H_G + I_G$  and the source is either on the roof of the building, somewhere in the distance of  $0.25 \cdot I_G$ , or located less than  $3 \cdot I_G$  directly in or against the dispersion direction, as seen from the building, then the effective emission height  $H$  has to be modified to gain  $h'$  [AVV, 2012]:

$$\text{For } H > H_G \text{ the effective emission height is } h' = 0.5 \cdot [3H - (H_G + I_G)] \quad (1.1.1 \text{ xiii})$$

$$\text{For } H \leq H_G \text{ the effective emission height is } h' = H - 0.5 \cdot I_G \quad (1.1.1 \text{ xiv})$$

For a few specific values of  $h'$  the AVV also provides some additional instructions, not shown here [AVV, 2012].

- The influence of cooling towers is to consider, however here the AVV does not provide any specific formula that has to be used [AVV, 2012].
- A Gaussian model requires the orography to be reasonably flat, i.e. no angles above  $5^\circ$  in steepness [AVV, 2012]. For a mild orography the calculation of the dispersion factors can account for its influences depending on the dispersion category [AVV, 2012].  
For dispersion categories A to D:

- For  $h(x,0) < H/2$ :

$$\begin{aligned} \hat{X}(x, y, z = h(x,0)) &= \frac{1}{\pi \cdot u \cdot \sigma_y(x) \cdot \sigma_z(x)} \cdot \exp\left(-\frac{y^2}{2\sigma_y^2(x)}\right) \cdot \\ &\exp\left(-\frac{(H - h(x,0))^2}{2\sigma_z^2(x)}\right) \end{aligned} \quad (1.1.1 \text{ xv})$$

- For  $h(x,0) \geq H/2$ :

$$\hat{X}(x, y, z = h(x, 0)) = \frac{1}{\pi \cdot u \cdot \sigma_y(x) \cdot \sigma_z(x)} \cdot \exp\left(-\frac{y^2}{2\sigma_y^2(x)}\right) \cdot \exp\left(-\frac{(0.5 \cdot H)^2}{2\sigma_z^2(x)}\right) \quad (1.1.1 \text{ xvi})$$

For dispersion categories E and F:

- For  $h(x, 0) < H$ :

$$\hat{X}(x, y, z = h(x, 0)) = \frac{1}{\pi \cdot u \cdot \sigma_y(x) \cdot \sigma_z(x)} \cdot \exp\left(-\frac{y^2}{2\sigma_y^2(x)}\right) \cdot \exp\left(-\frac{(H - h(x, 0))^2}{2\sigma_z^2(x)}\right) \quad (1.1.1 \text{ xvii})$$

- For  $h(x, 0) \geq H$ :

$$\hat{X}(x, y, z = h(x, 0)) = \frac{1}{\pi \cdot u \cdot \sigma_y(x) \cdot \sigma_z(x)} \cdot \exp\left(-\frac{y^2}{2\sigma_y^2(x)}\right) \quad (1.1.1 \text{ xviii})$$

Here  $h(x, 0)$  is the height of the orography in dispersion direction  $x$  [AVV, 2012].

## 1.1.2 Lagrange-Particle-Model

The Lagrangian particle model uses an ensemble of simulation particles that are carried through the simulation area by the occurring winds [VDI 3945 part 3, 2000]. Here, one such a simulation particle can represent several different substances at the same time and also different amounts of it [VDI 3945 part 3, 2000]. These propagate in time intervals with length  $\tau$ , considering the different velocities, such as the mean wind velocity  $\vec{V}$ , the turbulence velocity  $\vec{u}$  and an additional velocity  $\vec{U}$  [VDI 3945 part 3, 2000]. The mean wind velocity transports every particle and can vary in dependency of the location [VDI 3945 part 3, 2000]. The turbulence velocity is independent for each particle and varies in every time step, causing a drift-away of the particles from each other [VDI 3945 part 3, 2000]. The additional velocity is used to parameterise additional processes affecting the particle, such as plume rise or sedimentation [VDI 3945 part 3, 2000]. A particle therefore changes its position according to (1.1.2 i) [VDI 3945 part 3, 2000].

$$\vec{x}_{new} = \vec{x}_{old} + \tau \cdot (\vec{V} + \vec{u} + \vec{U}) \quad (1.1.2 \text{ i})$$

The turbulence velocity is determined in each time step by the Markov process (1.1.2 ii) [VDI 3945 part 3, 2000].

$$\vec{u}_{new} = \Psi \cdot \vec{u}_{old} \cdot \vec{w} \quad (1.1.2 \text{ ii})$$

With tensor  $\Psi$  representing the auto-correlation coefficient of a simple 1-dimensional Markov process (details on the Markov process can be found in VDI 3945 part 3 in the appendix A) and  $\vec{w}$  being a stochastic velocity increment, which is given by (1.1.2 iii) [VDI 3945 part 3, 2000].

$$\vec{w} = \vec{W}(\vec{x}_{old}) + \vec{\Lambda}(\vec{x}_{old}) \cdot \vec{r} \quad (1.1.2 \text{ iii})$$

$\bar{W}(\bar{x}_{old})$  is called drift velocity and acts only with inhomogeneous turbulence or a with the time varying in dependence of the space [VDI 3945 part 3, 2000].  $\bar{\Lambda}(\bar{x}_{old})$  is the Cholesky decomposition of tensor  $\Omega$ , and  $\bar{r}$  consists of random number components, which possess a distribution density  $\rho(\bar{r})$  [VDI 3945 part 3, 2000].

$$\Lambda \cdot \Lambda^T = \Omega \quad (1.1.2 \text{ iv})$$

The random numbers are determined independently for each time step, showing the mean value  $\bar{\bar{r}} = 0$  and a variance of  $\bar{\bar{r}}\bar{\bar{r}} = 1$  [VDI 3945 part 3, 2000].

$$\int \rho(\bar{r}) d^3 r = 1 \quad (1.1.2 \text{ vi})$$

$$\int \bar{r} \rho(\bar{r}) d^3 r = \bar{\bar{r}} = 0 \quad (1.1.2 \text{ v})$$

$$\int \bar{r}\bar{r} \rho(\bar{r}) d^3 r = \bar{\bar{r}}\bar{\bar{r}} = 1 \quad (1.1.2 \text{ vi})$$

For the stochastic velocity increment this results in (1.1.2 vii) [VDI 3945 part 3, 2000].

$$\bar{\bar{w}} = \bar{W} \quad (1.1.2 \text{ vii})$$

$$(\bar{w} - \bar{\bar{w}})(\bar{w} - \bar{\bar{w}}) = \bar{\Omega} \quad (1.1.2 \text{ viii})$$

The basic principle is, that all particles start the dispersion at the emission source [VDI 3945 part 3, 2000]. In case of a spatially extended source, the particles have a randomly distributed starting location within the source area [VDI 3945 part 3, 2000]. They get individual turbulence velocities  $\bar{u}$  assigned with a random starting value  $\bar{u}_0$ , following the condition  $\bar{\bar{u}}_0\bar{\bar{u}}_0 = \Sigma(x)$ , with  $\Sigma(x)$  being the variance of the wind speed fluctuations [VDI 3945 part 3, 2000]. The particles propagate according to the equations above and if a particle hits a limiting surface, such as the soil or the side of a building, it is reflected elastically (with the exception mentioned below) while getting assigned a new turbulence velocity [VDI 3945 part 3, 2000]. Similarly the upper end of the mixing layer can be handled; either by defining it as a boundary like the soil, or by defining it as a region with decreased diffusion [VDI 3945 part 3, 2000]. If a particle exits the simulation area, it is not considered any further in the simulation [VDI 3945 part 3, 2000]. The simulation particles can relate to one or more substances  $\nu$  being dispersed and represented by their mass  $m^{(\nu)}$  [VDI 3945 part 3, 2000].

Whenever a particle hits the soil or a limiting surface, a fraction  $p_d^{(\nu)}$  of its initial mass  $m_{old}^{(\nu)}$  is being deposited and therefore taken out of the simulation [VDI 3945 part 3, 2000].

$$m^{(\nu)} = (1 - p_d^{(\nu)}) \cdot m_{old}^{(\nu)} \quad (1.1.2 \text{ ix})$$

For wet deposition, it is described via a wash-out frequency  $r_w^{(\nu)}$  within the time step  $\tau$  [VDI 3945 part 3, 2000].

$$m^{(\nu)} = (1 - r_w^{(\nu)} \cdot \tau) \cdot m_{old}^{(\nu)} \quad (1.1.2 \text{ x})$$

To obtain the concentration distribution  $c^{(\nu)}$  of the substance  $\nu$ , all particles  $N_p$  in a volume element  $\Delta_{i,j,k}$  for a time period  $[t_A, t_B]$  are counted and represented through their mass  $m_\kappa^{(\nu)}$  ( $\kappa = 1, \dots, N_p$ ) [VDI 3945 part 3, 2000].

$$\lambda_{i,j,k}^{(\kappa)}(t) = \begin{cases} 1 & \text{if particle } \kappa \text{ is in } \Delta_{i,j,k} \text{ at time } t \\ 0 & \text{else} \end{cases} \quad (1.1.2 \text{ xi})$$

Including the function (1.1.2 xi), the spatial and temporal mean concentration value  $\bar{c}_{i,j,k}^{(\nu)}$  for this volume element is given with (1.1.2 xii) [VDI 3945 part 3, 2000].

$$\bar{c}_{i,j,k}^{(\nu)} = \frac{\sum_{\kappa=1}^{N_p} \int_{t_A}^{t_B} \lambda_{i,j,k}^{(\kappa)}(t) m_\kappa^{(\nu)}(t) dt}{\Delta_{i,j,k} (t_B - t_A)} \quad (1.1.2 \text{ xii})$$

### 1.1.3 Comparison between Gaussian plume model and Lagrange particle model

Gaussian models show several limitations in their capabilities, for example the orography influence throughout the entire model area and turbulences due to changes in the surface cover are not reflected in the calculation results [Mayall, 2003]. These models consider external influences, such as orography or buildings only via parametrisation and therefore can be used as described in chapter 1.1.1.

Lagrangian particle models, though, need the wind conditions for each cell of the entire simulation area in each time step as an input to the simulation. Therefore, prior to a simulation with a Lagrange model, a wind field model has to generate these complex wind fields covering all situations that appear during the simulation time period.

This requires larger computing and data storage capabilities for the Lagrangian model than for the Gaussian model, and was a reason for choosing the Gaussian plume model, when the StrlSchV and the AVV were put in place.

Comparing the results of Gaussian and Lagrangian particle models, represented by an early ARTM (Atmospheric Radionuclide Transport Model) version, Martens, et al (2007) found that the obvious differences in the plumes generated by both models show that the plume in the Lagrange model describes a slight curve and is thinner than the Gaussian one. During a small comparison study between the LAR (Long-term Dispersion Calculation; German: Langzeitausbreitungsrechnung) and ARTM at the German Federal Office for Radiation Protection, H. Wildermuth found that the Gaussian model produces maximum concentration values of around one order of magnitude larger than the Lagrangian model, effecting the concluding dose calculations accordingly.

Another study by Lutman et al. (2003) compared a Lagrangian particle model, called NAME, from the United Kingdom, with a conventional Gaussian model, called PLUME. They also discovered differences in the simulated air concentrations, however their findings show that they vary around plus/minus one order of magnitude; sometimes the Gaussian model delivered the higher concentration, sometimes it was the other way round [Lutman et al., 2003].

As they did not compare simulation and real measurements, no statement on the accuracy of both programmes can be given.

## **1.2 Atmospheric dispersion models used in this study**

While in the past Gaussian plume models were the atmospheric dispersion models of choice due to their lower requirements in computing power, they have slowly begun to be replaced in operational applications by the more realistic Lagrangian particle models as more powerful computers have become available. In German legislation, especially the AVV (2012), Gaussian models have been the standard for atmospheric dispersion simulation, as they have been validated to be used as basis before applying the calculation of dose exposure of the population around nuclear facilities [AVV, 2012, BMUB, 2014]. Although Gaussian models do not simulate atmospheric dispersion entirely realistically, they are safe to base decisions upon, because their conservative assumptions – especially when considering the dose – ensure that simulation values are always much higher than real values would ever be, and therefore always represent the worst case [BMUB, 2014].

Current progress in the development of Lagrangian models suggests that they could soon be integrated into German Legislation for regulatory purposes, but this would require in-depth studies and validation of these models [Martens et al. 2007].

This work focuses on two Lagrangian particle models currently in use and/or under development for different application purposes at the German Federal Office for Radiation Protection (BfS); the simulation of long-term nominal emissions and accidental or explosive short-term releases. A specific focus here is laid upon the verification and validation of the long-term Atmospheric Radionuclide Transport Model (ARTM). According to ISO 9000, ‘verification’ refers to the objective confirmation that the product meets certain requirements and properties, ‘validation’ specifies the objective confirmation that the requirements for a special use case are fulfilled [DIN EN ISO 9000, 2015].

### **1.2.1 Atmospheric Radionuclide Transport Model (ARTM)**

The Atmospheric Radionuclide Transport Model (ARTM) is a simulation software used to simulate and predict the atmospheric dispersion of radioactive nuclides from nuclear facilities and to calculate the exposure of the population to long-term dispersion during regular operations by additionally applying the dose module DARTM [Richter et al., 2013a].

ARTM was developed for the BfS by the Gesellschaft für Anlagen- und Reaktorsicherheit (GRS), based on the AUSTAL2000 (Ausbreitungsmodell der TA Luft, [AUSTAL2000]) programme for “atmospheric dispersion of substances and odorants”, and is currently still under development [Janicke Consulting, 2011; Richter et al., 2013b]. Both ARTM and AUSTAL2000 are mathematically based on a Lagrangian particle model (see chapter 1.1.2), following the guidelines of the Association of German Engineers (VDI) and the Technical Instructions on Air Quality Control (TA Luft) [Richter et al., 2013a].

While AUSTAL2000 was designed to simulate chemical particles and gases released by industrial facilities, ARTM was specifically designed for radioactive aerial releases [Richter, et al., 2013b]. As such, ARTM provides the opportunity to visualise dry and wet deposition of radioactive particles and cloud gamma submersion as well as dose calculations with the DARTM dose module developed by the BfS [Richter et al., 2013b].



### 1.2.1.1 Operating Mode of ARTM

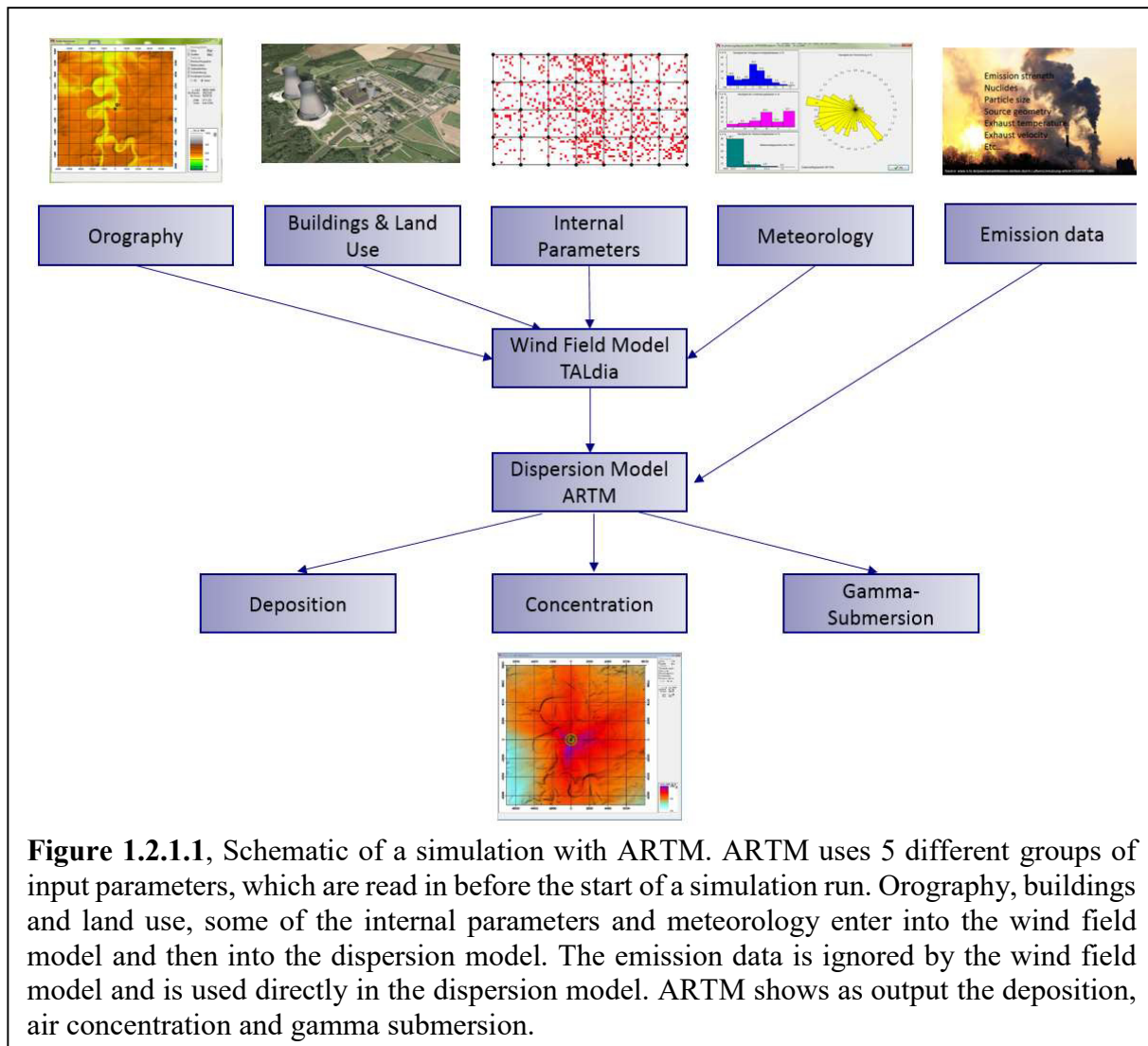
ARTM consists of two main parts, wind field model and a dispersion model, and can be operated either with a Disk Operating System (DOS) interface or with a Graphical User Interface (GUI), called GO-ARTM, provided in the programme package [Richter et al., 2013b]. While both ways of running a dispersion simulation with ARTM can be performed using prepared input parameter files, running a simulation with GO-ARTM also offers the opportunity to insert and change the input parameters in the GUI.

The input parameters for ARTM can be grouped in 5 categories (see figure 1.2.1.1):

- The orography file provides the terrain altitudes. This is used by the wind field model to simulate wind speeds and wind directions for each point on the map and each meteorological situation.
- Buildings and land use can introduce turbulences into the wind field. While buildings are directly simulated as obstacles in the wind field model, the land use, i.e. water surface, sub-urban structures, farm lands, forests, or other vegetation, is simply parameterised based on the CORINE (Coordination of Information on the Environment) land cover. Details about it can be found in the CORINE land cover technical guide by Bossard et al. (2000).
- Internal parameters are all parameters that are not explicitly given by the input data sets that come from measurements. Internal parameters can be chosen by the user. These include the grid size, which goes into the wind field model, or the number of simulation particles and their starting distribution, expressed by a starting random number, which go into the dispersion simulation. The internal parameters will be discussed in detail in chapter 2.1.2.
- The meteorological data file includes the wind speeds, wind directions, dispersion categories and precipitation for each hour of the simulation time period. This is the main input for the wind field model.
- The emission data, which include emission strength, type of nuclide(s), dimensions and altitude of the emitting source, velocity of emission, water content, latent heat, and other source parameters, are used for the dispersion model.

Four of these input parameter groups – the orography, buildings and land use, meteorology and some of the internal parameters – go directly into the wind field model, and later on are again used for the dispersion model. ARTM uses the TALdia model, a diagnostic wind field model based on the regulations of the German TA Luft [Richter et al., 2013a, 2013b; BMU, 2002]. This model calculates the wind situation in the entire simulation area for all different meteorological situations and corresponding turbulence parameters, and stores them in a wind field library. Details on the wind field calculation for TALdia can be found in Appendix A.1.

In the next step, the dispersion model ARTM takes the emission data and, from the internal parameters, the simulation particle distribution and amount, and performs the dispersion simulation following the Lagrangian formalism (see chapter 1.1.2). For each hour of the simulation period ARTM accesses the wind field library and loads the corresponding wind field situation to provide the movement of the simulation particles. At the end, the amount of simulation particles per volume is scaled with the emitted nuclides and output files are produced with the resulting data. Basically, ARTM can show 3 different outputs; one, the deposition of the simulated nuclides, separated into wet and dry deposition; two, the overall air concentration in  $Bq/m^3$ ; three, the  $\gamma$ -Submersion values. ARTM does not calculate any dose rates; this can be done with the D-ARTM-tool.



### 1.2.1.2 Limitations for global application

Since ARTM was developed mainly for the simulation of German nuclear facilities, the applicability of the here used version (Appendix B.1) is limited to regions around 50°N. This is due to many programme-internal settings and parameters. For example, ARTM uses the Coriolis parameter to calculate a 3-dimensional flow field via shifting of the wind direction with distance from the meteorological station and the altitude above ground [Richter et al., 2013a]. This Coriolis parameter is different at different latitude positions – for example, in the north and south hemispheres its spin direction is opposite. In ARTM, the Coriolis parameter is fixed at the value valid for Germany. Also, ARTM uses a boundary layer model based on the VDI guidelines 3783, part 8 (2002), in which the mixing layer altitude was determined for a typical situation within Germany [Richter et al., 2013a]. While ARTM offers an option to manually input mixing layer altitudes, this feature is inactive, so for example maritime layering and tropical and polar conditions are not yet supported. In theory, ARTM could still be used for more exotic locations, but these limitations could result in entirely wrong outputs for the atmospheric dispersion, when applied for these scenarios. Another limitation of the here used version is that the orographical input data must be provided in the Gauss-Krüger coordinate system (GK), a mapping projection which is defined only for Germany and a few neighbouring areas. This requirement can be circumvented with a simple adjustment (see Appendix B.1), but

the programme still requires an equidistant input grid and the programme handbook does not give any hints on minimum or maximum possible cell size [Richter et al., 2013b]. In this work, the minimum cell size used was  $5m \times 5m$ , and the maximum  $500m \times 500m$ . Also, the cells must be quadratic in shape in order to deliver local exactness in the simulation results. Another limitation comes with the orographic data; if there are steep inclines in elevation (above 20%), the simulation can break, or at the very least give results that cannot be used for normal regulatory purposes [Richter et al., 2013b].

The extent of the simulation area can range from a few tens of metres up to several 100km, but as ARTM uses one-point measurements for the meteorological data, which are likely to be more inaccurate for regions further from the meteorological measurement station, simulation results in far distances might be entirely inaccurate. The smaller the simulation area chosen, the higher the meteorological accuracy for points further away from the measurement station. Usually ARTM is used for areas of only 10 to 20 km around a nuclear facility to find the locations of maximal exposure, which typically are within 2 km of the source.

### **1.2.1.3 Limitations in the field of application**

ARTM was developed for steady or near steady releases of radioactive nuclei from nuclear facilities, such as nuclear power plants, research facilities, and radioactive waste repositories. It requires a constant emission time period between six minutes and one year. Variations, however, can be introduced by inserting different hourly emission strengths for working days (Monday to Thursday), Fridays, Saturdays and Sundays and German holidays) to account for facilities that are operating during the week, but not, or decreased, on weekends [Richter et al., 2013b].

ARTM was not developed for sudden releases during an emergency in a nuclear facility, nor for the simulation of explosive dispersion. These scenarios cannot be simulated appropriately by ARTM.

The standard options are applicable for an emission period of at least one day up to one year. To simulate emission scenarios shorter than one day, the non-standard option 'NODAY' of ARTM must be applied [Richter et al., 2013b].

### **1.2.1.4 Necessary inputs for ARTM**

In principle, ARTM only requires two types of input in order to conduct a minimal simulation. The first requirement is an input file with meteorological data for the period of the release scenario and the anemometer position, and the second requirement is basic information about the source parameters (emission strength, emission altitude). These data alone are enough for ARTM to conduct a simple simulation, although the results might be far from realistic.

In most cases, the landscape is not flat, but orographically structured. In order to account for the orographic influence, a file with altitude information can be read-in. The orographical information must be provided in an equidistant grid with square-shaped grid cells. This means that each cell must have the same dimensions in length and width, with an altitude value given for each corner of the cell. Each orography file must include a header that indicates the dimensions of the orographical grid, the number of rows and columns, the location of the lower left (south-western) corner of the simulation area in GK coordinates (See appendix C.1) and the grid size i.e. width of one cell. ARTM also supports the input of up to 100 buildings, up to 50 monitoring points, 84 different radioactive nuclides (in up to 7 different forms – aerosol, noble gas, gaseous, gaseous bound as  $CO_2$ , in elementary form, within organic molecules, or as water

– and with up to 5 grain sizes for the aerosols) and many other input parameters, as can be seen in table 1.2.1 [Richter et al. 2013a, 2013b].

### **1.2.2 Lagrange Simulation of Dispersion and Inhalation of Radionuclides (LASAIR)**

The Lagrange Simulation of Dispersion and Inhalation of Radionuclides, short LASAIR, is a decision support system for preventing nuclear hazards and conducting safety analyses [Janicke & Janicke 2007]. Developed in 2001 by Janicke Consulting and commissioned by the BfS, LASAIR is a quick prognosis programme for sudden short-term releases of radioactive material, for example after detonation of an improvised explosive device containing radioisotopes [Janicke & Janicke 2007]. In contrast to ARTM, it does not support simulating long-term releases or releases that last longer than 24 hours, or operate with more than one emission source. LASAIR's mode of operation and grade of automatisisation are also different from ARTM's. As LASAIR was specifically developed as an operational tool for simulations in dense urban areas, it can calculate the atmospheric dispersion even with many complex building structures in the simulation area [Walter, H., Heinrich, G., 2016]. Its basis is the diagnostic wind field model Lprwnd, which was developed in accordance with the VDI-guidelines and which is similar to the TALdia model used in ARTM [Walter & Heinrich, 2016]. Dispersion is calculated with the LASAT (Lagrange Simulation of Aerosol Transport) model [Walter & Heinrich, 2016]. LASAIR allows for simulations of around 900 different types of radioactive nuclides [Janicke Consulting, 2001-2013].

#### **1.2.2.1 Operating Mode of LASAIR**

As for the use of LASAIR in emergencies, it is solely operated manually via GUI, a command line call is not necessary and not supported. The software guides the user step by step (see figure 1.2.2.1) through the inputs, leading to quick and easy simulation results to serve the operational aim for emergency situations. Apart from that, LASAIR also allows for certain optional inputs, some of which are only recommended for use by experts.

The optional settings must be chosen before starting a new simulation project. This is done by manually changing and saving a parameter file in the LASAIR program folder. Here, the experienced user can adapt certain standard parameters, such as extending the total simulation period from the default 8 hours to a maximum of 24 hours, or raising the number of simulation particles from the standard 60,000. The number of simulation particles must be handled with care, as a too high particle number can cause programme aborts due to memory overflow in the simulation process.

For the simulation of building wake effects, a user can optionally create an urban landscape with an included tool. Here he can load a cut-out of the simulation area and place, via GUI, polygonal and cylindrical shaped buildings with user defined dimensions on the map [Janicke Consulting, 2001-2013]. The only limitation for the buildings is the maximum height of 200 metres and the internal modelling domain, which is maximum  $2\text{ km} \times 2\text{ km}$ . This map with user-defined building structures must be saved separately as a file and then can be called in the first mandatory step of the simulation preparation process.

The first mandatory step in the process of running a simulation with LASAIR is to create a new project. Then the user must choose the centre of the simulation area, either by using the graphical map interface, or by inserting the desired UTM coordinates [Janicke Consulting,

2001-2013]. The centre of the simulation area also acts as the origin for internal coordinates. Next, the user can select the simulation area (options are  $80\text{ km} \times 80\text{ km}$ ,  $40\text{ km} \times 40\text{ km}$  or  $20\text{ km} \times 20\text{ km}$ ), and the resolution (grid size), which can be  $5\text{ m}$ ,  $10\text{ m}$  or  $20\text{ m}$  [Janicke Consulting, 2001-2013]. Also in this step, there are options to implement a previously designed and saved building scenario and/or to include orographical structure in the simulation. LASAIR then downloads the according maps from the Open Street Maps in the desired size and resolution. Finally, the anemometer position, which is relevant for the wind field computation, must be assigned before moving on to the next step.

In the second step, the release data are inserted. These include the position and start time of the release, details about the particle size distribution and the type of the emission source.

The particle size distribution is specified using four grain size intervals:  $< 2.5\mu\text{m}$ ,  $2.5\mu\text{m} - 10\mu\text{m}$ ,  $10\mu\text{m} - 50\mu\text{m}$ , and  $> 50\mu\text{m}$ . The allocation is done by percentage, i.e. the user can allocate the percent of all particles below the size of  $2.5\mu\text{m}$ , below  $10\mu\text{m}$ , and below  $50\mu\text{m}$ . The default values are 20%, 60% and 80%, which translates to a distribution of 20% of particles  $< 2.5\mu\text{m}$ , 40% of particles in the range of  $2.5\mu\text{m} - 10\mu\text{m}$ , 20% of particles in the range of  $10\mu\text{m} - 50\mu\text{m}$ , and 20% of particles larger than  $50\mu\text{m}$ .

For the release type there exist four types:

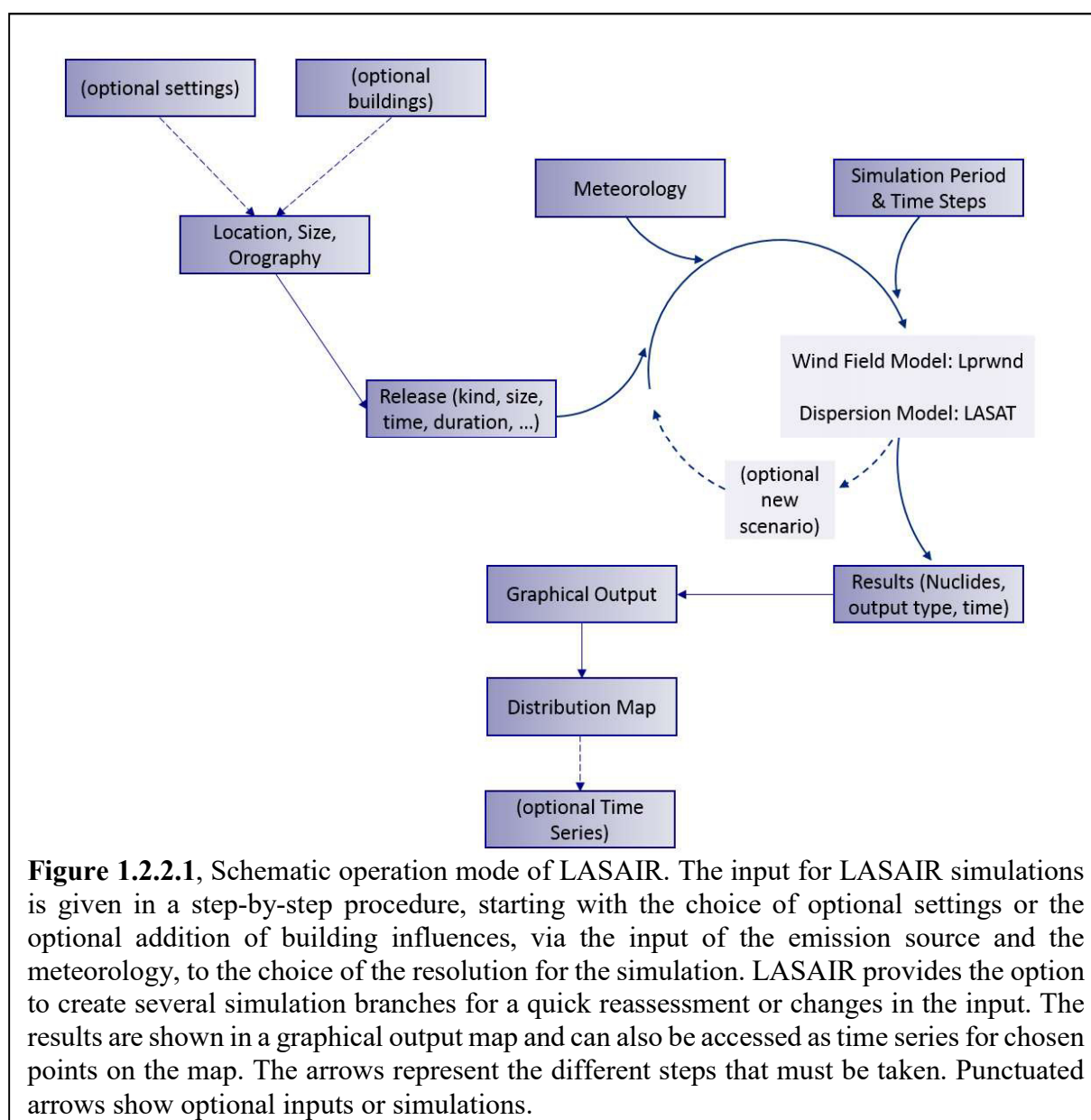
- Explosive Release  
As a result of LASAIR's main operational purpose, this is the default choice. The user can enter here the amount of explosive material (maximum at 100,000g), the horizontal and vertical extension of the explosion cloud and the time of release [Janicke Consulting, 2001-2013].
- Stack  
For the stack option, the stack height (maximum 200m), diameter and emission time must be given [Janicke Consulting, 2001-2013]. In the current version, LASAIR, in contrast to ARTM, does not automatically consider the plume rise of warm exhaust. This needs to be calculated manually and added to the stack height. In this work, the stack option is the only release option that was applied in order to have best comparability to ARTM simulations.
- Horizontal Jet  
The horizontal jet is defined by the release height, exhaust velocity, affected area, width and vertical extension of the release area, angular direction of the jet and release duration [Janicke Consulting, 2001-2013].
- Vertical Jet  
The parameters for the vertical jet are nearly the same as for the horizontal one, except for the vertical extension of the release area, which is replaced by the length of the release area [Janicke Consulting, 2001-2013].

After the input of the release parameters, the meteorology parameters must be given. Here the user has to manually insert time, wind speed, wind direction and dispersion category according to Klug-Manier [Janicke Consulting, 2001-2013]. The anemometer position must also be inserted in this step. Optionally, the user can assign roughness lengths to areas on the map, according to the CORINE categories [Janicke Consulting, 2001-2013]. If nothing is chosen, LASAIR uses the default value of  $0.5\text{ m}$  for the entire simulation area.

Then, after choosing the simulation period and the time resolution for the results, the simulation can be started.

For each of the time steps, the wind field model Lprwnd (explained in appendix A.2) calculates the current situation for the whole simulation area, and the dispersion model LASAT performs the distribution of particles. This allows the user to access and view the results for the first time steps already while the remaining ones are still being calculated.

Finally, the user can visualise the results of the simulation. Here he has the option to choose between visualising inhalation dose, activity concentration, surface deposition, gamma dose and gamma activity. For both of the dose types, additional dropdown menus allow the choice of different organs and the age of the affected person. In addition, a deposition option allows for an input of precipitation, which is assumed to be constant over the entire simulation period and homogeneous over the model domain.



According to the user manual, LASAIR allows the user to choose from a list of over 900 nuclides [Janicke Consulting, 2001-2013]. The user can select up to 5 different nuclides at the same time to show the combined results [Janicke Consulting, 2001-2013]. The released amount

is the total amount of radioactivity released per nuclide over the entire simulation period [Janicke Consulting, 2001-2013]. It assumes that for every simulation interval the same fraction of the total amount is released.

The chosen outputs are displayed in the distribution map. Different time periods can be visualised, by clicking on this visualisation absolute values are given, and the user can create a data table summarising the results of the whole map [Janicke Consulting, 2001-2013].

Additionally, there is the option to display time series distributions for any point on the map [Janicke Consulting, 2001-2013].

Once the initial simulation has been completed, in order to allow for quick changes in the input parameters, or to insert new conditions that may appear during the release, the user has the option to create new simulation scenarios that are split up to the main scenario like branches, starting either at the very beginning of the first simulation, or at any time during the first simulation [Janicke Consulting, 2001-2013].

If a new branch is created, the user can edit release and meteorology input data again, before simulating the new scenario, and potentially later creating more branches.

### **1.2.2.2 Limitations of LASAIR**

Due the primary purpose of LASAIR for its use as a quick decision support system for dirty bomb scenarios, it has limitations for other areas of application such as simulating constant releases via a stack [Walter & Heinrich, 2016].

During the work with LASAIR for the comparison with ARTM, as it was performed here for the Šoštanj scenario (see chapters 1.4.3 and 4), several limitations were identified for the stack release mode and continuous emissions. These are as follows:

- Vertical extension of buildings  
Buildings can only have a maximum height of 200m. This constraint is due to the diagnostic wind field.
- Stack height  
The maximum possible stack height is 300m.
- Anemometer altitude  
The anemometer can range from 2m above ground to maximum 200m altitude.
- Plume rise  
LASAIR, in the version applied, does not internally calculate the plume rise for hot sources; this needs to be done manually.
- Emission parameters  
Besides the above listed parameters, stack height, diameter and emission duration, there are no further inputs possible. It is not possible to set many important variables, such as emission velocity, humidity, heat transfer, and time-dependent changes in the exhaust.
- Number of emission sources  
LASAIR only allows for one emission source per simulation project. Simulations with two or more emission sources have to be split into multiple projects and the results of the simulations must then be added up manually.

- Amount of parallel emitted nuclides  
LASAIR allows only for a maximum of 5 different nuclides to be emitted at the same time.
- Simulation period  
The maximum simulation period is only 24 hours. This is a considerable limitation for applications of LASAIR on medium-term emissions longer than one day.
- Lack of automation  
The used LASAIR version does not allow for an automated read-in of input parameters. This is particularly problematic for the meteorological data, which have to be entered manually for each new simulation, significantly decreasing the practicality of using LASAIR for detailed studies involving long release times.
- Grid size  
LASAIR only allows for grid sizes of 5m, 10m and 20m. Other, user-defined grid sizes cannot be applied for the simulation.

### **1.2.2.3 Necessary inputs for LASAIR**

All the inputs in figure 1.2.2.1 that are not marked as ‘optional’ are necessary for LASAIR. If the user does not provide values for necessary input parameters, LASAIR uses the default values given in the GUI.

## **1.3 Additional programmes**

In order to apply ARTM and LASAIR for marginal cases or cases slightly outside their original scope of use, and to post-process and analyse the resulting large amount of data, some additional tools were required. Some of them were already available for use, whereas others had to be specifically developed to perform the necessary tasks, using the programming languages C and Python.

As ARTM and LASAIR have different input requirements and also have different layouts of the output data, the developed programme tools had to be specific for use with one or the other simulation software. The used existing and in this work developed programmes are briefly explained in the following sub-sections.

### **1.3.1 ARTM support programmes**

The tools and programmes used to support the simulations with ARTM can be grouped into three different sets. The largest one was a set of tools to convert orographical information from raw data, via several steps, into a format that ARTM can read and use. The other two sets included a programme to convert meteorological data into the ARTM data input format and a programme to assign dispersion categories, and a programme to sum up and combine the ARTM simulation results from several individual simulations to obtain average values.



### 1.3.1.1 Programmes for orography conversion

For non-standard input data and international cartographic data, some preparatory work is necessary before they can be used in ARTM, due to the restrictions and limitations of the software described earlier.

For example, at <http://data.geocomm.com/catalog/index.html> worldwide Digital Elevation Models (DEMs) are freely accessible. These are available in  $1^\circ \times 1^\circ$  grids with a cell size of  $0.0083^\circ$  (or  $0.0167^\circ$  for far northern/southern grids). Since these raw data exist only in binary format and in geo-coordinates instead of in an equidistant grid as necessary for ARTM, the DEM must be converted into an ASCII file and then adapted to meet the grid requirements using a set of small programmes, 'Grid Maker 1.0', specially developed for this purpose. This package currently includes the routines 'Grid Calculator' and 'Grid Equaliser'. The other programmes listed and explained below will be part of the future 'Grid Maker 2.0' package.

#### i. MicroDEM

MicroDEM is a free-ware programme that can be downloaded at [http://softpicks.com.de/software/Multimedia/Bildnissezuschauer/MICRODEM\\_de-295860.htm](http://softpicks.com.de/software/Multimedia/Bildnissezuschauer/MICRODEM_de-295860.htm). It can be used to read-in any kind of DEM. Although it has multiple map reduction tools, here it will only be used to convert the input DEM from binary (dt0) into an ASC file as it can be used for ARTM. To do this, the .dt0 file must first be opened in MicroDEM. In the 'File' Menu, the option 'Open DEM' needs to be chosen. Once the input DEM is opened, it will then simply be saved as an 'ASCII Arc Grid'. In order to allow for flawless processing with the Grid Equaliser, it is of advantage to name the file with 'longitude\_latitude', e.g. 'N48\_E11'.

#### ii. Grid Size Calculator

The Grid Size Calculator (GSC) is a C programme that calculates the number of rows and columns necessary for conversion of a DEM into an ARTM-readable file with the Grid Equaliser follow-up tool. The user inserts the latitude of the southern edge of the DEM (for DEM from the southern hemisphere, the latitude of the northern edge needs to be inserted) as a decimal geo-coordinate, the number of rows and columns of the original DEM and the preferred grid size for the ARTM simulations, which can be at maximum 500 meters. GSC has an internal input parameter for the size of the original grid, which is set by default to  $0.0083^\circ$ . If the input grid has a different size, this needs to be changed within the programme code and recompiled before using.

Using the mathematical formulations described below, GSC calculates and prints out the mean latitude, which goes through the middle of the DEM area in  $^\circ$ , the Earth radius at the mean latitude in metres, the maximum latitude of the DEM in  $^\circ$ , the Earth radius at the maximum latitude in metres, the total length of the input DEM in the x-and y-directions, the average cell size of the input DEM, and – most important for the next preparatory step – the dimensions of the later output grid file in numbers of rows and columns for the chosen final grid size.

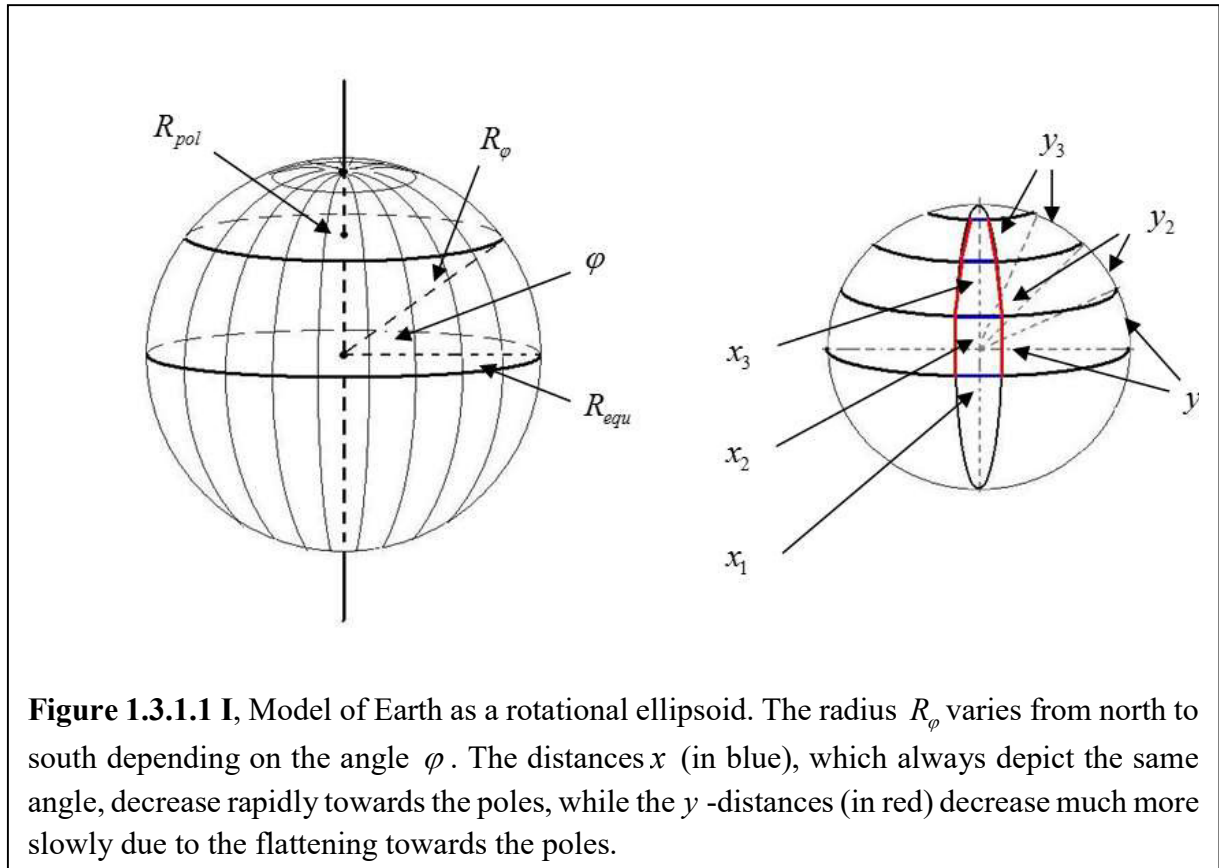
The following description of the algorithm was translated and updated from the unpublished Grid Maker 1.0 User Handbook (available in German only), written by the author of this thesis.

In GSC, Earth is approximated as a rotational ellipsoid rather than a perfect spherical object in order to account for pole flattening. The polar ( $R_{pol} = 6356.752\text{km}$ ) and equatorial radii (

$R_{equ} = 6378.137km$ ) differ in  $21.385km$ . Between the poles and equator, the radii vary with latitude. In order to account for this variation, GSC individually calculates the earth radius  $R_\varphi$  of the chosen DEM as in equation (1.3.1.1 i) using the angle  $\varphi$  (see figure 1.3.1.1 I).

$$R_\varphi = \sqrt{\frac{(R_{equ}^2 \cos(\varphi))^2 + (R_{pol}^2 \sin(\varphi))^2}{(R_{equ} \cos(\varphi))^2 + (R_{pol} \sin(\varphi))^2}} \quad (1.3.1.1 \text{ i})$$

From the approximation of Earth as a rotational ellipsoid deduces that the distances  $y_1, y_2, y_3$ , for the same change in angle, decrease from the equator towards the poles. Even larger differences can be observed in the  $x_1, x_2, x_3$  distances between two longitudinal lines, due to the increasingly rapid decrease towards the poles of the length of the latitudinal lines, which is why areas defined by angle sizes have a more or less trapezoidal shape. These are incompatible for the direct read-in into ARTM.



GSC initially calculates the total angles in latitudinal and longitudinal directions of the input DEM by using the inserted coordinates, the number of rows and columns in the DEM data file as well as the input DEM specific step size in degrees.

Here  $x_{total}$  is the total angle in longitudinal direction in degree, with  $x_{step}$  being the angular step for the longitudinal direction, and  $n_x$  the total amount of columns of the DEM data file.

$$x_{total} = x_{step} \cdot n_x \quad (1.3.1.1 \text{ ii})$$

The next step of GSC calculates the mean latitude  $y_{middle}$  of the DEM using (1.3.1.1 iii) with  $y_{latitude}$  being the input latitude value in  $^\circ$ ,  $y_{step}$  being the angular step for the latitudinal direction and  $n_y$  being the total amount of rows in the input DEM.

$$y_{middle} = y_{latitude} + y_{step} \cdot \frac{n_y}{2} \quad (1.3.1.1 \text{ iii})$$

The resulting  $y_{middle}$  goes directly into the equation (1.3.1.1 i), which gives the mean radius  $R_{middle}$  for the DEM (1.3.1.1 iv).

$$R_{middle} = \sqrt{\frac{(R_{equ}^2 \cos(y_{middle} \cdot \pi/180^\circ))^2 + (R_{pol}^2 \sin(y_{middle} \cdot \pi/180^\circ))^2}{(R_{equ} \cos(y_{middle} \cdot \pi/180^\circ))^2 + (R_{pol} \sin(y_{middle} \cdot \pi/180^\circ))^2}} \quad (1.3.1.1 \text{ iv})$$

Since for the calculation of the optimal grid size the most northern (for DEMs of the northern hemisphere) or the most southern (for the southern hemisphere) latitudes are necessary, this  $R_{max}$  has to be calculated as well, as described in (1.3.1.1 v).  $R_{max}$  is not the maximal value for  $R$ , but is the radius where  $y$  is at its maximum  $y_{max}$ .

$$R_{max} = \sqrt{\frac{(R_{equ}^2 \cos(y_{max} \cdot \pi/180^\circ))^2 + (R_{pol}^2 \sin(y_{max} \cdot \pi/180^\circ))^2}{(R_{equ} \cos(y_{max} \cdot \pi/180^\circ))^2 + (R_{pol} \sin(y_{max} \cdot \pi/180^\circ))^2}} \quad (1.3.1.1 \text{ v})$$

$$\text{with } y_{max} = y_{latitude} + y_{step} \cdot n_y \quad (1.3.1.1 \text{ vi})$$

Once the radii are calculated, the mean distances,  $X_{total}$  and  $Y_{total}$ , the longitudinal and latitudinal distances (1.3.1.1 vii and 1.3.1.1 viii) as well as the most northern (for northern hemisphere) or the most southern (for southern hemisphere) latitudinal distance  $X_{max}$  (1.3.1.1 ix) of the DEM can be determined.

$$X_{total} = 2\pi \cdot R_{middle} \cdot x_{total} \cdot \frac{\cos(y_{middle} \cdot \pi/180^\circ)}{360^\circ} \quad (1.3.1.1 \text{ vii})$$

$$Y_{total} = 2\pi \cdot R_{middle} \cdot \frac{y_{total}}{360^\circ} \quad (1.3.1.1 \text{ viii})$$

$$X_{max} = 2\pi \cdot R_{max} \cdot x_{total} \cdot \frac{\cos(y_{max} \cdot \pi/180^\circ)}{360^\circ} \quad (1.3.1.1 \text{ ix})$$

Finally the amount of rows  $N_{row}$  and the amount of columns  $N_{col}$  are calculated, which are a required inputs for the Grid Equaliser to calculate a constant equidistant grid with cell size

$cellsize_{Column / Row, out}$  . Therefore the total lengths in both  $x$ - and  $y$ - directions (for the  $x$ -direction only the most northern, or for southern hemisphere the most southern latitudinal distance  $X_{max}$  is used) are divided by the desired cell size and subtracted by one (1.3.1.1 x). This is necessary to account for boundary issues that can occur within Grid Equaliser to avoid the creation of boundary rows and columns with false values.

$$N_{Column} = \frac{X_{max}}{cellsize_{Column, out}} - 1$$

$$N_{Row} = \frac{Y_{total}}{cellsize_{Row, out}} - 1$$
(1.3.1.1 x)

### iii. ASC Restructure

The ASC Restructure support programme is a simple tool (programmed in C) to order the ASC files produced with MicroDEM in a readable form and print them out in a separate file. The original ASC files are simply a list of values, not structured in rows and columns that represent the DEM area. This makes it hard for the user to view the DEM, for example as an MS Excel sheet, which is necessary if only a smaller part of the large map should be selected. This selection can be done manually after applying the ASC Restructure tool, but in many cases it is more comfortable to perform the selection of a smaller area after the equalisation operation as performed by Grid Equaliser. Only for cases in which a small grid size is anticipated, is it suggested to first shrink the DEM area and then to use the Grid Equaliser.

### iv. Grid Equaliser

The Grid Equaliser (GE) programme is the main tool (programmed in C) to prepare an input DEM based on geo-coordinates into an equidistant grid of elevation values. It is based on an older source code that was developed internally by K. Arnold for the purpose of preparing maps from the Fukushima area to be used within ARTM. The GE programme explained here builds on the formalism used in the previous version, but, due to its adaptations, especially its more detailed algorithm for calculating the grid, allows for a more global application. The credits for the interpolation method applied here go to K. Arnold.

The description of the algorithm was translated and updated from the Grid Maker 1.0 User Handbook (in German only) written but unpublished by the author of this thesis.

GE reads the input ASC file previously prepared with MicroDEM or ASC Restructure. Note that before use of the input ASC file, its header lines have to be deleted. The user inserts the filename of the input file, which should be named by the coordinates and the file type, e.g. 'N48-E11.ASC'. The file type is based on the geocomm.com data file sizes, which come either in 121 rows and 61 columns or in 121 rows and 121 columns. In case of different row and column numbers (for example if a certain area has been cut out), the user has to apply the desired changes in the source code and recompile before usage. Also, the output cell size can only be changed in the source code and is by default 500m. As C only allows for a maximum of 40,000 table entries, it is recommended for small cell sizes to first decrease the DEM area before applying GE.

GE is based on the approximation of Earth as a rotational ellipsoid as described above for the Grid Size Calculator (see also figure 1.3.1.1 I). The basic principle of GE is to transform a grid

based on geo-coordinates into an equidistant grid. As can be seen in figure 1.3.1.1. II, the – from the view of the metrical system – trapezoidally shaped grid cells of the geo-coordinates need to be turned into perfectly squared grid cells. Each point on the grid symbolises one altitude value.

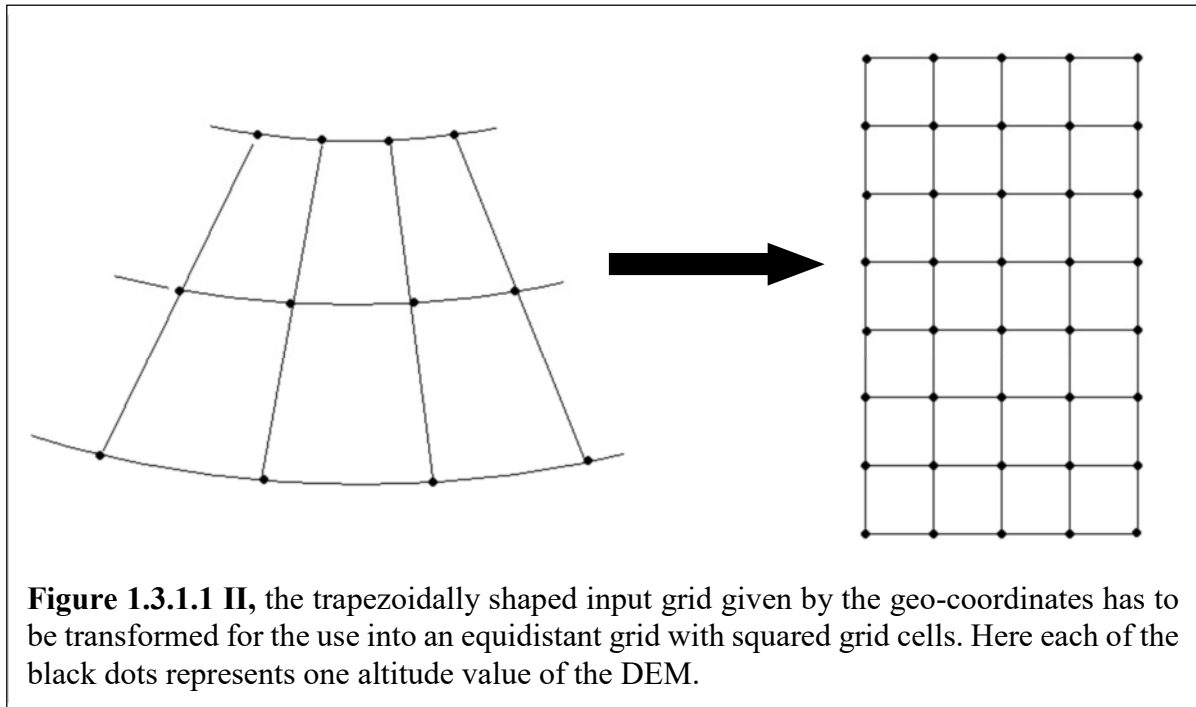


**Figure 1.3.1.1 II**, the trapezoidally shaped input grid given by the geo-coordinates has to be transformed for the use into an equidistant grid with squared grid cells. Here each of the black dots represents one altitude value of the DEM.

The GE programme proceeds by first adapting the cell sizes in the vertical (north-south) direction to the desired cell size (figure 1.3.1.1 IIIa) and afterwards adapting the horizontal (east-west) cell sizes (figure 1.3.1.1 IIIb). For example a grid cell in Geo-coordinates with  $0.0083^\circ$  grid size can have for latitudes around  $45^\circ$  the four cell sides with  $a=600\text{m}$ ,  $b=900\text{m}$ ,  $c=610\text{m}$  and  $d=900\text{m}$ . These differences between the northern and southern edges become even more severe when going further pole-wards, where the difference can be a few hundred meters. For ARTM, only grids with constant sizes, for example  $500\text{m}$  by  $500\text{m}$ , can deliver useful simulation results. Altitude values for the new grid corners are calculated via linear interpolation, as described below in more detail.

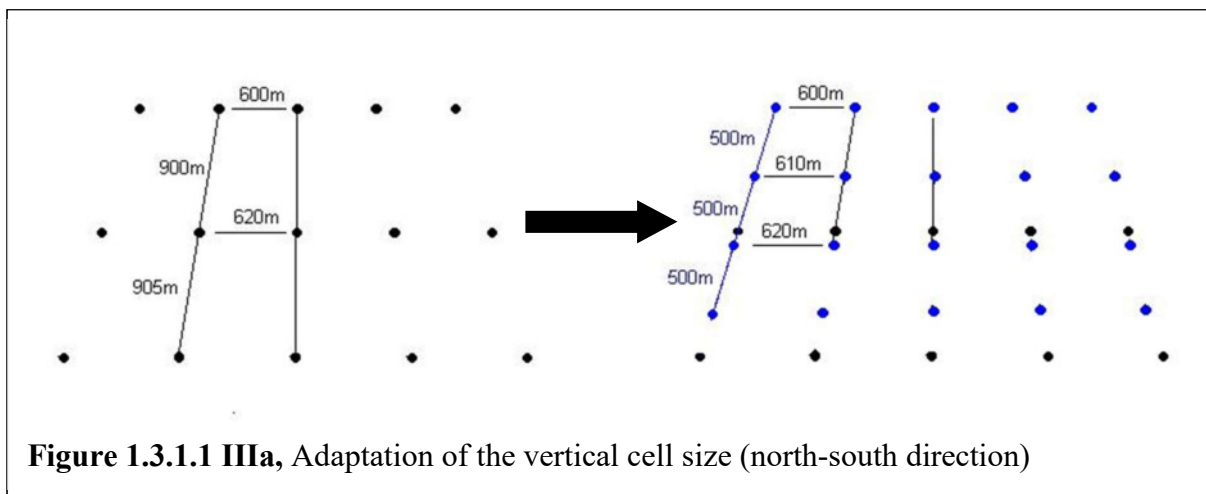


**Figure 1.3.1.1 IIIa**, Adaptation of the vertical cell size (north-south direction)

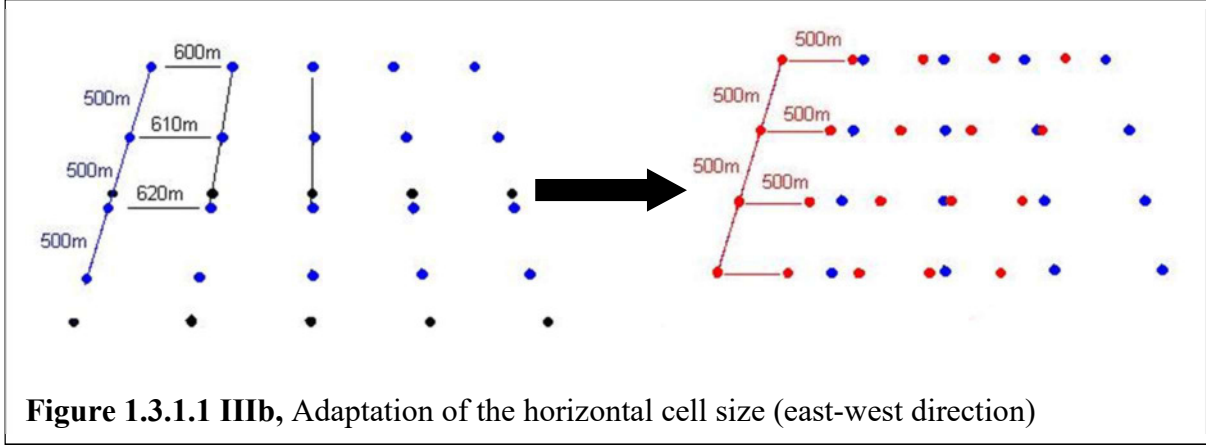


**Figure 1.3.1.1 IIIb, Adaptation of the horizontal cell size (east-west direction)**

After successfully inputting the starting parameters, GE reads the DEM data and saves them internally, and then creates a working grid of 250 rows and 160 columns (these numbers can be adapted in the source code), which serves as internal storage for the first calculation step. This first step is, as shown in figure 1.3.1.1 IIIa, the adaptation of the vertical distances. Therefore, the first row of the DEM data gets copied into the working grid and the values of the following rows are calculated via linear interpolation starting from there.

This is performed by calculating the longitude and latitude for each data point with equation (1.3.1.1 xi). Here *longitude* and *latitude* are the initial values that define the position of the DEM, for example 48°N and 11°E. To these values an angle is added for each point on the grid that refers to its position in the working grid. Therefore it uses  $step_{we}$  and  $step_{ns}$ , which are the initial values given by the type of input grid, for example 0.0083°, the  $we_o$  and  $ns_o$  values, which are the initial column and row numbers, respectively, and  $q$  and  $p$ , which are running numbers in the programme code to address each of the entries of the grid.  $\frac{we_o}{we_o}$  is the relation between

input grid and working grid, however for this first calculation step, where only the north-south direction is adjusted, the amount of points in the east-west direction is kept constant.

While the defining coordinate is the lower left entry in the grid, to determine the correct north-south values, the maximum north extension has to be calculated by adding  $step_{ns} \cdot ns_o$  and then subtracting the north coordinate for the following lines.

$$\Delta_{we} = longitude + \left( q + \frac{1}{2} \right) \cdot step_{we} \frac{we_o}{we_o}$$

$$\Delta_{ns} = latitude + step_{ns} \cdot ns_o \left( 1 - \frac{p + \frac{1}{2}}{ns_n} \right) \quad (1.3.1.1 \text{ xi})$$

With  $\Delta_{ns}$  inserted into (1.3.1.1 iv) as the  $y$ -value, for each point in the grid, the individual earth radius  $R_{ind}$  is calculated individually and enters into (1.3.1.1 xii) for the individual cell size of the input grid.

$$dy = 2 \cdot \pi \cdot R_{ind} \frac{step_{ns}}{360^\circ} \quad (1.3.1.1 \text{ xii})$$

Although  $dx$  is also calculated the same way, it is not used for the first step. Now in (1.3.1.1 xiii) the position of the next new grid point is calculated with  $cellsize_{out,ns}$  being the desired output cell size, for example 500m.

$$Pos_{new,ns} = p \cdot cellsize_{out,ns} \quad (1.3.1.1 \text{ xiii})$$

This position will then be compared with the position of the old point  $Pos_{old,ns}$ , while  $i$  runs in a for-loop from 0 to  $ns_o$ , to keep the indices of the old grid points, which are direct neighbours in the north-south direction to the new point (1.3.1.1 xv). That means that in the programme the loop is stopped at the first position of the old grid that has a larger difference to the edge of the grid than the new position has. The latter one will be given the index  $i$  and therefore the value with index  $i-1$  lies directly below the new value, which means that the neighbouring altitude values will then be the ones used for the interpolation of the altitude at the new position point.

$$Pos_{old,ns} = i \cdot dy \quad (1.3.1.1 \text{ xiv})$$

$$\begin{aligned} above_{old,ns} &= i \\ below_{old,ns} &= i - 1 \end{aligned} \quad (1.3.1.1 \text{ xv})$$

The interpolation to create a new altitude value, based on the formalism by K. Arnold, is performed in dependency of the position of the new grid point in support of the two indices shown in (1.3.1.1 xv). In the source code, to each grid point  $[p, q]$  a corresponding value is assigned that represents the value of the input grid  $i-1$ , plus a value that represents the altitude difference between the points with the indices  $i$  and  $i-1$  multiplied by the ratio of how the new point separates the distance between the two old points. The according mathematical description is shown in (1.3.1.1 xvi) below:

$$V_{grid_{work}}(p, q) = V_{grid_{old}}(i-1, q) + (V_{grid_{old}}(i, q) - V_{grid_{old}}(i-1, q)) \cdot \frac{Pos_{new,ns} - (i-1) \cdot dy}{i \cdot dy - (i-1) \cdot dy} \quad (1.3.1.1 \text{ xvi})$$

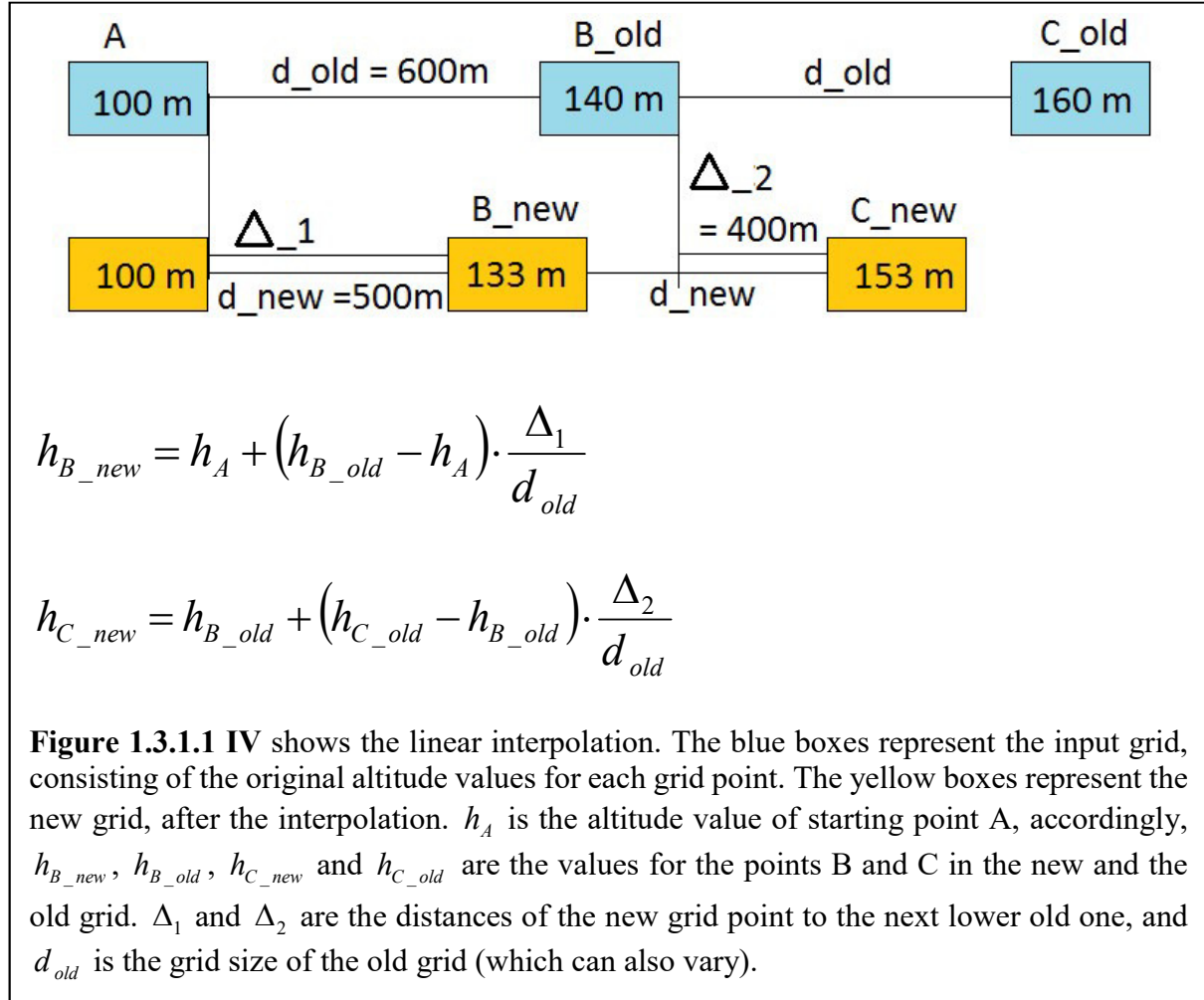
Here,  $V_{grid_{work}}(p, q)$ ,  $V_{grid_{old}}(i-1, q)$  and  $V_{grid_{old}}(i, q)$  represent the altitude values of the corresponding positions on the grid for both, the working and the input grids. The ratio of  $\frac{Pos_{new,ns} - (i-1) \cdot dy}{i \cdot dy - (i-1) \cdot dy}$  represents the ratio of the distance between the new grid point and the next lower old grid point to the distance between the two old grid points.

Figure 1.3.1.1 IV demonstrates graphically how the process of linear interpolation is applied. In the example, the input grid (here called ‘old grid’) has a grid size of 600 m and the desired output grid (‘new grid’) a grid size of 500 m. The first altitude (of a row or column) is directly copied from the ‘old grid’ into the ‘new’ one, as it is not changed. In the example this means that point A, with an altitude of 100 m, is identical in height in both grids. Now point B in the old grid is 140 m in altitude. In order to calculate the altitude of the second point in the ‘new grid’, the formula shown in the graphic is used: the difference in altitude between point A and point B in the old grid is multiplied by the ratio of  $\Delta_1$  to the ‘old’ grid size. Added to the altitude  $h_A$  of point A, this results in the altitude  $h_{B\_new}$  for the new point B\_new.  $\Delta_1$  is the

distance  $d_{new}$  between B\_new and the old point A, which in this case happens to be the grid size of the 'new grid'.

Calculating the altitude of C\_new follows the same algorithm. The only difference is that now  $\Delta_2$  is not necessarily the same as the 'new' grid size. That means that now the 'old points' need to be used for adding the additional altitude.

For all further points this procedure is applied to calculate the new altitude values.



Once the working grid is filled in the north-south direction with the new altitude values, in a second step the east-west direction is handled in the same way in order to obtain the final equalised output grid.

The only difference lies now in (1.3.1.1 xi) where the  $we_o$  divisor has to be replaced with  $we_n$  to obtain (1.3.1.1 xvii).

$$\Delta_{we} = longitude + \left( q + \frac{1}{2} \right) \cdot step_{we} \frac{we_o}{we_n}$$

$$\Delta_{ns} = latitude + step_{ns} \cdot ns_o \left( 1 - \frac{p + \frac{1}{2}}{ns_n} \right) \quad (1.3.1.1 \text{ xvii})$$



All other formulas used for calculations in the north-south direction stay the same, except that now the east-west parameters are used, as well as  $q$  instead of  $p$ , as in (1.3.1.1 xviii).

$$Pos_{new,we} = q \cdot cellsize_{out,we} \quad (1.3.1.1 \text{ xviii})$$

## v. Location Calculator

This support tool is a small C-programme developed for the purpose of calculating the distances of points of interest in relation to other points. For example, it can be used when the coordinates of a source or building are known only in geo-coordinates, but in order for ARTM to use them they need to be given as distances to the south-western corner of the simulation area (or wherever the coordinate origin is located). The Location Calculator (LC) reads in the geo-coordinates of the requested location and the coordinates of the reference location (coordinate origin) and then prints out the distances in the  $x$ - and  $y$ -directions in metres. LC can also output a file with all the calculations.

LC calculates first the differences in the latitudinal and longitudinal directions with (1.3.1.1 xix) and (1.3.1.1 xx).

$$\Delta_{lat} = lat_{location} - lat_{reference} \quad (1.3.1.1 \text{ xix})$$

$$\Delta_{lon} = lon_{location} - lon_{reference} \quad (1.3.1.1 \text{ xx})$$

It then calculates the Earth radius  $R_{middle}$  at the mean latitude using the formula (1.3.1.1 iv) as described for the GSC programme, with  $y_{middle}$  being the mean latitude of the requested location and the reference location (1.3.1.1 xxi).

$$y_{middle} = \frac{lat_{location} - lat_{reference}}{2} \quad (1.3.1.1 \text{ xxi})$$

The final distances in the  $x$ - and  $y$ -directions are then calculated using (1.3.1.1 xxii) and (1.3.1.1 xxiii), respectively.

$$dist_{lon} = 2 \cdot \pi \cdot R_{middle} \cdot \cos\left(\frac{y_{middle} \cdot \pi}{180^\circ}\right) \cdot \frac{\Delta_{lon}}{360^\circ} \quad (1.3.1.1 \text{ xxii})$$

$$dist_{lat} = 2 \cdot \pi \cdot R_{middle} \cdot \frac{\Delta_{lat}}{360^\circ} \quad (1.3.1.1 \text{ xxiii})$$

## vi. Application of the Programmes

All of the programmes described in the sections above were specifically developed to prepare input data for the data sets ‘La Hague’ and ‘Šoštanj’ for use in ARTM, as there were either no orographical data provided or the provided data could not be used successfully in ARTM.

Therefore, for these scenarios the corresponding digital elevation maps were downloaded from geocomm.com as binary files in geo-coordinates of the size  $1^\circ$  by  $1^\circ$ . In order to make these files readable, the MicroDEM programme was applied as described above to convert the file format.

At this point the ASC restructure programme could be used to view the DEM, for example in Excel, and to manually cut out an area of interest.

As a next step it is necessary to use the GSC, in order to find out the optimal grid size for the output grid and to ensure feasibility within the grid size constraints. The GSC programme gives as an output the number of rows and columns as well as the desired grid size.

This information is then inserted into the source code of the GE programme (more detailed information on where the values need to be inserted can be found in the comments of the source code). GE then creates the final output map, which is in the right format for inputting into an ARTM simulation.

As ARTM not only requires an altitude map, but also requires that all locations, such as locations of the emission source, the anemometer, monitoring points and buildings, be given in terms of distance to the origin location of the input map, the LC programme can be used to easily calculate these distances if the user only has the geo-coordinate locations available.

### **1.3.1.2 Conversion of Meteorological Data**

Diffusion Class Calculator (DCC) is a C-programmed tool that was developed in order to assign diffusion categories to meteorological data sets lacking diffusion categories. Diffusion or dispersion categories are a method to parameterise atmospheric turbulences due to different atmospheric layering. Besides the Monin-Obukhov-length, ARTM uses the Klug-Manier classification system and consists of 6 different dispersion categories, ranging from very stable to neutral to very unstable layering [Richter et al., 2013a, 2013b].

DCC was developed specifically for use with the meteorological raw data provided with the 'Šoštanj' scenario data set. As described in chapter 2.1.1.4, the dispersion category cannot be measured directly, but there are multiple methods to estimate it. The one that was applied in this measurement campaign were vertical wind velocity measurements via SODAR (Sonic Detection And Ranging). The KTA 1508 (2006) includes a table to categorise the dispersion class depending on the horizontal and vertical wind velocity (see table 2.1.1.4 II).

DCC now uses the values in these tables to assign a dispersion category for each of the meteorological measurements and then prints out a meteorological file in the correct formatting to be used for simulations with ARTM.

### **1.3.1.3 Analysis of Simulation Results**

In order to combine the results of multiple ARTM simulations of the same scenario but with different initial particle distributions, the 'ARTM results combinator' (ARTMres) was developed. It automatically calculates mean values, maximum values and standard deviations. This programme was written in Python. Upon inserting the path and the names of the simulation project folders, ARTMres reads the '.dmna'-files for concentration, deposition and gamma submersion that were produced with ARTM.

ARTMres can create 5 different output file types, depending on the number of input types; it creates a file that

- i. only contains the maximum values for a particular nuclide, their position in the simulation area and their percentage deviation from the mean value of all maxima.
- ii. combines the concentration/deposition/gamma submersion maps of all simulation of the ensemble by creating the mean values for each grid cell of all different input simulations.

- iii. contains a map of the absolute values of the standard deviations of the concentration/deposition/gamma submersion.
- iv. contains a map of the percentage values of the standard deviations of the concentration/deposition/gamma submersion.
- v. combines all the time series of all chosen monitoring points into a mean time series and their standard deviations in absolute and percentage values.

The standard deviation  $\sigma$  typically is described by the square root of the variance  $Var(x)$ , with the variance being dependent on the expected value  $E[x]$ .

$$\sigma_x = \sqrt{Var(x)} \quad (1.3.1.3 \text{ i})$$

$$Var(x) = E[x^2] - (E[x])^2 \quad (1.3.1.3 \text{ ii})$$

Since we base the calculation of the standard deviation on a small sample, we use the unbiased sample standard deviation described by Richard M. Brugger [Brugger, 1969]. He states that (1.3.1.3 iii) is a viable approximation of the standard deviation that is valid also for small sample sizes  $n$  [Brugger, 1969].

$$\hat{\sigma} = \sqrt{\frac{1}{n-1.5} \sum_{i=1}^n (x_i - \bar{x})^2} \quad (1.3.1.3 \text{ iii})$$

As he shows, sample sizes larger than 6 can deliver fairly accurate estimations, if significant digits are limited to 2; for 3 significant digits, 10 samples are sufficient [Brugger, 1969].

Here in this work 16 different samples were always used to calculate the standard deviation, to ensure a high accuracy while keeping the amount of simulation runs as low as possible. ARTMres uses the unbiased estimation of the standard deviation as described in (1.3.1.3 iii) for all analyses performed on ARTM output files.

The created output files ii. to iv. are in the same format as the inputs, so that they can be viewed in GO-ARTM, given that the user copies additionally an ARTM.txt file into the folder of the output files, so that GO-ARTM recognises them as a simulation project.

### 1.3.2 LASAIR support programmes

As LASAIR, due to its application purpose (as described in 1.2.2), requires the manual input of all parameters, there is little scope for employing an easily programmed tool to simplify the inputs.

The only support tool that was developed for LASAIR is a tool called LASAIRres that combines time series results. As LASAIR does not allow for calculations with different initial particle distributions, as is the case with ARTM and the starting random number, there is no reason to calculate also a standard deviation for the results as is done in ARTMres (see section 1.3.1.3).

LASAIRres is, like ARTMres, programmed in Python. It serves the sole purpose of combining multiple time series results into one file in order to be easily handled with Excel to view and plot the data.

## 1.4 Data sets descriptions

While there exist quite a few experimental data sets on atmospheric dispersion measurement campaigns, the majority of these are on a micro-scale (in the range of tens to hundreds of metres) and involve only short term releases ranging from a few milliseconds (e.g. for explosions) up to a few hours (e.g. accidentally increased releases). There exists little to no freely available measurement data of radionuclide immissions for continuous long-term releases in high resolution.

While the emissions from the stacks are quite well monitored for most nuclear facilities, the artificially emitted radionuclide contents are usually too small to be measured above the natural background radiation in the surrounding local area [LfU, 2016]. There exist only a few facilities, such as the AREVA La Hague nuclear reprocessing plant, where larger quantities of artificial radionuclides are emitted that can be found in immission measurements in far-off locations, and usually these data are restricted and hard to access.

As an alternative, the data from conventional emissions can be used in order to simulate the atmospheric dispersion, and then compare the simulation results with the immission measurements.

Here, several data sets are described that were used for the verification and validation of ARTM.

### 1.4.1 La Hague

The data set for the La Hague scenario has been derived mostly from a publication of Connan et al. (2013) about modelling the  $^{85}\text{Kr}$  release of the AREVA La Hague nuclear reprocessing plant. There they describe several short-term measurement campaigns in the region nearby, and the application of different simulation models to simulate and reconstruct the measurement results [Connan et al., 2013]. Out of these measurement campaigns, the one of interest for the simulation with ARTM is the one that was conducted from the 26<sup>th</sup> to the 27<sup>th</sup> of February 2009, where a 2-day continuous measurement of the  $^{85}\text{Kr}$  immission (in Bq per cubic meter) at the IRSN (Institut de Radioprotection et de Sûreté Nucléaire) Cherbourg was taken [Connan et al., 2013].

The publication contains several diagrams on the meteorology, emission and immission data. Due to the non-existence of data tables, the data were read out directly from these diagrams, therefore introducing a small ‘read-out’ deviation.

The following data were taken or derived from Connan et al. (2013):

#### i. Meteorological Data

The meteorological data used in Connan et al. (2013) comprise wind speed and wind direction from the release location only. These were read out from the diagrams and put into the tabular input format required by ARTM. The resulting table can be seen in appendix E. The estimated ‘read-out’ uncertainty for the wind direction is  $5^\circ$  and for the wind speed  $0.5\text{ms}^{-1}$ .

The anemometer height is, at 100 metres, the same as the release height [Connan et al., 2013].

#### ii. Emission Data

Connan et al. (2013) lists two release sources, the stacks UP2-800 (located at  $49.67705^\circ\text{N}$ ,  $1.87941^\circ\text{W}$ ) and UP3 ( $49.67797^\circ\text{N}$ ,  $1.87606^\circ\text{W}$ ) of the AREVA La Hague reprocessing

plant, each of them with a stack height of 100 metres. As for the  $^{85}\text{Kr}$  emission, only the hourly release values in  $\text{Bq} \cdot \text{s}^{-1}$  for the 26<sup>th</sup> of February are given in the publication. The estimated ‘read-out’ uncertainty is  $\pm 5 \cdot 10^8 \text{Bq} \cdot \text{s}^{-1}$ . The release data can be found in table 1.4.1 below.

### iii. Immission Data

The immission data for the measurement period were also read from a diagram in the publication. The  $^{85}\text{Kr}$  activity concentration in  $\text{Bq} \cdot \text{m}^{-3}$  was measured at the IRSN Laboratory of Radioecology (LRC) located in Cherbourg (48.635°N, 1.645°W) [Connan et al., 2013]. The uncertainty introduced by the manual read-out is estimated to be  $\pm 20 \text{Bq} \cdot \text{m}^{-3}$ . The immission data are listed in table 1.4.1.

### iv. Surface Roughness

The surface roughness in the area surrounding the AREVA La Hague fuel reprocessing plant, was given as 0.1 m. The surface roughness length is a method to parameterise the land coverage in order to apply surface turbulences in the simulation. The more obstacles dominate the landscape, the higher is this roughness length number.

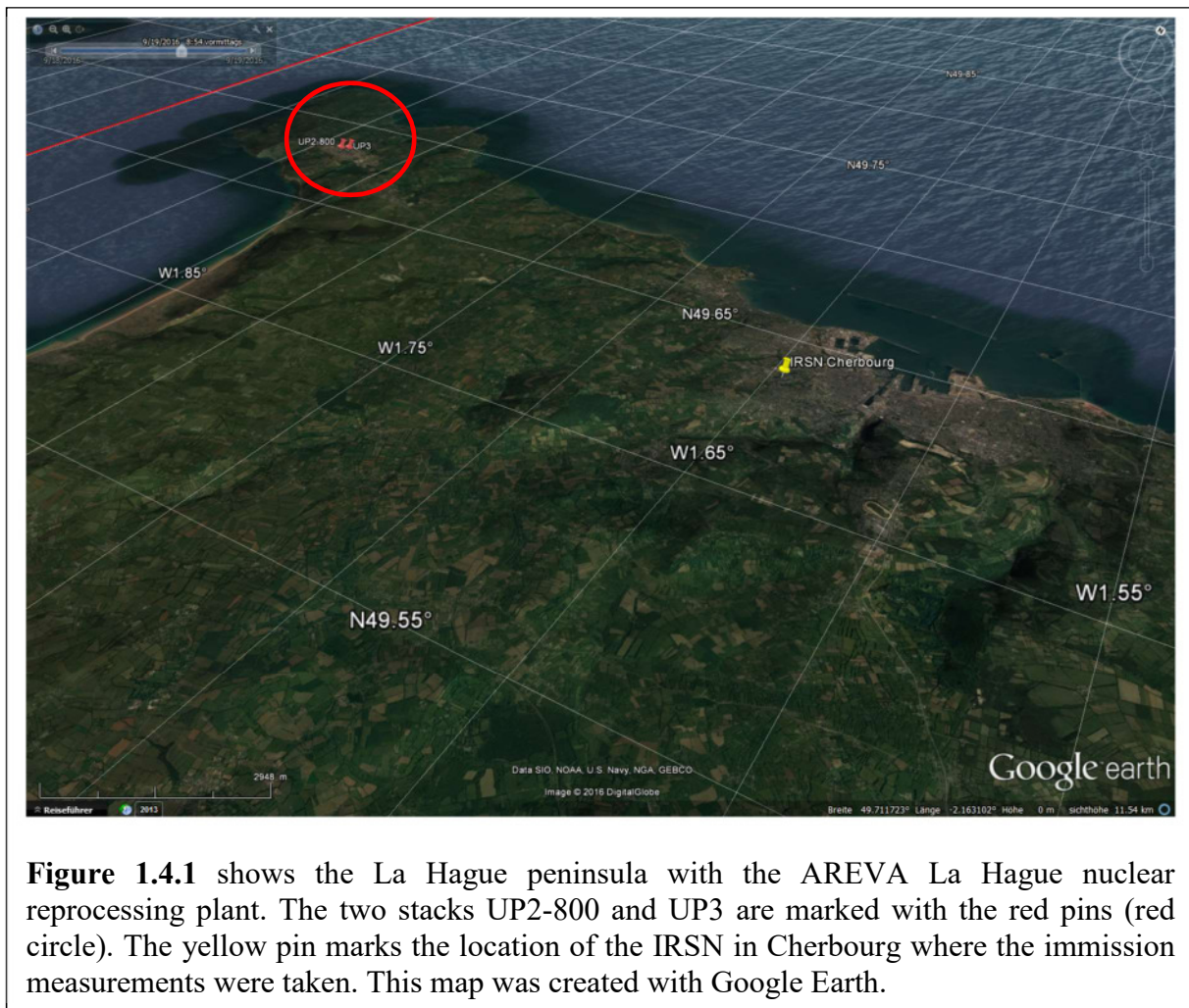


**Figure 1.4.1** shows the La Hague peninsula with the AREVA La Hague nuclear reprocessing plant. The two stacks UP2-800 and UP3 are marked with the red pins (red circle). The yellow pin marks the location of the IRSN in Cherbourg where the immission measurements were taken. This map was created with Google Earth.

**Table 1.4.1** lists the emission and immission values given in Connan et al. (2013). The emission data for the 27<sup>th</sup> of February and for 23:00 on the 26<sup>th</sup> of February (marked with \*) were not explicitly given, so they were assumed to be equivalent to the mean value of the emissions from the 26<sup>th</sup> of February. The immission values shown here were read from the diagrams for the measurement location at the IRSN LRC, here named IRSN.

Time in UTC	26 <sup>th</sup> February 2009		27 <sup>th</sup> February 2009	
	<sup>85</sup> Kr release in $10^{10} \text{ Bq} \cdot \text{s}^{-1}$	<sup>85</sup> Kr immission in $\text{Bq} \cdot \text{m}^{-3}$	<sup>85</sup> Kr release in $10^{10} \text{ Bq} \cdot \text{s}^{-1}$	<sup>85</sup> Kr immission in $\text{Bq} \cdot \text{m}^{-3}$
00:00	1.05	100	0.841*	100
01:00	0.75	50	0.841*	1700
02:00	0.95	100	0.841*	4400
03:00	1.05	100	0.841*	100
04:00	0.8	150	0.841*	20
05:00	1.05	1100	0.841*	50
06:00	0.6	20	0.841*	100
07:00	0.65	20	0.841*	1600
08:00	1.15	0	0.841*	100
09:00	0.8	100	0.841*	50
10:00	0.75	50	0.841*	900
11:00	0.85	50	0.841*	100
12:00	0.8	0	0.841*	1100
13:00	0.55	100	0.841*	1100
14:00	1	150	0.841*	1250
15:00	0.5	1800	0.841*	150
16:00	0.55	2800	0.841*	50
17:00	0.8	0	0.841*	300
18:00	1	0	0.841*	20
19:00	1.1	50	0.841*	50
20:00	0.8	0	0.841*	1000
21:00	1	20	0.841*	600
22:00	0.8	1000	0.841*	500
23:00	0.841*	3200	0.841*	200

Other input data were estimated or taken from different sources. The orography file was downloaded from [www.geocomm.com](http://www.geocomm.com) and prepared for use in ARTM as described in section 1.3.1.1.

The meteorological data provided in the diagrams of the Connan et al. (2013) publication are insufficient for use with ARTM, as it additionally requires the dispersion categories. These had to be estimated using synoptic observations of the cloud coverage from satellite images for the period of the measurement campaign. Details on this method and the weather charts can be found in Appendix D. The dispersion categories are listed in appendix E.

The two emission sources UP2-800 and UP3 are given in Connan et al. (2013) with their height and location, but the diameters of the stack openings had to be estimated using Google Earth, as they were not listed in the publication. The diameter of the stack opening was estimated for UP2-800 at 5 metres and for UP3 at 3 metres. The uncertainty of these numbers is estimated to be  $\pm 1\text{m}$  for each of the two stacks.

Since emission rates are only given for the 26<sup>th</sup> of February are given until 22:00, for the release at 23:00 and for the following day the mean value of the measured values was used for the release throughout the 27<sup>th</sup> February. Of course this assumption can lead to deviations from the measurements in the simulation results.

Also, the publication does not clearly state how much each stack contributes to the total emission. Therefore, for the validation of ARTM with the La Hague scenario (described in chapter 3), three scenarios were examined: the two extremes (either all emissions from UP2-800 or all emissions from UP3) and a 1:1 distribution between the two stacks.

The La Hague scenario data were used in simplified form for the sensitivity studies in chapter 2, in which the basic input parameters from Connan et al. (2013) were partially altered to study the behaviour of the simulation results.

These input parameters were used in their unaltered, detailed form for the realistic simulation described in chapter 3.

The ARTM input files for these can be found in appendix G.

For this scenario, all times are given in UTC/GMT.

#### **1.4.2 Neckarwestheim**

The dataset for Neckarwestheim does not include any immission measurement data, as all potential immission values lie below the detection limit. The purpose of this scenario is solely to extend the sensitivity analysis from the short term La Hague scenario to a long-term scenario of a location in Germany. The aim is to verify if the effects from the short-term scenarios also appear in the long-term ones.

Neckarwestheim is the location of a German nuclear power plant that is located in a moderate orographical environment on the bottom of a river valley, surrounded by hills.

The meteorological data, in hourly resolution, of the year 2009 were used because of their small number of measurement station failures and a data availability of 98.81%, which makes a solid data file for the simulation with ARTM.

The orographical data, taken from the digital elevation model DGM50 M745 provided by the Federal Office for Cartography and Geodesy, did not need processing in order to be read into ARTM.

The release data were reported in quarterly measurement values by the plant operator and can be retrieved from the annual report [BMU, 2009]. They include a broad variety of radioactive nuclides, some of which originate directly from fission products, but most of which are activation products such as  $^{14}\text{C}$ . The types and quantities of emitted radionuclides are given in the ARTM parameter file provided in appendix G.



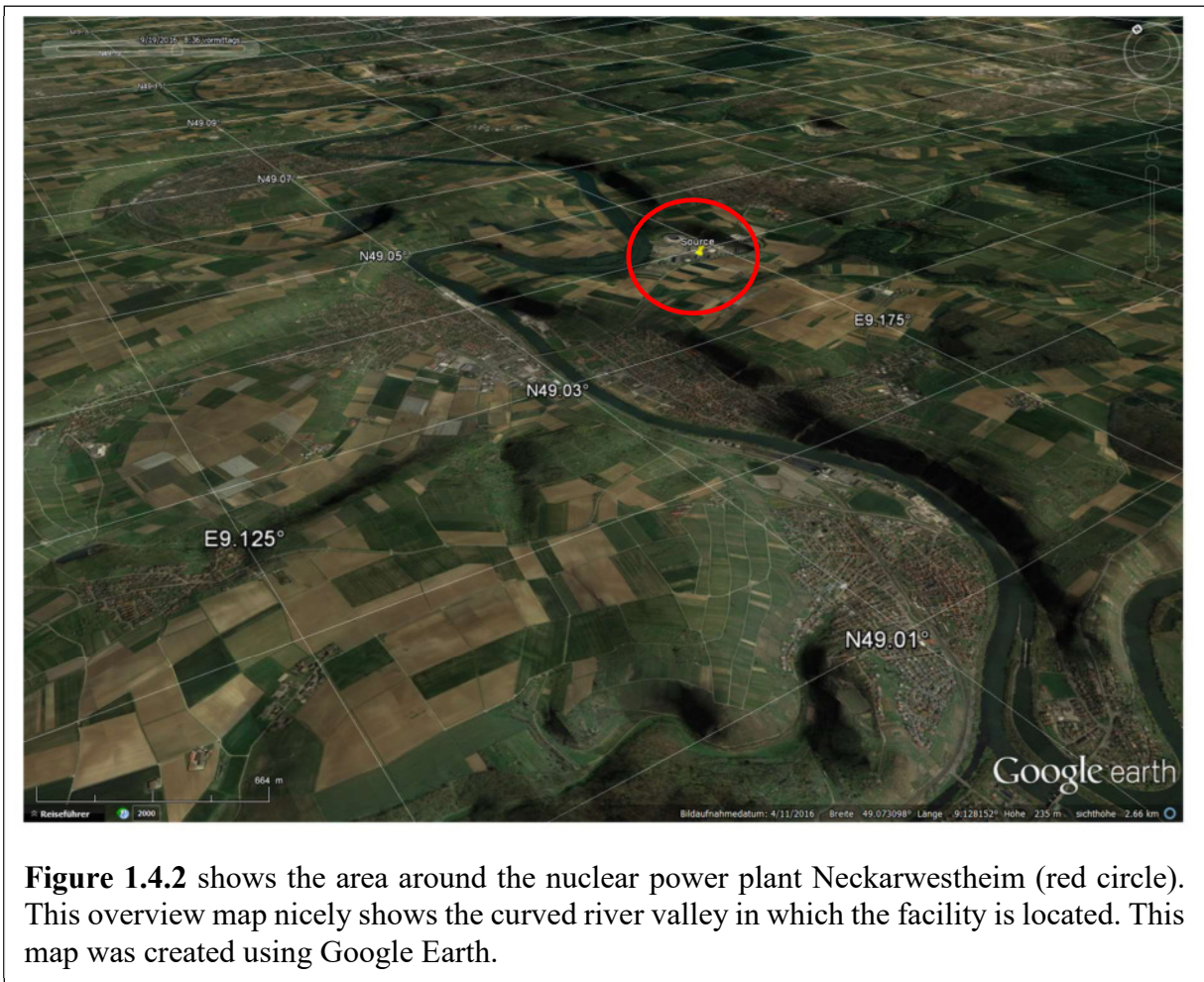


**Figure 1.4.2** shows the area around the nuclear power plant Neckarwestheim (red circle). This overview map nicely shows the curved river valley in which the facility is located. This map was created using Google Earth.

### 1.4.3 Šoštanj

In Šoštanj, a small town in northern Slovenia, there is a thermal power plant (TPP) using the locally abundant brown coal to generate electrical energy. In 1991, TPP Šoštanj emitted large quantities of  $SO_2$  that polluted the surrounding area. The Šoštanj data set, kindly provided by Marija Zlata Boznar and Primoz Mlakar from MEIS (Modelling, Meteorology, Measurement Environmental Information Systems Engineering, Education, Informatics Consulting, Systems) in Slovenia, includes data from a measurement campaign that was conducted in March and April of 1991 in the area around the TPP [Elisei et al., 1992, Mlakar et al., 2015 (in press)]. Despite not being a nuclear facility with radioactive emitters, it can be used to validate atmospheric dispersion models, which is why this scenario was chosen to be included in the IAEA MODARIA (Modelling and Data for Radiological Impact Assessments) working group 2 on ‘Exposures in contaminated urban environments and effect of remedial measures’ [IAEA, 2017 (expected)].

The Šoštanj scenario represents a challenge for dispersion modelling [Mlakar et al., 2015 (in press)]. Due to the complex terrain (steep hills, deep valleys) in close proximity to the TPP facility, as described in Mlakar et al. (2015), dispersion models require an advanced wind field model. Additionally, the meteorology of Šoštanj is very variable. Its position in a wide valley with a nearby lake places it in a complex mountain-valley wind system driven by thermal differences [Mlakar et al., 2015 (in press)]. The wind directions at the release point can change dramatically over the course of only a few hours. These features make the Šoštanj data set very



interesting for validating advanced atmospheric dispersion models based on the Lagrangian particle model.

The Šoštanj data set contains:

**i. Orography and Land use**

Orography and land use parameters, following the CORINE land cover system are provided in two separate files with a resolution of 150 metres for an area of  $15 \times 15 \text{ km}^2$  [Mlakar et al., 2015 (in press)].

**ii. Emission data**

The emission rates of  $SO_2$  in  $10^3 \text{ kg} \cdot \text{h}^{-1}$  released from the two operational stacks ‘Blok 123’ and ‘Blok 5’ are available with a half-hour resolution. Additionally the values for the temperature of the exhaust gases in  $^{\circ}\text{C}$  and the gas flow in  $\text{m}^3 \cdot \text{h}^{-1}$  rates are given.

‘Blok 123’ is the oldest stack, with a height of 100 metres and a diameter of 6.5 metres, and is located in the western part of the facility at (46.3728107°N, 15.05224246°E) [Mlakar et al., 2015 (in press)].

‘Blok 5’ has an altitude of 230 metres and a diameter of 6.2 metres and is located at (46.37195429°N, 15.05528409°E) [Mlakar et al., 2015 (in press)].

**iii. Meteorology data**

The dataset includes a comprehensive collection of meteorological data. Not only does it contain half-hourly measurement data from the SODAR location (46.38053016°N, 15.05708729°E), measuring a wind profile (vertical and horizontal wind speeds and directions) in 18 different layers from 50 metres up to 974 metres above the ground, but it also includes wind measurements, air temperature and relative humidity for each of the six immission measurement locations:

- Graška Gora (46.41460872°N, 15.12399162°E),
- Šoštanj (46.37718572°N, 15.0537187°E),
- Topolšica (46.40406449°N, 15.02089386°E),
- Velenje (46.36032121°N, 15.11191047°E),
- Veliki Vrh (46.35119776°N, 15.04114773°E)
- and Zavodnje (46.42822053°N, 14.99834513°E) [Mlakar et al., 2015 (in press)].

Dispersion categories are not explicitly given, but can be assigned according to the guidelines for SODAR measurements listed in the KTA 1508 (see table 2.1.1.4 II), using the tool explained in chapter 1.3.1.2.

**iv. Immission measurements**

The  $SO_2$  - concentrations in  $\mu\text{g} \cdot \text{m}^{-3}$  are measured in half-hour steps for each of the six measurement stations mentioned above. The stations are shown in figure 1.4.3.

Despite being the most complete data set available for the validation in this work, some of the input parameters had to be processed before use with ARTM. The included orography file was at too high a resolution, and therefore included too steep inclines, to be handled in ARTM.

Therefore here again a DEM from [www.geocomm.com](http://www.geocomm.com) was retrieved and processed using the software tools described in chapter 1.3.1.3. This led to a smoother orography file for the simulation area.

As for the roughness lengths, the ARTM version used for these simulations could not use the given roughness length file, as this feature was not implemented. Instead, a global roughness length of 0.74 metres was used, which was the mean value of the roughness lengths in the original roughness lengths file.

The dispersion categories were derived (as mentioned above) from the SODAR measurements of the horizontal and vertical wind velocities using the parameter table of the KTA 1508 (see table 2.1.1.4 II).

Building sizes and heights were not given in the data set. As the simulation for this scenario was to include building effects, the sizes and altitudes of the TPP buildings had to be measured and estimated using old building plans and image files of the 1991 configuration of the Šoštanj TPP. Details about this method can be found in appendix F.

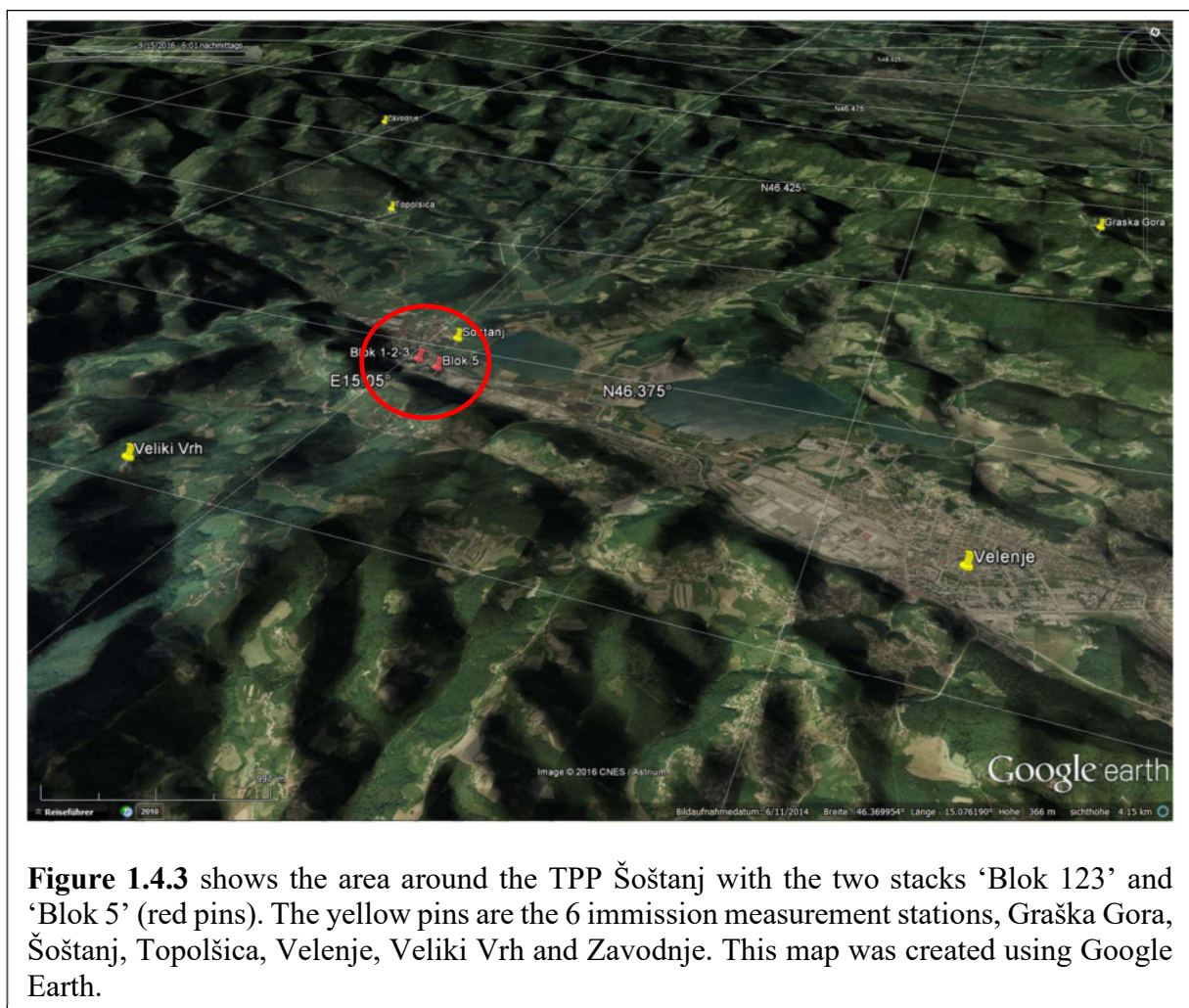


**Figure 1.4.3** shows the area around the TPP Šoštanj with the two stacks ‘Blok 123’ and ‘Blok 5’ (red pins). The yellow pins are the 6 immission measurement stations, Graška Gora, Šoštanj, Topolšica, Velenje, Veliki Vrh and Zavodnje. This map was created using Google Earth.

#### 1.4.4 Urban Buildings Scenario

The urban buildings scenario is a purely fictive scenario created to evaluate the application of ARTM for complex urban structures near the release point. To allow comparison, the scenario was developed to be suitable also for simulation with LASAIR, which was specifically developed for use in urban environments.

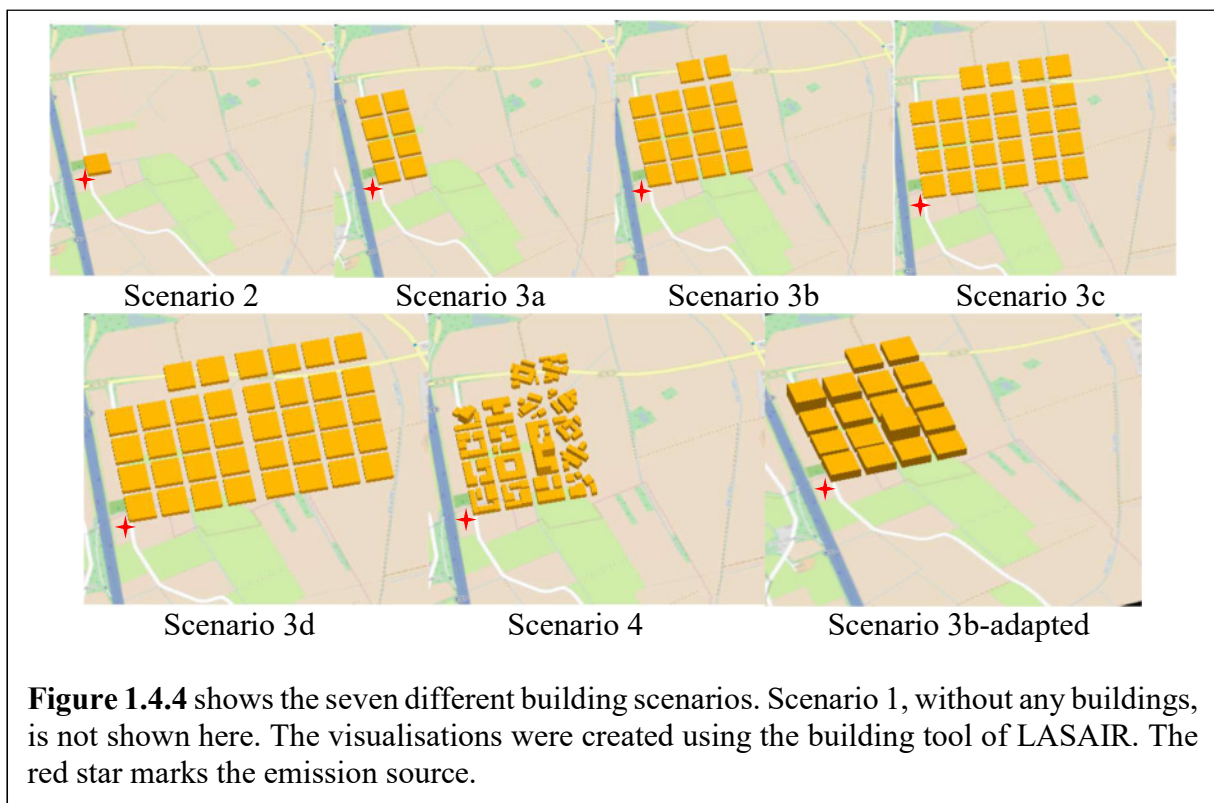
To keep it simple and limited to only the building influences, this scenario did not include the influence of orography.

To concentrate the investigation only on the effects from the buildings, the meteorology was also kept simple, by including only a steady wind from  $240^\circ$  with a wind speed of  $1 \text{ ms}^{-1}$  for the entire 4-hour simulation period. In LASAIR a total of  $10^{12} \text{ Bq}$  of  $^{131}\text{I}$  was released during the simulation scenario. In ARTM the release rate was given with  $10^{12} \text{ Bq} \cdot \text{s}^{-1}$ , so its results had to be divided by 3600 to be comparable. Due to the linearity between emission strength and immission results (described in chapter 2.1.1.1), this is a legitimate and mathematically correct operation.

Emission took place only during the first 60 minutes of the simulation period.

20 monitoring points were set up to allow comparison of the time series results of the two simulation programmes.

The urban buildings were arranged in seven different configurations and one control scenario without any building structures (see figure 1.4.4).



While scenario 1 is just an empty field without any building structure, scenario 2 contains one building, a block  $100 \times 100 \text{ m}^2$  and  $20\text{m}$  in height to simulate an urban street block.

The scenarios 3a to 3d each add 2 rows of these building blocks leaving  $20\text{m}$  in distance for the smaller streets and  $40\text{m}$  for 2 larger ones. Scenario 4 is a detailed variant of scenario 3b. Here the individual buildings of these building blocks are worked out, including structures with small yards, lower buildings and higher office complexes, diagonal streets, parking spaces, etc, in order to simulate a real city quarter.

Scenario 3b-adapted is a mixture of scenario 3b and scenario 4, where the altitudes of the building blocks have been adjusted to match the highest building from scenario 4 within their respective blocks.

The emission source for each of the scenarios is located  $40m$  west and  $20m$  south of the first building block at an altitude of  $5m$  above the ground.

## 1.5 Modelling Results

In this study, the main focus is to evaluate the atmospheric dispersion of the models considered. For this reason, the simplest possible output was chosen in order to perform comparisons: the activity concentration in air of the desired radionuclide, measured in  $Bq \cdot m^{-3}$ . All other simulation results, such as dry and wet deposition and gamma submersion were neglected for this study.

In ARTM the resulting values are the average values of the volume grid. That means, that in one 3-dimensional grid cell, the activity concentration is imagined to be distributed homogeneously, without local maxima or minima within the grid cell. Therefore, increasing the cell size can alter the simulation results and produce lower or higher values.

Also, measurement stations usually have a much smaller sphere of influence than the entire cell volume. It can happen that the measurement catches one of the maxima of the cell or anything in-between. This can cause the simulation results to over- or underestimate the real values.

## 2. Sensitivity Analysis of ARTM

Every simulation model is just that, a simulation of the real world based on assumptions and approximations due to yet undiscovered or not yet well-enough understood aspects, and as such a simulation can not 100% exactly reproduce or predict the reality.

So, before starting to apply a simulation model to a use case, be it for operational mode to reproduce or predict results based on some real measurement data as an input, or be it to perform a validation of the simulation model for a realistic scenario, the relation between input parameters and output results of the simulation software need to be understood. Also fluctuations and deviations of the results depending on these inputs need to be studied and quantified to allow for reliable error margins of the simulation results.

In order to discover and allocate the origin of these margins, a comprehensive series of ARTM simulations has been conducted to perform a sensitivity analysis. The aim was to also evaluate the weighting of changes or variations in certain input parameters and their impact on the statistic error of the simulation results, and which countermeasures could be taken to minimise the deviations.

Basically one can differentiate between input parameters of external and internal nature:

- External parameters are mainly predefined sizes, or measurement data, that are obtained from the plant operator (e.g. emission terms) or other external sources such as the weather service (e.g. meteorological data) or institutes providing cartography. These data and parameters come with measurement uncertainties and other variations that the user of the simulation model has no influence on.
- Internal parameters are the ones that can be freely chosen by the user. The essential parameters thereof are the starting number for the random number generator, the size of the calculation grid, or the amount of simulation particles.

The strategy for the sensitivity analysis here is to use realistic, or only partially simplified scenarios, then varying always only one parameter per simulation series and finally gain some insight into the kind of relation between the respective input parameter and the variations in the results. Depending on what is desired, the results can be analysed in several different ways; for example the time series for the activity concentration in  $Bq \cdot m^{-3}$  of certain chosen points can be examined. For some cases it might also be interesting to view the distribution of the mean activity concentration for the entire simulation period in the whole simulation area, or to take only the results for a line in a certain direction, for example from the source in the direction of the dispersed cloud. In certain cases also the points of maximum concentration might be interesting in the comparison. Even though ARTM also handles dispersions at multiple layers in different altitudes over ground, in all here handled cases only the distribution within the ground layer (0-3m over ground) was analysed, as for operations this is the layer where humans, agriculture or wildlife is most affected by exposure.

Two scenarios were selected to perform this sensitivity analysis of ARTM.

The first one is a short term scenario over a duration of only 2 days at the La Hague nuclear fuel reprocessing plant, which is used to address the influence of external as well as internal input parameters on the final results.

The second one is an annual simulation at the German nuclear power plant Neckarwestheim. Here especially the impact of the variation of internal input parameters on the results of a long term simulation was studied.

## **2.1 Sensitivity analysis with La Hague scenario**

To conduct a sensitivity analysis of the basic input parameters for ARTM, a realistic scenario for an existing nuclear facility in an orographically interesting location was chosen. The location of choice was the AREVA nuclear fuel reprocessing plant in La Hague, France (for more detailed description of the scenario, see chapter 1.4.1). In order to obtain realistic input parameters, the work of Connan et al. (2013) was used to derive meteorological data (wind speed and wind direction) as well as the emission data from table 1.4.1. For most of the sensitivity analysis, only the average value for the emission was used (see appendix G). The orographical data was obtained from geocomm.com and processed as described in chapter 1.3.1.1. To keep it simple for the beginning, it was calculated with only one fictive source roughly placed in the eastern end of the AREVA nuclear fuel reprocessing plant, about 750 to 1000 metres east to the real existing stacks UP2-800 and UP3. The choice of this source for the sensitivity analysis arose historically as the first test simulations used only roughly the real locations. These preliminary simulations were then the starting points for all sensitivity analysis simulations performed in this scenario.

However, for the sensitivity analysis, this does not make any difference since they were kept constant for the whole series of simulations. For the real La Hague scenario calculations of chapter 3, the exact coordinate values of the stack locations (as provided in chapter 1.4.1) were applied.

### **2.1.1 External input parameters**

The term ‘external input parameters’ describes all input parameters that are predetermined by the scenario. External, because the user of the simulation software has no influence on these values, since these are absolute values from measurements, guidelines or given by the specifics of the location of the simulation area. These include all types of information on the simulation area, such as the orography, the surface roughness according to the CORINE Land Cover data base, or the urban environment, i.e. buildings existing in the close vicinity to the source, which could influence the dispersion.

The second type of external input data is the meteorological situation for the time period of interest. Here three main parameters need to be provided: wind speed, wind direction and dispersion category according to Klug-Manier, but also in some cases precipitation data are of use, especially for scenarios where, unlike here, not exclusively noble gases are released [Richter et al., 2013a, 2013b]. In those cases, precipitation causes a wash-out additional to the dry deposition. Washed-out nuclides are not available anymore for further dispersion.

The last – but not least – third type of external input parameters are all data regarding the source. This means; the source term, i.e. how much of which nuclide is emitted when, the source geometry, or the type of source, for example hot or cold sources. There are further input options regarding the source, such as humidity, exhaust velocity, etc, which are not studied in detail within this work.

In general, these three types of data are obtained by external companies, such as the company that runs the nuclear facility or the national weather service. The user has little or no information on how these data were obtained and what is the error range originating from the measurement instruments and procedures.

While the user in general has no means of knowing whether his data is sufficiently exact or if it is afflicted with large errors and measurement uncertainties, he is bound to use the statutory

sources for the simulation process. In the following, an assessment has been made to estimate the impact of errors in some of the external input parameters on the results of the simulation. The details on these input parameters are given in appendix G.

#### 2.1.1.1 Emission strength

The first external parameter to be evaluated on its effect for the result was the emission strength. The emission strength is the value of the amount of a released substance per time interval. For conventional emissions, this emission strength is given in  $kg \cdot s^{-1}$ , for radioactive nuclides – and therefore in all for this work utilised simulation programmes – it is  $Bq \cdot s^{-1}$ .

One could argue that the emission strength and the resulting calculated immission data are always in a linear correlation as in the theory this should be the case. However, the complex Lagrangian dispersion model and the application on a realistic scenario might cause some unpredicted effects. In order to exclude this possibility for errors in more sophisticated simulations later and to prove the model's congruence with the theory, this short pre-study on varying emission strengths was conducted.

An application for the result of this pre-study would be to provide the ability to apply loss factors to the simulation results. For example, if the emission term is measured with an in-situ measurement instrument, radioactive aerosols can be lost in the tubing due to impact deposition and sedimentation [Vogl, 1994]. These losses can lead to inaccurate emission terms. As Vogl (1994) describes, these losses can be up to 90% for particles larger than  $10\mu m$ , leading to a total in activity of up to 30%. Also the measurement uncertainty and the systematic error of the detector itself can add to this inaccuracy. If these errors are known, and the emission to immission ratios are in a linear dependency, the loss factor can simply be multiplied to the simulation results.

In order to evaluate the sensitivity of the simulation results in respect to errors in the emission strength, the in La Hague scenario was used for assessment. During the simulations, all parameters were kept the same, except for the emission strength. The starting value was  $1/8$  of the original emission strength of  $8,413,043,500 Bq \cdot s^{-1}$ , and was increased during the simulation by the factors 2, 4, 8, 10, 100, 1,000, 10,000 and 100,000. Reference point for the simulation results was the measurement station 'IRSN Cherbourg', where the time series in hourly steps was considered. In figure 2.1.1.1 the simulation values for all time periods of the two days of the simulation are plotted in respect to the multiplication factors. In the double logarithmic scale of the x-and y-axis, it is clearly visible that all results show a linear behaviour.

That means in conclusion that if the emission strength is multiplied by a multiplication factor, the results of the previous simulation can be multiplied by the same factor, i.e. errors that occur during the measurement of the emission strength directly go into the final simulation result.



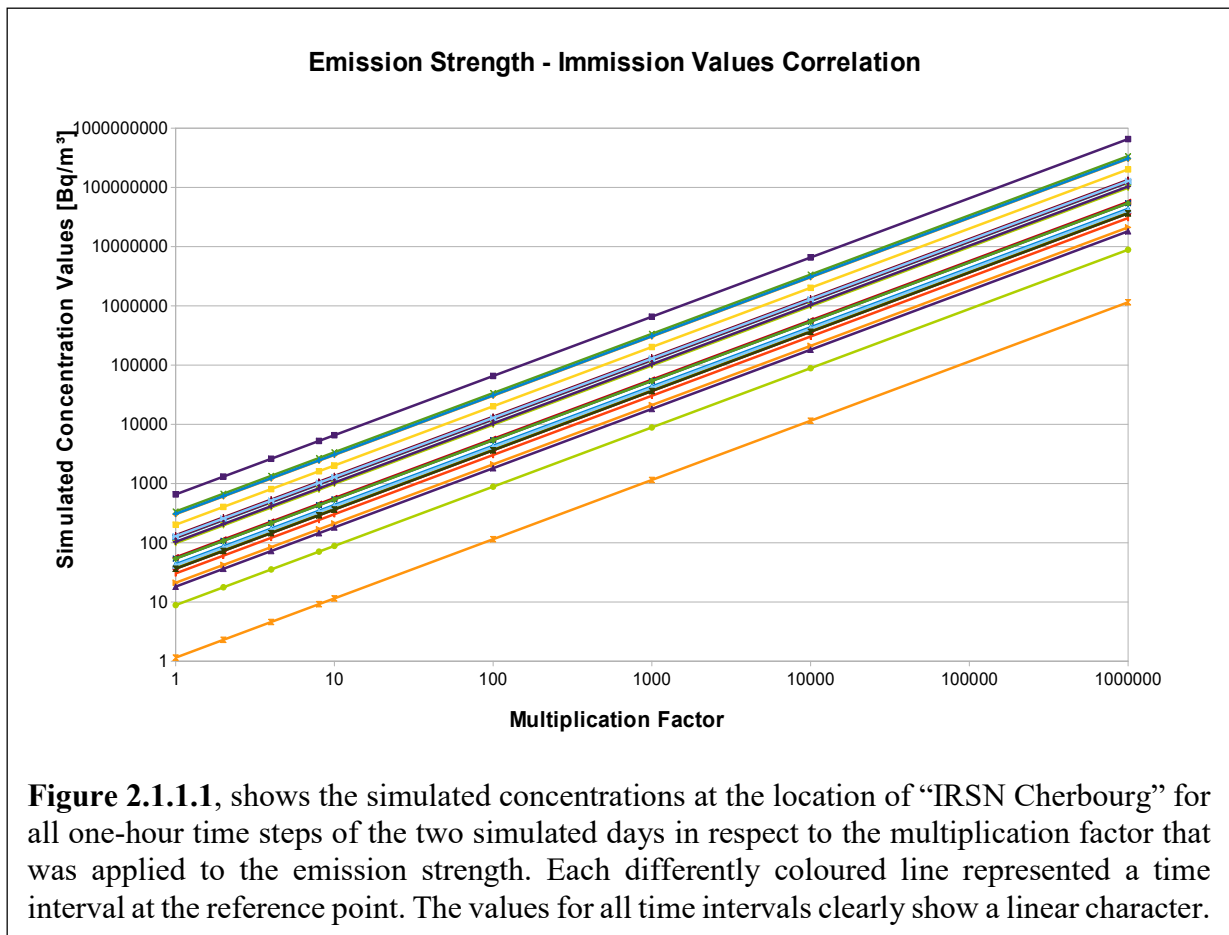


**Figure 2.1.1.1**, shows the simulated concentrations at the location of “IRSN Cherbourg” for all one-hour time steps of the two simulated days in respect to the multiplication factor that was applied to the emission strength. Each differently coloured line represented a time interval at the reference point. The values for all time intervals clearly show a linear character.

### 2.1.1.2 Source geometry

As a second parameter, the source geometry was studied regarding its influence on the final simulation results. The key questions that motivated this study were the following:

- Given the case that the exact source size is not known or contains an unknown measurement error and has to be approximated by estimation, what range of the deviation in the simulation can be expected?
- Which dimension (length, width, source height (not emission altitude)) of the source has the major influence on potentially occurring differences?

To address these questions, the same La Hague emission scenario as in 2.1.1.1 was applied (with the parameters given in appendix G) varying the source geometry. Three cases were studied; at first a horizontal linear emission source ranging from 1 to 10 metres in length with steps of 1 metre in 2 scenarios, secondly a quadratic geometry was chosen again with side lengths ranging from 1 to 10 metres, and finally a cubic source with the same range. Each case was simulated using the standard particle quality qs 0 (see table 2.1.2.2 I), and the highest particle quality, qs 4, resulting in a total of 80 simulations.



The results were analysed in two ways; by comparing the time series diagrams at the ‘IRSN Cherbourg’ measurement station, roughly 18 kilometres down-stream from the emission source, and secondly by studying the mean activity concentration over the entire simulation period for a direct line from the emission source in plume direction towards the measurement location (see figure 2.1.1.2 I). This way the near vicinity of the emission source, as well as the further-away locations can be analysed in regards to possible differences in the results.

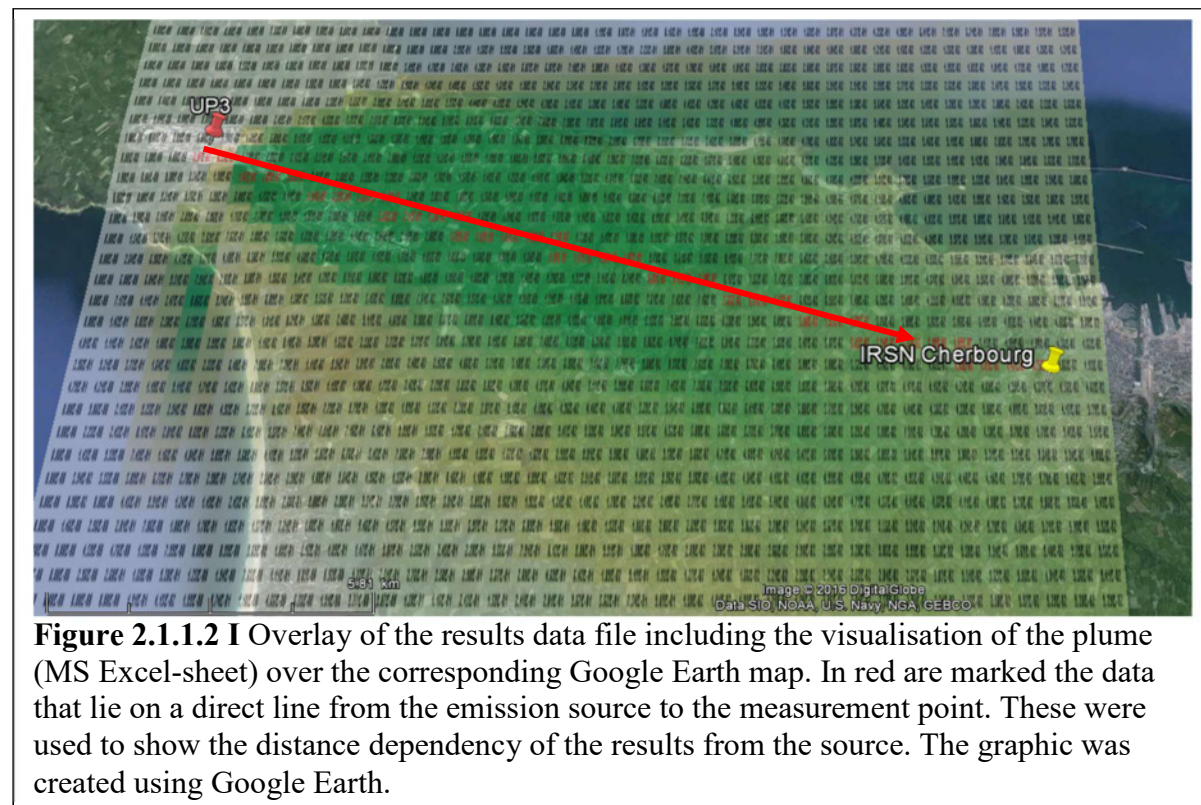


**Figure 2.1.1.2 I** Overlay of the results data file including the visualisation of the plume (MS Excel-sheet) over the corresponding Google Earth map. In red are marked the data that lie on a direct line from the emission source to the measurement point. These were used to show the distance dependency of the results from the source. The graphic was created using Google Earth.

## i. Linear source geometry

A linear source is somewhat a fictive construct, as pure line sources do not exist, they are at best box-shaped with side  $a \ll$  side  $b$ , for example a long narrow street could be approximated with a linear emission source. ARTM, however, provides the opportunity to simulate the dispersion from linear source geometries, which is why it was studied here for comparison with square and cubical sources. The line sources chosen range from 1 metre up to 10 metres applying a step size of 1 metre. This line can be directed in different positions to the main wind direction which might cause different effects for the simulation result, depending on if it is more parallel or more orthogonal to the wind direction.

In order to study this question, two scenarios were chosen; ‘Linear source geometry 1’ which an angle of  $10^\circ$  towards the east direction (illustrated in figure 2.1.1.2 IIa) and ‘Linear source geometry 2’ which is orthogonal to the first scenario (fig. 2.1.1.2 IIb)). The main wind direction is shown in both figures by the yellow arrow, and is for both cases neither orthogonal nor parallel to the chosen lines.

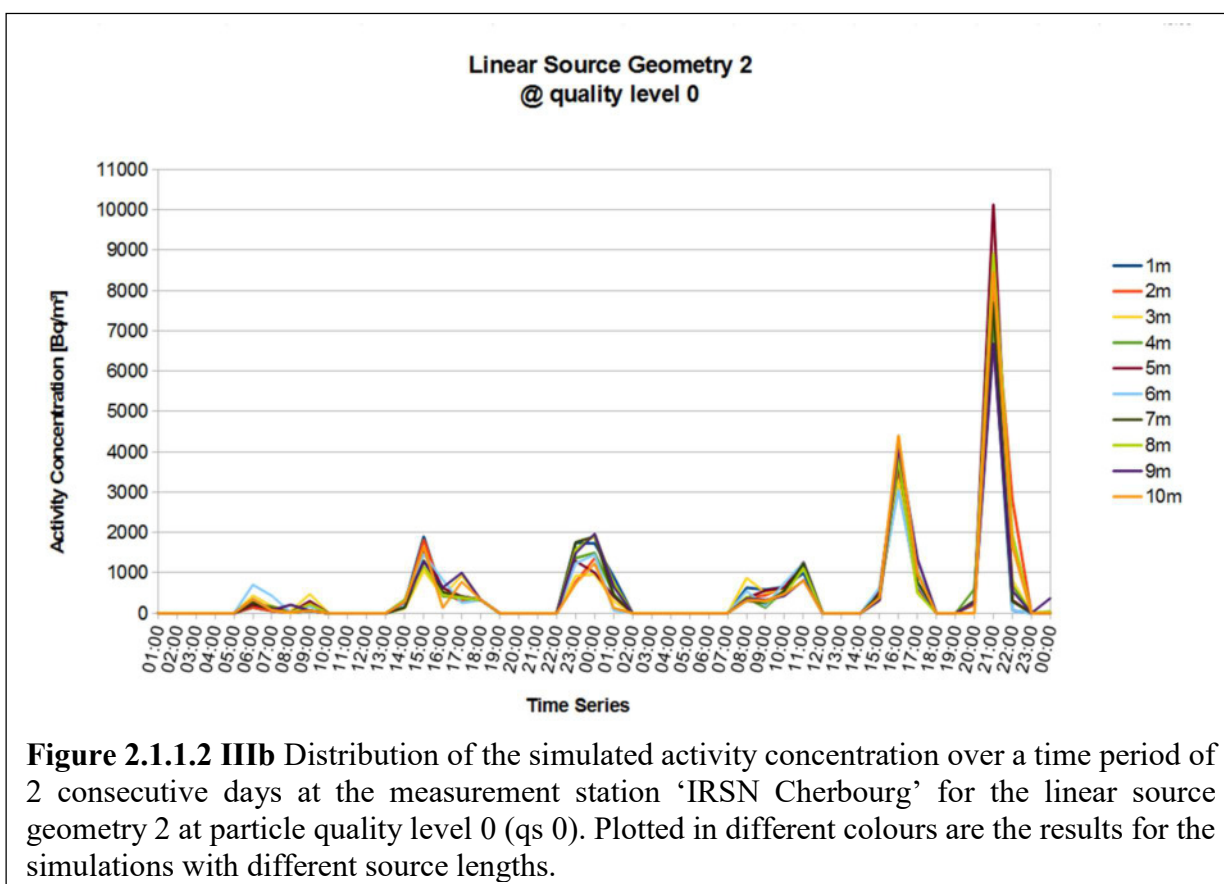
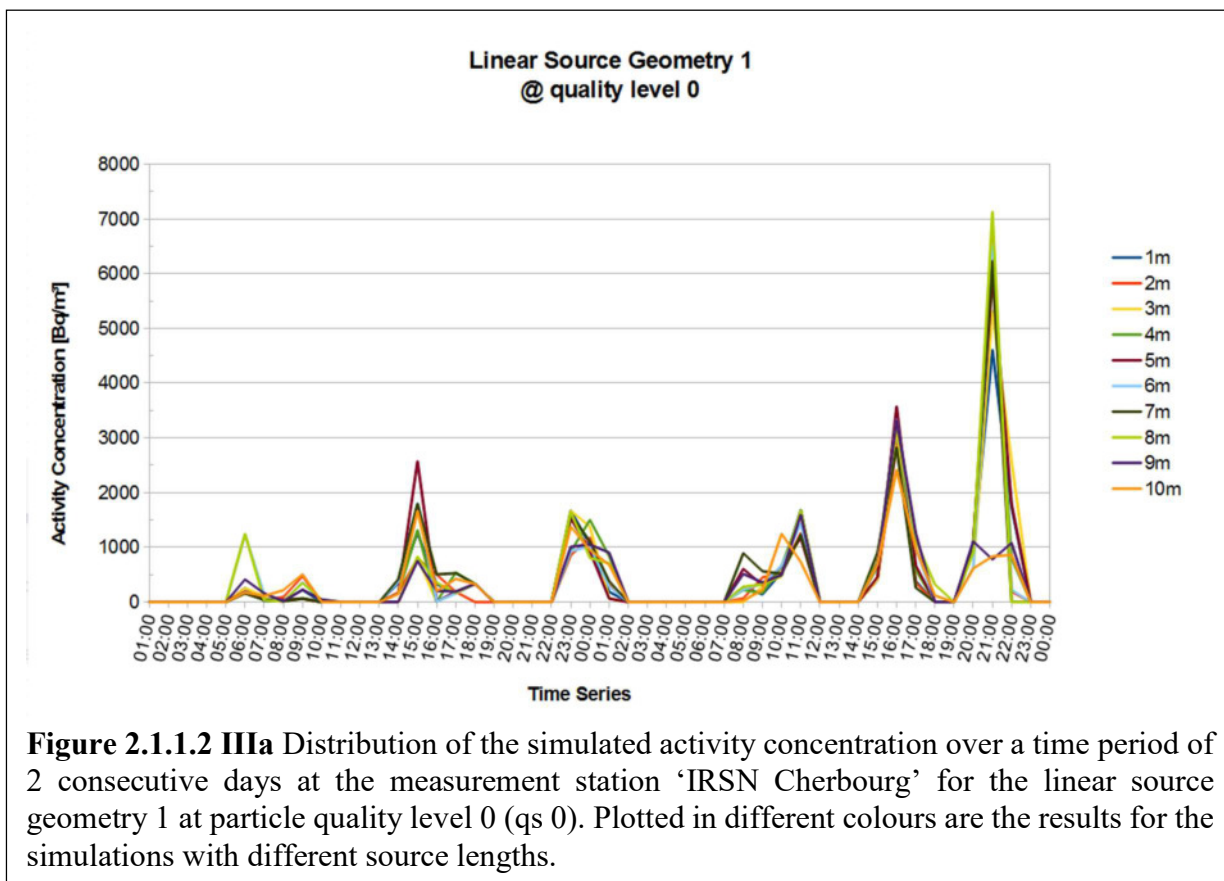


**Figure 2.1.1.2 IIa** Scenario ‘Linear source geometry 1’. In red is the line source with an angle of  $10^\circ$  towards the east direction. The length of the line is exaggerated by factor of 10 for demonstration purpose. The yellow arrow indicates the main wind direction for the simulated case. The graphic was created using Google Earth.



**Figure 2.1.1.2 IIb** Scenario ‘Linear source geometry 2’. In red is the line source with an angle of  $90^\circ$  towards the scenario “Linear source geometry 1”. The length of the line is exaggerated by factor of 10 for demonstration purpose. The yellow arrow indicates the main wind direction for the simulated case. The graphic was created using Google Earth.





For each of the two scenarios, 10 simulations with different source lengths have been performed at particle quality 0. For the exact input parameters, please look in appendix G. A time series of the simulated immission values for the measurement station ‘IRSN Cherbourg’ was created by ARTM as output. This station, which is approximately 18 km from the source, was chosen due to its appearance as a real measurement station point in Connan et al. (2013), and due to its position directly in the direction of the plume. In figures 2.1.1.2 IIIa and 2.1.1.2 IIIb, the simulation results are shown for both scenarios as a time series of the activity concentration at IRSN Cherbourg. As can be seen, the distribution of the peaks is similar, even though scenario 2 shows higher values at the peak on 21:00 of the second day.

The differences between the effects of different source lengths on the resulting activity concentration of up to a factor 7 for scenario 1 and up to a factor of 2 for scenario 2 do not show any explicable pattern, such as that one or the other source would deliver always the highest or the lowest values. Since the origin of these differences cannot be explained by the source geometry, other effects must play a role in this. Statistical error could be one explanation. In order to examine this possibility, the particle number was increased to reduce the statistical error, as described in section 2.1.2.2, while keeping all other input parameters identical. The results can be seen in figures 2.1.1.2 IVa and 2.1.1.2 IVb. There is now a clear difference to the results plotted above for the particle quality level 0. The results for the different lengths now show a drastically reduced error compared to the simulations before. Compared to the factor 2 to 7 in difference at maximum for the previous results, now the deviations of the maximum values went well below being a multiple of the minimum ones.

Interestingly, the differences between the 2 cases, ‘Linear Source Geometry 1’ and ‘Linear Source Geometry 2’ have also decreased after raising the particle numbers. A comparison between the diagrams shows that they are more or less following the same activity concentrations during the course of the two considered days of the time series.

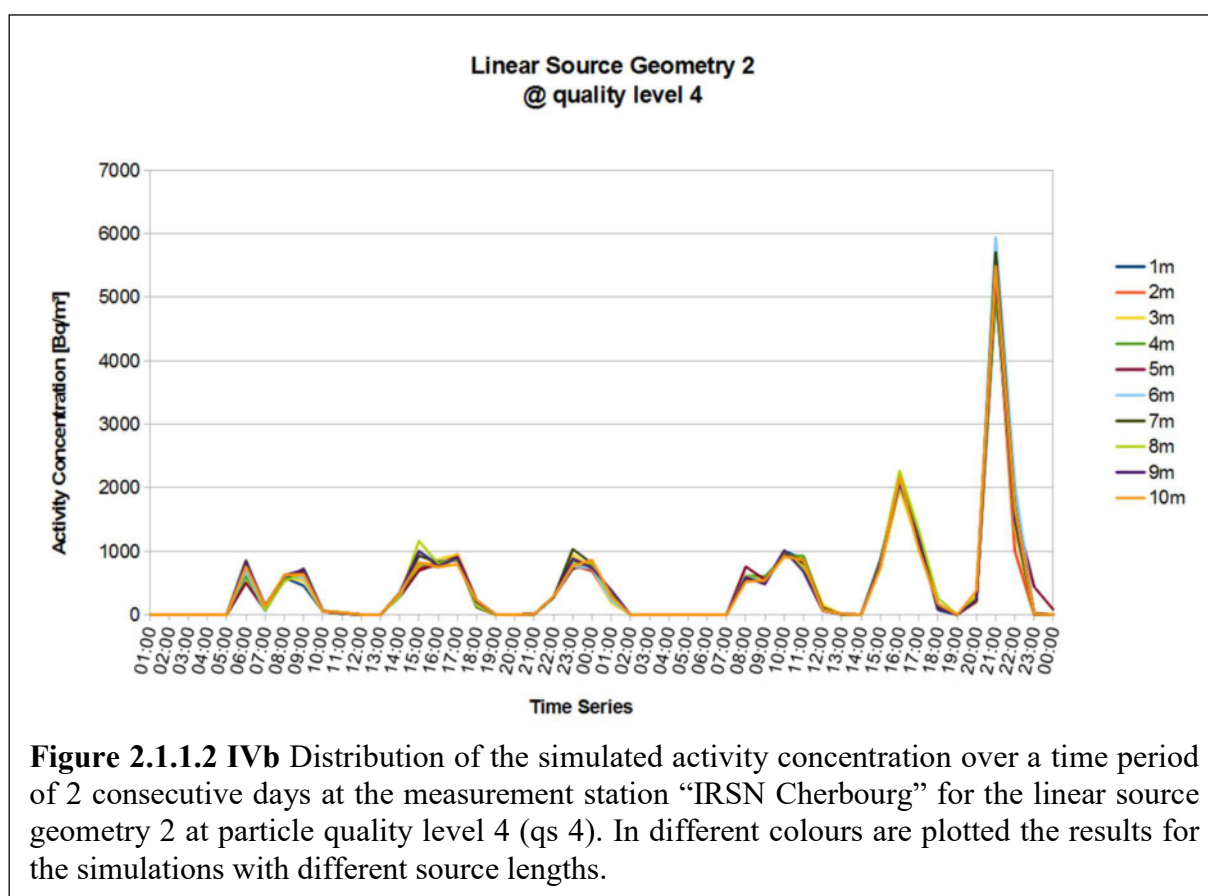
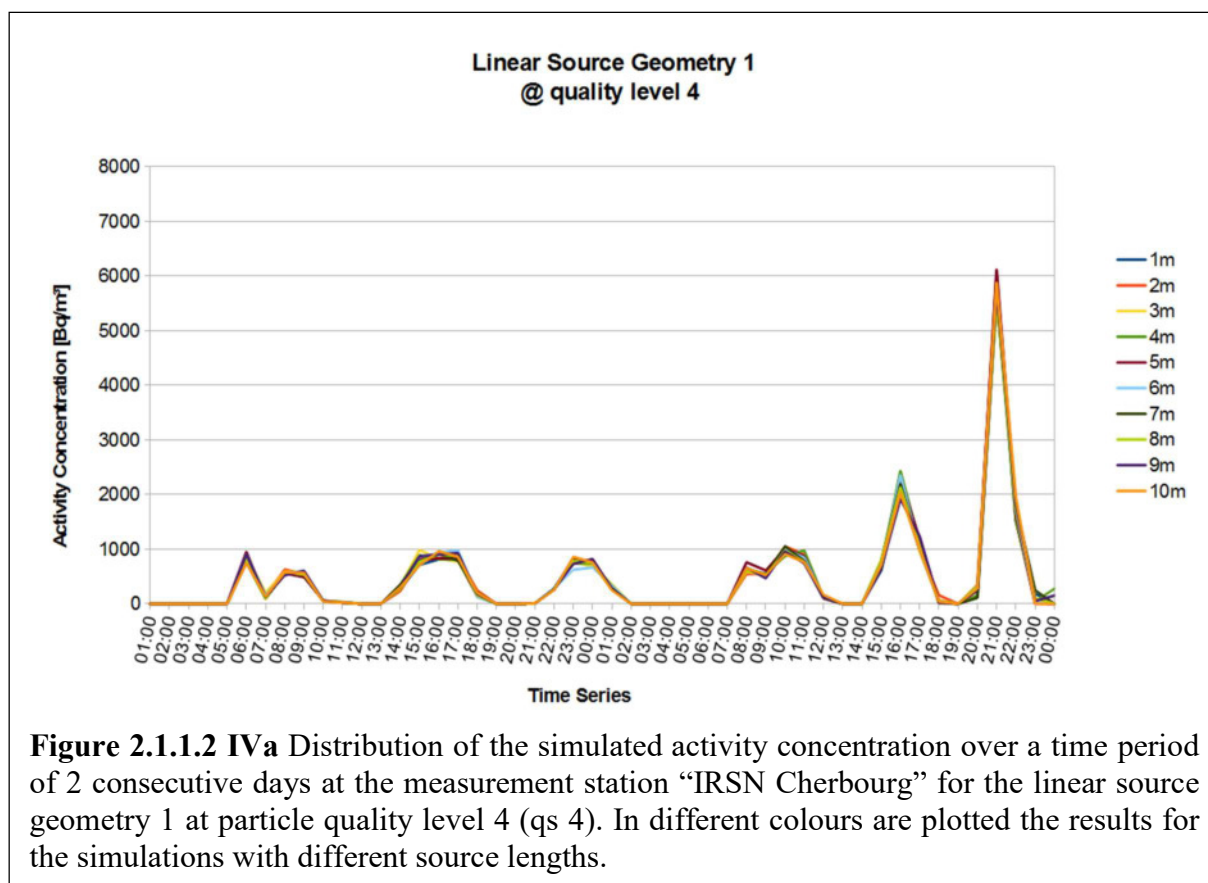
Also interesting is the effect that scenario 2, ‘Linear Source Geometry 2’, shows higher fluctuations in the results than scenario 1, in contrary to the simulations with less simulation particles as shown above, where scenario 1 possessed the higher fluctuations.

While there was not conducted an even more intense study on this effect, due to the above-mentioned observations regarding the decreasing deviations with increasing particle numbers and the lack of a trend towards one scenario with constantly higher deviations, it is expected to still be a statistical error. When performing more simulation runs, also with different starting random numbers, which determine the initial distribution of simulation particles (for further description see section 2.1.2.1), this effect is supposed to decrease even further.

Therefore it is suggested to always use particle quality level 4 to receive the most accurate and least statistically influenced results.

Until now, only the simulated time series of the ‘IRSN Cherbourg’ station was considered in the analysis. In order to check whether there are effects also regarding the distance to the source, the data that lie on a direct line between source and ‘IRSN Cherbourg’ were evaluated. Here not a time series was taken, but the mean activity concentration over the entire simulation time at each point on the line.

Again the studies were conducted using first particle quality 0, which lead to the observed fluctuations in the results that appear erratically and disappear when the same is done for the results from particle quality 4 in figures 2.1.1.2 Va and 2.1.1.2 Vb. The curves show, as expected, that near the source little to zero activity is found due to the stack height of 100 meters. In the near surrounding of around 2000 to 2500 metres, the highest activity per cubic meter has to be expected and then with increasing distance the activity concentration decreases. Again the curves of the two scenarios show a very good congruency and no indication of large differences due to the different direction of the linear emission sources.



In the figures it is visible that both scenarios, ‘Linear Source Geometry 1’ and ‘Linear Source Geometry 2’, still show some small fluctuations, as already discovered in the time series, which are different between the two scenarios, but in general the shape and also the values are in good agreement. Also, some small peaks can be seen in both diagrams at around 4,250 metres, 7,750 metres, as well as at around 11,000 and 12,500 metres. In order to find an explanation for this behaviour, it was thought to be triggered by the orographical structure of the region, which is why in blue the course of the surface altitude above sea level is shown. One can argue, that the first two peaks mentioned are coinciding with an increase in the orography. While the first peak occurs during an increase of the terrain altitude, the second peak is actually a less steep decline in the activity concentration, followed by a steep decline at the same position where the terrain is elevating. A potential cause could be either the overflowing or the surrounding of hills. To determine which case applies for each of the peaks, a more elaborated study on this than just on a 1-dimensional line would have to be conducted, to gain certainty. The two later peaks appear much softer in the diagram and while the correlation with increases in altitude can also be found for them, they could as well be within a statistical variability. In order to rule out this possibility, ensemble simulations (as performed in section 2.1.2) would be necessary. Also, it can be seen that not every steep elevation in the altitude automatically has an effect on the simulation results, for example at around 5500 metres there appears a steep incline, but in the simulation data, nothing is visible which indicates a correlation.

The explanation for this effect is a rather simple one; it appears where the direct line between the emission source and ‘IRSN Cherbourg’ cuts between two grid cells that are vertical neighbours. Due to the grid size of 500 metres, these grid cells show different mean values. Closer to the emission source, these differences can be significant, which then reflects in the graphic when these two neighbouring cells are considered, leading to the observed peaks.

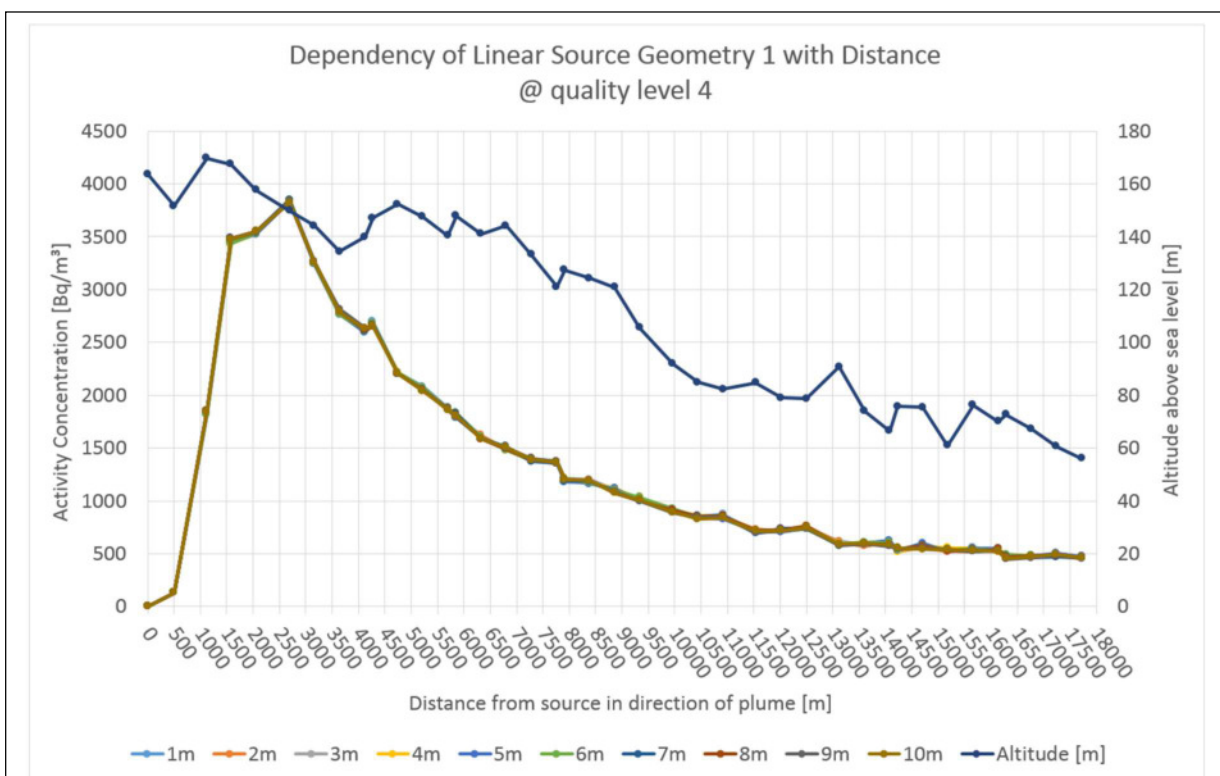


**Figure 2.1.1.2. Va** The mean activity concentration of the simulated time period plotted over the distance to the emission source in a direct line in plume direction towards ‘IRSN Cherbourg’ at particle quality level 4 (qs 4) for different source lengths for linear source geometry 1. Plotted in dark blue is the terrain elevation in metres above sea level to show possible accordance with the peak concentrations in the simulation results.

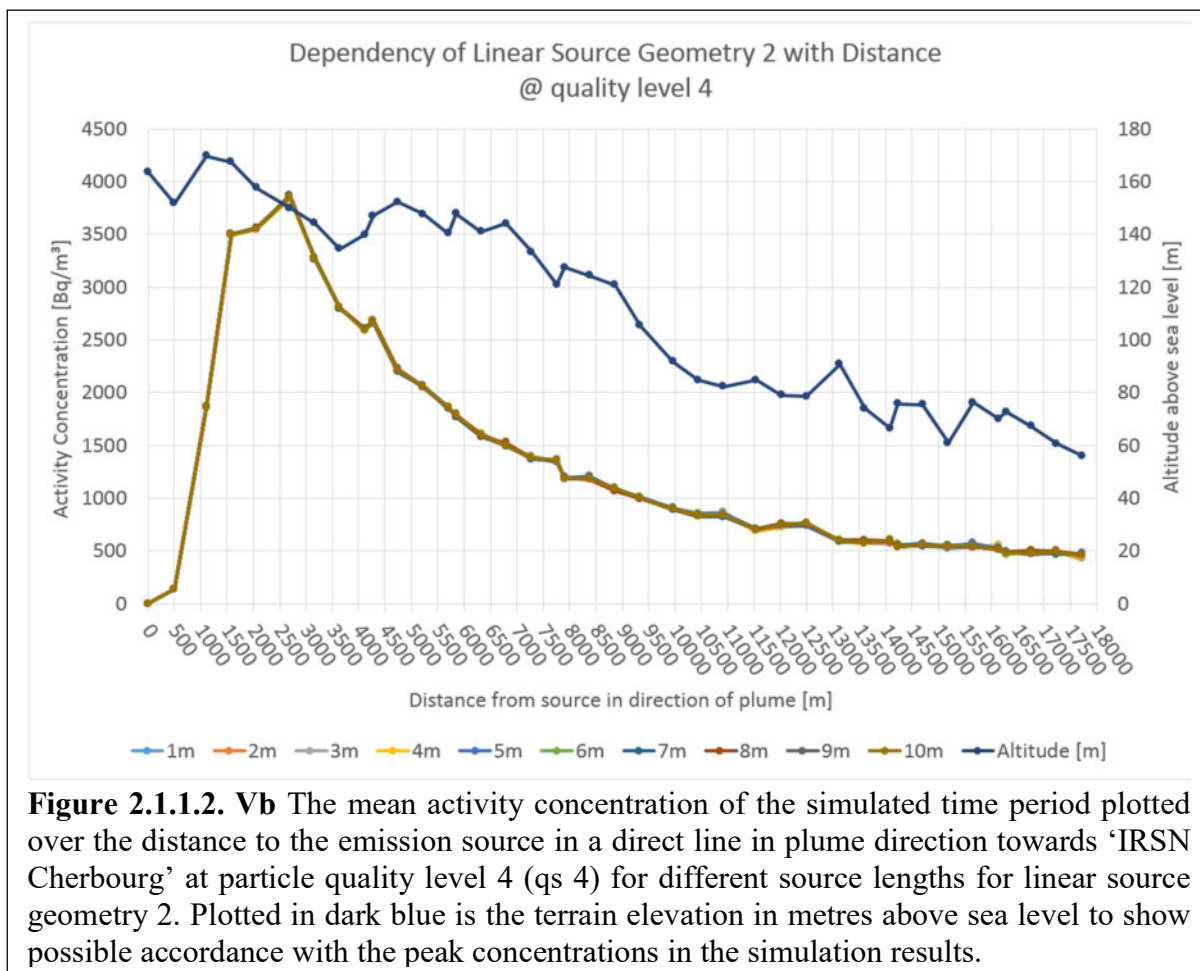


**Figure 2.1.1.2. Vb** The mean activity concentration of the simulated time period plotted over the distance to the emission source in a direct line in plume direction towards ‘IRSN Cherbourg’ at particle quality level 4 (qs 4) for different source lengths for linear source geometry 2. Plotted in dark blue is the terrain elevation in metres above sea level to show possible accordance with the peak concentrations in the simulation results.

## ii. Squared Source Geometries

The above described two linear source geometries were now combined respectively to span up squares, i.e. the lines of before are now the edges of the 2-dimensional squared source geometry to be studied here. Otherwise all simulation input data were kept the same and can be found in appendix G. Figure 2.1.1.2. VI shows the source geometry.

Also here, simulations with quality level 0 and quality level 4 were conducted. However, in the following figures only the results of the simulations at quality level 4 will be shown, as the results behave in a very similar pattern as for the scenarios with the linear source geometries. Figure 2.1.1.2 VII and figure 2.1.1.2 VIII show respectively the time series at the location ‘IRSN Cherbourg’ and the distance dependency of the result with increasing distance to the source in plume direction. Comparisons with the figures 2.1.1.2 IIIa,b, 2.1.1.2 IVa,b and 2.1.1.2 Va,b show that the results are nearly identical to the different linear source geometries, therefore suggesting that the influence of the horizontal size of the source, be it 1- or 2-dimensional is negligibly small compared to the statistical errors within the simulation.



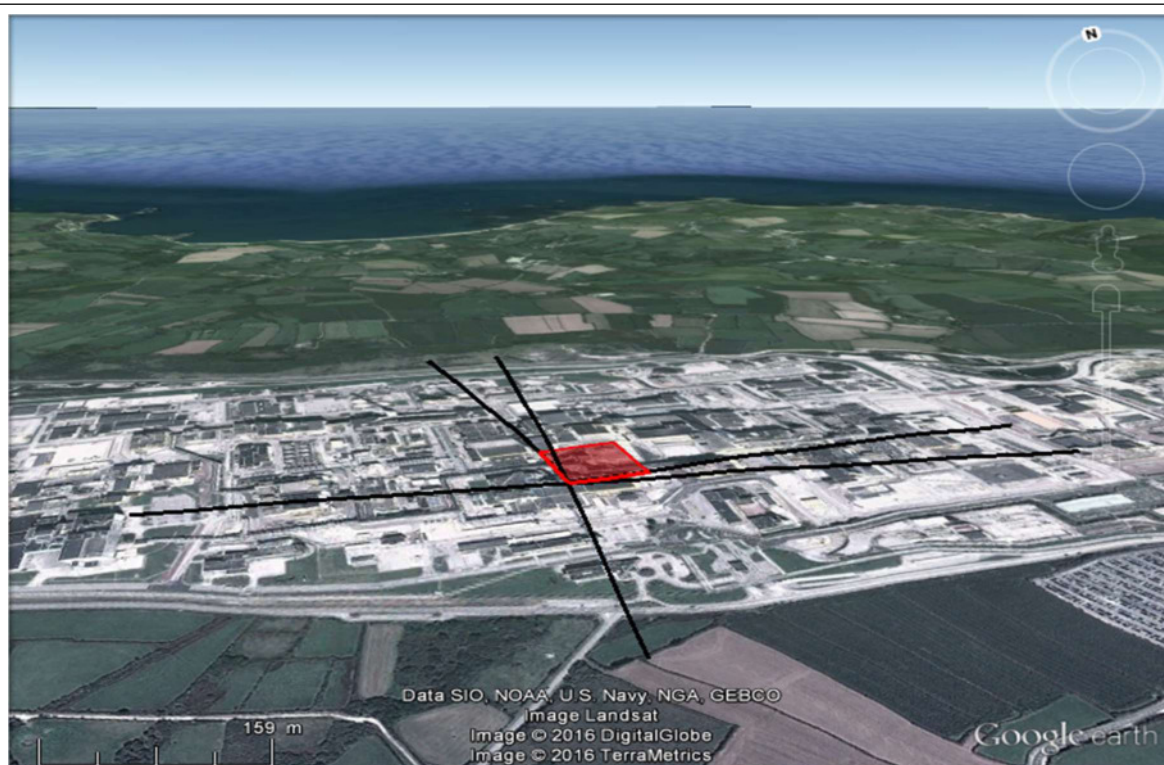


**Figure 2.1.1.2 VI** Scenario ‘Squared source geometry’. In red is the 2-dimensional squared source. The length of the lines are exaggerated by factor of 10 for demonstration purpose. The graphic was created using Google Earth.

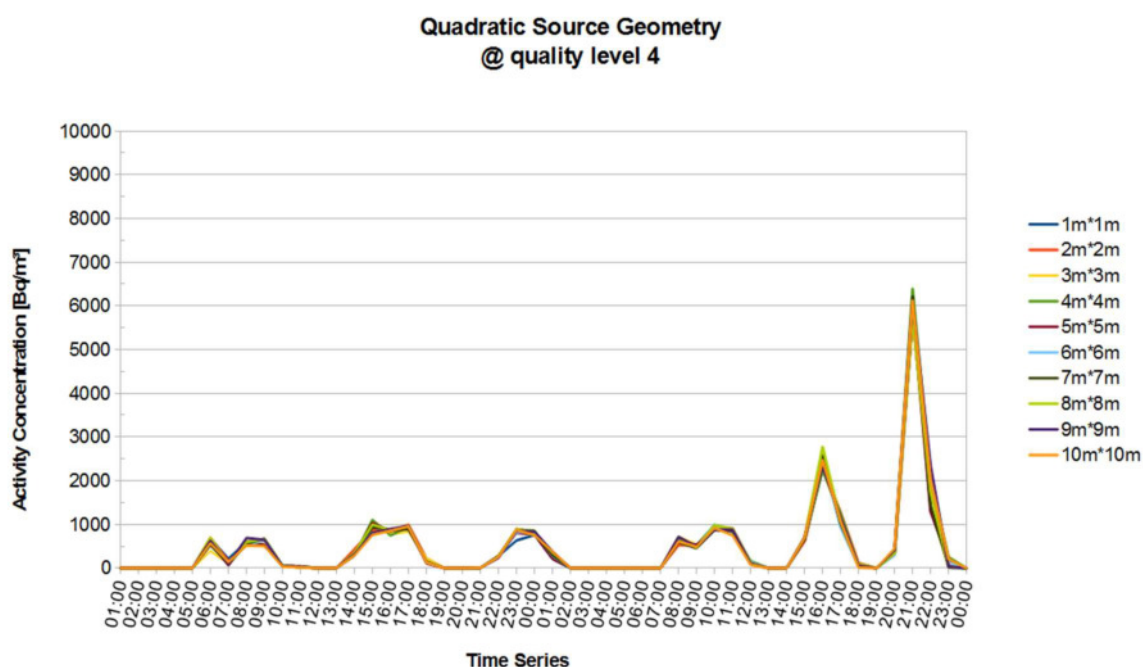


**Figure 2.1.1.2 VII** Distribution of the simulated activity concentration over a time period of 2 consecutive days at the measurement station ‘IRSN Cherbourg’ for the squared (quadratic) source geometry at particle quality level 4 (qs 4). Plotted in different colours are the results for the simulations with different source lengths.



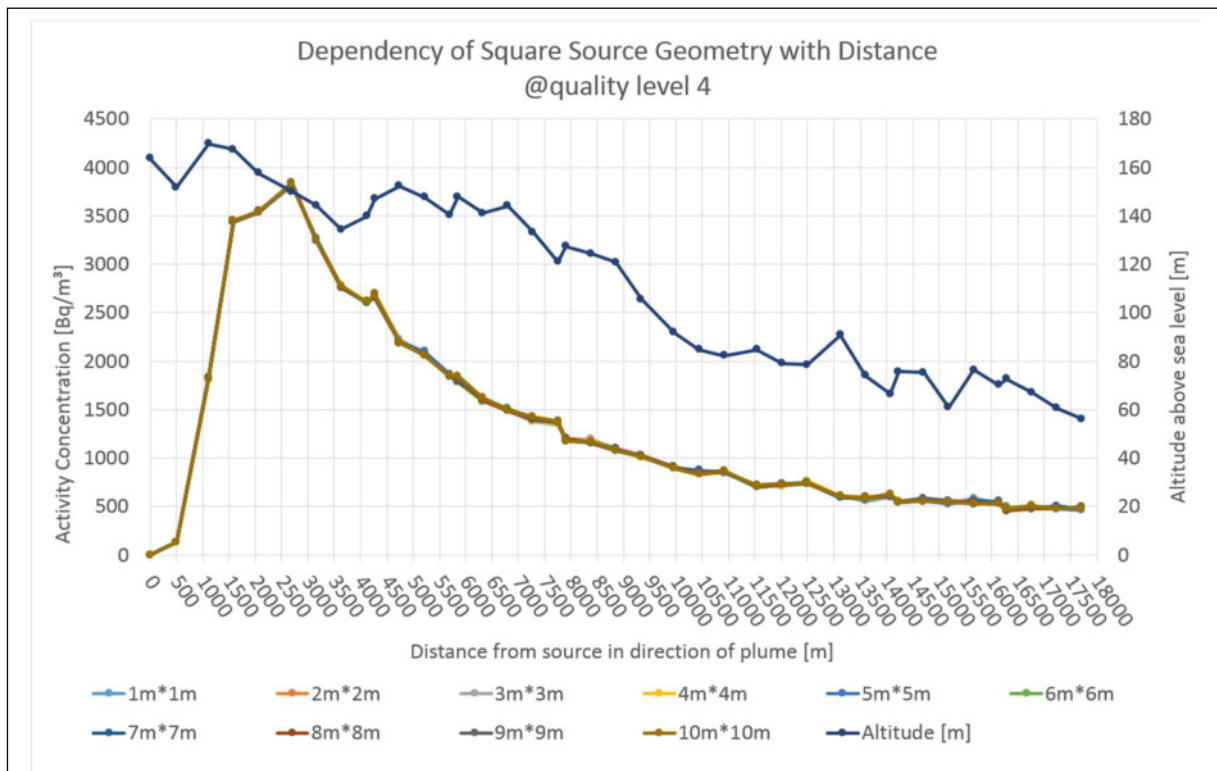


**Figure 2.1.1.2. VIII** The mean activity concentration of the simulated time period plotted over the distance to the emission source in a direct line in plume direction towards ‘IRSN Cherbourg’ at particle quality level 4 (qs 4) for different source lengths for the squared source geometry. Plotted in dark blue is the terrain elevation in metres above sea level to show possible accordance with the peak concentrations in the simulation results.

### iii. Cubic Source Geometry

Even though a 3-dimensional source is very unrealistic, usually sources are 2-dimensional (e.g. the circular end of a stack) it was studied here if and how such a 3-dimensional source geometry would affect the simulation results. The input parameters are the same as for the squared source geometry, with the additional extension into the vertical direction leading to a cubical source, as shown in figure 2.1.1.2. IX.

While the results of the time series (figure 2.1.1.2 X) show no difference to the time series results of the previous scenarios, there is a clear difference recognisable when plotting the mean activity concentrations over the distance from the source for the 10 different source sizes, as can be seen in figure 2.1.1.2. XI).

For the more distant locations there is little to no deviation between the activity concentrations, yet the closest points until around 4,000 metres distance from the emission show clear differences. Between the highest and the lowest, values can reach up to around  $500 \text{ Bq} \cdot \text{m}^{-3}$ , which is more than  $1/7^{\text{th}}$  of the actual value. It is easy to identify that the curve with the highest mean values in  $\text{Bq} \cdot \text{m}^{-3}$  for the simulation period is the one that originates from the smallest source geometry of  $1 \text{ m}^3$ , while the resulting curves for larger emission volumes gradually become lower. The lowest result values are produced by the largest emission volume of  $1,000 \text{ m}^3$ . The unchanging order of these lines suggest that this effect is more than just a simple statistical error in which case there would be more variations expected.

This effect can be explained by the presence of the  $3^{\text{rd}}$  dimension in the source geometry, the height. While the linear and square scenarios were all emitting in the same horizontal plane

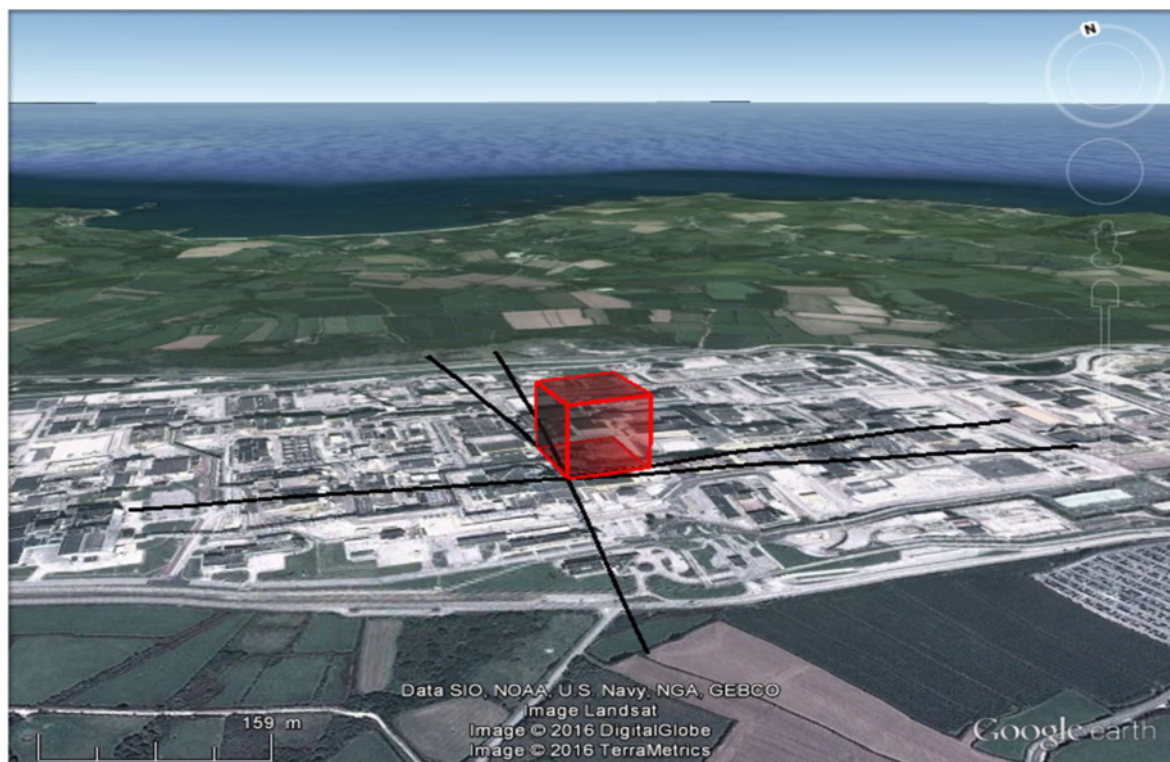


**Figure 2.1.1.2 IX** Scenario ‘Cubic source geometry’. In red is the 3-dimensional cubic source. The length of the edges are exaggerated by factor of 10 for demonstration purpose. The graphic was created using Google Earth.

parallel to the ground, now there is also the vertical component. With increasing altitude, of course also the wind field calculated by the model changes, for example due to increasing wind speeds with higher altitudes. While the horizontal extension by 1 metres does not make a noticeable difference, the vertical change of 1 metre has quite an effect. The emission volumes chosen might go from  $1 \text{ m}^3$  to  $8 \text{ m}^3$  to  $27 \text{ m}^3$  and so on until  $1,000 \text{ m}^3$ , but what makes the difference is not the volume itself, but only the height with is increased linearly in 1 metre steps. With this background it is now explainable that the lowest emission source volume shows the highest activity concentration levels. The emitted particles are distributed more or less homogeneously over the volume. If the volume reaches higher up, the particles get into regimes with a little bit higher wind speed and get carried away faster and further, which explains why the larger emission source geometries produce lower immission in the close vicinity of the source. On the other side, less high volumes get affected by lower wind speeds and therefore get mixed down to the ground earlier, which produces higher concentrations closer to the source. Of course, due to the stack height of 100 metres in this case and due to a neutral dispersion category, there is little to no immission directly at the source location and only after the first 500 metres the plume widened up enough to reach the ground and produce remarkable immission values.

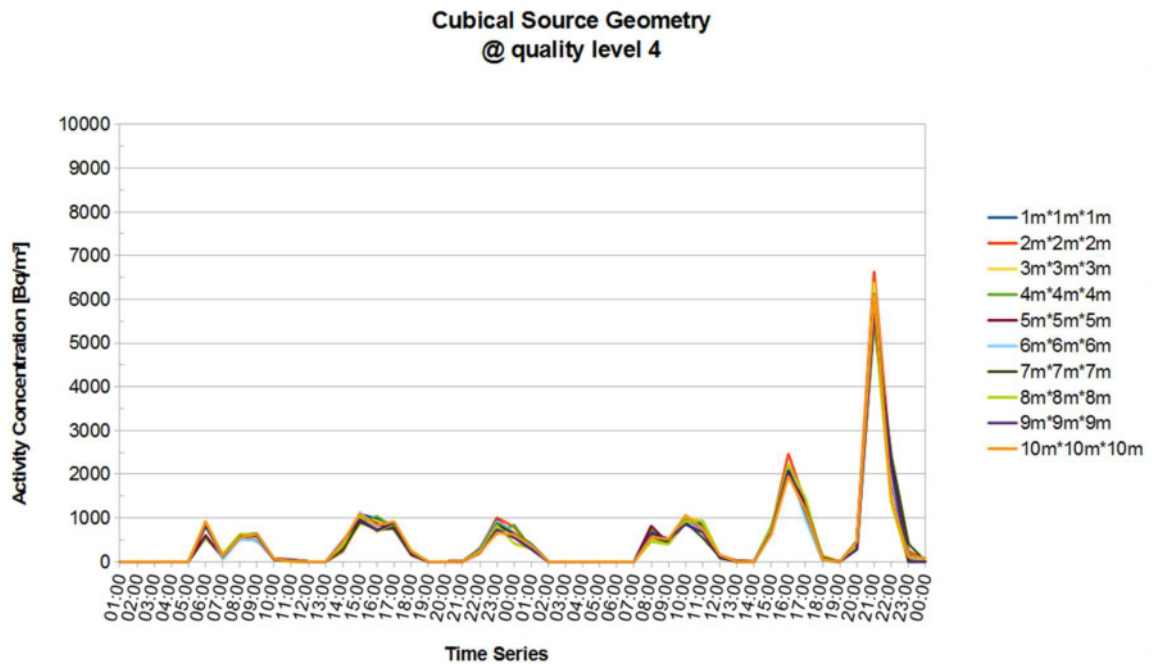


**Figure 2.1.1.2 X** Distribution of the simulated activity concentration over a time period of 2 consecutive days at the measurement station ‘IRSN Cherbourg’ for the cubic source geometry at particle quality level 4 (qs 4). Plotted in different colours are the results for the simulations with different source lengths.

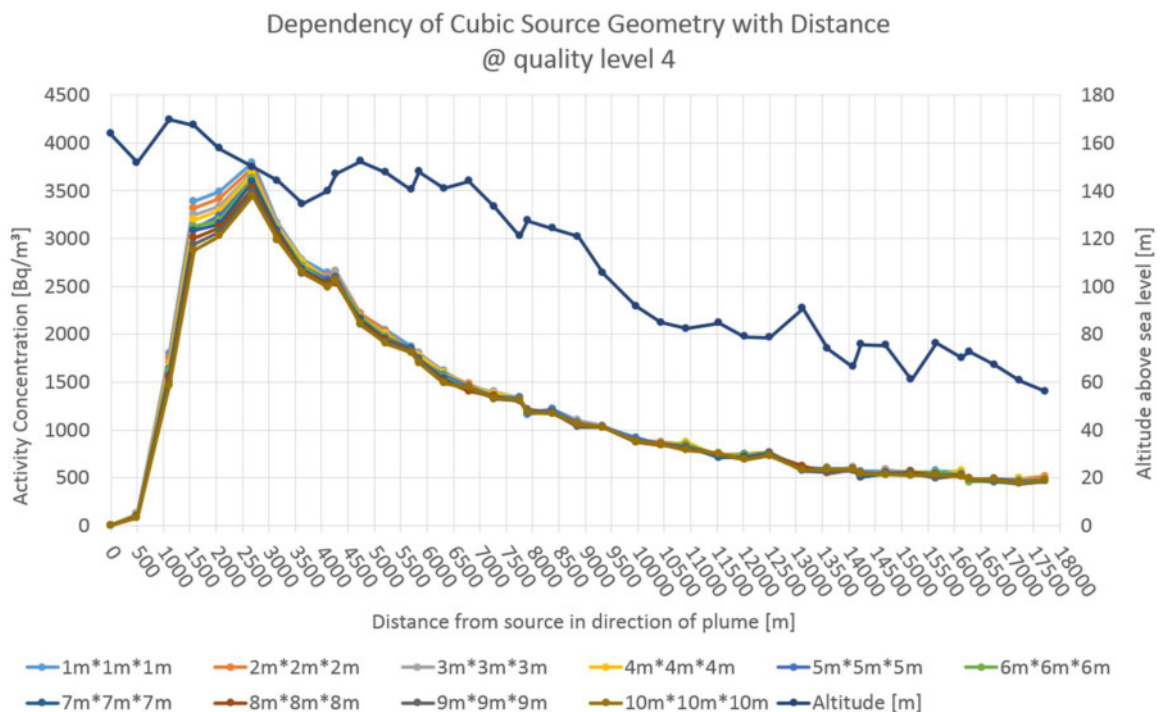


**Figure 2.1.1.2. XI** The mean activity concentration of the simulated time period plotted over the distance to the emission source in a direct line in plume direction towards ‘IRSN Cherbourg’ at particle quality level 4 (qs 4) for different source lengths for the cubic source geometry. Plotted in dark blue is the terrain elevation in metres above sea level to show possible accordance with the peak concentrations in the simulation results.

#### iv. Mathematical Description

Since the results for the scenarios in this chapter show very good congruence and especially the part with the decreasing activity concentration, it suggests an underlying mathematical function that can describe the curve and serve as a fitting line, or predict the concentrations for larger distances. (Following chapters will show the appearance of similar decreases in the concentrations.)

In order to determine a fit, the results curve was separated at its maximum value into the left side and the right side. In order to calculate the fits, the linear source geometry 2 was chosen, due to its very good congruency of the different curves.

The left side of the peak, which looked like a polynomial distribution, was approximated by a polynomial of 5<sup>th</sup> degree (2.1.1.2 i). Therefore the simulated points until the maximum value were inserted into a 5<sup>th</sup> degree polynomial function, with the exception of the point at around 1,500 metres who in a previous attempt to calculate the polynomial proved to disturb the results too much to be of use. With  $x$  being the distance from the source in metres,  $y_0^{(1)}$  the y-value of the first data point, and  $n$  being the number of different samples, here there are 10 different lines originating from the different emission source sizes.

$$f_1(x) = -2.45 \cdot 10^{-13} m^{-5} \cdot x^5 + 2.05 \cdot 10^{-9} m^{-4} \cdot x^4 - 6.62 \cdot 10^{-6} m^{-3} \cdot x^3 + 9.36 \cdot 10^{-3} m^{-2} \cdot x^2 - 2.99 m^{-1} \cdot x + \frac{1}{n} \sum_n y_{0,n}^{(1)} \quad (2.1.1.2 \text{ i})$$

The right side of the peak can be described by equation (2.1.1.2 ii), where the function is dependent on a normalised distance number  $N$  that starts with  $N_0 = 1$  at the data point  $P_2(x_0^{(2)}, y_0^{(2)})$ . This data point is located where the fitting curve has its maximum y-value, this is also where in the simulation data curves the maximum values can be found. The value  $y_0^{(2)}$  is taken from the result of the fitting function  $f_1$ , described in the equation (2.1.1.2 i) above. The x-value  $x_0^{(2)}$  is set to 0.

$$f_2(x) = y_0^{(2)} \frac{1}{\left( N_{n-1} + \frac{d_n}{d_0} \right)^{E_{n-2} - \frac{1}{N_n^{1.17}}}} \quad (2.1.1.2 \text{ ii})$$

The distance between  $P_2$  and the first point of the right side fitting curve is defined as  $d_0 = x_0^{(2)} - x_1^{(2)}$  with  $x_1^{(2)}$  being the distance to  $x_0^{(2)}$  in metres. Since the distances between two concluding points may vary,  $d_0$  is used to normalise the distances  $d_n = x_n^{(2)} - x_{n-1}^{(2)}$  to obtain a unit-less description  $\frac{d_n}{d_0}$ . Added to the distance number  $N_0$  via  $N_n = N_{n-1} + \frac{d_n}{d_0}$ , it results in a

decimal number. This number contributes to (2.1.1.2 ii) in several ways, once, being the base for the first exponent, secondly as being part of the exponent as well, and thirdly is used for the exponential value  $E_n = E_{n-1} - \frac{1}{N_n^{1.17}}$  with  $E_0 = 4$ . This value  $E_0$  as well as the number 1.17

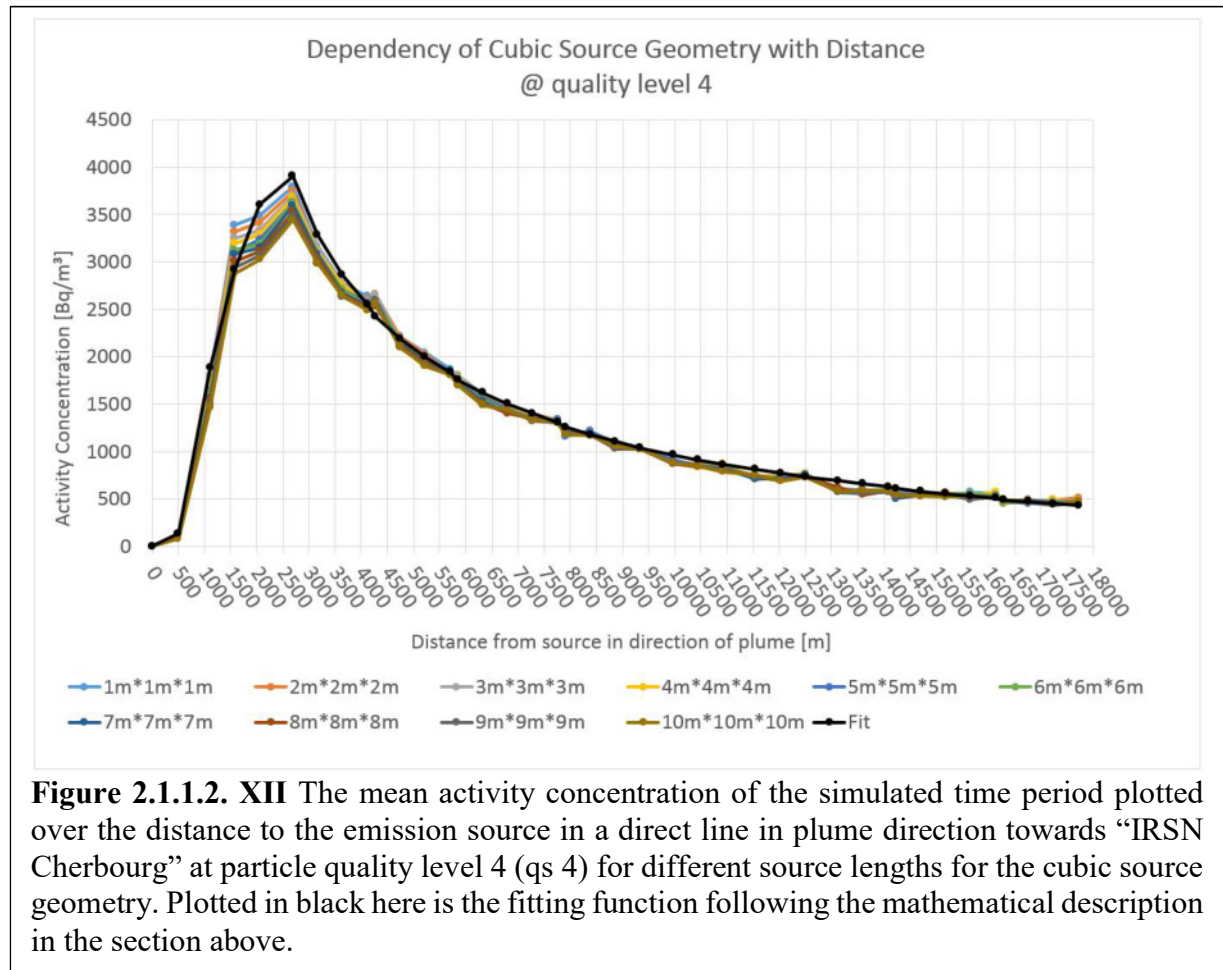
were determined via trial and error to fit the simulation data curves and turned out to be well suitable.

Combining both equations  $f_1$  and  $f_2$  in order to calculate and predict the y-values leads to (2.1.1.2 iii):

$$y_n = \begin{cases} f_1 & \text{for } f_1 \geq 0 \\ 0 & \text{for } f_1 < 0 \\ f_2 & \text{for } x_n^{(2)} > x_0^{(2)} \end{cases} \quad (2.1.1.2 \text{ iii})$$

In which  $f_1$  can be applied for all cases unless its values are getting negative, where the fit values are set to zero. Once  $f_1$  reaches its maximum y-value, which defines the point  $P_2(x_0^{(2)}, y_0^{(2)})$ , then for all follow-up values the equation  $f_2$  applies.

An example for this fitting function, here included in the cubic source geometry, is shown in figure 2.1.1.2 XII.



### 2.1.1.3 Terrain roughness

Another external parameter that might have an influence on the simulation results is the terrain roughness. The terrain roughness is a method to describe the land surface cover, for example the natural or artificial vegetation, open water surfaces, or urban structures. Vegetation or artificial barriers can have great influences on the wind field, as they induce turbulences by being over- or circum-streamed. Describing this process in detail would require more complex fluid dynamic models [Mayall, 2003], which would not be necessary for the application purpose of ARTM. ARTM accounts for these induced turbulences via the roughness length parameter



$z_0$  according to the CORINE (Coordination of Information on the Environment) land cover register (see table 2.1.1.3) [Richter et al., 2013a, 2013b]. The lowest  $z_0$  values are those of plain or nearly plain surfaces with low complexity, while the largest ones are from tall and complex structures that induce the biggest turbulences. These values are empirical and 9 roughness length categories  $z_0$  – 0.01 m, 0.02 m, 0.05 m, 0.1 m, 0.2 m, 0.5 m, 1.0 m, 1.5 m and 2.0 m (see table 2.1.1.3) – were selected to be integrated into the renewed TA-Luft in 2001, as communicated by H. Thielen via E-mail.

For simulation areas within Germany, the CORINE land register can be loaded into ARTM and then it automatically calculates the value  $z_0$  [Richter et al., 2013a, 2013b]. Therefore it creates the mean value of the roughness lengths in a circle with the radius defined by the tenth-fold of the emission/stack height around the emission source [Richter et al., 2013a]. It is assumed that this area has the highest influence on the dispersion in terms of turbulences that are induced by the land cover.

**Table 2.1.1.3** shows the roughness length values  $z_0$  for different types of land use, as defined by the CORINE land register (according CORINE number in brackets) [BMU, 2002]. The table was directly translated from BMU (2002).

$z_0$ in [m]	Category according to CORINE
0.01	Beaches, dunes and sandy areas (331), water surfaces (512)
0.02	Waste and mining disposals (132), grass and pasture land (231), natural green fields (321), areas with sparse vegetation (333), salt marshes (421), areas in tidal zones (423), flowing water bodies (511), estuaries (522)
0.05	Mining areas (131), sports and recreation areas (142), non-irrigated agricultural land (211), glaciers and areas of permanent snow cover (335), lagoons (521)
0.10	Airports (124), swamps (411), peat lands (412), seas and oceans (523)
0.20	Streets, rail-road tracks (122), urban parks (141), wine yards (221), complex parcel structures (242), agricultural and natural surface vegetation (243), heaths and swamp-heaths (322), rock areas without vegetation (332)
0.50	Port lands (123), fruit and soft fruit plantations (222), forest-shrub mixed areas (324)
1.00	Inconsistent urban structures (112), industry and commercial areas (121), construction sites (133), coniferous forests (312)
1.50	Broad-leaved forests (311), mixed forests (313)
2.00	Consistent urban structures (111)

Here in this section a study was conducted to analyse the difference between the different roughness lengths. Therefore, a set of 144 simulations was conducted and analysed. In order to decrease the statistical error, there were 16 simulations with different starting random numbers (see chapter 2.1.2.1) for each of the 9 roughness lengths performed. These always 16 simulations were unified in an average value that went into the analysis and a standard deviation (1.3.1.3 iii), which estimates the statistical error. The input parameters can be found in detail in appendix G.

Figure 2.1.1.3 I shows the averaged simulation results for the 9 different roughness length values plotted over the distance from the emission source. The standard deviation is indicated by the error bars, even though in this case they are very small and hardly distinguishable. The graphic shows that the simulation behaves logically; the highest roughness length value, indicating the largest induced atmospheric turbulences, creates the highest activity concentration in proximity to the emission source and the lowest activity concentration in the further distance. The large turbulence mixes down the plume earlier and more effective than the turbulences induced by smaller obstacles.

The 9 different plotting lines in the diagram order strictly by the size of their respective roughness length values. Until around 2,500 metres distance from the emission source, the highest activity concentration values are resulting from the largest roughness length, and from around 4,500 metres, the smallest roughness length results in the largest concentrations. Between 2,500 and 4,500 metres the order of the lines is inverting.

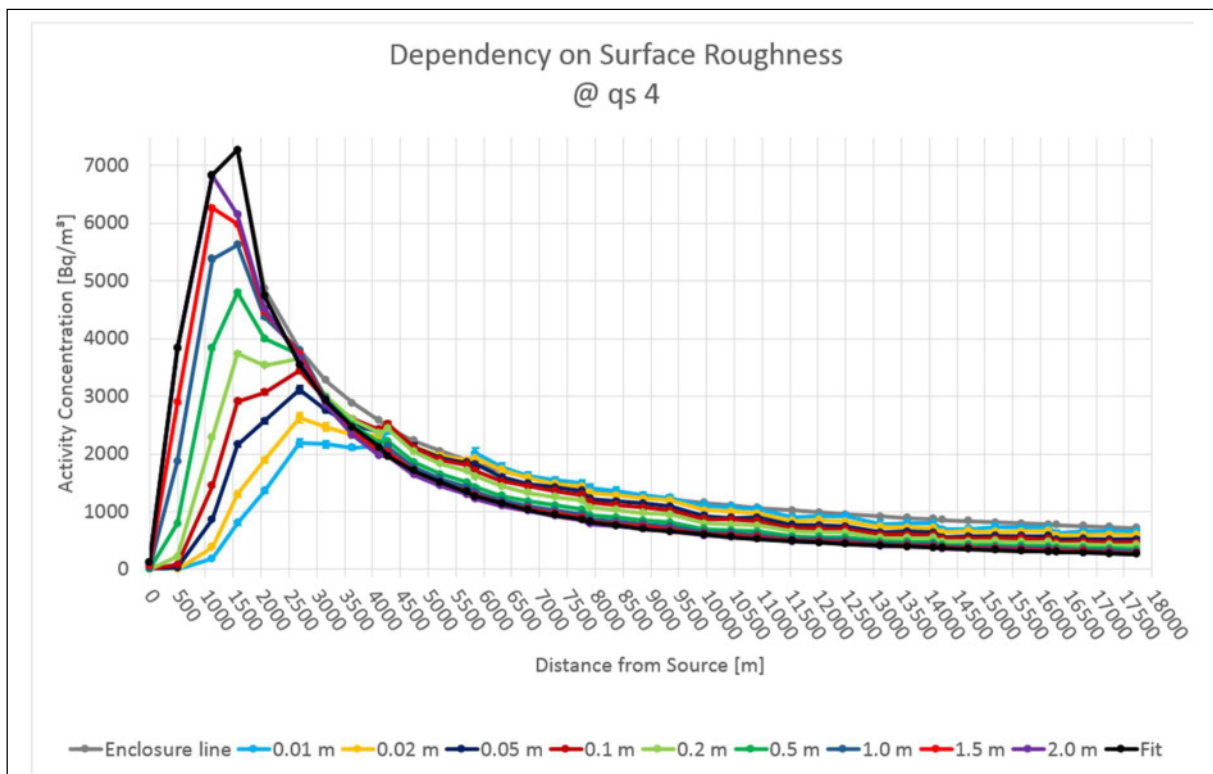


**Figure 2.1.1.3 I** The mean activity concentration of the simulated time period plotted over the distance to the emission source in a direct line in plume direction towards “IRSN Cherbourg” at particle quality level 4 (qs 4) for different surface roughness lengths. The black line shows the fitting line of the highest roughness length. The grey line is the enclosure line that depicts the worst case of all simulation results.

The black curve here is the fitting curve for the case when the roughness length is maximum. The attempt to fit this curve is nearly identical as for the source geometry in the previous section; the left side can be approximated with a polynomial  $f_1$  as in equation (2.1.1.2 iv), while the right side has the shape of (2.1.1.2 v) with  $E_0^{(1)} = 2.7$  and  $m_1 = 1.65$ .  $y_{0,\max}^{(1)}$  is of all the y-values for the plotted roughness length at  $x=0$  the one that is at maximum, with  $y_{0,\max}^{(1)} = 120$  in this case for the line with the roughness length value of 2.0 m. While  $d_n$  and

$N_n$  are the same as described in previous section 2.1.1.2,  $E_n^{(1,2)} = E_{n-1} - \frac{1.6}{N_n^{m_{(1,2)}}}$ . Again here

the function  $f_2$  is applied after  $f_1$  produced a peak with a maximum value. The only difference in the process here, in contrast to the process in the previous section, is that the y-value  $y_{0,s}^{(2)}$  was taken from the data point of the simulation data curve where also  $f_1$  has its maximum. It was not taken from the point of the fitting curve as it appears, so that in this case there is a large difference in the activity concentration of the simulation data point and the fitting data point.

$$f_1(x) = 2.55 \cdot 10^{-13} m^{-5} \cdot x^5 - 1.97 \cdot 10^{-9} m^{-4} \cdot x^4 + 3.65 \cdot 10^{-6} m^{-3} \cdot x^3 - 4.77 \cdot 10^{-3} m^{-2} \cdot x^2 + 9.12 m^{-1} \cdot x + y_{0,\max}^{(1)} \quad (2.1.1.2 \text{ iv})$$

$$f_2^{(1,2)}(x) = y_{0,s}^{(2)} \frac{1}{\left( N_{n-1} + \frac{d_n}{d_0} \right)^{\frac{1}{E_{n-2}^{(1,2)} - \frac{1.6}{N_{n-1}^{m_{1,2}}}}} \quad (2.1.1.2 \text{ v})$$

The grey curve is the enclosure line, which means that all values resulting from the dispersion simulation can be found below. This line shows always the worst case of all the data curves, and it directly derives from (2.1.1.2 iv), where it is identical with the black line and using following (2.1.1.2 v) with  $E_0^{(2)} = 3$  and  $m_2 = 1.75$ .

For both curves also the relation (2.1.1.2 iii) from section 2.1.1.2 is valid considering the above mentioned deviation in terms of the  $y_{0,s}^{(2)}$  value.

Also the time series for the roughness length was studied, yet the results do not show not bring any new in addition. It basically shows the same peaks as for source geometry in section 2.1.1.2 above, but this time with a clear ordering of the lines, depending on the roughness length (see figure 2.1.1.3 II).



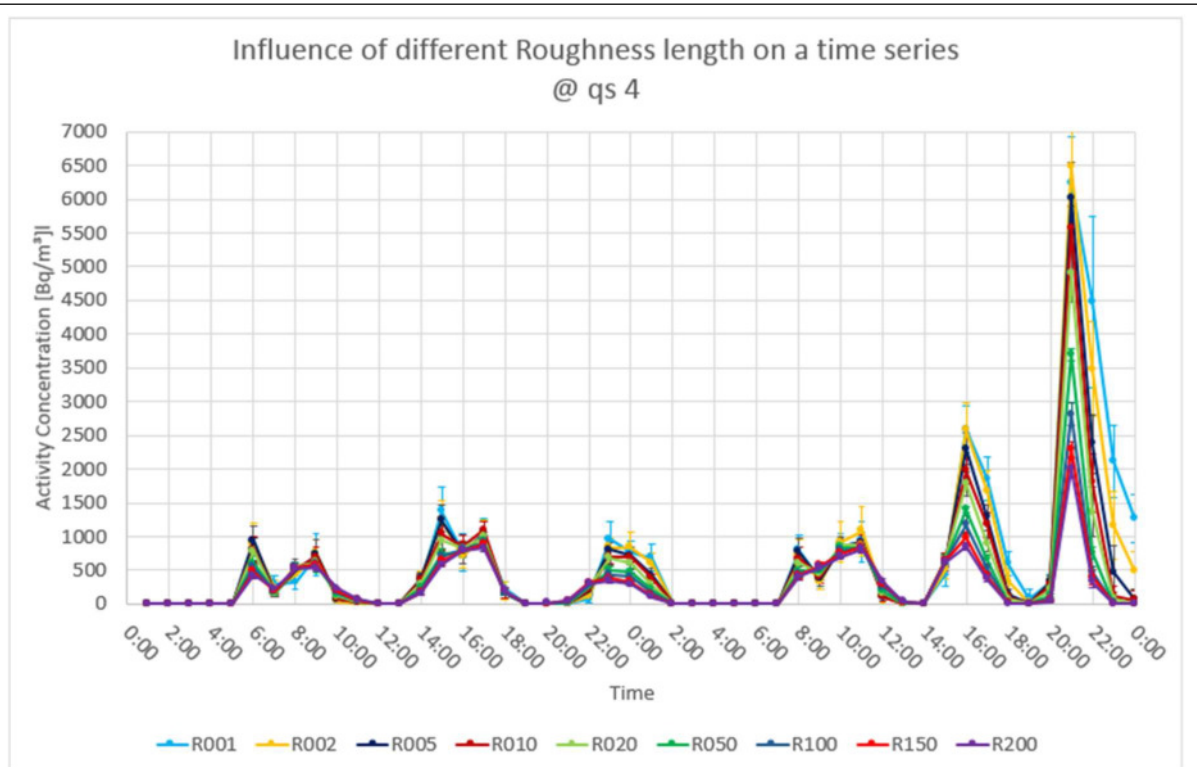


**Figure 2.1.1.3 II** Distribution of the simulated activity concentration over a time period of 2 consecutive days at the measurement station “IRSN Cherbourg” for the different roughness length values. The error bars show the standard deviations resulting from the 16 different simulations for each value.

#### 2.1.1.4 Dispersion Categories

Of course one of the most important inputs for any atmospheric dispersion simulation are the meteorological data. At minimum it requires wind speed, wind direction and the types of atmospheric layering and turbulence, expressed via the so-called dispersion categories.

Different wind speeds can have huge influence on the simulation results [Mayall, 2003]. For example higher wind speeds would result in lower activity concentrations as the same amount of emitted material is spread into a larger volume of air [Mayall, 2003]. Due to the larger speed, it would also get distributed over larger distances before decaying or being deposited. For lower wind speeds this works vice-versa. Different wind directions and especially when considering orography might lead to different results as well.

Atmospheric profiles show that with increase in altitude also the wind speed increases logarithmically (among also some other parameters that change with increasing altitude) [Rödel, 1992].

But since wind speed and wind direction can be measured quite well with high confidence, here only the turbulence is studied in more detail. Depending on some factors, such as solar radiation, there can exist more or less turbulences within the atmosphere, even without the influence of orography, surface cover or high buildings [Panofsky, 1982]. This is attempted to be described by different types of atmospheric layering that reach from very stable (almost no turbulences) via neutral (some medium turbulences) towards very unstable (highly turbulent) [Rödel, 1992]. During the course of the day, depending on solar radiation, the atmospheric layering can change and show a typical distribution over the day, with stable conditions at night, neutral in the morning and evening, and unstable around noon and in the afternoon, when the solar radiation is at maximum [Lochte, 2011].

ARTM was designed to either use the Monin-Obukhov-length or the dispersion categories defined by Klug-Manier [Richter et al, 2013a]. The Monin-Obukhov-length  $L$ , a way of parameterising the atmospheric turbulence can be described as in equation (2.1.1.4 i) [Jensen & Busch, 1982].

$$L_M = -\frac{u_*^3}{k \cdot \frac{g}{T_0} \cdot \overline{\theta'w'}} \quad (2.1.1.4 \text{ i})$$

It is based on the frictional velocity  $u_*$ , the reference temperature  $T_0$ , the gravitational constant  $g$ , which together as  $\frac{g}{T_0}$  make describe the buoyancy, the heat flux  $\overline{\theta'w'}$  and the von Kármán constant  $k$  [Jensen & Busch, 1982].

The Monin-Obukhov-length can be translated into the dispersion categories following the Klug-Manier notation as seen in table 2.1.1.4 I.

The mixing layer altitudes for positive Monin-Obukhov-lengths  $L_M$  have to be determined in dependency of the Coriolis parameter  $f_c = 10^{-4} \text{ s}^{-1}$  and a constant  $\alpha = 0.3$  as given in function (2.1.1.4 ii) [Janicke Consulting, 2008].

$$h_m = \begin{cases} \alpha \frac{u_*}{f_c} & \text{for } L_M > \frac{u_*}{f_c} \\ \alpha \frac{u_*}{f_c} \left( \frac{f_c L_M}{u_*} \right)^{0.5} & \text{for } 0 < L_M < \frac{u_*}{f_c} \end{cases} \quad (2.1.1.4 \text{ ii})$$

The dispersion categories are determined via a variety of different methods, such as radiative transfer, temperature gradients, standard deviations from horizontal wind directions, vertical wind velocity (e.g. measured by SODAR) or via synoptical observation of cloud coverage [SSK, 1995a; KTA 1508, 2006].

**Table 2.1.1.4 I**, Atmospheric dispersion categories and Monin-Obukhov-length. The dispersion categories following the Klug-Manier notation can be translated into Monin-Obukhov-lengths, with each category showing different mixing layer altitudes. The table is based on a table taken from Janicke Consulting, (2008).

Dispersion Category			Monin-Obukhov-Length [m] (at roughness length 1.5)		Mixing Layer Altitude [m]
Klug- Manier	KTA 1508	ARTM	Interval	Default	
I	F	1	$L_M^{(1.5)} < 100$	70	$h_m$ calculated using (2.1.1.4 ii)
II	E	2	$100 \leq L_M^{(1.5)} < 500$	250	
III/1	D	3	$500 \leq L_M^{(1.5)} \text{ or } L_M^{(1.5)} < -700$	99999	
III/2	C	4	$-700 \leq L_M^{(1.5)} < -200$	-300	800
IV	B	5	$-200 \leq L_M^{(1.5)} < -100$	-150	1100
V	A	6	$-100 \leq L_M^{(1.5)}$	-70	1100

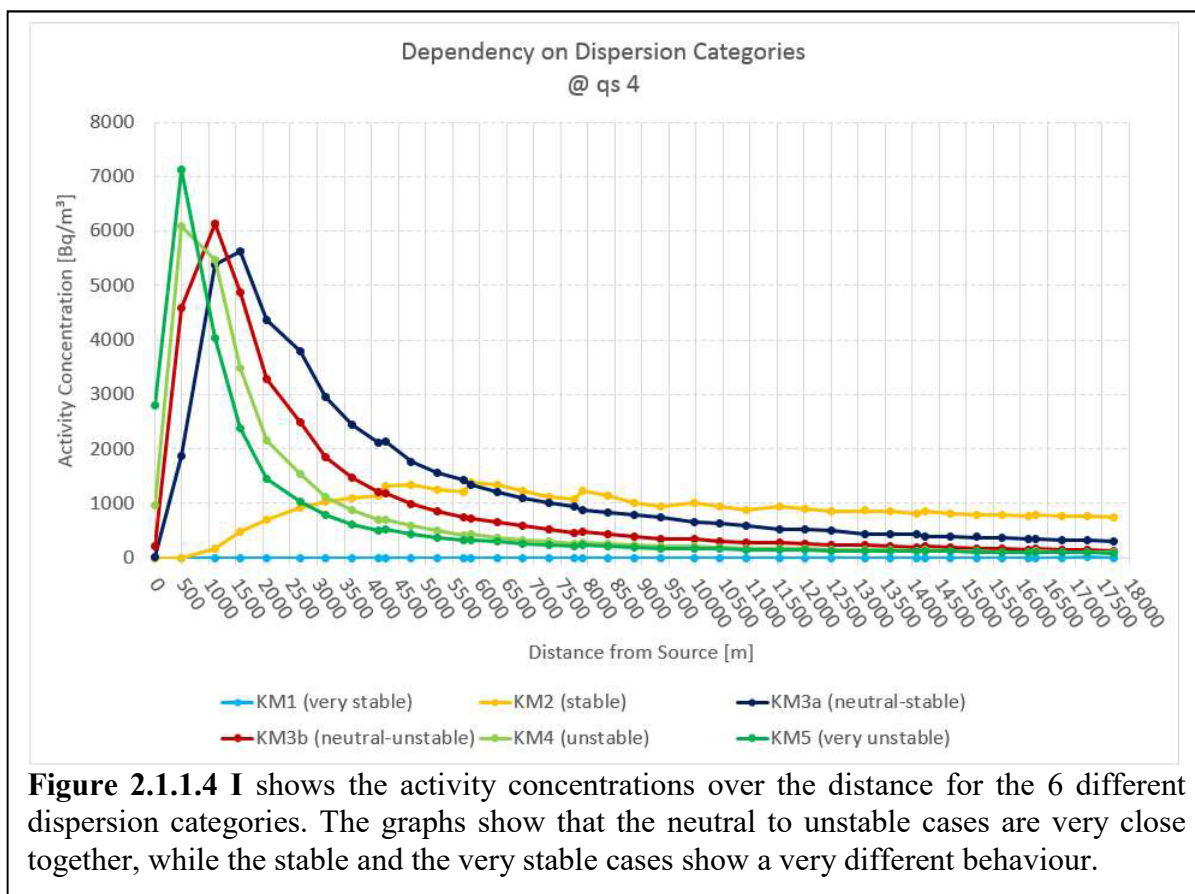
**Table 2.1.1.4 II**, Determination of the dispersion categories based on SODAR data. Table translated from KTA 1508, (2006).

U_mean in m/s	Sigma_vertical in m/s				
	Borders of the dispersion categories				
	A/B	B/C	C/D	D/E	E/F
0 to 0.9	0.51	0.42	0.32	0.2	0.14
1 to 1.9	0.55	0.43	0.33	0.2	0.14
2 to 2.9	0.63	0.47	0.35	0.21	0.15
3 to 3.9	0.72	0.53	0.38	0.22	0.15
4 to 4.9	0.83	0.58	0.42	0.22	0.15
5 to 5.9	0.94	0.66	0.45	0.23	0.16
6 to 6.9	1.07	0.73	0.49	0.25	0.16
7 to 7.9	1.2	0.81	0.54	0.26	0.17
8 to 8.9	1.33	0.89	0.58	0.27	0.18
9 to 9.9	1.46	0.98	0.63	0.29	0.18
10 to 10.9	1.59	1.06	0.68	0.31	0.19
11 to 11.9	1.74	1.15	0.73	0.32	0.2
12 to 12.9	1.88	1.24	0.79	0.34	0.21
13 to 13.9	2.03	1.33	0.84	0.36	0.21
14 to 14.9	2.15	1.42	0.89	0.38	0.22
15 to 15.9	2.29	1.5	0.94	0.4	0.23
16 to 16.9	2.44	1.59	1	0.42	0.24
17 to 17.9	2.58	1.68	1.06	0.44	0.25
18 to 18.9	2.73	1.77	1.11	0.46	0.26
19 to 19.9	2.87	1.87	1.17	0.48	0.27

In all of these cases, the dispersion category is not directly measured, but will be determined using data tables with experimentally defined boundaries for the different categories [KTA 1508, 2006]. Depending on which of these methods are applied, the resulting determination of the categories can have huge differences, suggesting that there is still the need of improving the methods to standardise the determination process of the dispersion classes in order to better describe the realistic cases and to minimise the deviations in the dispersion simulations [Lochte, 2011]. Table 2.1.1.4 II shows the determination of the dispersion categories for SODAR measurements, directly translated from the KTA 1508.

For this study 96 simulations with ARTM were performed, again in ensembles of 16 different starting random numbers (see chapter 2.1.2.1) for each of the 6 different dispersion categories defined in table 2.1.1.4 I. The other input parameters were kept the same as for the previous sections and can be found in detail in appendix G.

The average values of these 16 simulations for each of the 6 dispersion categories were calculated by ARTMRes (described in chapter 1.2.1.1) and plotted over the distance from the source, as can be seen in figure 2.1.1.4. The error bars, resulting from the standard deviation calculated as described in chapter 1.3.1.3, are too small to appear in the figure, as the standard deviation is two to four orders of magnitude smaller than the average values.



The graph shows that there is a huge difference between the dispersion categories, especially the ‘stable’ and the ‘very stable’ ones show the largest differences, while the curves of the other 4 categories have similar shape and could be described by functions of the form as mentioned in previous sections. The mathematical explanation for this phenomenon can be found in Appendix A.1.

The ‘very unstable’ case has the highest turbulence and therefore mixes down a lot of the emitted material already in close vicinity to the stack. Over the distance, this decreases rapidly and for far distances the resulting activity concentration values are lower than for most of the other dispersion categories. Also the ‘unstable’ and the two neutral cases behave in that way, except their contribution in the near being gradually lower and in the far being gradually higher than the ‘very unstable’ case.

Now for the ‘stable case’ it is to expect that the contribution in the near is much lower and that for the far there is a higher concentration to be expected. The graph shows exactly this, even though the curve is in the range of factor 5 to 6 lower in its peak as the other curves, and has at least on the scale of 18km downstream only a small decrease.

Interestingly, the effect of sudden inclines between points that are closer to each other (originating from the diagonal line shown in figure 2.1.1.2 I going through 2 grid cells) appears to be stronger for the ‘unstable’ case than for any other case, suggesting that the plume in proximity to the ground is quite tight, leading to larger differences between neighbouring cells that are not directly in plume direction.

The ‘very stable’ case does not mix and therefore with the stack height of 100 meter, the emission plume stays at this altitude for long distances without mixing down too much. The 18 km scale here in this scenario is too small to observe when the plume efficiently reaches down to the ground. As in figure 2.1.1.4 II can be seen, there is little concentration in the ground air and only at larger distance (P1 is the place of the measurement station). Starting from about 40

metres over ground, there is a slow increase in concentration around P1. The maximum concentrations can be found in the altitude of the emission source at 100 to 150 metres over ground. The plume does not widen in this height and the streaks show the different simulation periods with wind from different directions, suggesting a very narrow cloud that does not mix a lot in vertical or horizontal direction. The layer of 200 to 300 metres over ground already shows the end of the cloud. The cut-off effect around P1 can be explained by the orography in combination with the very stable atmospheric layering. Shortly after the P1 point, there is a valley in the south of Cherbourg, and beyond a valley an incline of up to 130 metres as the altitude profile in figure 2.1.1.4 III shows. The white overlay cuts out areas that lie lower than 70 metres above the sea level. Compared with the forth image in figure 2.1.1.4 II, it appears that the shape of the observed feature is well represented by the shape of the overlay, suggesting that here the orography play the important role. Since a very stable layering was chosen, the plume stays mainly in the same layer of air without much of a mixing. So while the emission stay in an altitude of around 300 over sea level (consisting of the latitude of the La Hague facility at 190 metres above sea level plus 100 metres of stack height), the simulation layers follow the orography and are therefore not parallel to the sea level. Here in this case it means that around the valley near P1, the 200 to 300 meters over ground layer reaches down into lower air layers and therefore dipping into the plume.

So one can conclude that in this very stable case, the most of the emitted nuclides stay in the emission altitude with little down or upward mixing.

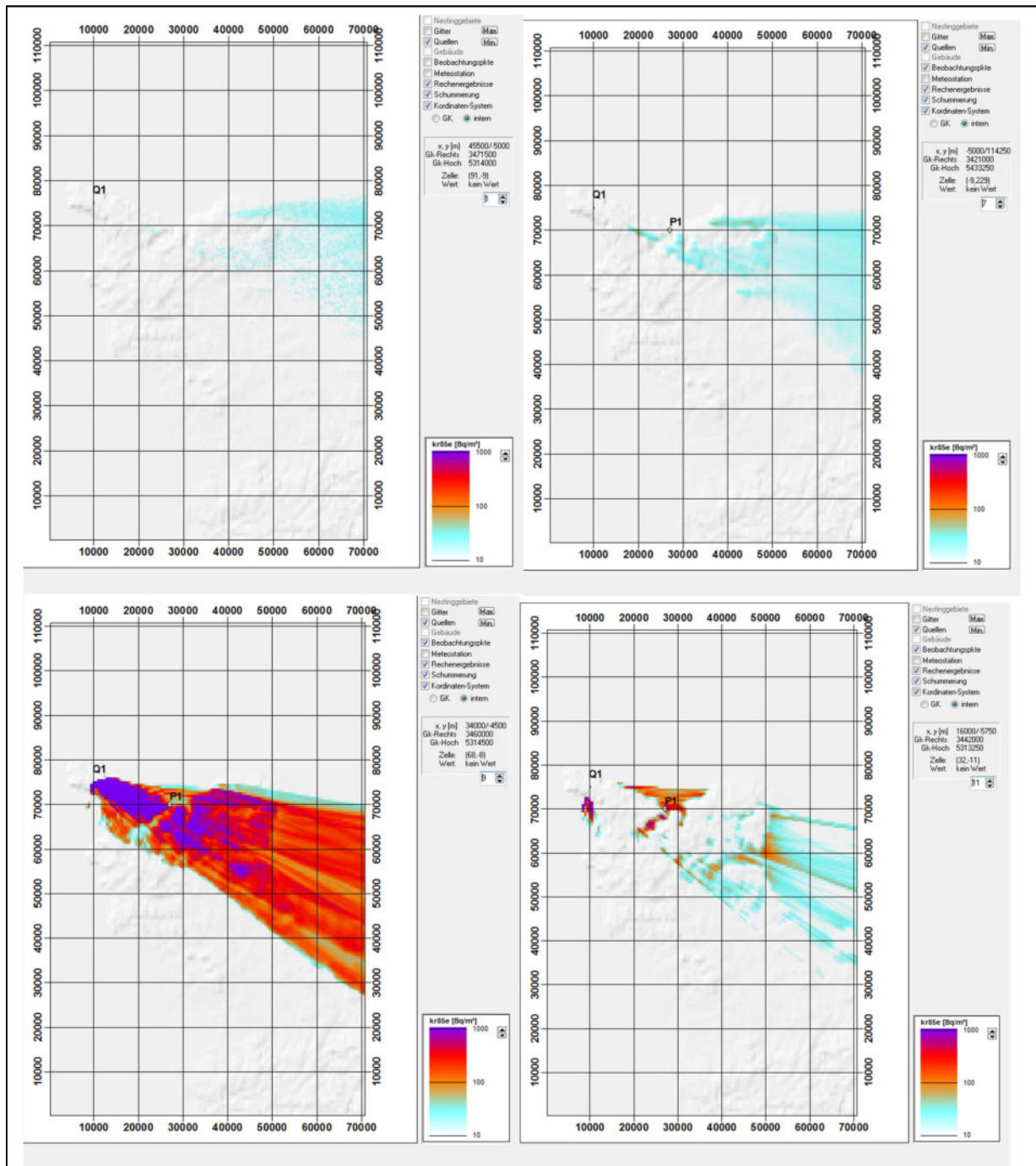
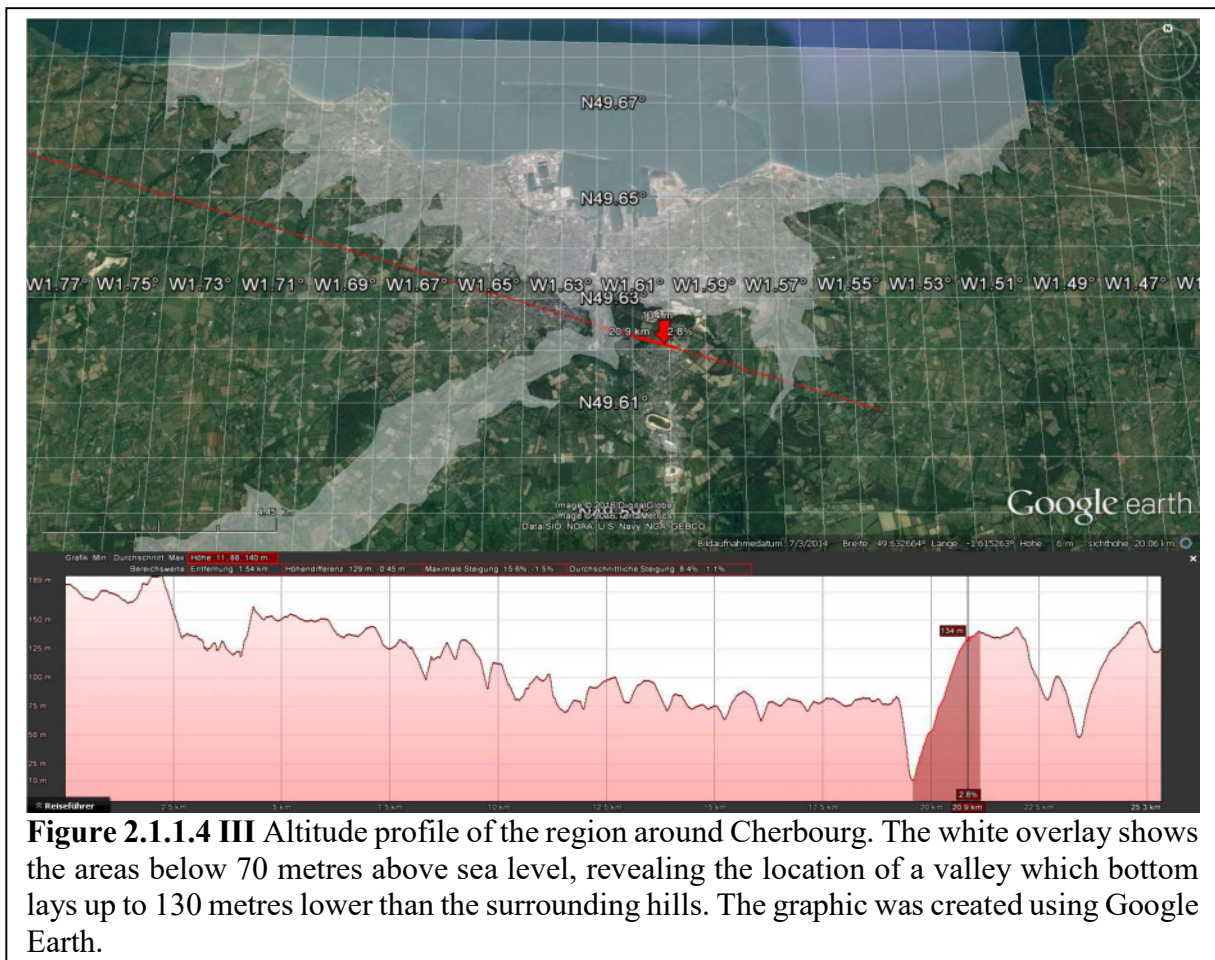


**Figure 2.1.1.4 II** The plume at very stable dispersion category in different altitude layers. Upper left: layer 1 (0-3 metres over ground), upper right: layer 7 (40-65 metres over ground), lower left: layer 9 (100-150 metres over ground), and lower right: layer 11 (200-300 metres over ground)





### 2.1.1.5 Summary external parameters

The studied variations of external parameters; emission strength, source geometry, surface roughness and dispersion categories, can be evaluated by the severity of their influence on the final simulation results.

An error or a deviation in the emission strength might have an effect on the results that can be significant, however this parameter possesses some linearity. This means that once the error is known, the simulation results, which behave linear to the emission strength, can simply be multiplied by the factor of the deviation, in order to gain the right values.

For the source geometry, it is a little more complex.

However, the study has shown that the effects only appear in close proximity to the emission source and vanish over the distance. Here the graphics (figures 2.1.1.2 Va, b, VIII and XII) show that while for differences in only the horizontal extension of the source, there is no clear difference in the results at high particle quality. Only the vertical extension of the source has some significant effects on the immission values of the nearby measurement stations.

Usually, no real 3-dimensional emission source exists as the opening of a stack is always just 2-dimensional. Therefore, the influence of the source geometry is rated to have a minor effect on the simulation results and could be neglected.

More important is the surface roughness in respect to altering the simulation results.

In the close surrounding of the source, i.e. the first three to four kilometres, the land cover has a large influence on the activity concentration in the air. Depending on the roughness length

chosen, the results might vary greatly, in the here shown example the largest variation shows up to two orders of magnitude in the close proximity, in further distance there still are factors of up to 3 between highest and lowest values. After the first four kilometres, the concentration curves are close together, the effect of the surface roughness here is decreasing.

The surface length therefore has a major effect in the close proximity of the source, and a lower, but still distinguishable, effect in the far distance. Therefore, the roughness length cannot be neglected.

Table 2.1.1.5 summarises the evaluation of these external input parameters. The largest effect on the simulation result has the variation of the dispersion category. Here the resulting curves even have entire different appearances. Especially in the close proximity to the emission source there are high differences with up to three orders of magnitude, and also for the far distance the differences make up to two orders of magnitude. With the dispersion category, the effect on the simulation results is quite significant and makes this in the evaluation the external input parameter with the largest influence. At the same time this parameter is the one that is the worst to determine (as mentioned in previous section 2.1.1.4). It is therefore important to gain the possible knowledge about the atmospheric layering at the time of the dispersion.

**Table 2.1.1.5** Evaluation of the external input parameters

Input parameter		Influence in		Trouble Shooting	Importance
		proximity	distance		
Emission Strength		high	high	Results can be multiplied by the factor of the variation	high
Source Geometry	Length	very low	very low	Can be neglected	very low
	Width	very low	very low	Can be neglected	very low
	Height	medium	very low	Close to source: use correct height In distance: can be neglected	low
Surface Roughness		high	medium	Close to source: use correct roughness length In distance: can be estimated (factor 3 between lowest and highest roughness length)	high to medium
Dispersion category		very high	high	Use correct dispersion category	Very high

## 2.1.2 Internal parameters

Opposed to the external parameters, internal parameters here are defined as all the input options an ARTM user has, which are not given by any measurements. These internal parameters are therefore purely user-defined, e.g. the grid size of the simulation area (i.e. the resolution), the number of simulation particles or the choice of the starting random number.

While the external parameters, as mentioned in previous sections, are predefined by the available measurement data including errors and uncertainties, the internal parameters are dependent on the user's choice.

Here it was studied, how the different user preferences for these internal parameters can effect possible deviations in the simulation results. All of the simulations explained in this chapter have been performed on multiple levels. The simulations for the different random numbers and particle quality evaluations summed up to 80 simulations, while the simulations to study the



grid size influences summed up to 1,280, considering 16 different starting random numbers for all five different particle qualities and for all eight different grid sizes, both; with and without orography influence.

### 2.1.2.1 Random numbers

ARTM uses random numbers to generate the initial distribution of the emitted simulation particles. Typically, a non-deterministic random number generator, creates a different number each time.

Since ARTM simulation results are required to be reproducible for regulatory purposes, this also needs to be considered for the simulation particle distributions. A non-deterministic random number generator that creates a different number every time, of course does not fulfil these criteria.

Therefore, the in ARTM integrated deterministic random number generator is initialised by a user-defined starting random number. Each simulation with the same input parameters and the same starting random number does lead to the same results and therefore meeting the requirements.

However, calculations with different starting random numbers can lead to a slightly different final distribution of the simulated radionuclide(s). This effect was studied by applying different starting random numbers in order to find out if there are any differences and how large the resulting deviations are.

In order to find a trade-off between the amount of simulations (and connected effort and simulation time) and to create a solid statistic, 16 different random numbers have been chosen; 1, 10, 100, 1000, 10000, 2476, 2475, 2477, 2466, 2486, 2376, 2576, 1476, 3476, 12476, and 22476.

Again the initial La Hague scenario, described in section 2.1 has been applied. The changes in the input parameters are shown in appendix G.

The simulation results with different starting random numbers on a time series is shown in figure 2.1.2.2 I in the next chapter. Here the standard deviation of the time series for the lowest particle number was calculated to be on average at 33.12%.

A look into the total concentrations (description see chapter below) shows even much higher numbers. While excluding the plume border areas, where, depending on the starting random numbers, values of zero and several hundred  $Bq \cdot m^{-3}$  can occur, the differences inside the plume still can reach values well over 100%.

If a larger particle amount is chosen, these numbers can be dramatically reduced and therefore the influence of the choice of a starting random number decreases down to values of 3.85% for the time series and of around 20% in the inner plume for the total concentration values.

### 2.1.2.2 Particle quality

The next internal parameter that was studied is the particle quality. Particle quality in ARTM means the amount of the released simulation particles. As a standard, ARTM uses  $6.3 \times 10^7$  particles at the default level 'qs0' [Richter et al, 2013b]. Each higher level doubles the particle numbers, so that at particle quality 4, ARTM uses  $1.008 \times 10^9$  simulation particles. Each level theoretically increases the simulation accuracy towards the previous one by a factor of  $\frac{1}{\sqrt{2}}$

due to increased statistics [Richter et al, 2013b].

Table 2.1.2.2 I shows the different particle number options in ARTM and the reduction in statistical error, both the theoretical mathematical one and the observed one. For the first one,

the particle quality level 0 was used as the standard and the values were calculated in reference to it using the above-mentioned factor.

The latter one was determined by a series of simulations using the La Hague scenario. Here the scenario was simulated using all five different particle quality levels. In order to minimise the statistical error introduced by different choices of starting random numbers (see section 2.1.2.1), the same 16 starting random numbers mentioned in the section 2.1.2.1 have been summarised in a mean value and the unbiased estimated standard deviation (see the description in chapter 1.3.1.3) to build the simulation result valid for this study of the error reduction.

The simulation results were evaluated both in time series and in total concentration values:

### i. Time series results

Here, the time series of concentration values for the IRSN Cherbourg location was examined in order to receive a quick estimate on how the standard deviation changes. Figure 2.1.2.2 I shows in each of the five different graphs the simulation results for each of the 16 different starting random numbers and in black the resulting standard deviation which was used as a way to measure the impact of the statistical fluctuations. What can be seen from the 5 graphs is, that, while in the beginning with the amount of simulation particles, they have huge differences in the values, these differences grow smaller and therefore also the standard deviation decreases.

In order to try comparing this to the theoretical value of the reduced error as shown in table 2.1.2.2 these results have to be processed to gain the value of error reduction.

This is done by normalising the standard deviation  $\hat{\sigma}$ , calculated according to (1.3.1.3 iii) in chapter 1.3.1.3, with the average value of all 16 simulations.

Taking (1.3.1.3 iii) and setting

$$x_i = \frac{1}{m} \sum_{j=1}^m y_{i,j} \quad \text{and} \quad \bar{x} = \frac{1}{n} \sum_{i=1}^n \left( \frac{1}{m} \sum_{j=1}^m y_{i,j} \right) \quad (2.1.2.2 \text{ i})$$

with  $n=16$  and  $m=45$ .

Now the normalised standard deviation  $s_{norm}$  can be created by putting  $\hat{\sigma}$  in relation to  $\bar{x}$  as in (2.1.2.2 ii).

$$s_{norm} = \frac{\hat{\sigma}}{\bar{x}} \quad (2.1.2.2 \text{ ii})$$

In order to obtain the percentaged error reduction  $r$  in relation to the lowest particle number, the relation (2.1.2.2 iii) must be applied for  $k \in \{0,1,2,3,4\}$ .

$$r_{k,0} = 1 - \frac{s_{norm,k}}{s_{norm,0}} \quad (2.1.2.2 \text{ iii})$$

Table 2.1.2.2 I shows the result of this calculation for the values from the time series results and in comparison to the theoretical values, the numbers in error reduction are much higher for particle quality level 1 and 2 as in the theory, however, the particle quality levels 3 and 4 with maximum of only around 80% are far below their corresponding theoretical values.

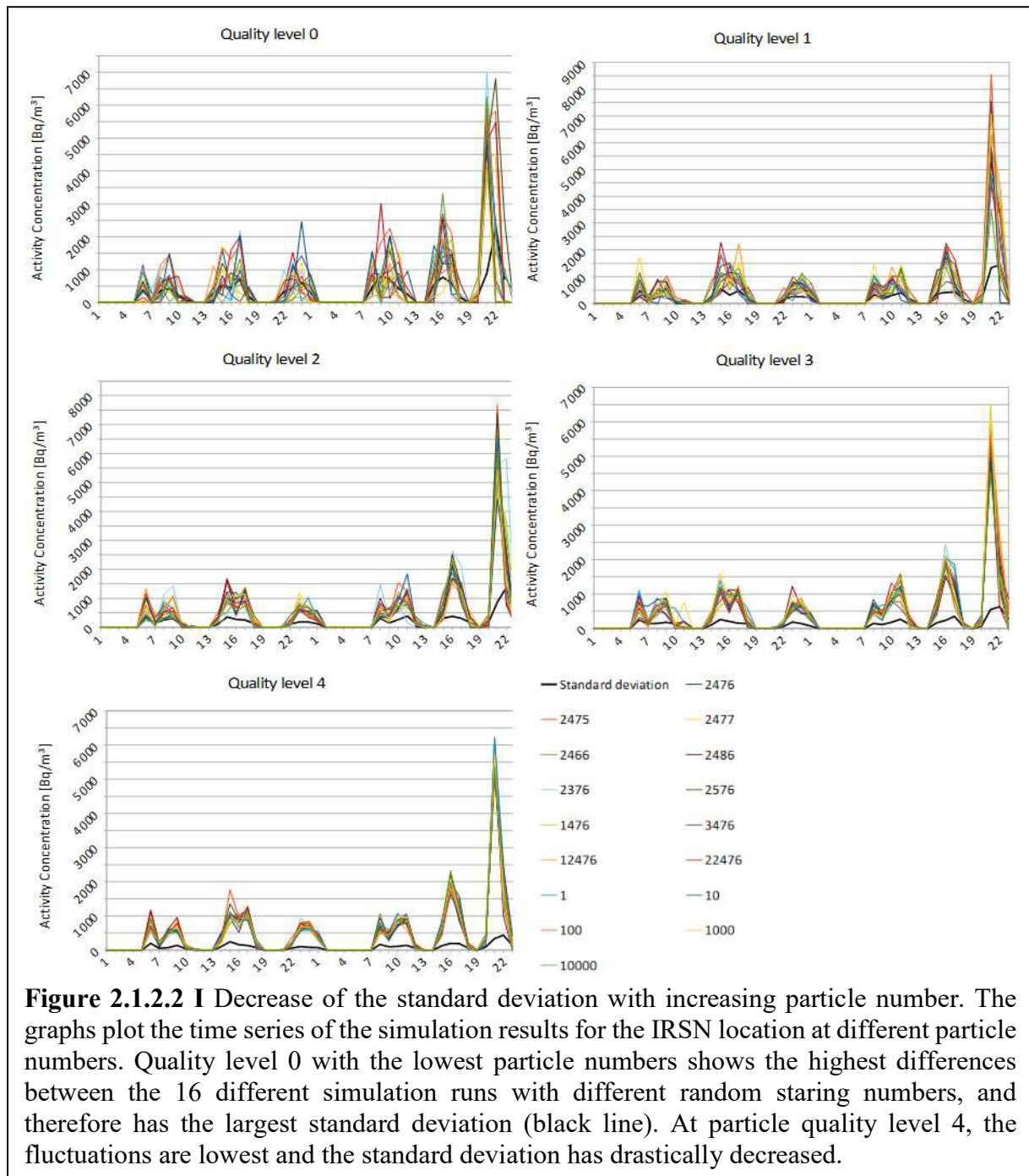


**Figure 2.1.2.2 I** Decrease of the standard deviation with increasing particle number. The graphs plot the time series of the simulation results for the IRSN location at different particle numbers. Quality level 0 with the lowest particle numbers shows the highest differences between the 16 different simulation runs with different random starting numbers, and therefore has the largest standard deviation (black line). At particle quality level 4, the fluctuations are lowest and the standard deviation has drastically decreased.

## ii. Total concentration values

In order to gain a better statistic result, a larger simulation area was chosen (142 by 222 cells) in order to evaluate also a larger amount of values (9,683 sample cells per particle quality level) from the resulting concentration files. These data provide the total concentration averaged over the simulation period for each grid cell. ARTMRes creates out of each set of 16 simulations with different random numbers for each of the five particle quality levels already the normalised standard deviation. These can be used by applying (2.1.2.2 iii) to generate files that contain the entire simulation area. Figure 2.1.2.2 II shows a visualisation of these five different files. In red is the file with particle quality 0, which was used as the reference, therefore it is entirely 0. The next 3 images go from particle quality 1 to 3, the colour getting more yellow with each step

indicates that the values are improving, but even at particle quality 4 where everything looks greener, still there are yellow and dark yellow spots. In each of the five files the same number of cells was used to create an average value and a resulting standard deviation.

Table 2.1.2.2 shows that in the error reduction it delivers values similar to those of the time series, which are with consideration of the deviations in the range of the theory vales, except for the value at the highest particle quality level, which is far below the 93,75%.

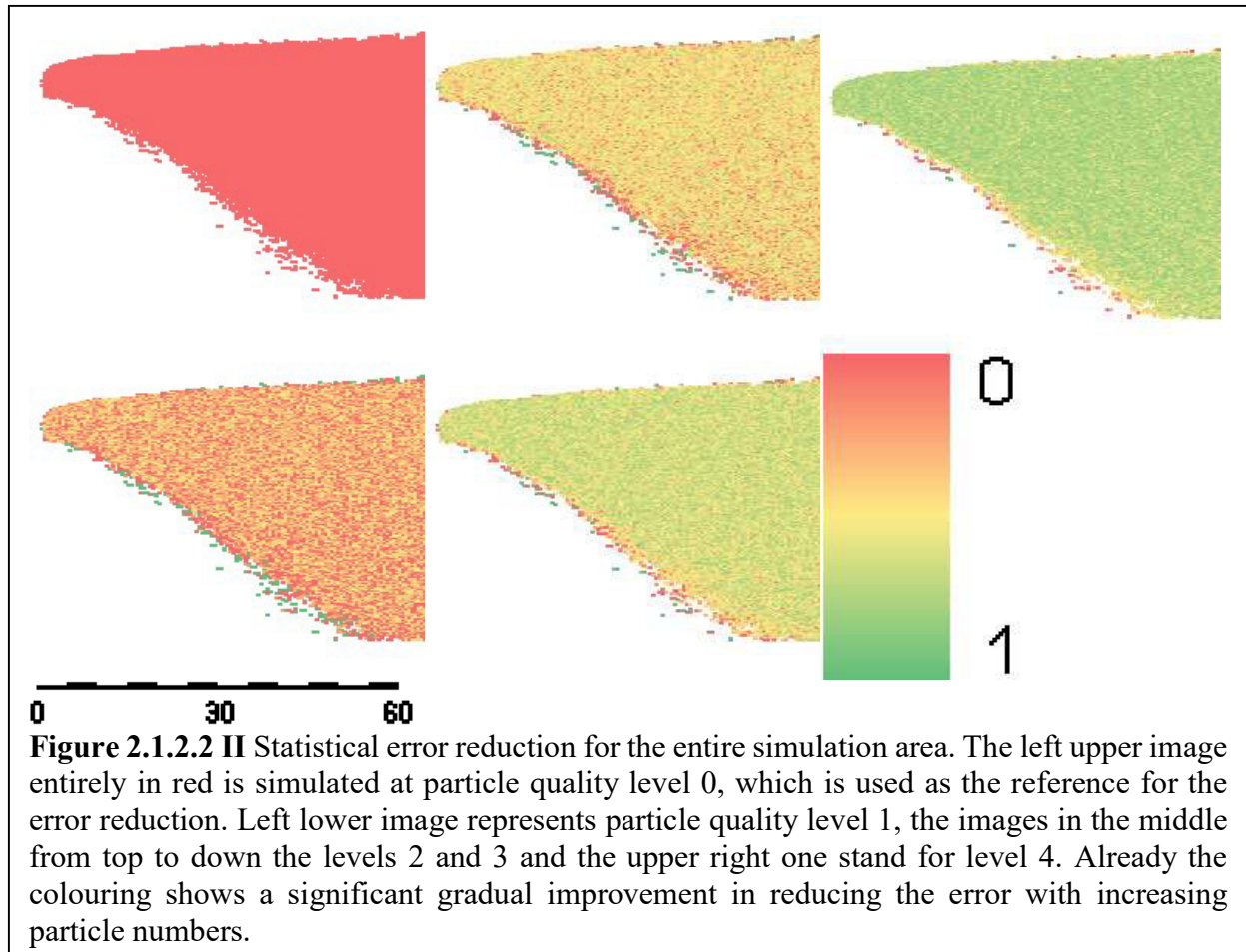


**Table 2.1.2.2 I** lists the standard particle quality levels as used in ARTM and their respective number of simulation particles. Each higher level reduces the total statistical error in the simulation results compared to the lowest level.

Particle quality	Number of particles [Richter et al., 2013b]	Reduction in statistical error (as taken from Richter et al., 2013b)	Measured range of statistical error reduction	
			Time series	Total plume
qs 0	$6.3 \times 10^7$	0	0	0
qs 1	$1.26 \times 10^8$	0.29289	0.50836	$0.24491 \pm 0.22778$
qs 2	$2.52 \times 10^8$	0.5	0.65507	$0.46214 \pm 0.16017$
qs 3	$5.04 \times 10^8$	0.75	0.69712	$0.61739 \pm 0.11242$
qs 4	$1.008 \times 10^9$	0.9375	0.79922	$0.72876 \pm 0.07951$

### 2.1.2.3 Grid size and Orography

As the last of the internal input parameters, the grid size influences were studied. As mentioned in chapter 1.5, the activity concentration is averaged for each grid cell, which implicates that a finer cell size resolution might lead to different values.

The same scenario as above was studied with 8 different grid sizes; 150 *m*, 200 *m*, 250 *m*, 300 *m*, 350 *m*, 400 *m*, 450 *m*, and 500 *m*. Each of these comes with its own orography file, as produced with Grid Equaliser (described in 1.3.1.1 v) for the specific grid size. The orography in these files therefore might be slightly different due to the different interpolation step sizes applied. In order to also study if this has an influence on the results, in a second study the orography files were excluded and simulations were performed solely for flat surfaces.

In order to gain some more solid conclusions, again all simulation scenarios were performed using the 16 different starting random numbers and at all five particle quality levels, leading to a total of 1,280 simulations. The input parameters can be viewed in appendix G.

To have more monitoring points for better examination and evaluation of the results, several of the surrounding villages in different distances to the AREVA nuclear fuel reprocessing plant in La Hague have been chosen for the output of additional time series results (see figure 2.1.2.3 I). These stations are also listed in the table 2.1.2.3 I with their locations and distances to the source.

**Table 2.1.2.3 I** List of the fictive measurement stations used for the evaluation of the grid size influence on the simulation results. For each of the stations the locations and their relative positions to the emission source is given. Distance values have a resolution of 250 meters in this case.

Name	Coordinate	Position relative to emission source [°]	Distance to emission source [km]
Beaumont-Hague	49.663000°, -1.837000°	115	3.25
Herqueville	49.668000°, -1.877000°	180	1.0
Jobourg	49.683000°, -1.904000°	290	2.0
Digulleville	49.699000°, -1.859000°	30	2.75
Gréville-Hague	49.675000°, -1.801000°	90	5.5
IRSN Cherbourg	49.634763°, -1.646122°	105	17.25
Biville	49.613455°, -1.822101°	150	8.25
Sainte-Croix-Hague	49.639475°, -1.761592°	115	9.5
Querqueville	49.664849°, -1.695095°	95	13.25
Vasteville	49.595604°, -1.772393°	140	11.75
Martinvast	49.594757°, -1.663516°	120	18.0
Flottemanville-Hague	49.622507°, -1.721819°	120	12.75

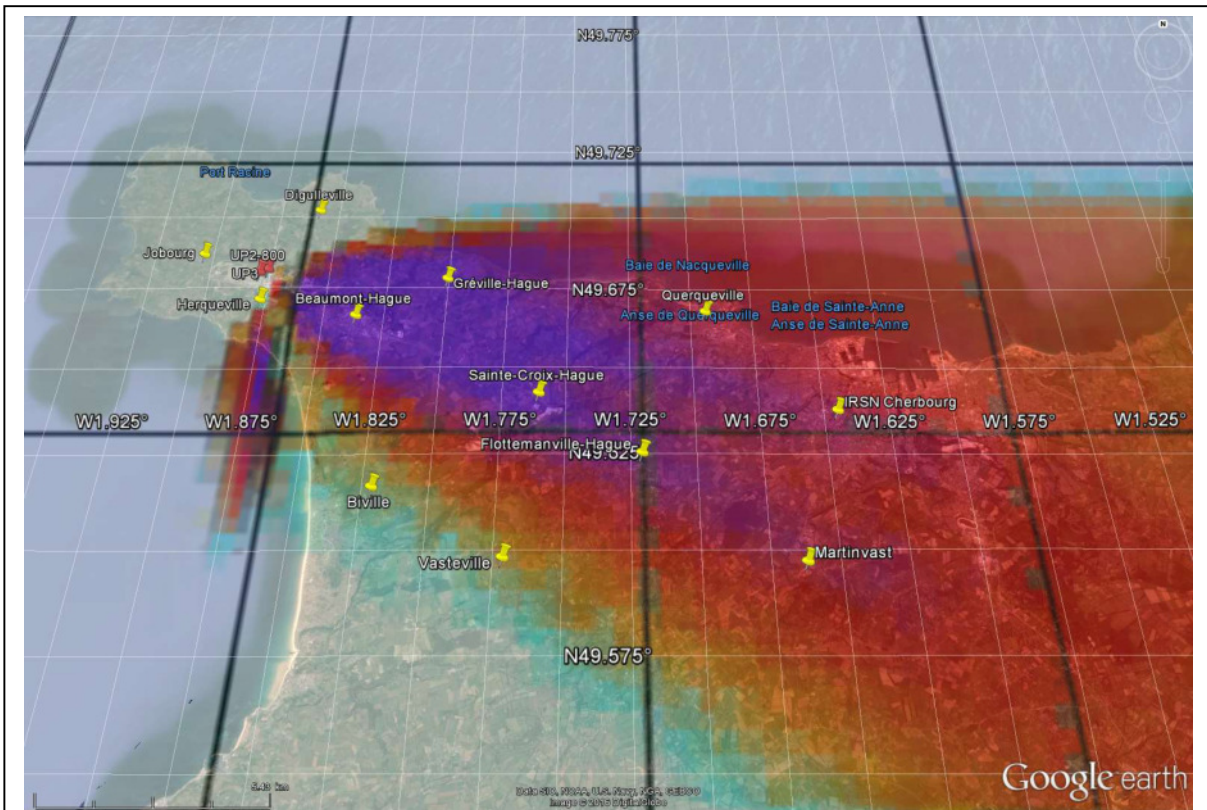


**Figure 2.1.2.3 I** Overview on the plume distribution and the evaluated monitoring points chosen in the villages surrounding the AREVA nuclear fuel reprocessing plant in La Hague. This image was created using Google Earth.

Figure 2.1.2.3 II shows the average concentration values for the entire simulation period for each of the different studied cell sizes, the error bars mark the standard deviation for each of the average values. The interrupted lines do not necessarily interpolate the results for potential cell size values in-between, but are simply for better visualisation.

As in figure 2.1.2.3 II shown, the different stations produced significantly different results. In the left images shown are the results for the simulations including the orography files, while the right ones are without orography. The upper two graphs are calculated at particle quality level of 0, while the lower ones are at quality level 4. The levels in-between, though simulated as well, were excluded in this graphic as they only show a gradual evolution from the upper to the lower graphs. Also, the two stations Jobourg and Digulleville were excluded, as they did not experience any immissions during the simulation.

Interestingly, the nearest station to the plant which is inside the main plume, Beaumont-Hague, is affected the most by the different chosen grid sizes, showing peaks for the 250 and 450 meter resolutions in both scenarios. Values there can vary between 76% and 122% of the average over all grid sizes for the case with orography, and between 83% and 125% of the average for the case without orography.

The largest range of differences appear at the border zone of the plume. For Herqueville this variation ranges from 19% to 300% of the averages, and between smallest and largest value there are two orders of magnitude in difference.

That this effect is solely based on the grid size and not for example on the amount of simulation particles is obvious since this feature appears as well for all five quality levels. The only effect



the increase in particle number has, is that the standard deviation decreases (shown by the error bars).

The further away stations are from the emission source, the lower the influence of the grid size appears. Yet this influence can still be significant, for example for IRSN Cherbourg there appear still differences of up to one third between highest and lowest value.

In respect to the realistic La Hague scenario in chapter 3, single time series results were studied as well instead of just the average values of the simulation period and they also show the same pattern as in figure 2.1.2.3 II. Here also significant differences showed up, for the IRSN Cherbourg, despite being further away from the source, building a foundation for the theory of the influence of the chosen grid size on the results in chapter 3.

This grid size influence on the simulation results, however, does not follow a certain pattern that would be predictable or could be applied one to one for different scenarios.

Here the suggestion is to use fine grids for values close to the emission facility, but higher resolutions mean also an increase in computing time. In this simple short term scenario, the simulation time of four different simulations per cell size were studied to observe the trend. Table 2.1.2.3 II shows the simulation times and their average, and draws a connection to the amount of cells in the simulation area. Basically, while the number of cells decreases exponentially (see figure 2.1.2.3 III), the average duration for the simulation shows a similar behaviour, but seems to have a certain off-set.

In order to investigate the value of this off-set and to find the calculation velocity  $v_{\text{calculation}}$  in calculated cells per second, the relation (2.1.2.3) can be applied. The number of cells  $n_{\text{cells}}$  of a chosen cell size  $i$  are divided by the average duration  $\bar{t}(i)$  minus the variable off-set  $t_{\text{offset}}$ .

$$v_{\text{calculation}} = \frac{n_{\text{cells}}(i)}{(\bar{t}(i) - t_{\text{offset}})} \quad (2.1.2.3)$$

For  $t_{\text{offset}}$  now values from 0 to 105 seconds (the minimum measured) have been applied for all different cell sizes. The aim was to look for results that are similar to each other (not increasing or decreasing lines of values. This turned out to be in the range of 70 to 75 seconds. The final result was brought by a look at where the lowest standard deviation could be found which clearly showed its minimum at an off-set of 73 seconds, and an average calculation velocity of 106.29 cells per second (see table 2.1.2.3 II).

Now this velocity can be used as a hint to estimate the duration when increasing the resolution of the grid and therefore its cell number. Of course, this has so far just been performed for this one scenario and only at the lowest amount of simulation particles for a short-term duration, which are all factors that might change or increase the total simulation times up to levels where these simulations can last significantly longer. Therefore, a trade-off for larger simulation areas and longer simulation periods would be to use nested grids, an option that ARTM allows for, and to then always use the finest possible grid for extracting the results.

**Table 2.1.2.3 II** Table to estimate the calculation velocity for different cell sizes. Shown here are the simulation durations of some of the simulations conducted with different grid sizes. The smaller the grid size the larger is the amount of grid cells and therefore also the simulation time is higher. In the lower part of the table a short study to obtain the simulation off-set is shown. The off-set seems to be around 73 seconds for this scenario.

Cell size [m]	150	200	250	300	350	400	450	500		
Simulation time [s]	457	281	205	165	143	124	111	107		
	479	291	208	165	142	124	118	106		
	454	279	201	164	154	124	109	106		
	453	222	203	166	143	113	111	105		
Average simulation time [s]	461	268	204	165	146	121	112	106		
Number of cells	39407	22184	14100	9750	7169	5394	4233	3404		
Processing speed [cells/s]	85.53	82.70	69.03	59.09	49.27	44.49	37.71	32.11		
Off-set [s]	Processing speed [cell/s] with off-set								Average	Standard deviation
70	100.85	111.90	105.03	102.63	94.95	105.25	100.19	94.56	101.92	5.70
71	101.11	112.47	105.82	103.72	96.23	107.34	102.62	97.26	103.32	5.33
72	101.37	113.04	106.62	104.84	97.54	109.52	105.17	100.12	104.78	5.07
73	101.63	113.62	107.43	105.98	98.88	111.79	107.85	103.15	106.29	4.99
74	101.89	114.20	108.25	107.14	100.27	114.16	110.67	106.37	107.87	5.13
75	102.16	114.79	109.09	108.33	101.69	116.63	113.64	109.81	109.52	5.51
76	102.42	115.39	109.94	109.55	103.15	119.20	116.77	113.47	111.24	6.14



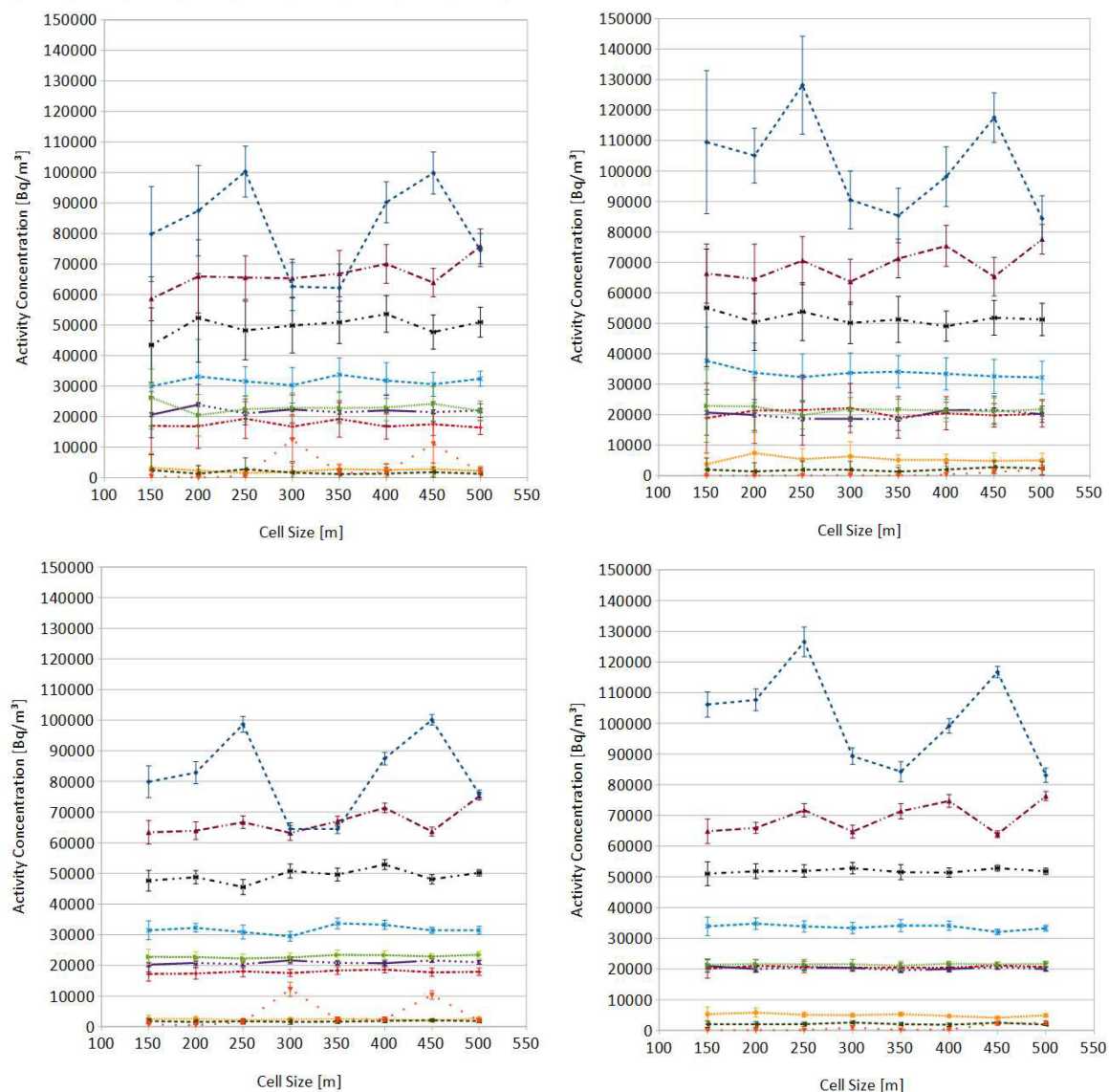
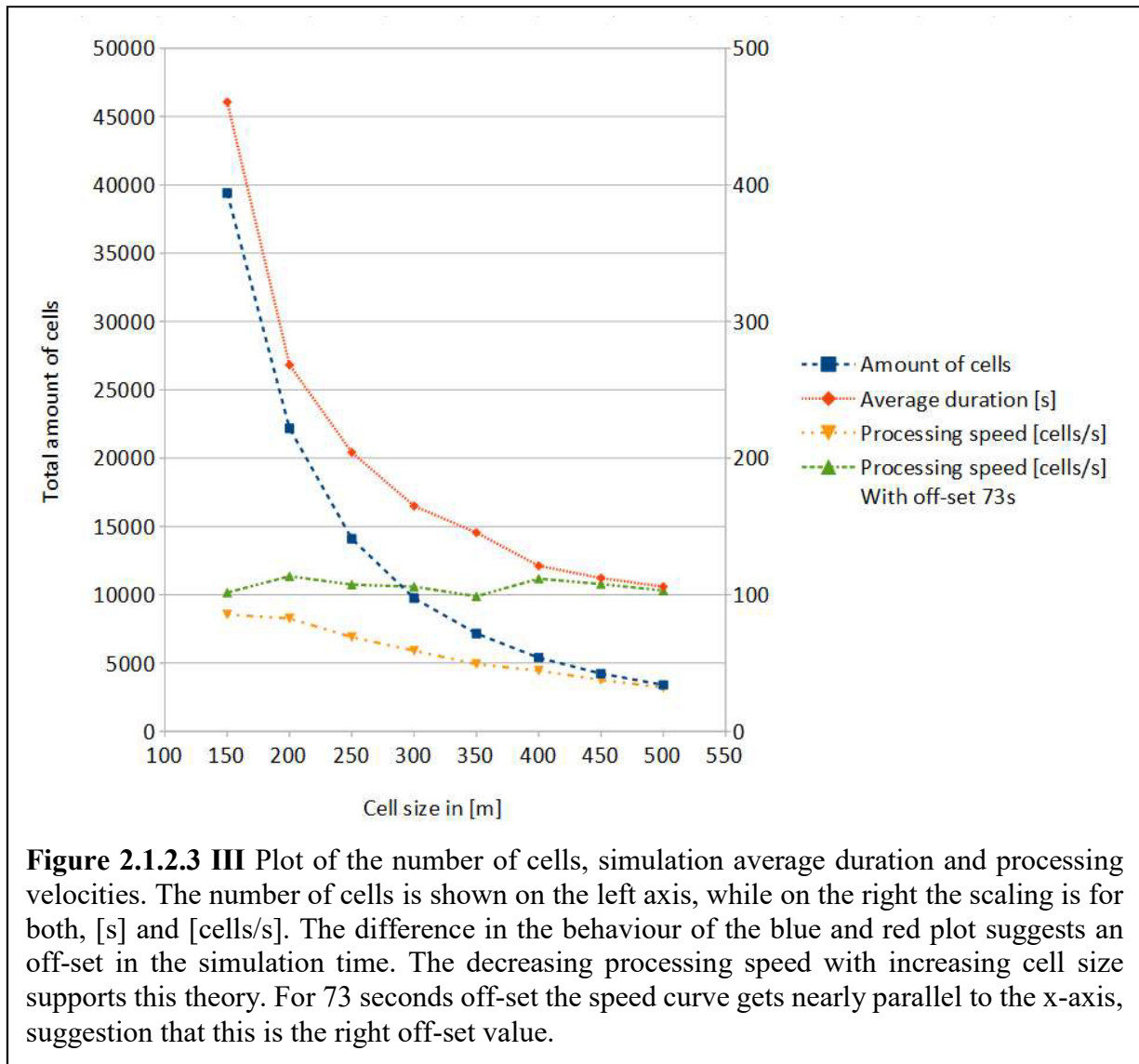


**Figure 2.1.2.3 II** Dependency of the average simulation results with different simulation grid size resolutions. The left two graphs show the average daily values for 10 monitoring stations in the surrounding area of La Hague under consideration of the orography, while the right graphs were produced without orography influence. In the upper two images the lowest particle quality level was chosen, in the lower two, the highest one. The intermediate levels were simulated, but are only intermediate steps between lowest and highest level. The error bars indicate the calculated standard deviation.





#### 2.1.2.4 Summary internal parameters

In general, it can be concluded that the influence of internal parameter variations is smaller than the effects that some of the external parameters (e.g. dispersion category, see chapter 2.1.1.5) have. Figures 2.1.2.4 I to 2.1.2.4 II show the distribution over the distance for starting random numbers, particle quality and the grid size, respectively.

Compared with the scale used in 2.1.1.5, the starting random number, although causing quite high deviations in the results in combination with low particle amount, rates at maximum with a 'medium'. As their results are also dependent on the amount of simulation particles, there are two very efficient ways to counteract this influence:

- increasing the numbers of simulations with different starting random numbers and creating the average values, or
- increasing the amount of simulation particles.

Basically, both methods increase the total amount of particles that were spread in the simulation area. For the maximum quality of possible results, a combination of both methods is suggested.

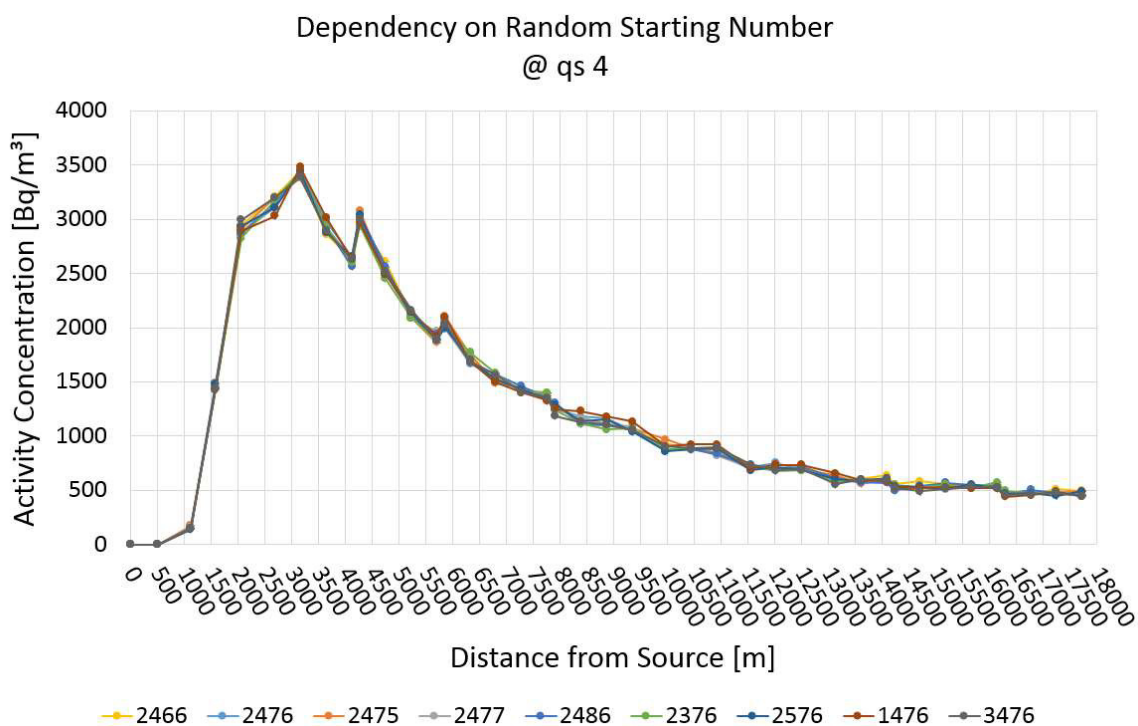
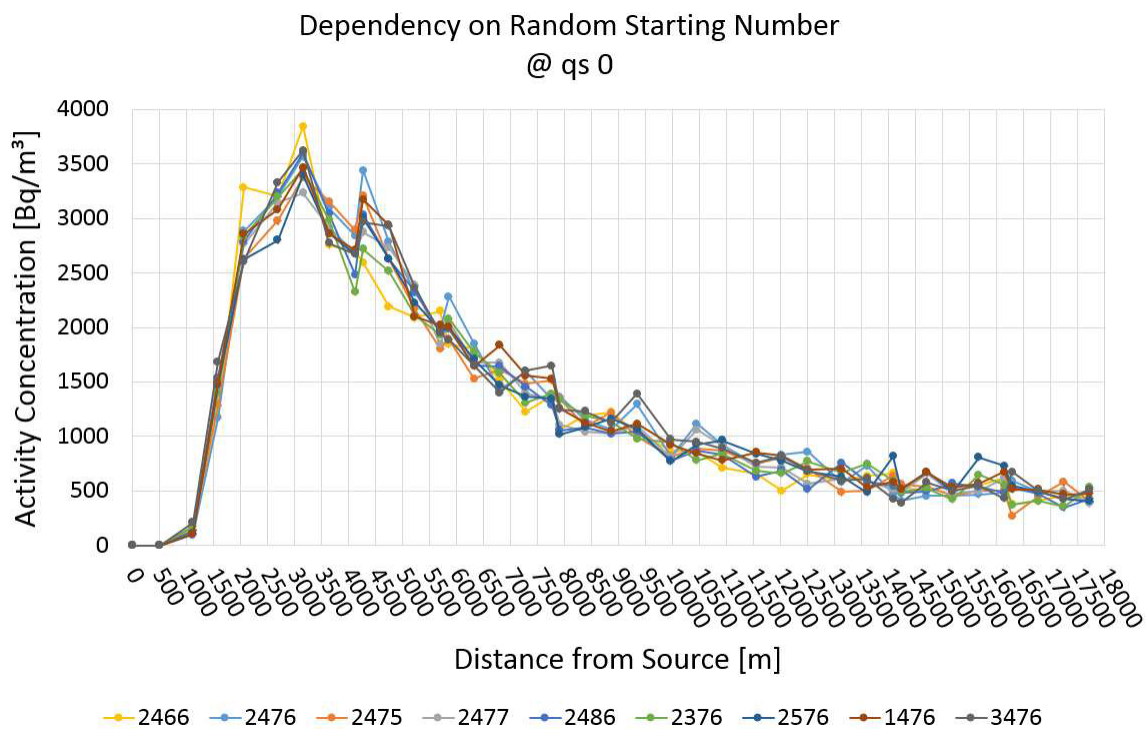
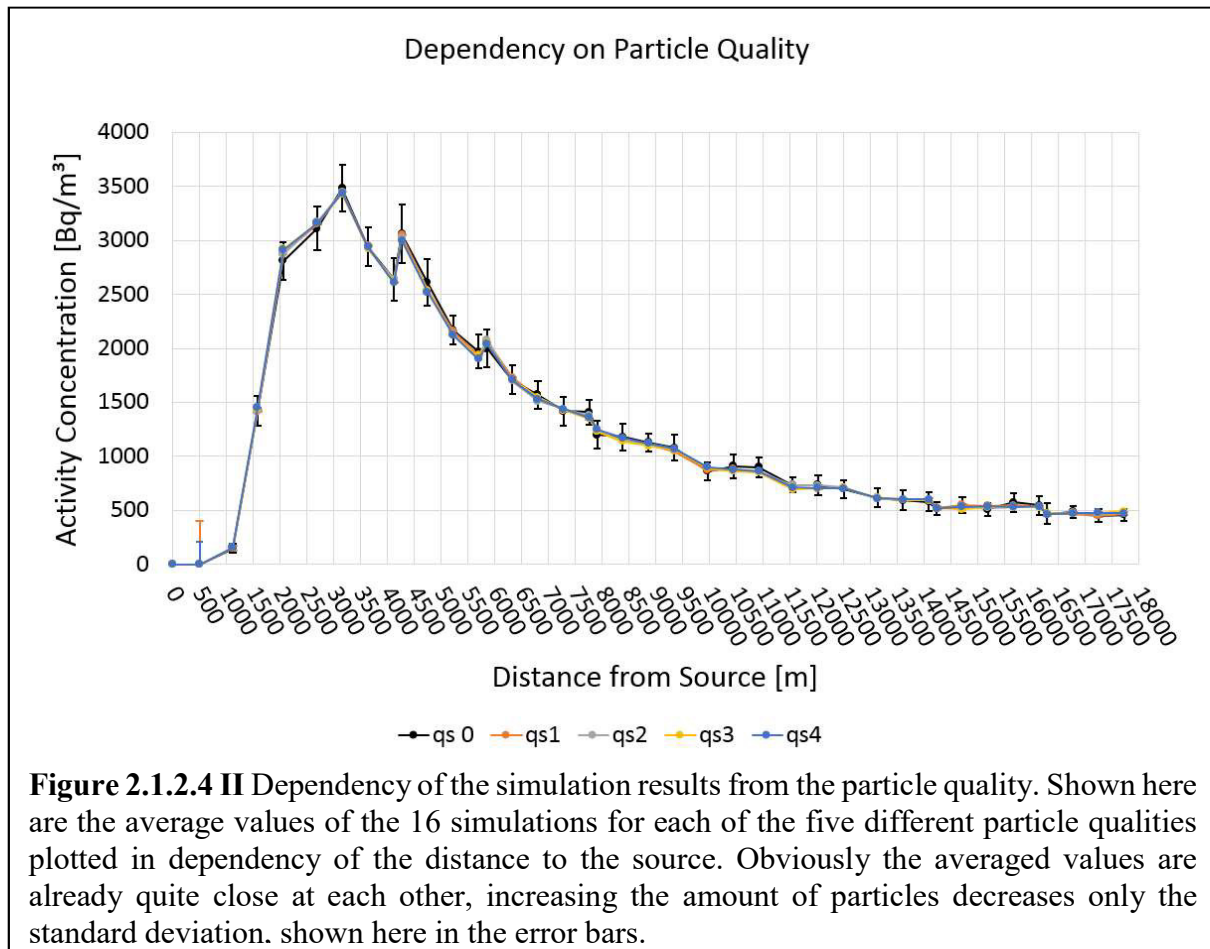


**Figure 2.1.2.4 I** Dependency of the simulation results from different starting random numbers. In the upper image, simulations were done with the lowest amount of particles. The effect in the close proximity to the source are medium and decreasing a little with distance. Decreasing these deviations can be done by increasing the particle amount (lower image).

In figure 2.1.2.4 II where the particle quality is addressed it shows how the average values are already aligned for different particle qualities. Rising the number of particles can take down the standard deviations, which in the near environment are higher than in the far. The influence is rated low to medium.



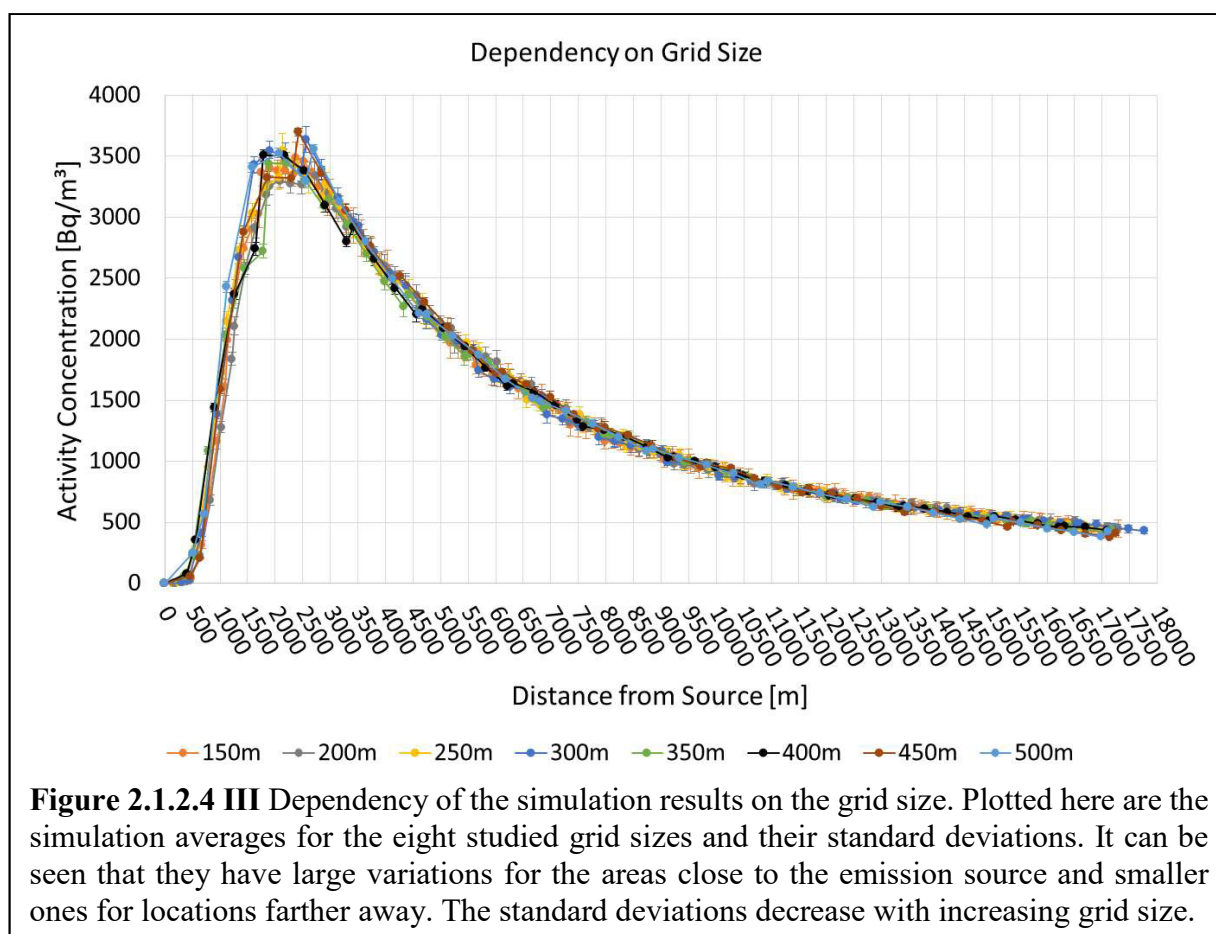
The influence of the different grid sizes as shown in figure 2.1.2.4 III suggests medium to low effects on the simulation results. Here also the close proximity is larger effected by variations than the locations further away from the source, supporting the theory in chapter 2.1.2.3 where close measurement locations have the largest variability. Farther away the differences between the results are much smaller, yet can still be observed. The standard deviations turn out to decrease with increasing cell size. One difficulty in comparing results from different grid sizes like that is to pick the exact same locations always. For figure 2.1.2.4 III it has been done analogue to the previous graphics; a direct line from the cell including the emission source to the cell including the location IRSN Cherbourg has been drawn and all cells being intersected by this line have been used for the evaluation.

As there is not a recognisable trend towards larger or smaller grids, only a suggestion of the most optimal solutions can be made, which is to use as high resolved grids as possible. A compromise between effort and effect can be to use nested grids for larger simulation areas. In general, can be said that the presence or absence of orography also plays a role.

Table 2.1.2.4 shows the rating of the studied internal parameters.

**Table 2.1.2.4** Evaluation of the internal input parameters

Input parameter	Influence in		Trouble Shooting	Importance
	proximity	distance		
Starting Random Number	medium	medium to low	Increasing the particle quality, more simulations with different starting random numbers	medium
Particle Quality	medium to low	low		low
Grid size	medium	low	Using high resolution grids and/or nested grids	medium



## 2.2 Sensitivity analysis with the Neckarwestheim-scenario

In order to verify if the deviations that occurred in the short-term scenario above are still so evident for simulations in the range of normal operations, i.e. annual simulations, a long term simulation was conducted.

As there were no data available for La Hague for the duration of an entire year, the location of a nuclear power plant in Neckarwestheim, Germany, was chosen due to its orographical structure. The meteorological data set of 2009 provided the least amount of failure measurements.

Studied here were only the internal parameters with focus on particle amount and random starting number. A total of 80 simulations has been performed and also additional information, for example the points of maximum concentration have been studied. While the scenario was



calculated using 15 different nuclides, only the  $^{85}\text{Kr}$  was considered in this work, as it is the noble gas with the largest half-life out of the emitted substances in this scenario. Figure 2.2 shows the result of such a simulation. From the distribution of the concentrations, it is clearly visible where the main wind directions are and that basically the whole area receives exposure throughout the year.

Due to the long simulation time of one to four weeks, depending on the particle quality levels, the effort to prepare the orography map and the potentially low outcome, there were no calculations done with varying grid sizes for the Neckarwestheim scenario.

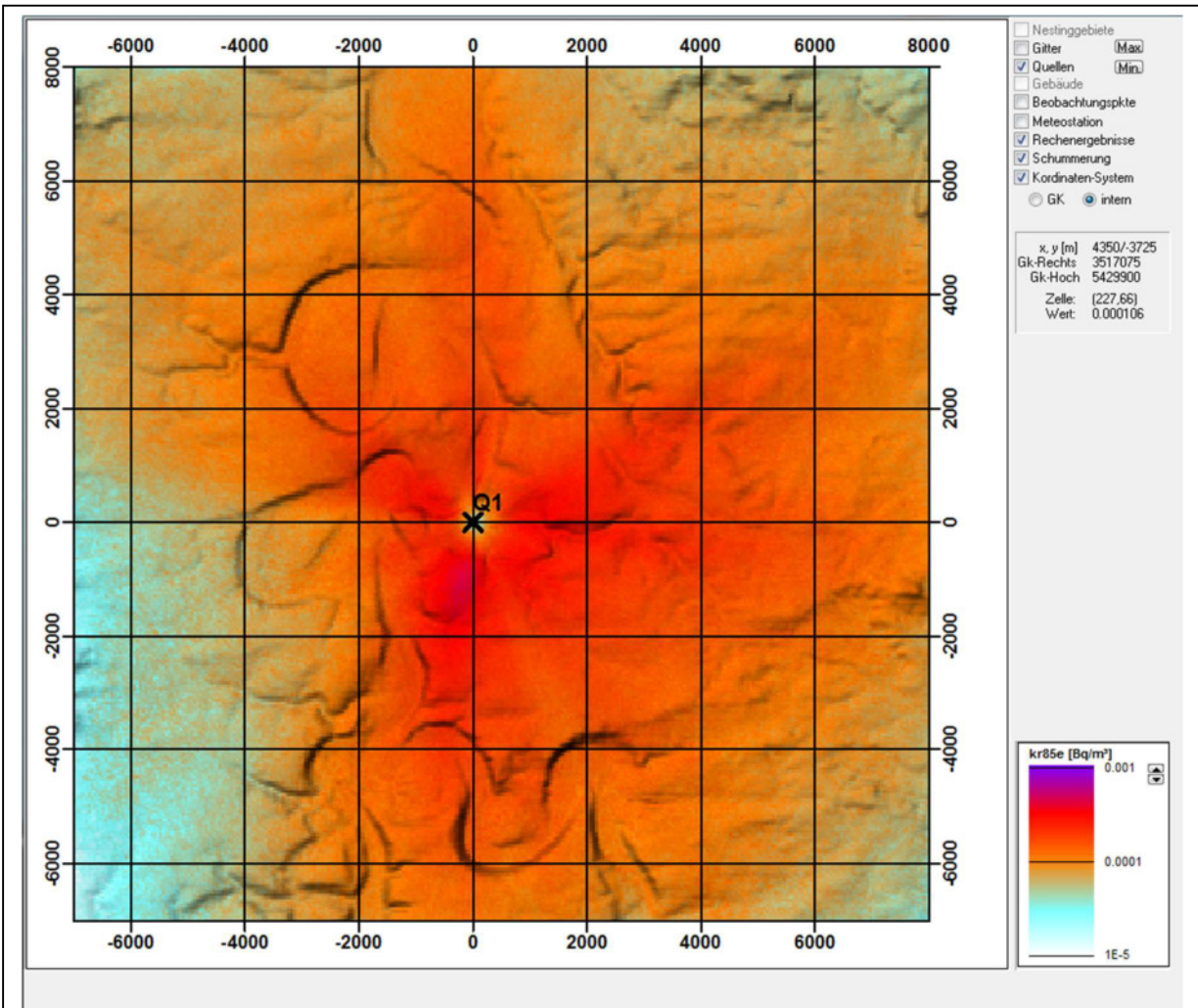


**Figure 2.2** Distribution of  $^{85}\text{Kr}$  activity concentrations throughout the year 2009 as simulated with ARTM. Q1 is the location of the emission source of the nuclear power plant. The colour distribution suggests that the largest concentrations can be expected nearby the facility and mainly in southern and eastern directions due to the dominating wind directions. The shades give a hint on the orographical structure.

### 2.2.1 Random numbers

Similar as to the La Hague scenario with only two consecutive days of simulation duration, also here different choice of random numbers can lead to significant deviations in the results. Due to the long simulation period of one year, no time series for certain points have been evaluated, but the total concentration values were studied and their standard deviations. For the lowest amount of simulation particles, the calculated range of the standard deviation goes from 2.56%

up to 46.8% of the average value from 16 simulations for that respective grid cell. The sample size was 300 by 300, so 90,000 grid cells. Even though effects like the plume edges, which appear in short-term simulations, are smoothed out in the annual simulations, deviations can be quite high. There it is of advantage to perform multiple simulations with different starting random numbers and to use the average values. Also, the deviation can be drastically reduced by increasing the amount of particles, as can be seen in table 2.2.1.

**Table 2.2.1** Minimum and maximum of the standard deviations for different random starting numbers in dependency of the particle quality. Here a total of 90,000 grid cells each for 16 simulations were evaluated. For each cell its average and its standard deviation has been calculated. The global minima and maxima provide an overview on the range of deviations to expect. For larger amounts of particles, these deviations decrease.

Particle quality	Minimum standard deviation in percent of the average	Maximum standard deviation in percent of the average
qs 0	2.56	46.8
qs 1	1.32	35.9
qs 2	1.18	24.4
qs 3	0.76	18.3
qs 4	0.642	13.7

## 2.2.2 Particle quality

Similar as for the La Hague scenario, also for the simulation results of the Neckarwestheim nuclear power plant, the influence of increasing the particle quality was studied by calculating the reductions in the standard deviation. Figure 2.2.2 I shows, analogue to figure 2.1.2.2 II, the error reduction values in percentage for the entire simulation area in relation to the standard deviation values at lowest particle quality. What can be seen is that, despite the graphic of the total distribution in figure 2.2 having distinct features and areas of higher or lower concentration, in the error reduction images, the appearances are more or less homogeneous for each of the 4 higher particle quality levels. In table 2.2.2 the mean values and their uncertainty for the 90,000 cells in the Neckarwestheim scenario results are compared to the ones of the La Hague scenario. While the mean values for Neckarwestheim are larger, and in the cases for the particle qualities qs1 and qs2 therefore getting close to the theoretical values, the values for qs3 and qs4 are still far from what would be expected mathematically. Considering the deviation, the results for qs1 and qs2 even overshoot the expected error reduction, qs3 gets close to its theoretical value, but qs4 would with around 80% maximum still be far off from the expected 93 to 94%. Thus leading to the conclusion, that here the cause probably is in the model itself creating this difference.

Taking a concentration profile over the distance from the source, as done in figure 2.2.2 II, reveals that the overall curve shape is very similar to the shape of the curves for the short-term La Hague scenario, proving that these are representative. The increase of the particle amount does not bring a direct improvement for the curves, if previously several simulations with different random numbers have been performed and its results been averaged. Basically, all five lines are more or less the same. What the increase in particle quality does, is that the standard deviations went down by far.

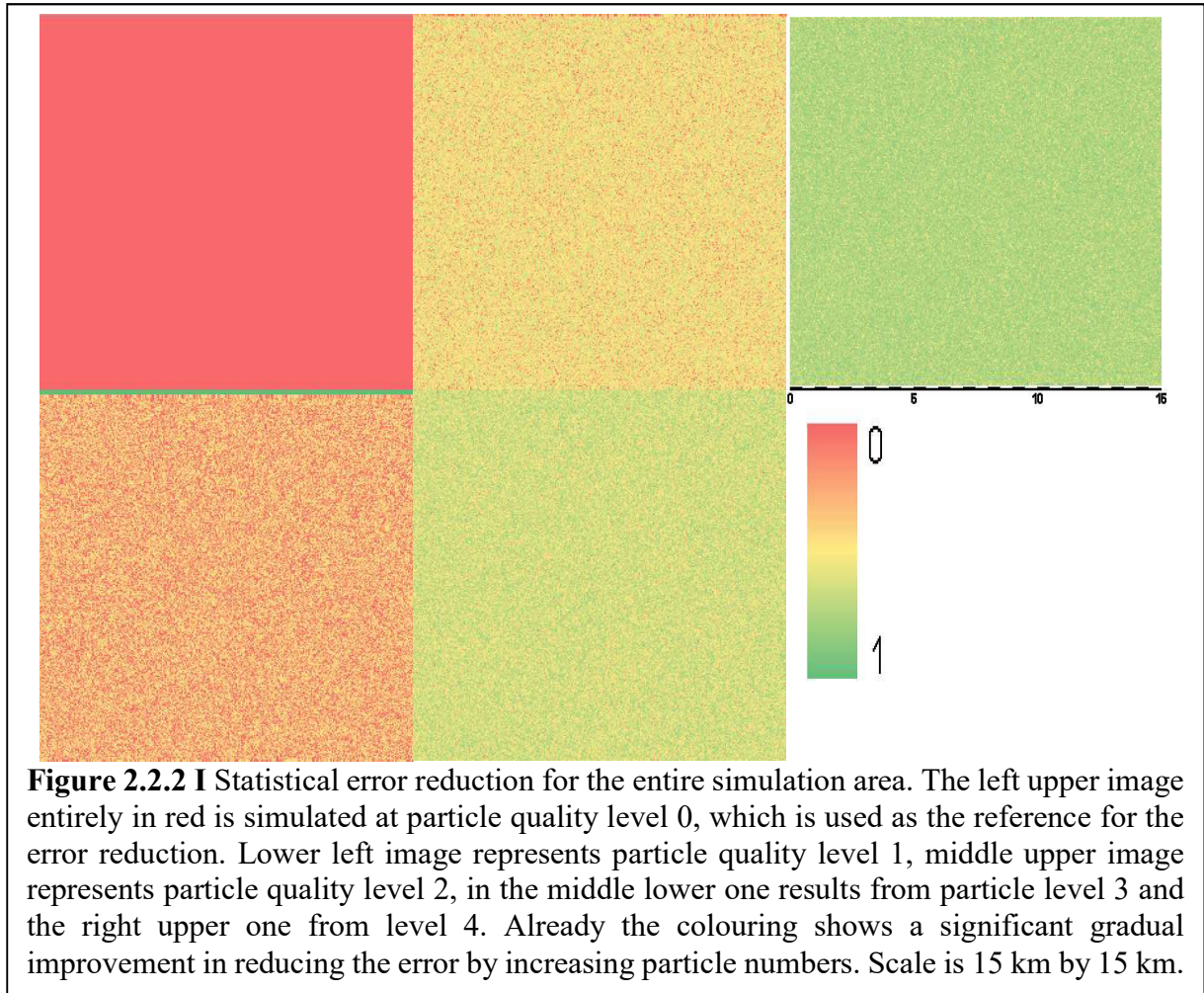
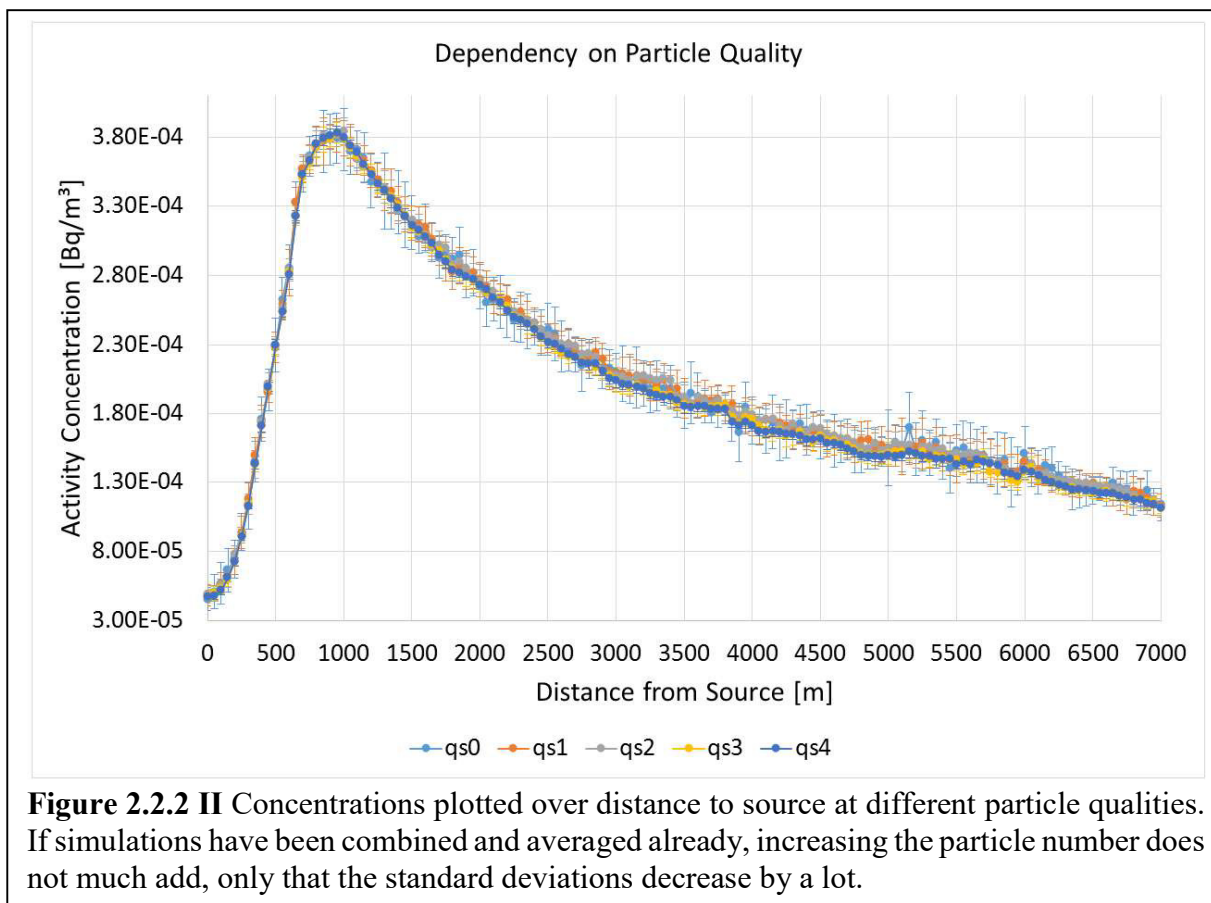


**Table 2.2.2** Comparison of the error reduction in the Neckarwestheim scenario and the La Hague scenario. It shows that while the values for the annual simulation are a bit larger and with less errors than of the La Hague scenario, the simulations with the largest particle amount are still not reaching the theoretical values for the error reduction

Particle quality	Number of particles [Richter, C., et al., 2013b]	Reduction in statistical error (as taken from Richter, C., et al., 2013b)	Measured range of statistical error reduction	
			La Hague	Neckarwestheim
qs 0	$6.3 \times 10^7$	0.000	0	0
qs 1	$1.26 \times 10^8$	0.293	$0.245 \pm 0.228$	$0.266 \pm 0.205$
qs 2	$2.52 \times 10^8$	0.500	$0.462 \pm 0.160$	$0.480 \pm 0.145$
qs 3	$5.04 \times 10^8$	0.750	$0.617 \pm 0.112$	$0.630 \pm 0.106$
qs 4	$1.008 \times 10^9$	0.938	$0.729 \pm 0.080$	$0.740 \pm 0.073$





### 2.2.3 Points of maximum concentration

Another aspect that was studied here is important for the regulatory use of ARTM: the so-called ‘point of maximum concentration’. This location is the cell on the map that receives the largest air concentration of a single radio nuclide.

Therefore, also the point of maximum concentration was studied to determine its variation in location and value. Unlike in the two chapters before, the point of maximum concentration is not an input variable that could be chosen. It rather is a different way to interpret and evaluate the previous aspects, particle amount and random starting number, in terms of how the variation of these two parameters influences the regulatory work with ARTM. Table 2.2.3 shows the results of this study. While it shows that depending on the choice of starting random numbers, there is always some range for the location of this point and for its value, these ranges tend to decrease with the increasing particle quality.

Figure 2.2.3 shows the spatial distribution of the different points of maximum concentration as they result from the simulations with 16 different starting random numbers at the lowest particle quality. In this case, it looks like they are all within a range of a few hundred meters. However, with a view on figure 2.2 it looks likely that for example for some initial particle distributions, the point of maximum concentration could not be within this area, but for example to the east of the source, where the concentrations come close to the ones in the south. If only one simulation is done, it cannot be automatically assumed that it is a representative result.

**Table 2.2.3** Assessing location and value of the points of maximum concentration. With increasing particle quality, the point of maximum concentration becomes more exact in location and in its values.

Particle quality level	Range of x-coordinate [m]	Range of y-coordinate [m]	Mean value [Bq/m <sup>3</sup> ]	Range of values [Bq/m <sup>3</sup> ]	In Percentage
Qs0	6800 - 6850	8850 - 9150	$4.565 \cdot 10^{-4}$	$4.475 \cdot 10^{-4} - 4.856 \cdot 10^{-4}$	-1.98 – 6.36
Qs1	6800 - 6900	8950 - 9100	$4.476 \cdot 10^{-4}$	$4.355 \cdot 10^{-4} - 4.564 \cdot 10^{-4}$	-2.71 – 1.96
Qs2	6750 - 6900	8900 - 9200	$4.398 \cdot 10^{-4}$	$4.333 \cdot 10^{-4} - 4.454 \cdot 10^{-4}$	-1.48 – 1.28
Qs3	6800 - 6850	8900 - 9050	$4.358 \cdot 10^{-4}$	$4.307 \cdot 10^{-4} - 4.459 \cdot 10^{-4}$	-2.05 – 2.31
Qs4	6800 - 6850	8900 - 9050	$4.322 \cdot 10^{-4}$	$4.261 \cdot 10^{-4} - 4.361 \cdot 10^{-4}$	-1.42 – 0.89

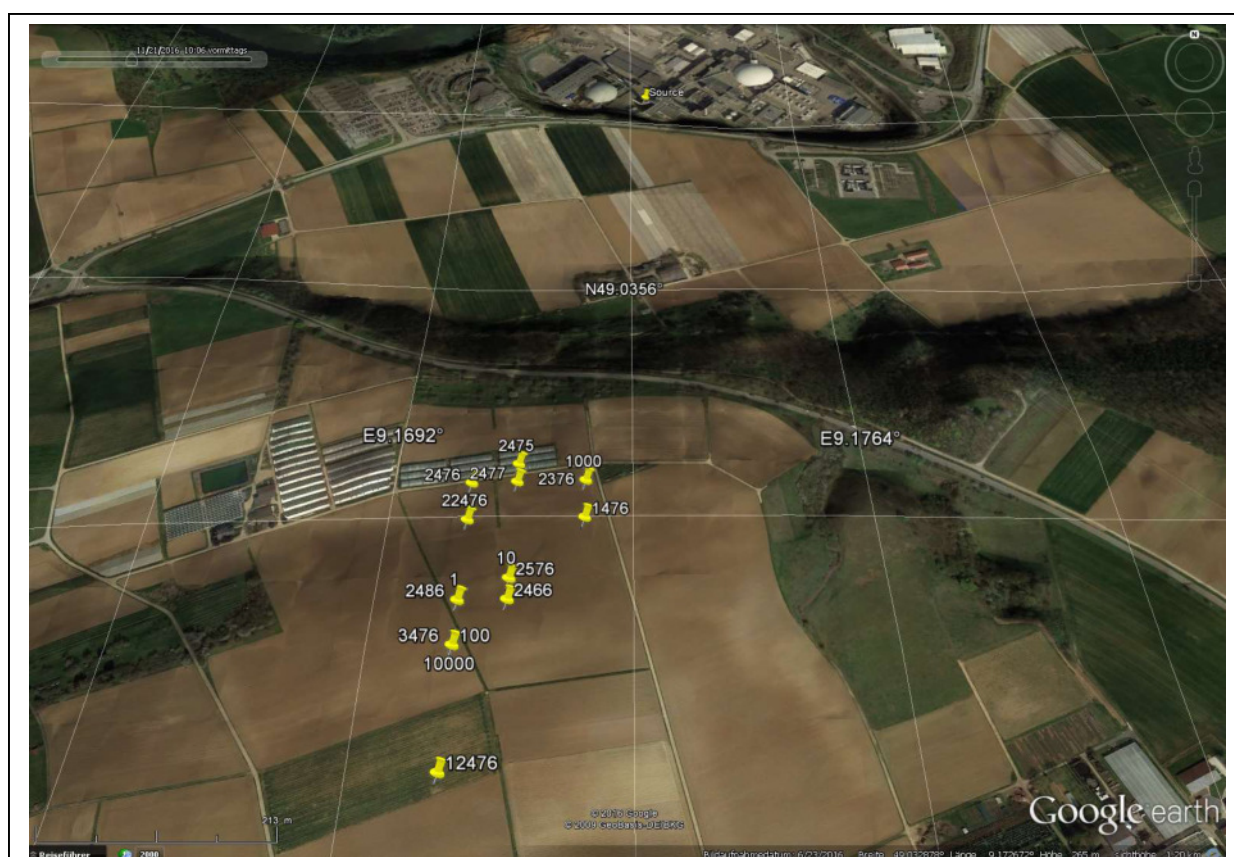


**Figure 2.2.3** Distribution of the points of maximum concentration. Depending on the starting random number, different points of maximum concentration can result. Here shown are the results for the 16 different starting random numbers at particle quality qs 0. The graphic was created using Google Earth.

#### **2.2.4 Summary of the Neckarwestheim scenario**

Basically, the Neckarwestheim scenario supports the finding of the La Hague scenario in terms of starting random number and the particle quality, which have medium or low effects on the simulation results. Interesting is the assessment of the point of maximum concentration, which experiences these variations both in location and its value.

### **2.3 Conclusion of the ARTM sensitivity analysis**

To summarise the results of the sensitivity analysis it can be said, that the largest effects on the simulation results are with the external parameters. The parameter influence ratings as shown in tables 2.1.1.5 and 2.1.2.4 try to give an estimation on where to expect the largest or the lowest influences, if parameters are changed. Here, especially the dispersion category has a big impact if chosen differently, which is also the most unreliable parameter, as it cannot be measured directly and as there are many different methods to determine these values. All other external values are easier to measure, even though there will always be measurement uncertainties and deviations.

The internal parameters have lower effects on the final results, yet a different choice can lead to different results, which are not necessarily incorrect. The deviations of the internal parameters can be kept very low if taken the highest amount of simulation particles for an ensemble of simulations with different starting random numbers and nested grids.

This will take away the dependency of user-defined deviations and makes the results dependent only on the external parameters.

An interesting result of the sensitivity analysis is, that the reduction in the error by increasing the amounts of particles does not reconstruct the theoretical predicted values, especially for the highest particle level.

### 3. Validation of ARTM with the La Hague scenario

After the model has been verified in the previous chapter using the La Hague scenario in a sensitivity study, now the real La Hague data as derived from Connan et al. (2013) were used to validate ARTM for this scenario.

Therefore, the measurement results of the campaign from 26<sup>th</sup> to 27<sup>th</sup> of February 2009 for the location at the IRSN in Cherbourg (as described in chapter 1.4.1) were compared with the results of an ARTM simulation.

A fairly wide grid size of 500 metres was chosen for this scenario in order to cover the large area with reasonable computing effort. A short assessment of computing times can be found in chapter 2.1.2.3.

Since not all of the necessary input parameters were provided in the publication, some of them had to be assumed such as the emission rate for 27<sup>th</sup> February or the dispersion categories. Details on these assumptions can be found in chapter 1.4.1 and in the appendix D. The input data files can be found in appendix E.1 and in appendix G.

For this scenario, three cases were considered due to the lack of information on the stack in operation in Connan et al. (2013):

- i. All emissions are released only from stack UP-2 800
- ii. All emissions are released only from stack UP3
- iii. Each of the two stacks contributes half of the total emissions

For each of the three cases 16 simulations were conducted (totalling 48 simulations), each with different random starting numbers in order to gain a better statistic (see chapter 2.1.2.1) and at particle quality level 4 to minimise the deviations (see chapter 2.1.2.2).

As target for the simulation results the exact location of the IRSN Cherbourg (in around 18 kilometres distance to the source) was inserted. In order to account for slight special deviations of the cloud, not only the grid cell that includes the IRSN facility was considered in the simulation, but also the 24 surrounding grid cells. Due to the stable dispersion categories in the meteorology of this scenario, the clouds usually appear to be slim, so that a slight error or deviation in the external factors like wind speed, wind direction, orography, etc., could cause the cloud to slightly miss the target in the simulation. If this would happen, it can be seen in the 5×5 cell target area grid with IRSN Cherbourg in the middle cell as shown in figure 3 I.

Figure 3 II shows the time series results of the three combined with the read-out of the measurement data from Connan et al. (2013). The solid dots in the simulation curves are the average values (calculated using ARTMRes as described in chapter 1.3.1.1) of the 16 simulations per case for the grid cell including the exact location of the IRSN Cherbourg. The error bars show the range of results for the 5×5 grid cells. The minimum value is the lowest value of the 25 cells minus its standard deviation (as described in chapter 1.3.1.3). The maximum value is the highest value of the 25 cells plus its standard deviation.

So each error bar intervals indicates the possible range of the simulation results, here called deviation range.

A closer look at figure 3 II shows that it makes not as big of a difference between the three cases of which the emitting stacks are. The respective curves more or less overlap and so do their deviation ranges. Only in the late evening of 27<sup>th</sup> February, there the lines can be properly



distinguished even though the differences are quite small between the different lines. This is also the weakest time period of the simulation in terms of being realistic.

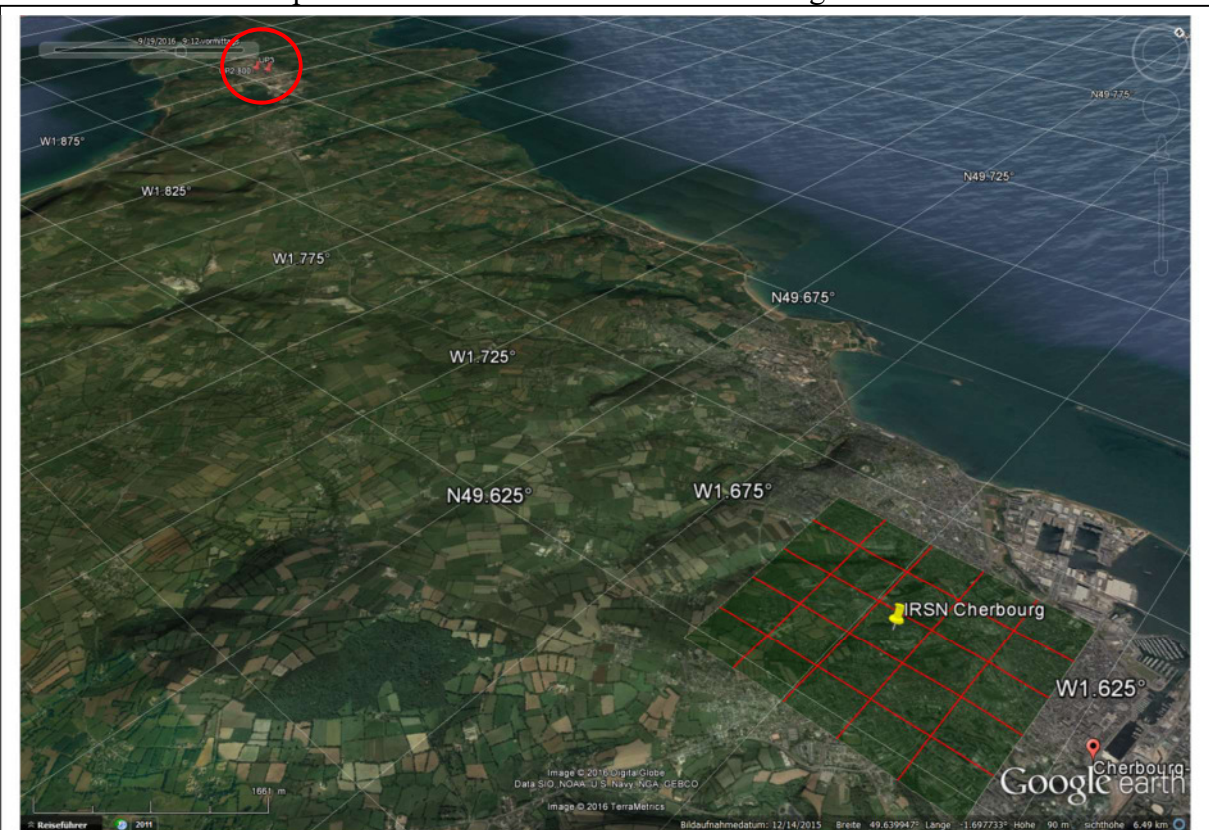


**Figure 3 I** shows the target area for the La Hague scenario. Each of the 25 cells is marked here by the red lines. The central cell includes the actual measurement location at IRSN Cherbourg. The graphic was created using Google Earth.

Now comparing the simulation results with the actual measurement data shows that, while underestimating or overestimating the real values, the measured peaks for the daytimes show up more or less in the simulation results, even though they might not exactly hit the time stamp in case for the 27<sup>th</sup> February. This phenomenon could be explained by the fact that the model uses a single measurement point for the meteorological data (see chapter 1.2.1.2). Therefore in 18 kilometres distance where the immission takes place, it is possible and most likely to have slightly different meteorological conditions, so that the cloud fully hits or misses the measurement location, which can lead to effects that the cloud arrives there sooner or later than the simulation can predict.

The height of the simulation peaks of course can vary as well. As mentioned in chapter 1.5, the simulation result is always just the average value of the target cell. The larger this cell is chosen, the more can this value deviate from the measurement. In order to gain better values, the grid size has to be decreased since this would decrease the volume over which the simulated particles are averaged, but at the same time it increases the simulation time as more cells have to be calculated.

For the 27<sup>th</sup> February, the simulation shows larger difference for the measurements, especially the three peaks in the night time period from 21:00 to 08:00 do not show up in the simulation, as well as the little peak in the night of 26<sup>th</sup> February. The later values on 27<sup>th</sup> show a large deviation range. Here it has to be mentioned that for the 27<sup>th</sup> February the data provided by Connan et al. (2013) were less sufficient (see chapter 1.4.1) than for the 26<sup>th</sup>, where a time series

for the emission strength in hourly resolution exists, while for the 27<sup>th</sup> only the average release

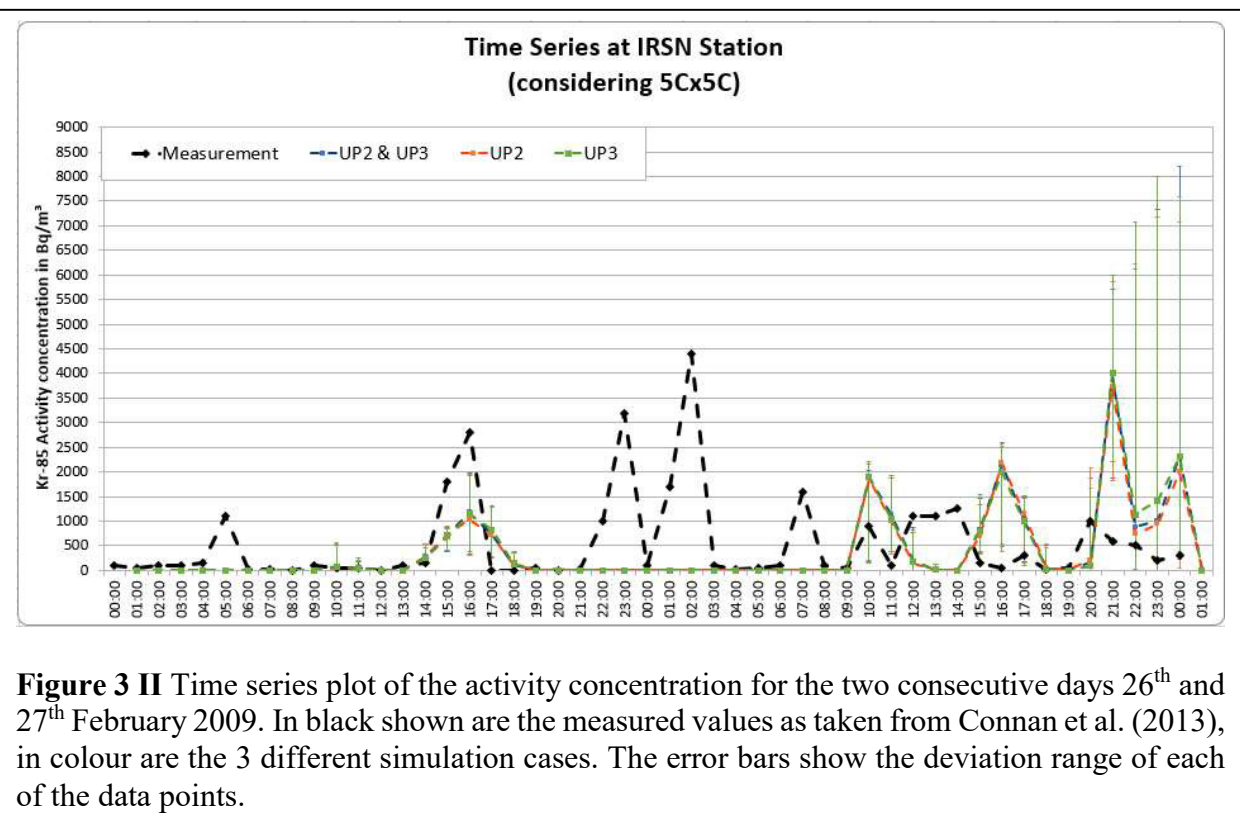


**Figure 3 II** Time series plot of the activity concentration for the two consecutive days 26<sup>th</sup> and 27<sup>th</sup> February 2009. In black shown are the measured values as taken from Connan et al. (2013), in colour are the 3 different simulation cases. The error bars show the deviation range of each of the data points.

of the 26<sup>th</sup> could be taken, therefore inducing some possible high deviations (see table 2.1.1.5).

The missed peak could be an effect of a thermally induced land-sea-wind-system, which cannot be simulated within the capabilities of the current ARTM version (see appendix B1).

A land-sea-wind-system develops from the different heat capacities of the two bordering surface cover types land and large water body. While during the day the land heats up faster than the sea, the warm air rises over land and is sucking cooler air masses from the sea [Rödel, 1992]. So during the day, the wind comes from the sea-direction [Rödel, 1992]. At night this is different as the water body contains more heat than the land, which cools down quickly after the solar illumination has decreased, so now the wind is going in the opposite direction from land to sea [Rödel, 1992].

Synoptic observations for this day (see appendix D) show that there was a tendency for such a land-sea-wind-system. The weather charts in appendix D and even more the satellite images of the period from 25<sup>th</sup> to 27<sup>th</sup> February show that it was mostly free of clouds, which allows

- a) for warming land and sea during the day time and
- b) for free thermal radiation of this stored heat during the night time.

Even though the temperatures with 5°C at night and around 10°C during the day of these February days were relatively low, it is possible that a light land-sea-wind developed which would be enough to shift the <sup>85</sup>Kr emission plume from missing the IRSN location (and the target area), so that in the measurement it hits the detectors and creates these peaks.

As mentioned above and in chapter 1.4.1 already, for 27<sup>th</sup> February there had to be made assumptions also on the emission strength. Since the emissions of the La Hague facility tend to

be highly variable, the peak height for the simulation results on 27<sup>th</sup> is most likely not realistic, while the position of the peak during the day is not influenced by this.

The high deviation range of the later hours of 27<sup>th</sup> February can be explained by the fact that the cloud border hits the target area while it has a narrow width due to the stable dispersion category. In figure 3 III the target area and their respective concentration values are shown from 16:00 to 23:00. In the first image it shows that the cloud is quite narrow. In the following images the cloud is touching the target area only in the southern part and then after 21:00 it touches it in the northern end. So, some cells have a very low resulting activity concentration while other have a high one. The cells shown in the graphic are not the actual simulation cells, but the lines are connections to the centres of the simulation cells, where the measurement points are, resulting in this 4 by 4 grid instead of the 5 by 5 of the simulation. In all images, the IRSN site is always in the middle.

In conclusion, it can be said that if given enough input information, ARTM could reproduce the position of the peaks during the day-time. A decrease in the grid size could possibly increase the accuracy of the values. During the night time, the scenario holds a land-sea-wind-system, which is not realised in ARTM yet, therefore the peaks of the night-time measurements could not be reproduced.

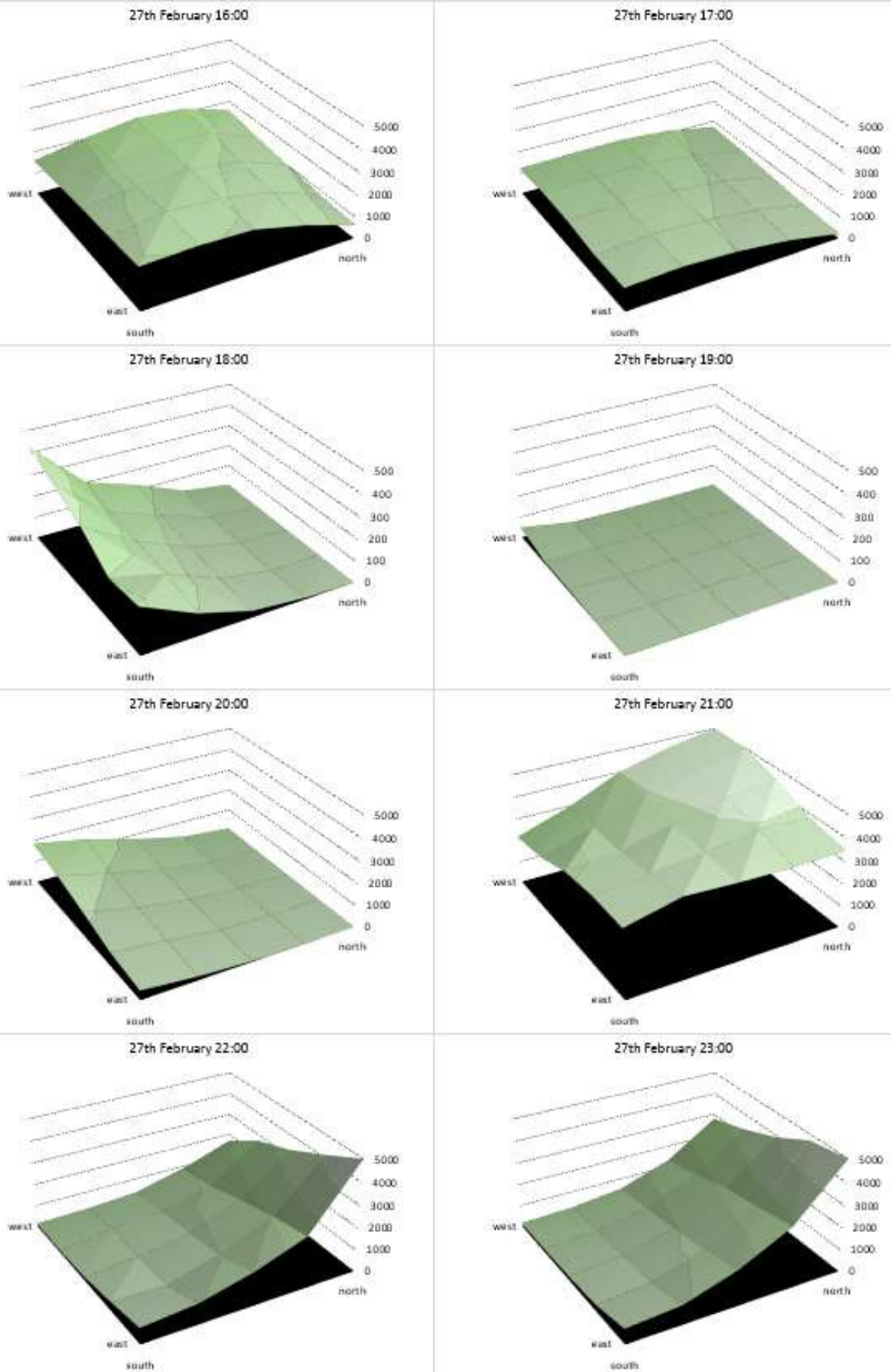


**Figure 3 III** The target area of the La Hague scenario. Each of the grid points is the central point of a simulation cell. The surface displays the activity concentration of  $^{85}\text{Kr}$  in  $\text{Bq} \cdot \text{m}^{-3}$ . It clearly shows that the target area was at the border of the cloud, leading to high deviation ranges in the diagram (figure 3 II).



## 4. The Šoštanj modelling exercise

The Šoštanj modelling exercise was an exercise conducted within the framework of the IAEA MODARIA project as one of the activities of working group 2 (see chapter 1.4.3). The Šoštanj release scenario was used to validate and compare various atmospheric dispersion models provided by the working group attendees of international origin, and a combined publication is currently in preparation.

Here in this work the focus is solely on the two models ARTM and LASAIR, which were applied to the Šoštanj scenario in the course of this modelling exercise. Additionally, some studies outside the MODARIA project have been done with this scenario and the results will be presented here.

The Šoštanj exercise was subdivided into two different study cases with different situations and difficulty:

i. Case 1 – 30<sup>th</sup> March 1991

Here the situation was that the wind direction mainly was from the north, so that the measurement station of interest was the Veliki Vrh station located on a hill top south to the plant (see figure 1.4.3) [IAEA, 2017(exp); Mlakar et al., 2015]. On 30<sup>th</sup> of March only one stack was in operation which additionally simplified this case.

The modelling task was to calculate the  $SO_2$  concentration in a time series for the Veliki Vrh station with a special focus on the noon hours where only little fluctuation in the wind directions were measured and therefore the plume directly hit the measurement station [IAEA, 2017(exp); Mlakar et al., 2015].

ii. Case 2 – 1<sup>st</sup> to 2<sup>nd</sup> April 1991

Case 2 was a more challenging scenario due to the complex meteorological situation. Over the course of the two consecutive days from the 1<sup>st</sup> to 2<sup>nd</sup> April, the wind direction varied greatly and an overnight inversion layer accumulated the emitted  $SO_2$ . Thermal effects during the first half of the 2<sup>nd</sup> April then mixed these down again leading to high concentrations at the measurement stations [IAEA, 2017(exp)]. The complex terrain of the surrounding area and the emission from the two stacks made case 2 a more challenging scenario for dispersion modelling than case 1 [IAEA, 2017(exp), Grašič et al., 2007].

### 4.1 The first modelling attempts and their difficulties

As in section above mentioned, the exercises were more or less complex by their meteorological and orographical nature, and by the details on the release of the  $SO_2$ -pollutant.

Within the MODARIA working group 2 not only the goal was to validate the models with the measurement data, but also to compare the model results among each other. In order to be capable of doing so, it needed to be ensured that all models have the same input parameters and deliver comparable results, which is challenging in itself as different models work differently and/or were developed to serve different purposes, such as ARTM and LASAIR (see chapters 1.2.1 and 1.2.2).

In order to obtain reasonable results, some preparatory work had to be conducted and several difficulties had to be solved.

### 4.1.1 Orography

The orography which was included in the scenario data set (see 1.4.3) needed to be slightly adapted in order to be read-in with ARTM.

The model requires some steepness limitations, so the initial maximum steepness of 0.87 in the orography file had to be brought down by using an alternative orography file from geocomm.com - prepared according to chapter 1.3.1.1- to reduce the maximum steepness to 0.58. Despite ARTM still printing out warnings that the steepness is higher than the 1:5 ratio the model foresees, but the wind field model could still produce results.

For LASAIR, which downloads the orography automatically from Open Street Maps it was a different issue. Dependent on the place of the coordinate origin chosen, a simulation run either was successful or not.

A small study of this phenomenon is shown in figure 4.1.1 I. In red are the locations of the coordinate origins where the simulation did not work, green where it worked, yellow where it only worked after rising the wind speed and the violet location caused a general crashing of LASAIR.

From communications with the programme developer Dr. U. Janicke resulted that in the red cases the vertical wind speed, as calculated by the wind field model Lprwnd (see appendix A.2), went over a programme internal threshold therefore causing the break-down of the simulation. In a provided patch to LASAIR, this issue was solved with the note that now the simulations are not anymore conform with the VDI guidelines, therefore it will not be applicable for regulatory or expertise purposes.

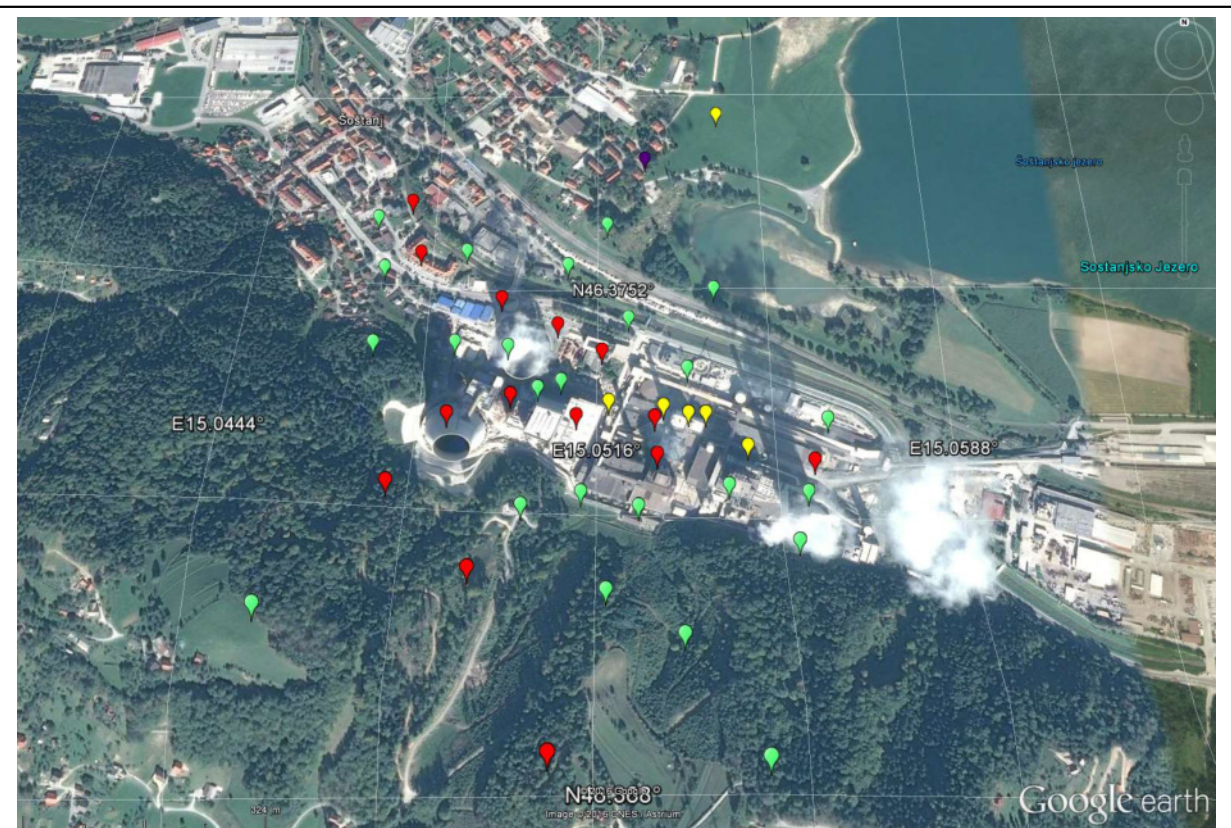


**Figure 4.1.1 I** Map of the coordinate origins of the initial simulation runs with LASAIR. In green the origin locations what worked properly, in yellow where the wind speed had to be raised, in red where LASAIR did not simulate and the purple location, where the programme crashed entirely. The graphic was created using Google Earth.

### 4.1.2 Meteorology

The original meteorology data came in a resolution of half-hour-steps. For the use in ARTM only hourly values can be used, therefore this half hourly meteorology had to be transformed into hourly resolution. This was done in two different ways:

- The first attempt was to simply exclude the half-hourly values and to only use the meteorological data falling onto each full hour. This was done at first to have a quick overview on the scenario results. Later it turned out that these results for some cases matched better to the measurements than the mathematical correct method to obtain hourly values from half-hourly inputs (see chapter 4.2).
- The correct method is to add half-hourly and hourly values in a vector addition, which is shown in detail in Appendix E.2, kindly provided by Primož Mlakar, MEIS, Slovenia.

Another parameter, the dispersion category, had to be determined as mentioned in chapters 1.4.3 and 1.3.1.2 from the SODAR measurement data provided in the Šoštanj data set.

Additionally, and in order to provide comparable results to the other models used within the MODARIA working group 2, Dr. Mlakar also provided the Monin-Obukhov values for the meteorology data of 30<sup>th</sup> March.

For LASAIR all these meteorological data could be applied only after converting the Monin-Obukhov-lengths back into dispersion categories of Klug-Mainer.

This altogether resulted in four different meteorology files for 30<sup>th</sup> March and two different ones for 1<sup>st</sup> to 2<sup>nd</sup> April. These files are named:

- ‘old’, referring to the very first attempts, where simply the half-hour values were excluded
- ‘averaged’ for the meteorological data that built up on the vector-addition of the half-hour values
- Additionally there is the naming ‘new categories’, if the Monin-Obukhov-length was used instead of the calculated dispersion categories.

An overview on the different performed simulations can be found below in chapter 4.1.4.

### 4.1.3 Emissions

While the temporal variance and the amount of sources was not an issue for ARTM, LASAIR lacked the option on putting different emission values for different time periods. For ARTM the half-hourly emission values had first to be averaged to obtain the hourly ones as shown in appendix E.2.

For LASAIR only the total amount of emitted material (see table 4.1.3) can be inserted and then go with the average for each time step, which (according to chapters 2.1.1.1 and 2.1.1.5) can lead to significant differences in the peak heights of the simulation results.

**Table 4.1.3** Total emission values for the input in LASAIR. Here the  $\mu\text{g}$  directly correlate with the Bq-values as requested by the programme.

Emissions from:	Stack 'Blok 123' [ $\mu\text{g}$ ]	Stack 'Blok 5' [ $\mu\text{g}$ ]
30 <sup>th</sup> March	$3.7 \cdot 10^{13}$	-
1 <sup>st</sup> April	$3.8 \cdot 10^{13}$	$9.4 \cdot 10^{13}$
2 <sup>nd</sup> April	$8.0 \cdot 10^{12}$	$1.3 \cdot 10^{14}$

For the simulation of these  $\text{SO}_2$  emissions, in both programmes the  $^{35}\text{S}$ -isotope was chosen in gaseous (ARTM) or near gaseous, i.e. all particles smaller than  $2.5 \mu\text{m}$ , (LASAIR) state were chosen. The emission strength in  $\text{Bq} \cdot \text{s}^{-1}$  (Bq) was directly substituted from  $\mu\text{g} \cdot \text{s}^{-1}$  ( $\mu\text{g}$ ) to simplify the analysis process.

With a mean half-life of  $T_{1/2} = 87.5\text{d} = 2100\text{hrs}$ , according to the Karlsruhe Table of Nuclides from 2006, and the population formula (4.1.3), one can estimate that after 24 (48) hours the initial material emitted at the very beginning still is with 99.21% (98.43%) available.

$$N(t) = N_0 \cdot 2^{-\frac{t}{T_{1/2}}} \quad (4.1.3)$$

In fact the emitted particles do not stay for long within the simulation area. The farthest corner is roughly 21 kilometres distant to the source, so assuming the lowest possible wind speed of  $0.5\text{m} \cdot \text{s}^{-1}$ , the material is for 12 hours in the simulation area leading to a value of 99.60% of the original material. Now here only the measurement stations are used to compare the results, and the farthest measurement station is only 7 kilometres from the source, leading to a transport time of 4 hrs and the availability of 99.87% of the original emitted  $^{35}\text{S}$ . So the nuclei that decayed on the way and don't get accounted for in the simulation results can be neglected in comparison to other potential error sources in the simulation.

Another limitation on the LASAIR side was that only one emission source was supported, therefore the case 2 scenario, where both stacks were in operation, had to be simulated separately for each stack and then the results were added up.

Also the maximum simulation period was only 24 hrs in LASAIR, so per meteorology scenario for case 2 four simulations had to be conducted with LASAIR, two for 1<sup>st</sup> April and two for 2<sup>nd</sup> April.

Of course, since a new simulation had to be started for the second day, all previous values were not considered any further in the new simulation leading to underestimation and potential absence of peaks shortly after midnight. These and other limitations of LASAIR are listed in chapter 1.2.2.2.

#### 4.1.4 Other issues

Some other difficulties that came up when trying to compare ARTM and LASAIR simulation results were related to:

- The amount of simulation particles:  
While ARTM uses by standard  $6.3 \cdot 10^7$  particles at the lowest particle quality level and a level 4 with  $1.008 \cdot 10^9$  particles is recommended (see chapter 2.1.2.2), this is, according to the developer Dr. Janicke, not a suitable option in LASAIR as the programme's purpose did not foresee large amounts of simulation particles. So instead  $1.008 \cdot 10^6$  particles were chosen here, one per mill of the ARTM particle value.
- The plume rise:  
ARTM internally calculates the plume rise from the inserted emission parameters and also has an option to insert a time series for the heat emission, according to the VDI guidelines 3782 Part 3 (1985). LASAIR on the other hand does not have this feature implemented, so the plume rise needs to be calculated manually and added to the stack height. With (4.1.4 i) the heat emission  $Q$  in MW is given [VDI 3782 part 3, 1985].

$$Q = c_p \cdot R \cdot (T - T_A) \quad (4.1.4 \text{ i})$$

With  $T, T_A$  the exhaust temperature and the ambient temperature in °C are considered in the heat emission [IAEA, 2017 (exp)]. The mean specific heat capacity for pit coal firing  $c_p$  is given in (4.1.4 ii) [VDI 3782 part 3, 1985; IAEA, 2017 (exp)].

$$c_p = 1.36 \cdot 10^{-3} \text{ MW} \cdot \text{s} \cdot \text{m}^{-3} \cdot \text{K}^{-1} \quad (4.1.4 \text{ ii})$$

$R$  is the emission volume flux (4.1.4 iii) with  $d_s$  being the source diameter, and  $v$  the exhaust velocity in  $\text{m} \cdot \text{s}^{-1}$  [IAEA, 2017 (exp)].  $T_s$  is the exhaust temperature multiplied by  $\text{K}/^\circ\text{C}$ .

$$R = \left( \frac{d_s}{2} \right)^2 \cdot \pi \cdot v \cdot \frac{273.15 \text{ K}}{273.15 \text{ K} + T_s} \quad (4.1.4 \text{ iii})$$

Since the gas flow volume in  $\text{m}^3 \cdot \text{hr}^{-1}$  is given in the Šoštanj data set the average of these values  $\bar{\dot{V}}$  can be directly used as in (4.1.4 iv) [IAEA, 2017 (exp)].

$$R = \bar{\dot{V}} \cdot \frac{273.15 \text{ K}}{273.15 \text{ K} + T \cdot \frac{\text{K}}{^\circ\text{C}}} \quad (4.1.4 \text{ iv})$$

Using the VDI guidelines 3782 part 3, the plume rises for the different time steps were calculated and a solid average (excluding the largest and the smallest value) was taken and added to the stack height.

This showed up another limitation in LASAIR, especially for the case 2 scenarios; the stack height plus average plume rise was in some cases larger than the maximum possible stack height of 300 metres. Here only the 300 metres could be set.

These and the in 4.1.3 mentioned issues can lead to high uncertainty in the results of LASAIR for simulation case 2, simply because LASAIR was operated here at the very edge of its applicability.

- The influence of the facility buildings  
The Šoštanj scenarios were also simulated both with and without including the buildings (see Appendix F) in both models. While LASAIR did not have an issue in the simulations, ARTM could not simulate the cases for 30<sup>th</sup> March, where the ‘new categories’ were used. The reason is that here in the meteorology a ‘very stable’ dispersion category appears which in combination with the buildings leads to a breakdown of TALdia. Same thing for the ‘old’ dispersion categories on 1<sup>st</sup> and 2<sup>nd</sup> April in connection with buildings.

An overview on the performed and successful/unsuccessful simulations with ARTM and LASAIR is shown in table 4.1.4. The green fields indicate where the simulations were successful and delivered results, in red are the above mentioned cases when the building influence in ARTM produced a breakdown of the wind field model. The white ones were not simulated, because here the ‘new categories’ were not provided, therefore no inputs for these cases. In total 132 ARTM and 24 LASAIR simulations have been performed.

**Table 4.1.4** Overview on the performed cases and sub-scenarios. In green are the successful simulations, red boxes mark unsuccessful ones, while the white boxes indicate that no simulations there have been done due to lack of the necessary Monin-Obukhov values for these [IAEA, 2017 (exp)]. The numbers show the amount of performed simulations.

Cases	ARTM				LASAIR			
	1: 30 <sup>th</sup> March		2: 1 <sup>st</sup> - 2 <sup>nd</sup> April		1: 30 <sup>th</sup> March		2: 1 <sup>st</sup> - 2 <sup>nd</sup> April	
Buildings	no	yes	no	yes	no	yes	no	yes
‘old’	16	16	16	1	1	1	4	4
‘new categories’	16	1			1	1		
‘averaged’	16	16	16	1	1	1	4	4
‘averaged and new categories’	16	1			1	1		

## 4.2 Results of the Šoštanj Modelling Exercise

Here now the results of the Šoštanj scenario, as performed during the MODARIA exercises, are shown. These results can be viewed as well in a shorter form in the IAEA MODARIA final reports, which is currently under development.

### 4.2.1 ARTM modelling results

The graphs in figure 4.2.1 I show the simulation results for the case 1 scenario of the 30<sup>th</sup> March. Here the main wind direction was North, so that the Veliki Vrh station was directly in the plume for most part of the day. In the diagrams the black curve indicates these measurements, and what can be seen is that the main peak is around 12:00 and a second one again in the evening at 23:00. Between the 8:00 and the 12:00 o'clock peaks the plume has been hitting the measurement stations peripheral, similar to the afternoon hours, which is why there is a lower amount in concentration. Figure 4.2.1 II shows the plume and its dispersion over the entire simulation period of the 30<sup>th</sup> March.

The upper diagram included the buildings of the Šoštanj power plant, while the lower diagram shows the results for simulations without buildings. The blue squares show the values for the cell including the Veliki Vrh station for the 'old' meteorology data, i.e. where the half-hour values were ignored, while the red diamonds show the values for the 'averaged' meteorology. The simulations with 'new categories' were entirely discarded as they did not deliver any proper results. In all of them there was only one large peak at around noon, but zero values for morning, afternoon and evening hours. The error bars show the deviation range of the five by five cells target grid around the Veliki Vrh station. Within this grid, inaccuracies in the location and time of the air concentration are captured, e.g. if the main plume in the simulation passes by the neighbouring cells to the cell of the measurement station, the error bars show the largest and lowest values including their standard deviation resulting from the 16 different simulations. The statistical effect however is negligible for this case.

What can be seen in the diagrams is that most of the peaks are well represented in the simulation results. While the exact location in many cases does not exactly hit the measurement curve, the according error bars include them in most cases, suggesting that there might have been a spatial deviation leading to the over- or underestimations.

Further can be seen that the 'old' and mathematical incorrect meteorology seems to better estimate the real measurement data than the 'averaged one, especially for the 8:00 and the 23:00 peaks. The peak at 12:00 is better for the 'averaged' meteorology. Despite the difference in wind speed and direction being small between both meteorologies for this time, it is sufficient to create a better simulation result for the Veliki Vrh station.

Another effect that can be taken from the diagrams is that the simulations without buildings create a larger deviation range. The station values show in some periods larger differences to the measurement curve than for the simulations which include the plant buildings, while at other times they meet the curve better, for example for the 23:00 o'clock peak.

The afternoon and evening peaks before 23:00 are not met by any of the 4 different simulation modes, only two error bars reach up to them.

In conclusion to case 1 it can be said that none of the four modes is superior to the others in terms of best fit to the measurement data. The optimal simulation would contain parts of all four modes: From 01:00 to 08:00 the 'old with buildings' fits best, for 09:00 to 11:00 it is the 'old without buildings', then from 12:00 to 14:00 the 'average without buildings' takes over, from 15:00 to 20:00 all modes are equally off from the measurement data, before from 20:00 to 22:00 at least the 'averaged without buildings' hits the measurement curve with the deviation range, and finally the "old without buildings" recreates the 23:00 peak and its decrease.



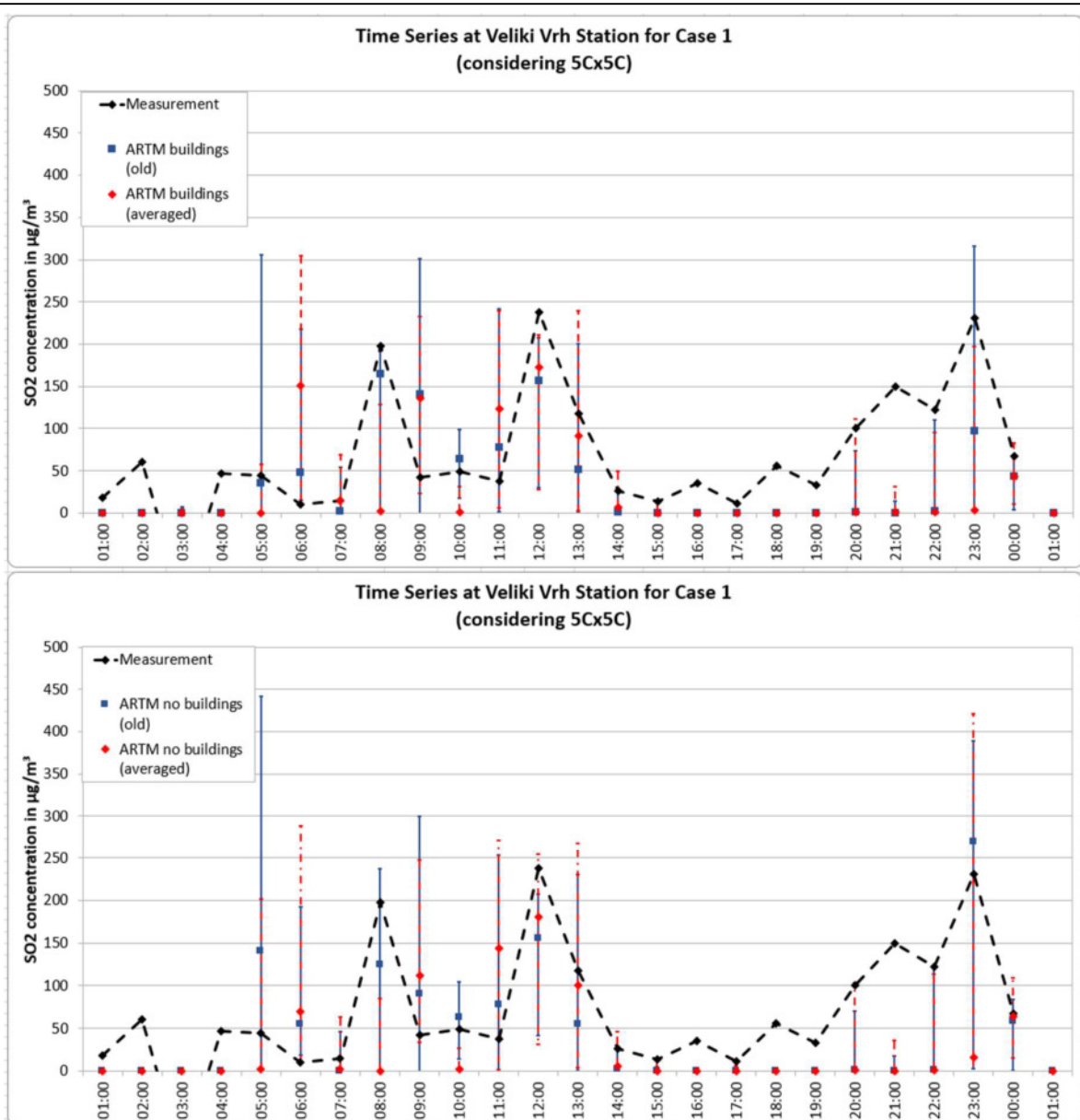


**Figure 4.2.1 I** Simulation results compared with measurement data for case 1 for the Veliki Vrh station. The upper diagram shows the results for the ARTM simulations including the Šoštanj buildings, while the lower diagram does not account for building influence. The black curve shows the measurements, in blue and red the simulations for ‘old’ and ‘averaged’ meteorology, respectively. The error bars represent the deviation range for a five by five cell target grid. These diagrams can be found in similar form in IAEA (2017 exp).

Case 2, the simulation period from 1<sup>st</sup> to 2<sup>nd</sup> April, was simulated in a similar way. Difference here was that the inclusion of buildings produced an error in the simulation software which could not be solved, therefore the simulations were performed only without buildings. The ‘new categories’ were not provided for this simulation time period which shrinks it down to the two modes ‘old’ and ‘averaged’. Due to the increased amount of measurement stations to be monitored and the limited amount of possible monitoring stations in ARTM, only a three by three cell target grid could be chosen for each of the locations.



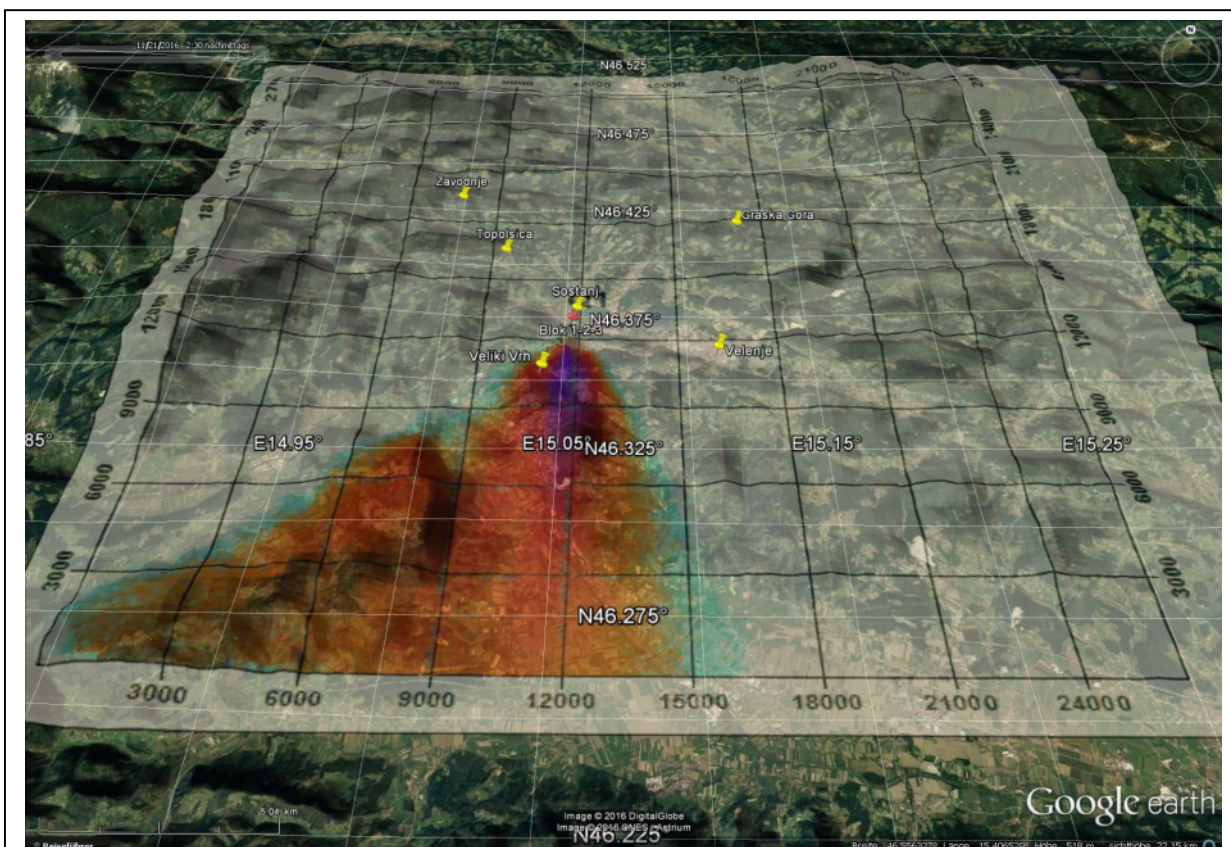
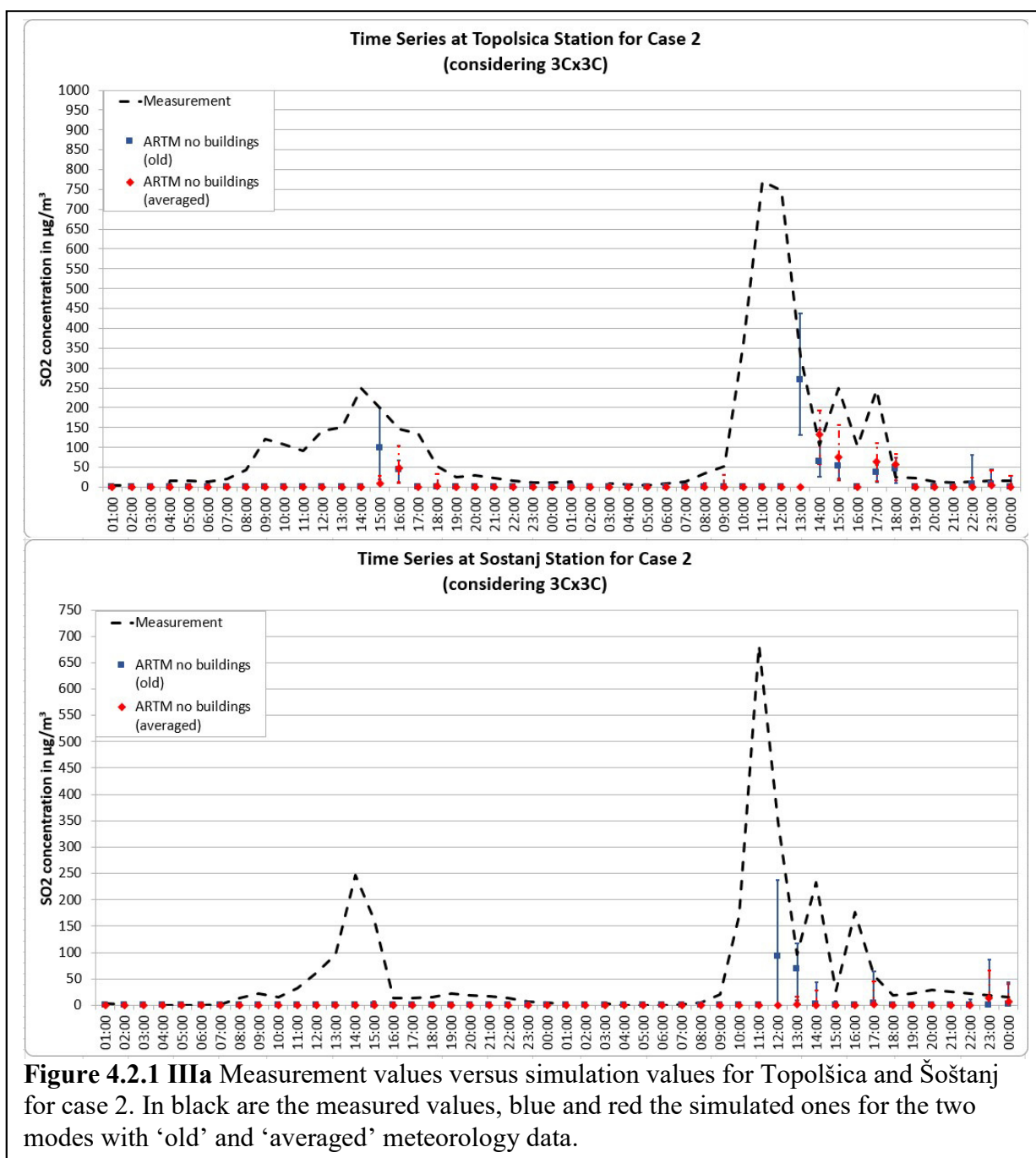


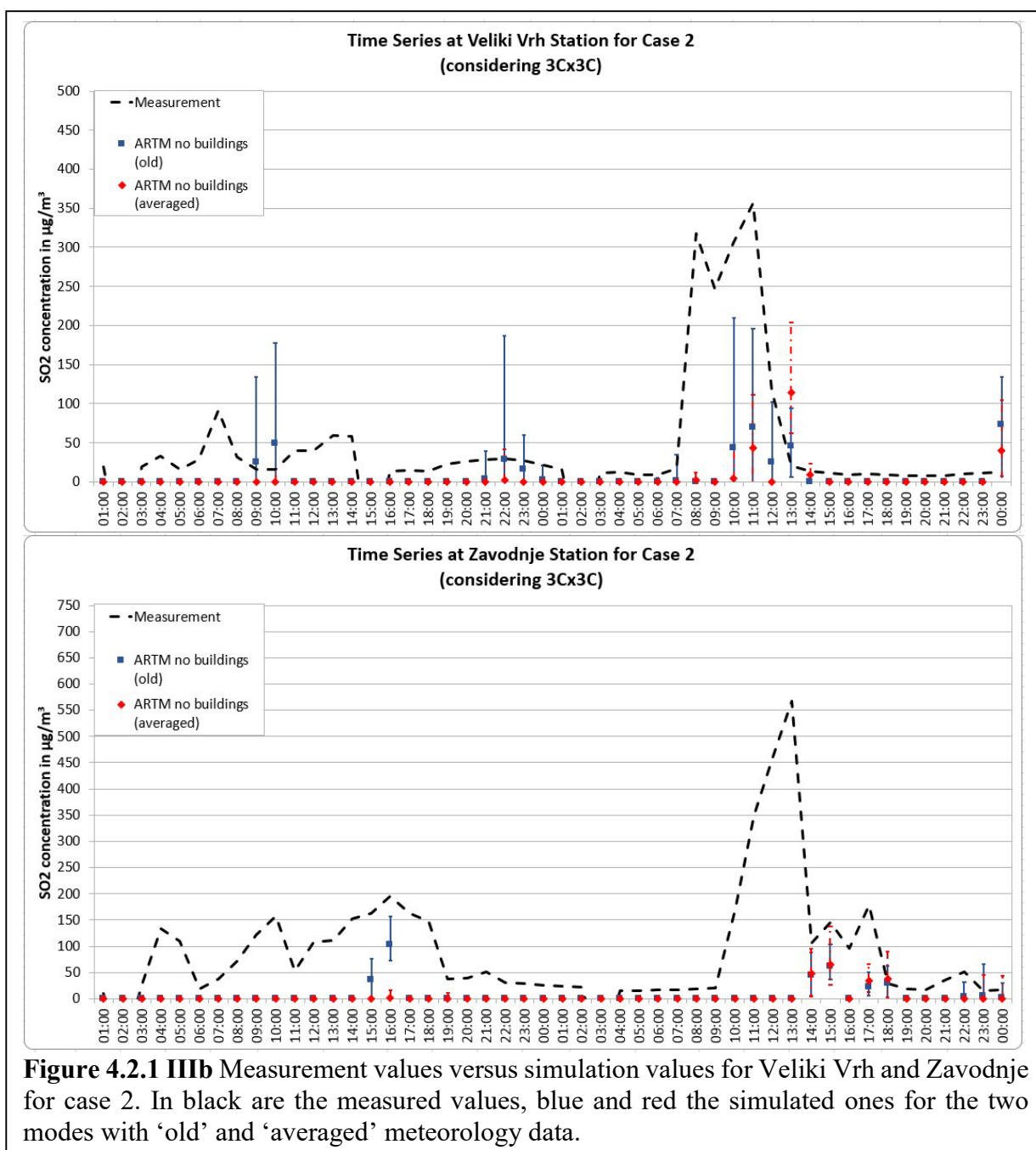
**Figure 4.2.1 II** Distribution of the concentration values over the simulation area for case 1. Here the plume for the entire simulation period of the 30<sup>th</sup> March is shown, the violet areas are the most effected by the emitted  $SO_2$ . The Veliki Vrh station is slightly west of the plume core area. Also good to see that for this case, only wind from Northern directions was influencing the dispersion, therefore all other measurement stations (yellow pins) did not receive anything in the simulation. The graphic was created using Google Earth.

The measured immissions (black curves) in all of the diagrams of figures 4.2.1 IIIa and 4.2.1 IIIb show a common and very significant feature appearing in the morning of 2<sup>nd</sup> April. This peak is, as mentioned in chapter 4, caused by thermal effects and the down-mixing of accumulated  $SO_2$  concentrations. Here only the four locations are shown, which led to significant results in the simulation; Topolšica, Šoštanj, Veliki Vrh and Zavodnje. Graška Gora and Velenje were not hit by the plume in the simulation.

The simulation results here for the case 2 are rather poorly congruent to the measurement results. For the first day of the two days' simulation period, where in the measurements one up to three main peaks occur, these are mostly not evident in the simulations. The Topolšica station shows at 15:00 a peak for the 'old' meteorology, whose deviation range reaches the measurement, however for the peak's highest point one hour earlier there is a zero in the simulation. At Veliki Vrh also the first peak is missing, two values at 9:00 and 10:00 o'clock symbolise the increase towards the next peak, yet then have again a zero. The increase in the evening is better represented, even though its values are lower than for the morning peaks. At Zavodnje station, the third peak was found by ARTM, yet even considering the deviation range, it does not hit the measurement curve. In generally, it can be said that for the first day of the two days, the simulation results were not good, even more so, if the mathematical correct 'averaged' meteorology was used.



For the 2<sup>nd</sup> of April, the high peak mentioned above was not accounted for in any of the simulation results. At Topolšica the decreasing side of the high peak is represented in the simulation with ‘old’ meteorology, however the high peak is not visible. Also at Šoštanj and Veliki Vrh there is a hint in the simulation data, that there is something large than zero, but also there, the beginning of the peak is does not appear in the results and the height of the simulated values stays far below the measured values for the peak, so it can be assumed that the model cannot handle this meteorological situation properly. The following smaller peaks, which are connected to the appearance of the large peak and the meteorological situation, show up in the simulation results, but are as well underestimating the maximum concentrations.



## 4.2.2 LASAIR modelling results

For the case 1, the simulation results with LASAIR show up the peaks in the measurements at the Veliki Vrh station (figure 4.2.2 I). A comparison between the scenario with buildings and the scenario without buildings show that while results in the no-building case fit better (such as at 08:00 and 00:00), there are larger deviation ranges, especially for the ‘averaged’ mode, where also the actual measurement locations appear overestimated in the morning hours.

Here as well, there is not one single simulation that is better than the others, but again a mixture would make the best fit:

Until 06:00, the buildings plus ‘averaged’ suits best, at 07:00 it is the ‘old’ for both, building and no-building case. At 08:00, the no-building ‘averaged’ fits again. From 9:00 to 11:00 the no-building ‘old’ and from 12:00 to 13:00 the buildings ‘averaged’ comes closest to the measurement. At 14:00, the buildings ‘old’ case hits the black line. Most of the afternoon values



are entirely off, only some deviation ranges reach out into the line of measurements. At 22:00 the no-buildings ‘averaged’ case comes closest and from 23:00 to 00:00 it is again the no-buildings ‘old’ case.

So basically, all modes are more or less the same good or bad in terms of representing the measurements, and a more realistic input (buildings plus averaged meteorology) does not necessarily produce better results in this case.

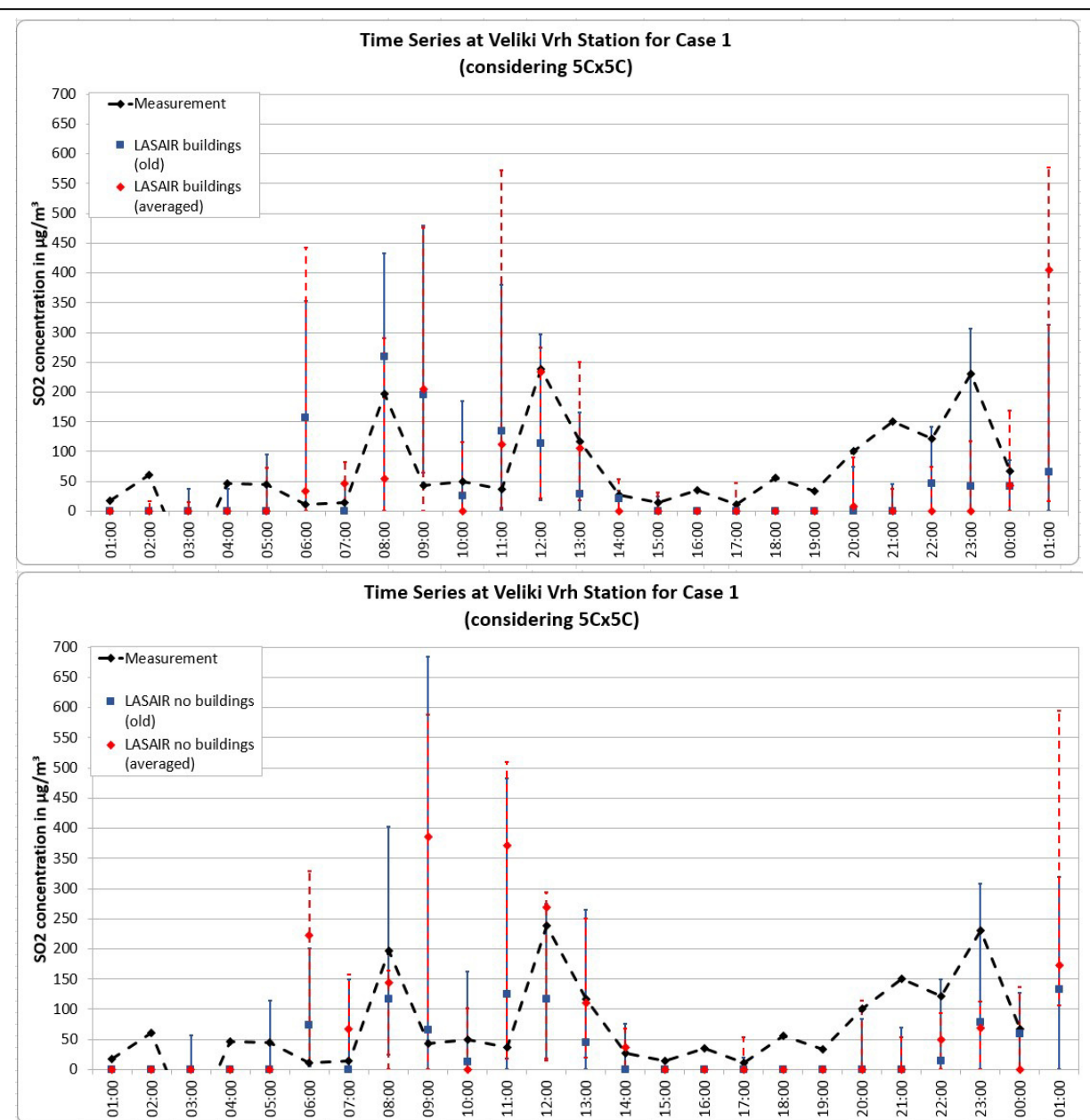
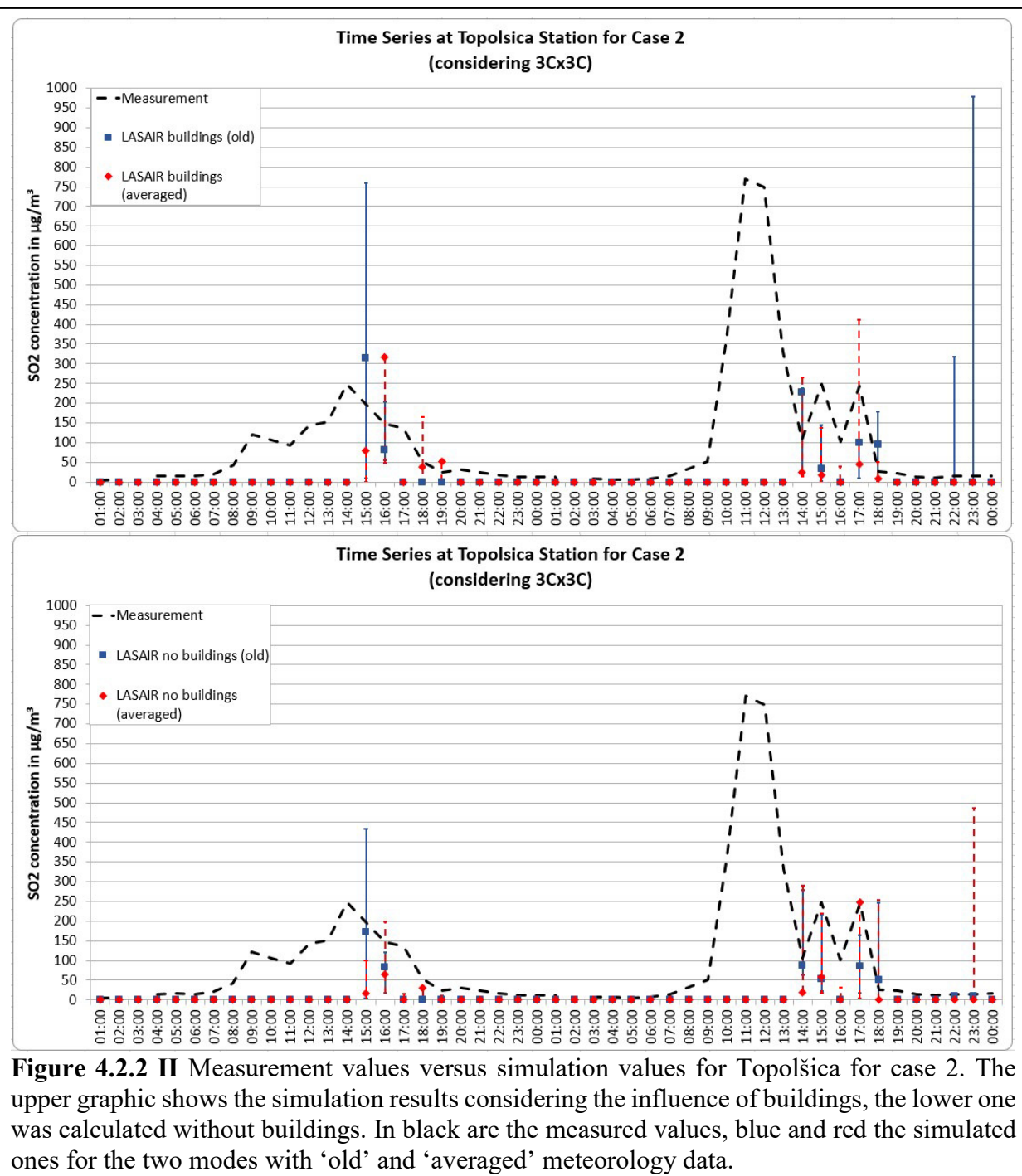
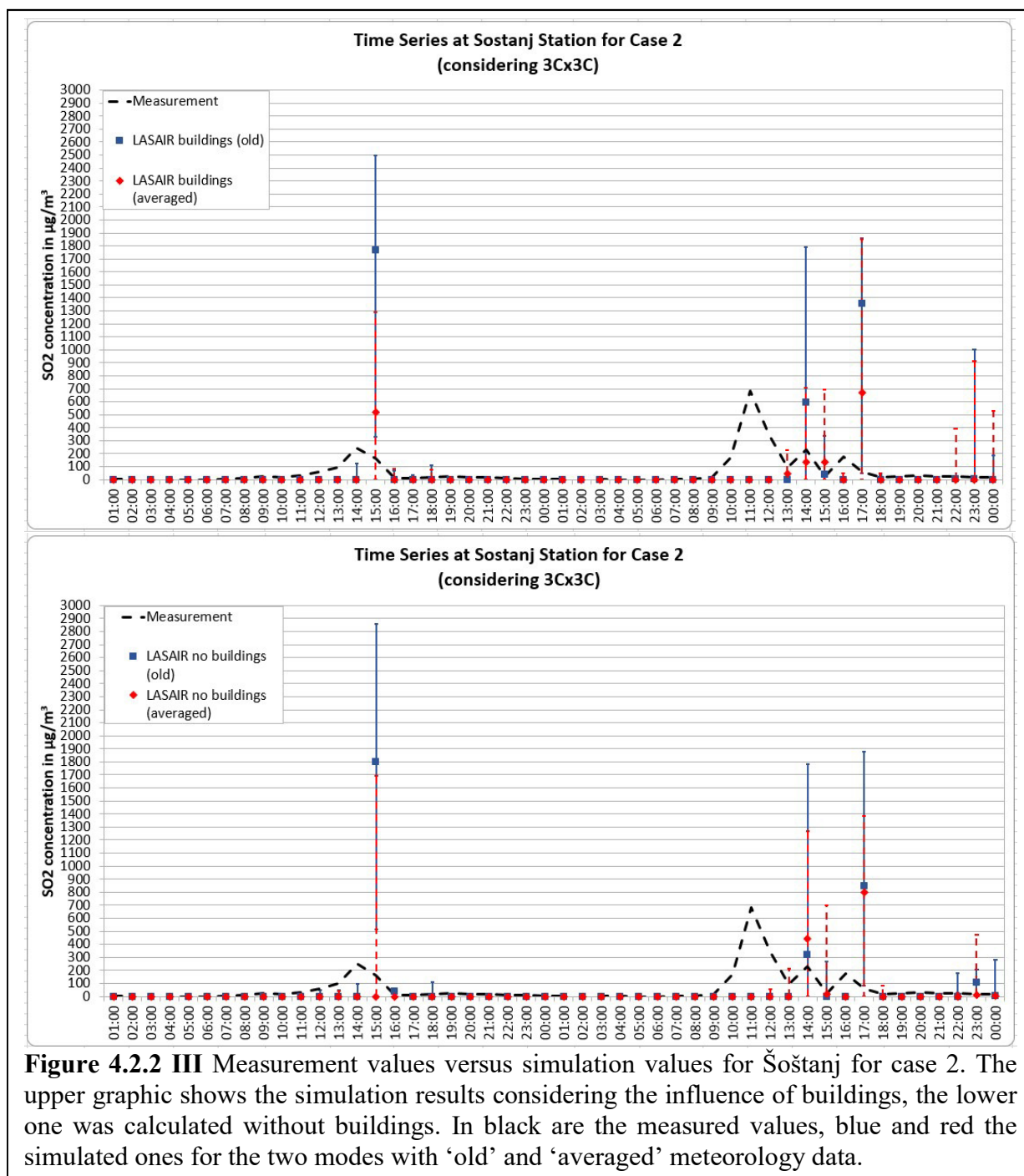


**Figure 4.2.2 I** Simulation results compared with measurement data for case 1 for the Veliki Vrh station. The upper diagram shows the results for the LASAIR simulations including the Šoštanj buildings, while the lower diagram does not account for building influence. The black curve shows the measurements, in blue and red the simulations for ‘old’ and ‘averaged’ meteorology, respectively. The error bars represent the deviation range for a five by five cell target grid. These diagrams can be found in similar form in IAEA (2017 exp).

For case 2, the same stations as for the ARTM simulations showed significant results. The excluded ones, Graška Gora and Velenje, did as well not show signs of being hit by the plume in LASAIR simulations. For the four stations Topolšica, Šoštanj, Veliki Vrh and Zavodnje, simulations with and without buildings were performed in LASAIR. Figure 4.2.2 II shows the results for Topolšica. Here the simulation without buildings seems to produce the largest deviations. While in the no-building scenarios, the ‘old’ meteorology recognises the decline of the 14:00 o’clock peak, the building scenarios over- or underestimate it. However, in both cases it is within the deviation range. The first peak and the maximum of the second one do not appear in the simulation. Also, the large peak on the second day is not represented. The most likely reason is, as for ARTM, that the model cannot handle thermal effects.



Also the limitation in stack height of 300m cuts off the calculated plume rise in most cases for the case 2 scenarios, as it would be larger than these 300m. This can also have a significant impact on the results. Additionally, the LASAIR simulations are not as continuous as it seems from the graphic. Due to the limitation of LASAIR to maximum 24 hours of simulation time, the simulation for the second day starts again at zero, i.e. the previous dispersion is gone and does not affect the time series values anymore, as it would be possible for example if the wind direction changes. Therefore the second day's simulation results have already an artificial error.



The Šoštanj station (figure 4.2.2 III) shows vast overestimation of the first peak for almost all simulations, except for the 'averaged' one without buildings, which is located at zero. Also here the first peak of the second day is not depicted, while the two following smaller peaks show up, but are mainly overestimated.

The Veliki Vrh station has two huge deviations. The first small peak in the measurements, which is slightly above zero, is in all modes poorly or not at all represented. The peaks on the second day are better hit by the simulations, yet also here the first peak is not shown in the simulations.

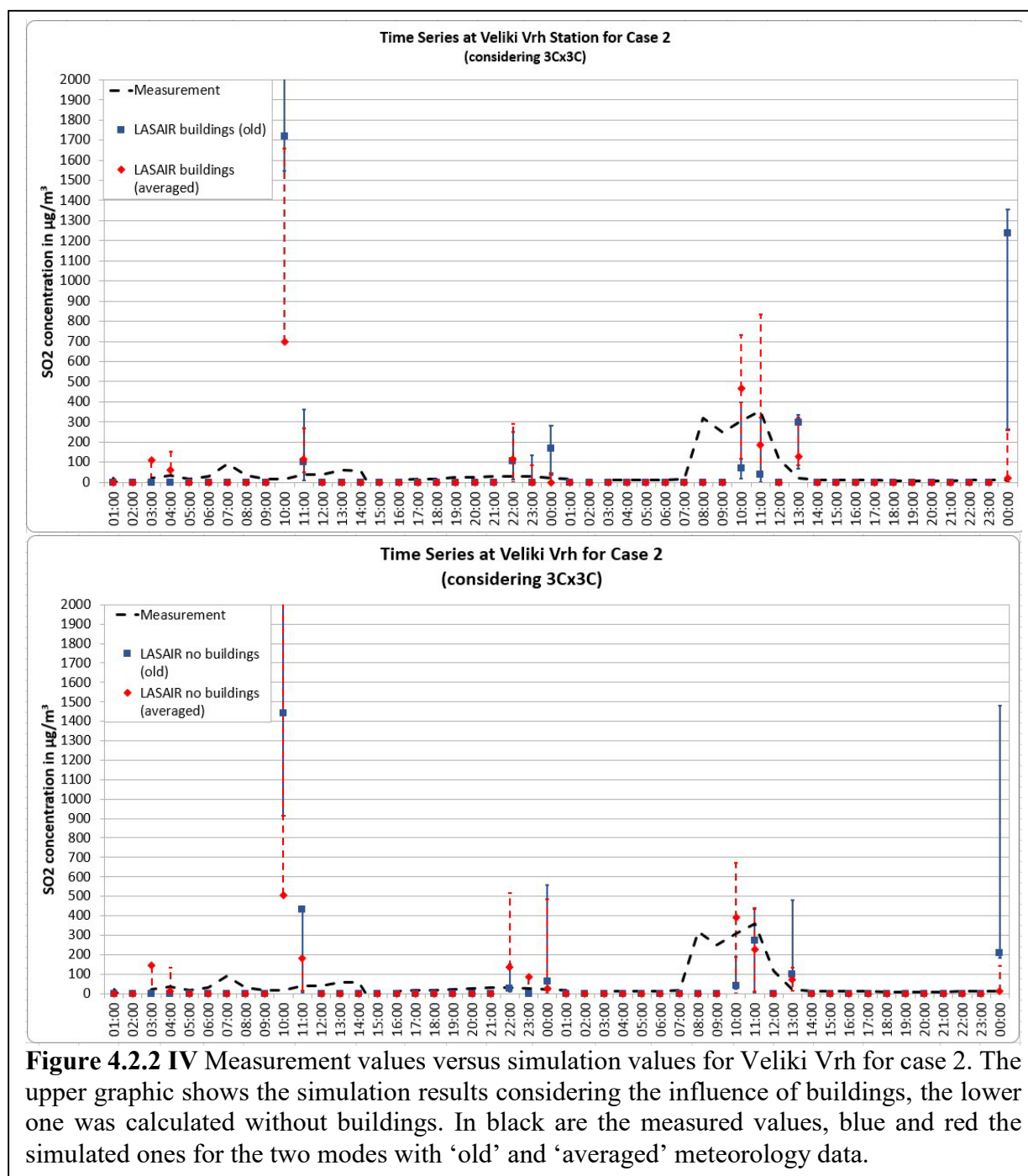


**Figure 4.2.2 IV** Measurement values versus simulation values for Veliki Vrh for case 2. The upper graphic shows the simulation results considering the influence of buildings, the lower one was calculated without buildings. In black are the measured values, blue and red the simulated ones for the two modes with 'old' and 'averaged' meteorology data.

At Zavodnje, shown in figure 4.2.2 V, there appear comparably low deviation ranges compared to the previous measurement station locations and the results look similar to the ones of Topolšica; the first peaks during the night and the morning of 1<sup>st</sup> April did not appear in the simulation results, only the 3<sup>rd</sup> and broad peak can be somewhat represented by the simulation,

however the simulated value at the peak maximum shows only half the measured value, and also the large peak on the second day is not represented in the simulation.

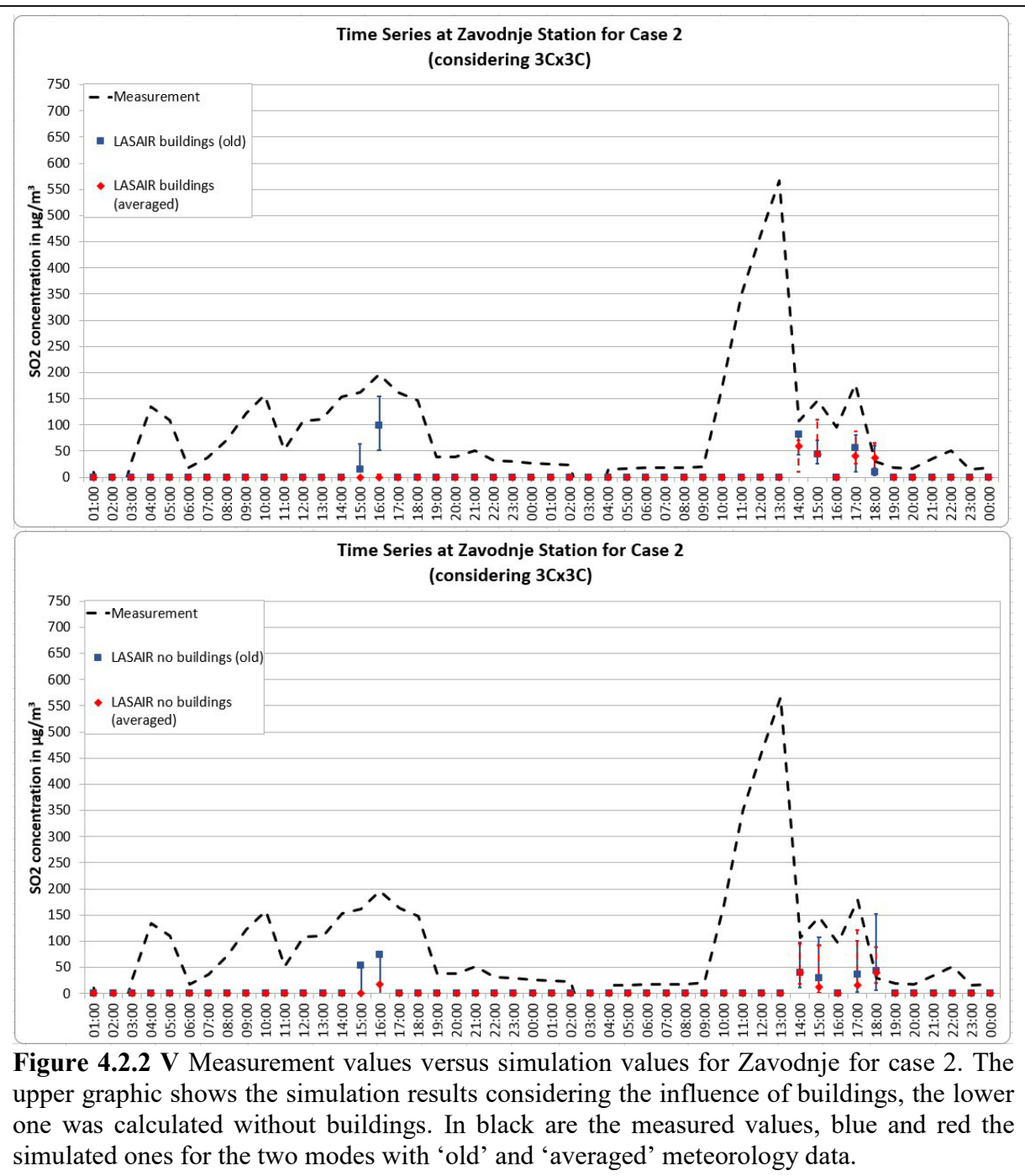
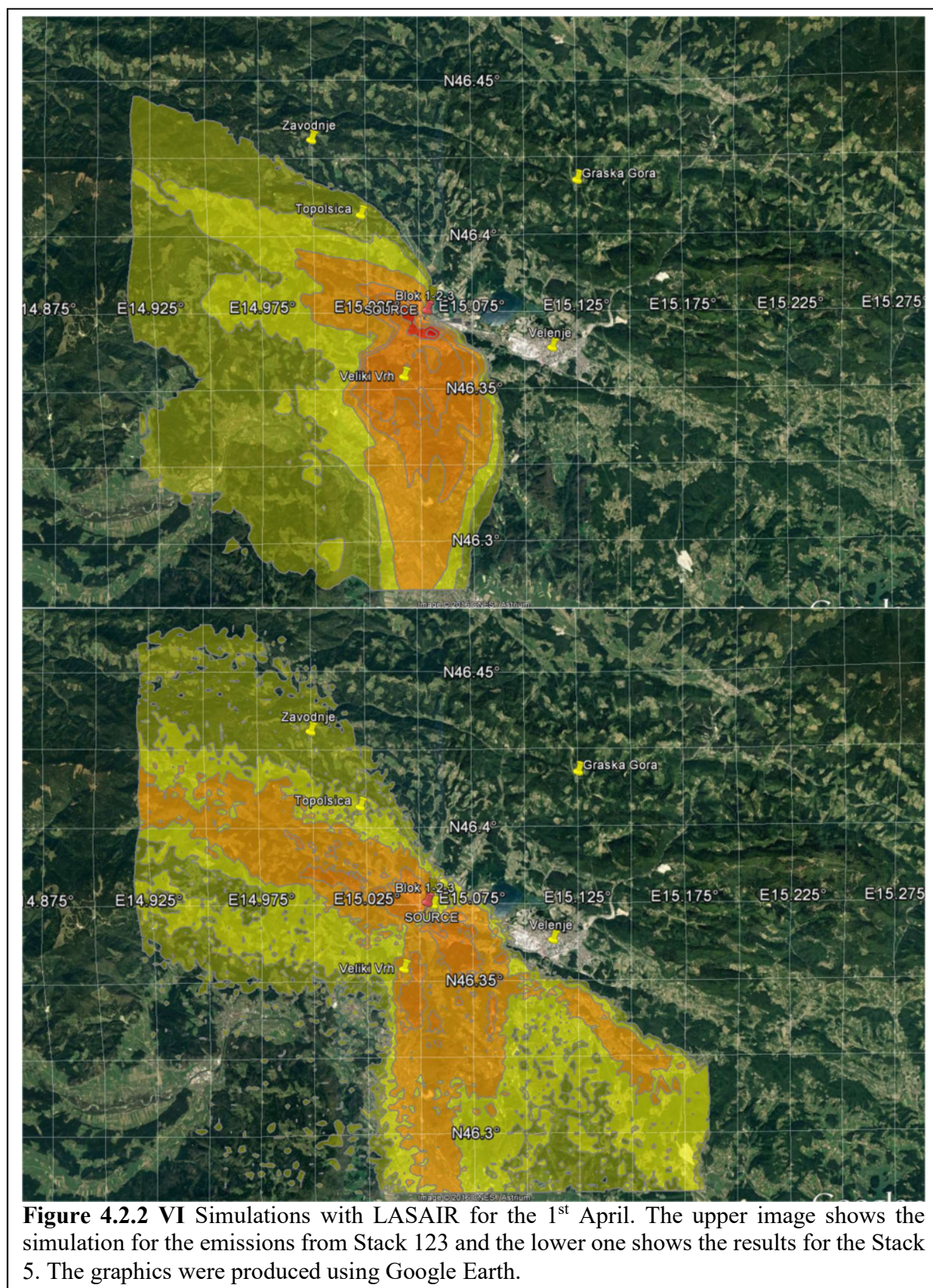


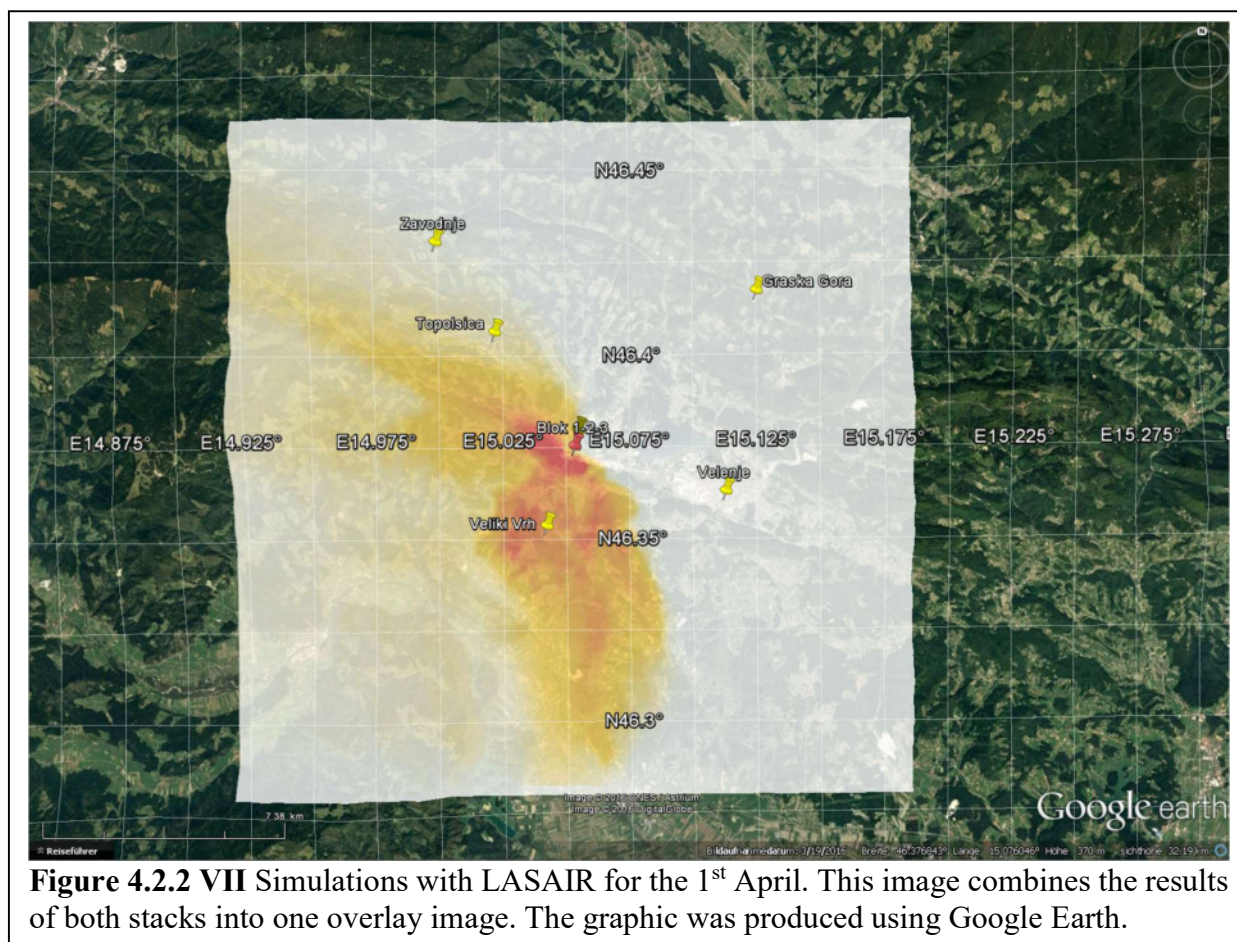
Figure 4.2.2 VI shows the plumes as simulated with LASAIR for the first day of the case 2 simulations. As mentioned in 4.1.3, LASAIR supports only one source per simulation, which is why the two stacks had to be simulated separately. The upper image in the figure results from the simulation of the emission of the stack called 'Blok 1-2-3', while the lower image results from 'Blok 5'. While the colour scaling is kept the same for both images, it can be seen that the higher stack 'Blok 5' has a bit of a different spreading. In order to obtain the total plume from both stacks for this time period, they need to be added.



The resulting numbers were colour-coded and used to produce a Google Earth overlay, as can be seen in figure 4.2.2 VII, although here the scaling of the colours does not scale the same as to the images in figure 4.2.2 VI.







### 4.3 Conclusion of the Šoštanj scenario

The Šoštanj scenario showed again the difficulty of applying existing models like ARTM and also LASAIR to complex orography and highly varying meteorology that includes also thermal effects. Both models have been used at the borders of their applicability, LASAIR even more so than ARTM. The results show that direct effects, which are not thermally influenced, can be well reconstructed in both models, such as in case 1 for 30<sup>th</sup> March.

For LASAIR it has to be mentioned that the simulation duration was just 24 hours, the heat flow was almost constant and the resulting plume rise did – after adding the stack height – not exceed the 300m limitation.

For the case 2, the results showed that both models performed poorly in the presence of thermal effects. Especially LASAIR tends to tremendously overshoot in some points the actual measurements. Even with ARTM not performing much better here, its results seem to be more founded by the model capabilities, as too many assumptions, approximations and trade-offs have to be made to fit the scenario into the limitations given by LASAIR.

The comparison between the different meteorologies used in this scenario showed that while one method to combine half-hourly measurements might be mathematically more correct than the other one, it does not necessarily produce better matching results.

Also, the influence of buildings, which has been neglected long time in Gaussian models, can change the results to the better or the worse, but fact is, that they have an impact. For LASAIR more examples for this impact of buildings are shown here, simply because the calculations

appeared to be more robust than in ARTM simulations in this aspect. As mentioned in chapter 4.1.4, ARTM could not handle the case 2 scenario with the influence of the facility buildings, as the wind field model aborted with an error for this case. It would be interesting to investigate these building versus no-building cases further in order to obtain the understanding when and how to apply facility buildings to a scenario.

For this, it would be also interesting to study the wind fields that each of the two models create, formally having the same mathematical background (see Appendix A) they seem to show differences in their results.

Directly from this here used data set there could be more follow-up studies, as there are more meteorological data available for each of the surrounding stations and at multiple altitudes rather than just at the emission height.

The simulations with LASAIR could be improved in a way that generates an overlap for the night between 1<sup>st</sup> and 2<sup>nd</sup> April, in order to not lose the previous dispersion.

Overall, the Šoštanj scenario provides a good platform to study the limitations of the models in all facets and there are still many more things that can be learned from this scenario.

In general, one difficulty is to compare the measurement data which is obtained from a small surface area with the simulated values which are average concentration values of the 150m by 150m area. So very local concentration peaks cannot be reconstructed and might cause that measurement results cannot be identically represented by simulation data.

## 5. The urban building scenario

The AVV states that buildings with a certain height and a certain distance from the source can be neglected for Gaussian models (see chapter 1.1.1) [AVV, 2012].

For Lagrangian models it seems however that buildings can greatly influence the results. For example, Rotach (2001) describes that considering urban structures for the simulation with a Lagrangian model leads to better model performance. In three different scenarios he showed that his ‘urban’ simulations produce better compliance between simulated and measured values, opposed to the ‘non-urban’ mode [Rotach, 2001].

However, the model used in Rotach’s study only parameterises the buildings as a roughness length sublayer, instead of directly modelling the buildings as boundaries in the wind field model [Rotach, 2001].

In contrast to Rotach’s model, ARTM and LASAIR use the direct approach to calculate the building effects in the wind field model. The Šoštanj scenario in chapter 4 has been simulated with and without the influence of the nearby facility buildings, and it showed that the results differed even in several kilometres distance.

Therefore, based on the research by Rotach, and the experience gained from the Šoštanj scenario, it suggests that including buildings in the simulation changes the results significantly. In order to investigate how these programmes calculate the ‘urban’ and ‘non-urban’ – here called ‘building’ and ‘reference’ scenarios – and if there are clear differences in the results, the urban building scenario was designed (see chapter 1.4.4).

It further aims also to

- 1) directly compare ARTM and LASAIR and to
- 2) study the behaviour of the plume while adding more buildings.

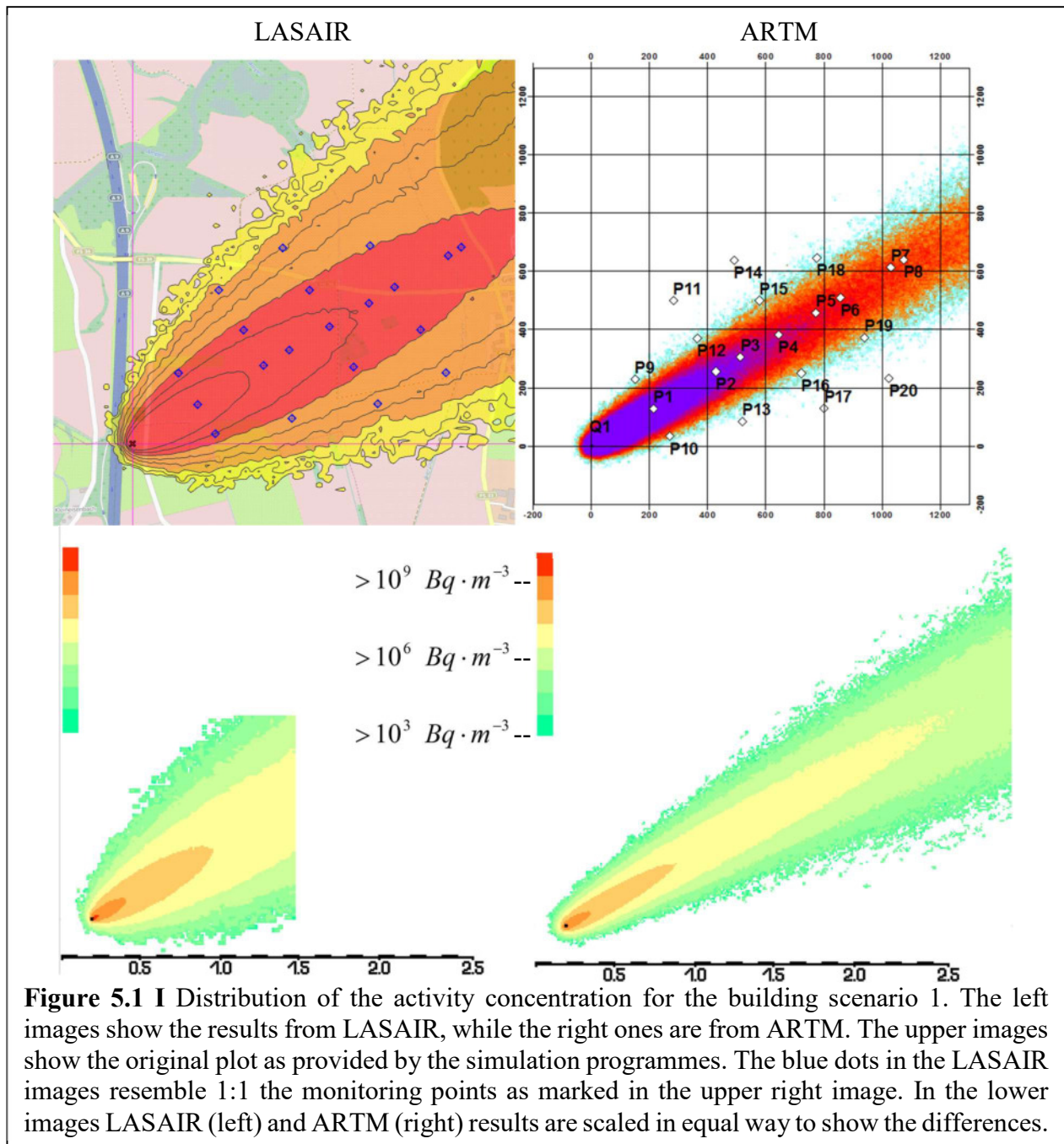
Therefore the scenario had to be simple, i.e. flat terrain, simple meteorology, and the inputs chosen had to be compatible to both models. The urban building scenario splits up into four sub-scenarios.

The emission height for all sub-scenarios was kept at 5 metres over ground.

### 5.1 The reference scenario – building scenario 1

Here the very simple case of ‘no-building’ was chosen. Building scenario 1 serves as a reference scenario to the other building scenarios and to study where LASAIR and ARTM differ.

Figure 5.1 I shows the resulting dispersion plume for LASAIR and ARTM covering each the same simulation areas for the zoomed-in case. The graphics indicate that the ARTM plume is slimmer than the one calculated with LASAIR, but graphics are by default not given in a directly comparable scale by the programmes, and therefore cannot be compared. In the lower images, both, LASAIR and ARTM, results have been brought to the same scale in order to display the differences between both plumes, and what can be seen here is that, indeed the plume extends more broadly in the LASAIR results than it does for ARTM.

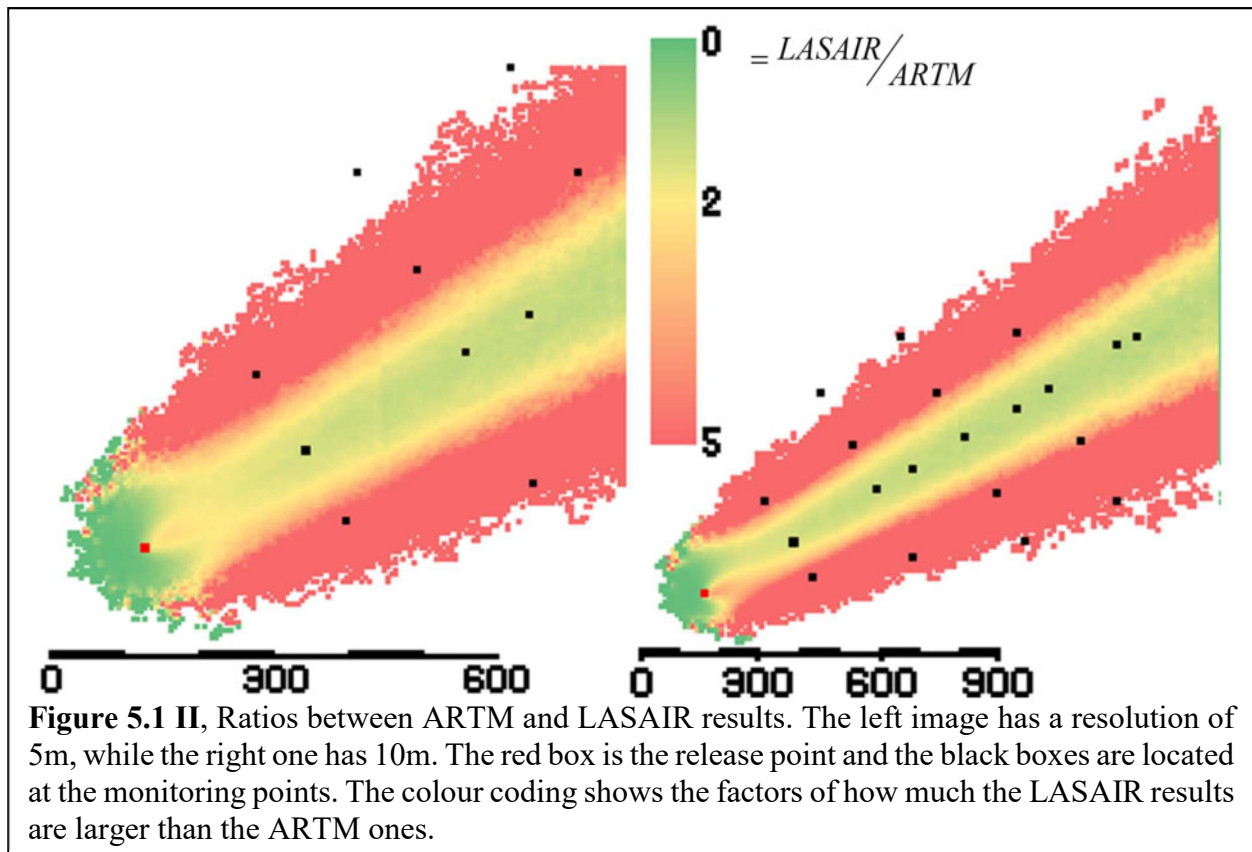


In order to properly compare the two simulation results, the activity concentrations of the entire simulation areas were put in relation by dividing the LASAIR results through the ARTM ones. Figure 5.1 II shows the results for the 5 metres and 10 metres resolution. The colour scheme indicates the different factors:

- Dark green is zero. Grid cells in dark green have a zero value in the LASAIR results and a non-zero value in ARTM.
- If the values of LASAIR and ARTM are the same, so the factor is around 1, then these cells would appear in light green.
- Bright yellow is around factor 2, which means here the LASAIR results are around twice as high as the ones calculated with ARTM.

- Red indicates that here the values are five or more times higher in LASAIR than in ARTM.

What can be seen in this graphic is that in the comparison the plume of ARTM indeed is narrower than the one of LASAIR. The red areas indicate that here the values of the ARTM results are much smaller than the LASAIR ones. So while in LASAIR these areas still lie within the plume, they are already at the edge of the plume in ARTM. Also, in ARTM the plume extends a little further against the wind direction than in the LASAIR results which show the green fields to the south-western side of the source.



In the direct line of the wind direction, the difference appears rather low, and the plume centre is in light green. The numbers in table 5.1 support this impression; here the 20 monitoring points were evaluated on their difference. P1 to P8 lie in direct line of the dispersion and show factors of 1.16 to 1.52. The other points are already in the border or even outside the ARTM plume and therefore much larger or not defined at all.

An interesting feature is that directly behind the emission source a more orange spot occurs, meaning that LASAIR here has values between 2 and 5 times larger than ARTM, while shortly afterwards in the dispersion direction the factors go down to yellow and light green again. In the 5 metres resolution this effect appears in the middle symmetrical. The 10 metres resolution result however looks somewhat asymmetrical with this feature.



**Table 5.1** Differences in the results of LASAIR and ARTM at the monitoring points. Here the 20 monitoring points and the source point are listed. The values for the 5m and 10m resolutions show the factors of the ratio LASAIR/ARTM. The deviations arise from the ensemble simulation in ARTM and are the statistical error for each value.

Monitoring Point	5 m Resolution		10 m Resolution	
	mean value	deviation	mean value	deviation
Source Q	1.11	0.02	1.01	0.01
P1	1.45	0.06	1.52	0.05
P2	1.29	0.13	1.29	0.07
P3	1.46	0.15	1.36	0.12
P4	N/A	N/A	1.16	0.11
P5	N/A	N/A	1.24	0.11
P6	N/A	N/A	1.18	0.11
P7	N/A	N/A	1.25	0.14
P8	N/A	N/A	1.24	0.15
P9	13.92	19.56	8.17	3.03
P10	8.88	2.48	10.96	3.31
P11	--	--	--	--
P12	11.19	5.56	9.45	4.32
P13	145.27	99.52	86.11	80.94
P14	--	--	--	--
P15	7.69	6.56	5.61	1.70
P16	N/A	N/A	7.95	3.82
P17	N/A	N/A	821.66	214.87
P18	N/A	N/A	8.47	4.88
P19	N/A	N/A	3.88	1.50
P20	N/A	N/A	498.81	130.21

## 5.2 One single building – building scenario 2

Building scenario 2 is a simple scenario which contains solely one large building with dimensions  $100m \times 100m \times 20m$ . Before applying more and more buildings, the aim here was to study how just one single building can affect the results at the monitoring points and the overall shape of the plume.

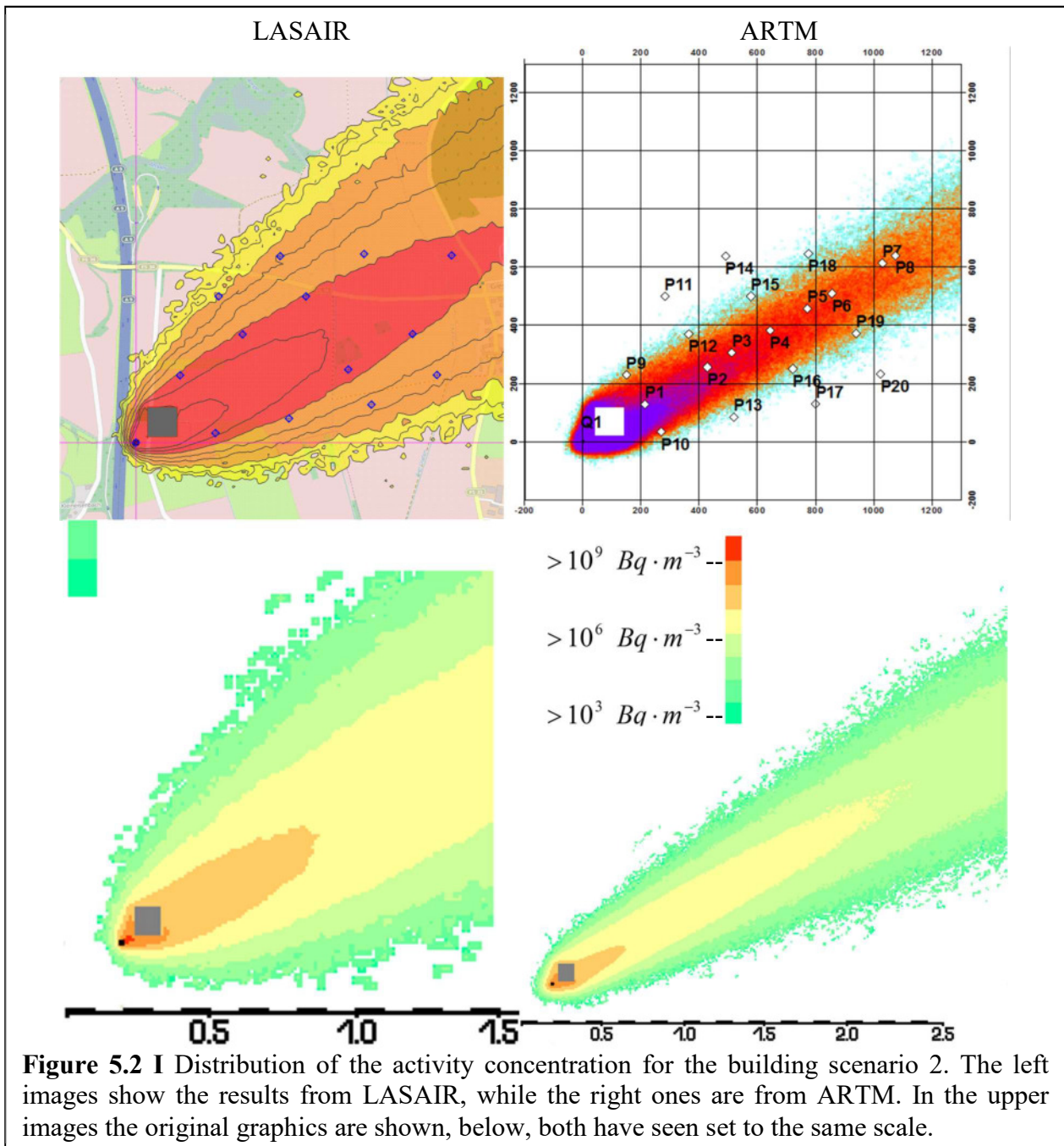
Figure 5.2 I shows the graphical outputs of the simulations for this scenario, the building widens the plume after dividing the main part of the plume and directing them around it. In comparison to the figures 5.1 I, the core of the largest concentration values covers a much smaller area and does not reach much further than the P1 monitoring point.

Figure 5.2 II shows again the factors of how much the values in LASAIR are higher than in ARTM. The building is displayed as a grey square.

Here actually another interesting result came out; figure 5.2 III shows the building area before being greyed-out, and what can be seen is that there is a red frame around the green zero value area. In ARTM the building covers 10 times 10 cells, while in LASAIR it is only 9 by 9, but having 10 metres of grid size in both models. This results from the fact, that LASAIR and ARTM allocate and read out the cells differently. While ARTM calculates the values for the centre of a cell, i.e. the value for 10 metres results from the interval of 0 to 10m, LASAIR takes the range from 5 to 15m.

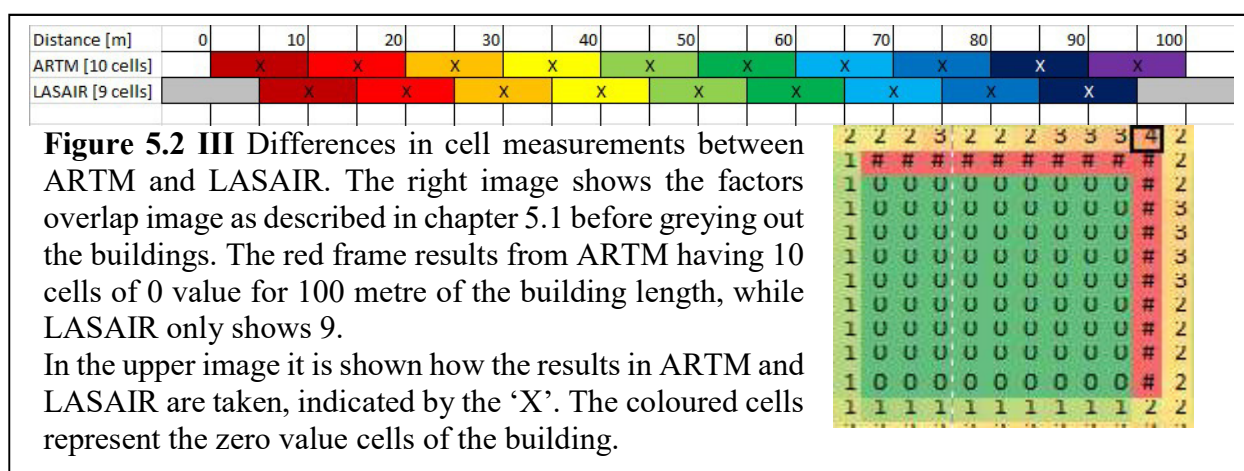
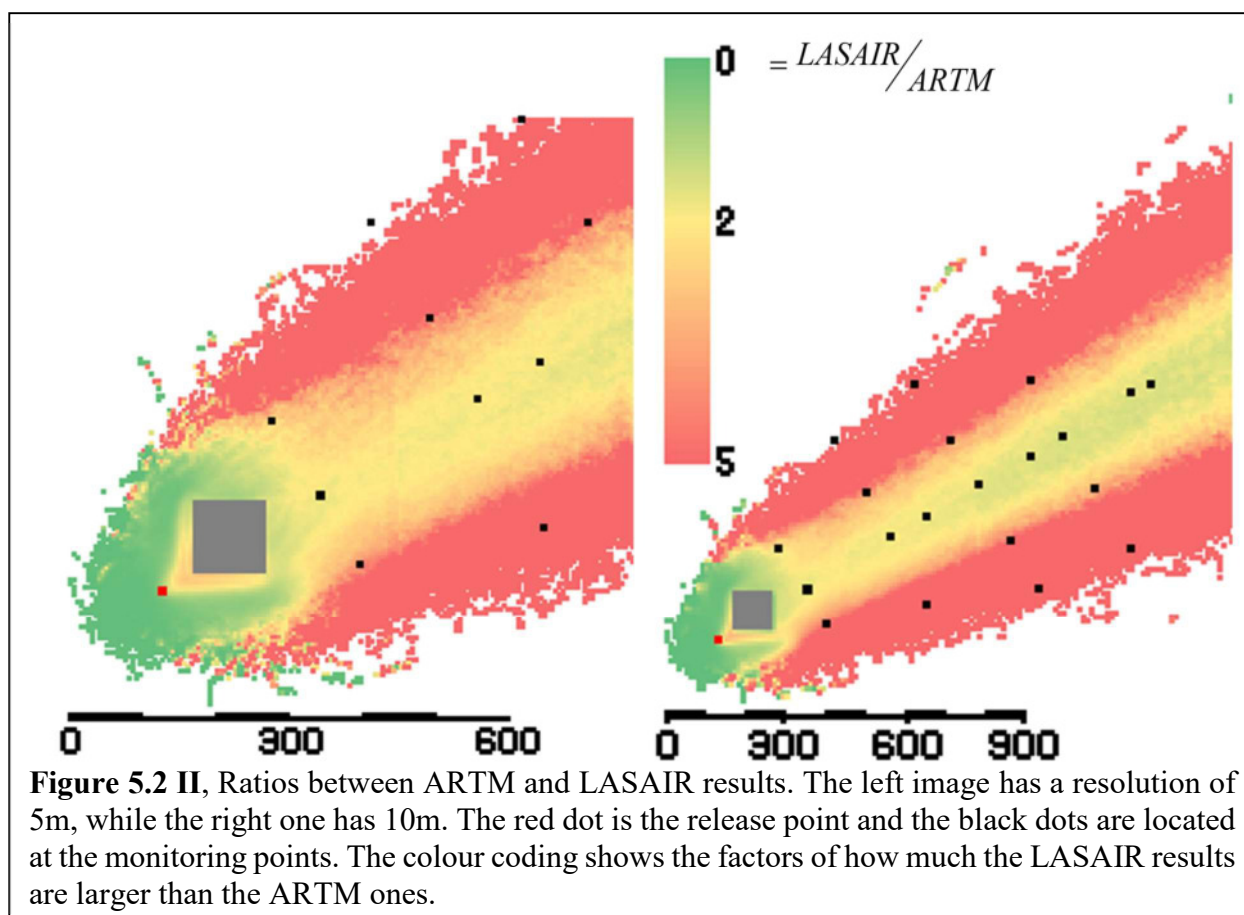


If these results are now compared as done with the ratio graphics, it becomes obvious that here all these graphics have a small spatial inaccuracy of half a grid cell.



**Figure 5.2 I** Distribution of the activity concentration for the building scenario 2. The left images show the results from LASAIR, while the right ones are from ARTM. In the upper part images the original graphics are shown, below, both have been set to the same scale.

From the graphics in figure 5.2 II it can be seen, that on the building front sides, i.e. the two sides that are facing to the source, the LASAIR results were higher than the ARTM ones. The plume in general widens compared to the reference ‘no-building’ case. The lee sides of the building show a better ratio; here the colour spectrum is mostly in the yellow and light green area. Following in plume direction, there is a yellow stream surrounded by red edges. Compared with the reference, there appears to be less in the light green here.



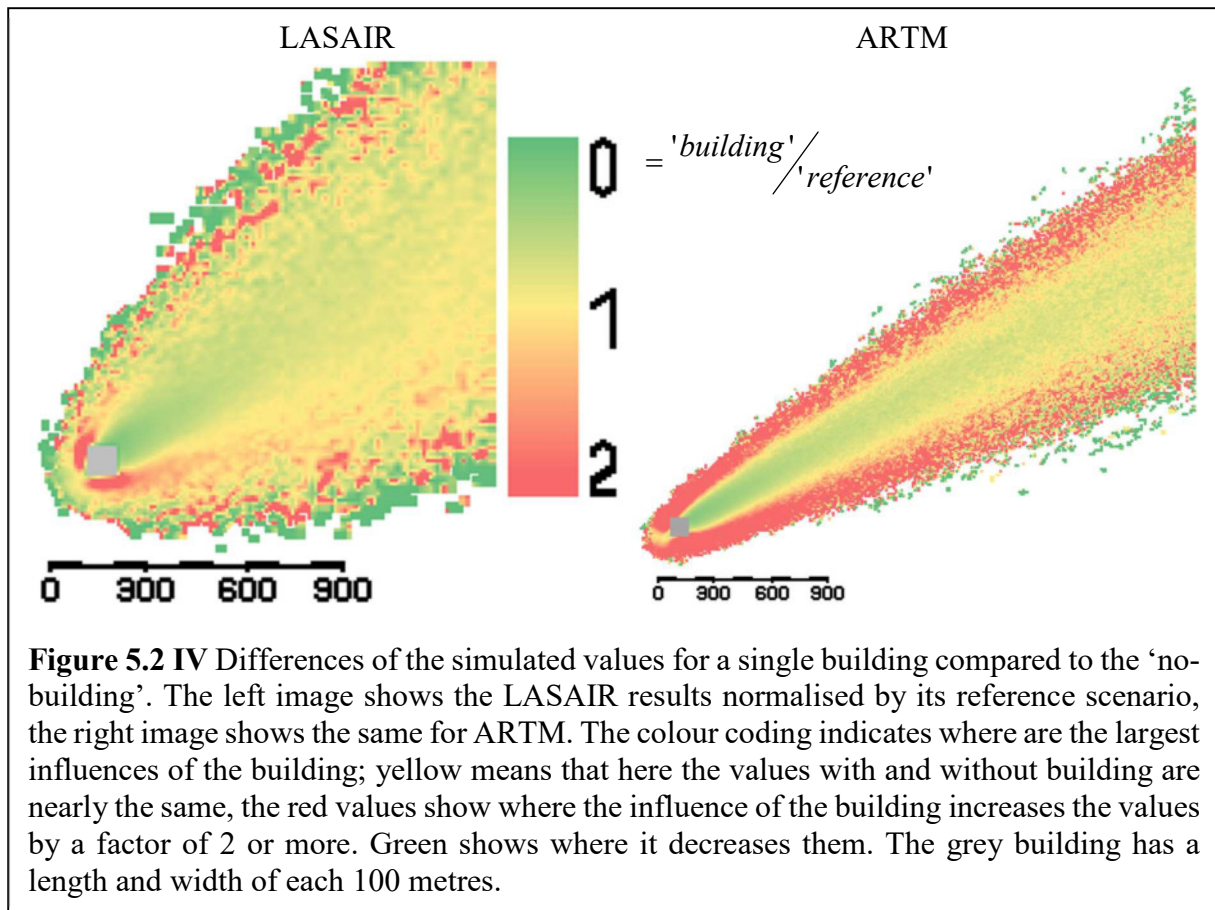
This can also be seen in table 5.2 for the values of the monitoring points in the central plume. Here the values for P1 to P8 are with 1.45 to 1.95 also higher than the ones for the same point in the reference scenario.

Figure 5.2 IV shows now the comparison of the building cases with the non-building reference case. Here the values for the simulation with the building are divided by the reference values and it shows that, for both model the values on the lee-side of the building decrease and on the luv-side increase. It also shows that the building seems to have a higher impact in ARTM than in LASAIR; in ARTM there are less yellow areas near the building than in LASAIR, meaning that here the values show larger variations. Also, in ARTM the plume widens, which can be seen by the larger values to the borders, while for LASAIR it seems like the plume actually gets narrower, as here green values appear at the edges of the plume. It definitely shows that

buildings have an influence in the closest surrounding, i.e. 200 to 300 metres around the building, and in case of ARTM also that even further away ( $> 1$  km) the influence of the building is measurable.

**Table 5.2** Differences in the results of LASAIR and ARTM at the monitoring points. Here the 20 monitoring points and the source point are listed. The values for the 5m and 10m resolutions show the factors of the ratio LASAIR/ARTM. The deviations arise from the ensemble simulation in ARTM and are the statistical error for each value.

Monitoring Point	5 m Resolution		10 m Resolution	
	mean value	deviation	mean value	deviation
Source Q	0.86	0.05	0.80	0.06
P1	1.93	1.44	1.81	1.19
P2	2.02	0.84	1.95	0.80
P3	1.97	0.60	1.91	0.75
P4	N/A	N/A	1.73	0.45
P5	N/A	N/A	1.64	0.43
P6	N/A	N/A	1.45	0.41
P7	N/A	N/A	1.57	0.34
P8	N/A	N/A	1.64	0.36
P9	2.46	1.28	2.06	0.60
P10	3.94	1.06	5.17	1.30
P11	--	--	--	--
P12	5.18	3.32	3.91	1.05
P13	32.88	127.10	28.93	860.49
P14	--	--	74.21	19.37
P15	112.83	29.46	4.31	1.15
P16	5.19	3.54	5.41	2.51
P17	N/A	N/A	138.53	46.75
P18	N/A	N/A	5.13	3.89
P19	N/A	N/A	2.96	0.78
P20	N/A	N/A	39.50	42.17



### 5.3 Building an approximated urban structure – building scenario 3a-d

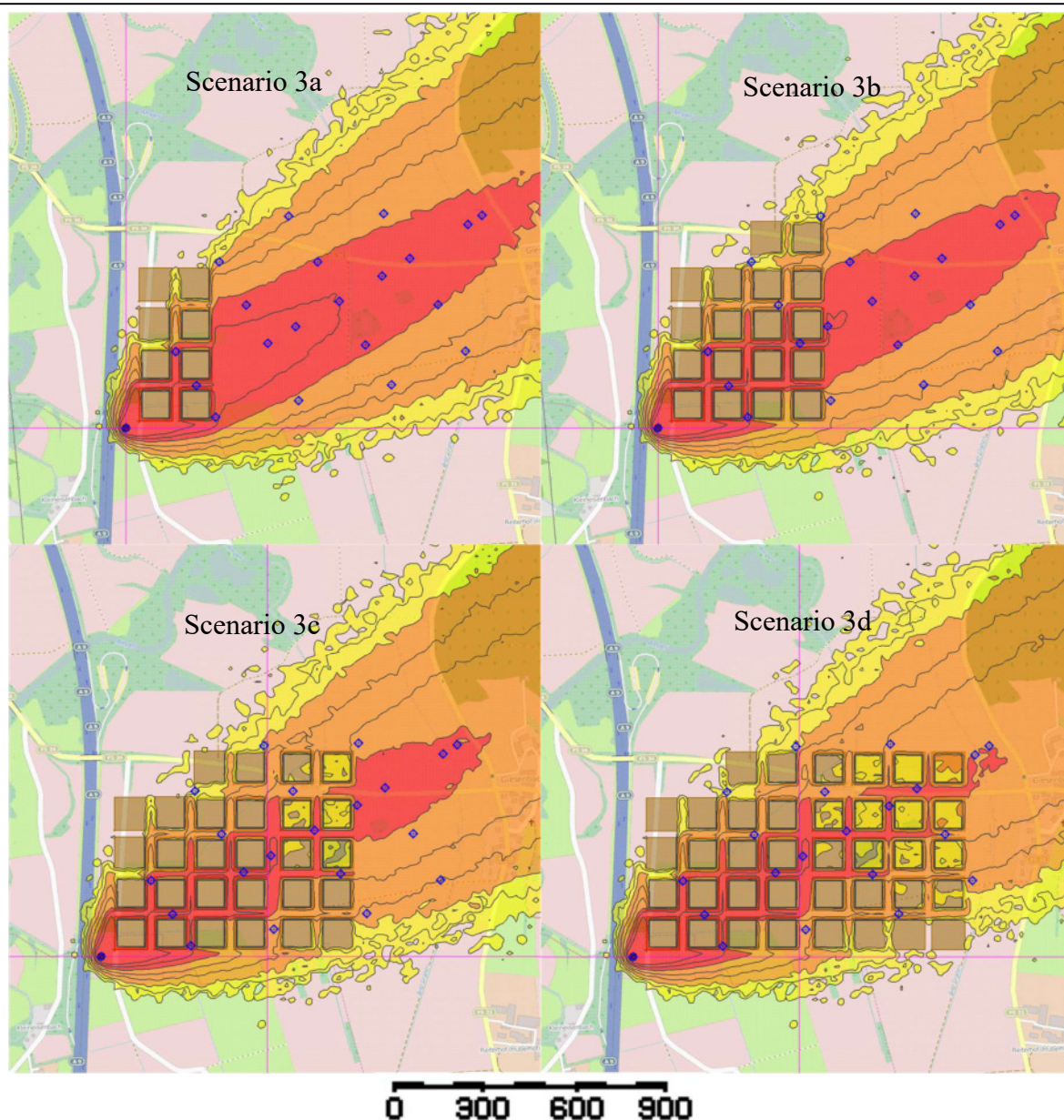
The building scenarios 3a to 3d gradually add more rows of building blocks to see how the concentration values behave. Figure 5.3 Ia shows the LASAIR simulation results for 3a (upper left image) to 3d (lower right image) and figure 5.3 Ib shows the same for ARTM.

The adding of more buildings decreases in both models the concentration values in the further distance as can be seen by the iso-lines in LASAIR and by the purple and red cells in ARTM. The largest amount of the concentration is kept within the street valleys between the building blocks. Here in this scenario the first two rows of buildings trap most of the contaminated air with up to one order of magnitude larger activity concentration values than in-between the last building blocks of scenario 3c and 3d.

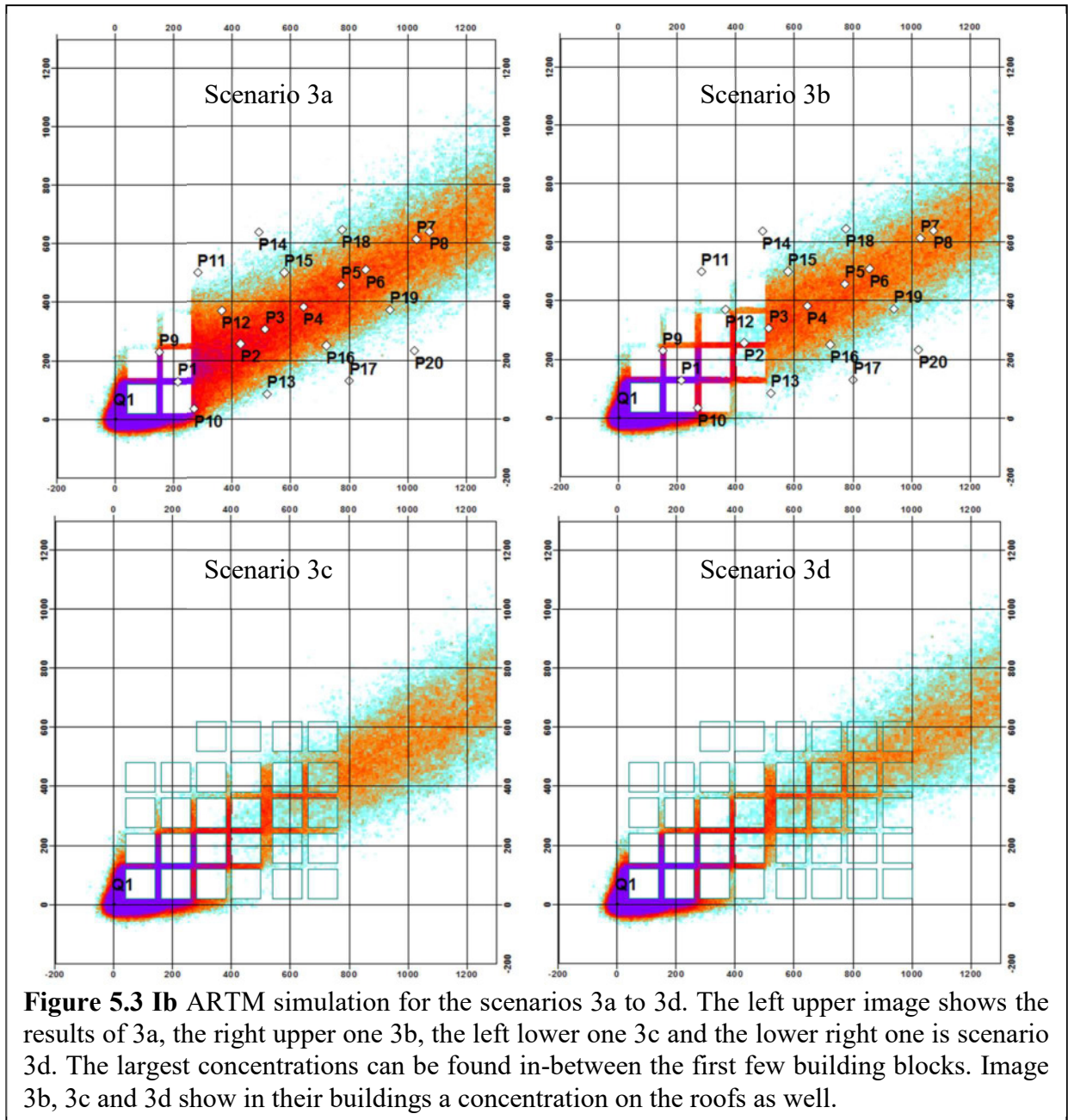
While the emission source with 5 metres height is quite close to the ground and so is the contaminated air mass, the simulations also show that for the down-wind buildings, also the building roofs show some concentrations indicating that here some of the pollutant is mixed up from the streets. This upwards mixing and the turbulence induced by the buildings also play a role in reducing the concentrations in the far.

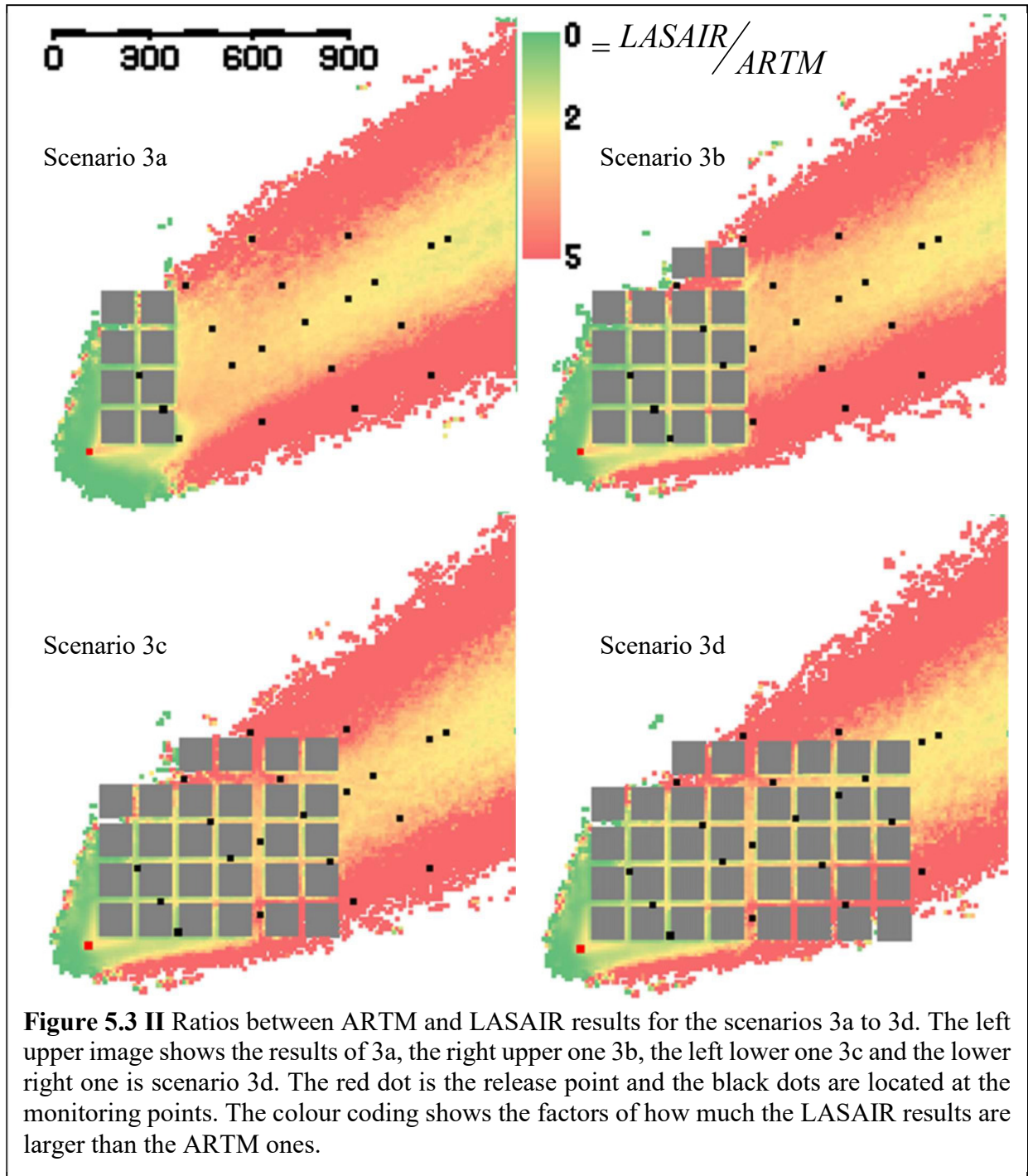
Figure 5.3 II shows again the ratio between the simulation results for LASAIR and ARTM. In all four images it shows that the LASAIR plume is wider than the ARTM one, indicated by the large red border stripes where the ARTM values already decrease, while LASAIR still calculated higher values here. While the differences grow larger with the distance, the values in-between the first two building rows are quite congruent for both models and show light green to values in the ratio indicating that here the values are nearly the same or slightly different. This can be seen also with a look on the values in table 5.3, as there is not a clear trend for the





**Figure 5.3 Ia** LASAIR simulation results for the scenarios 3a to 3d. The left upper image shows the results of 3a, the right upper one 3b, the left lower one 3c and the lower right one is scenario 3d. The largest concentrations can be found in-between the first few building blocks. Image 3c and 3d show in their buildings a concentration on the roofs as well.

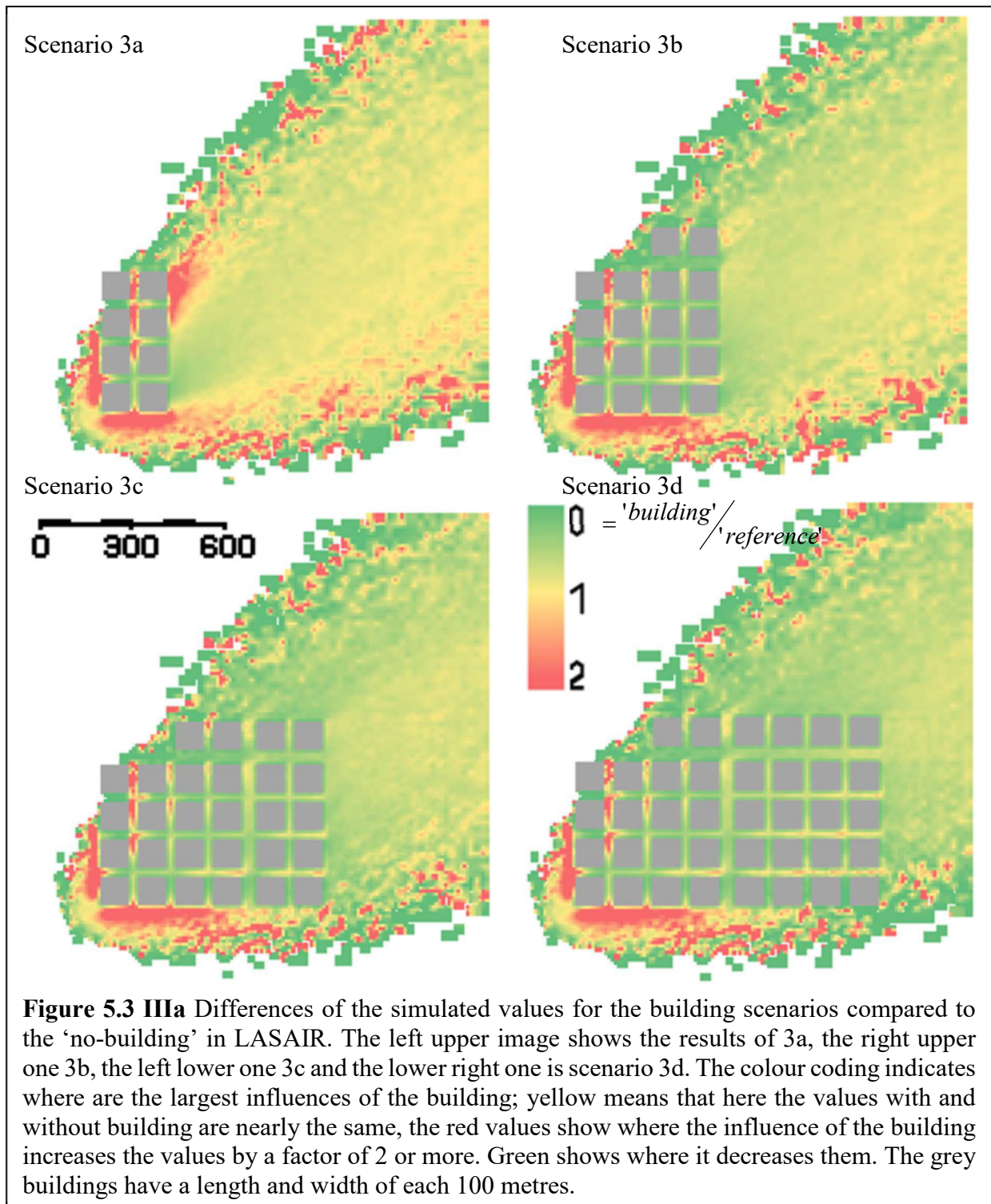


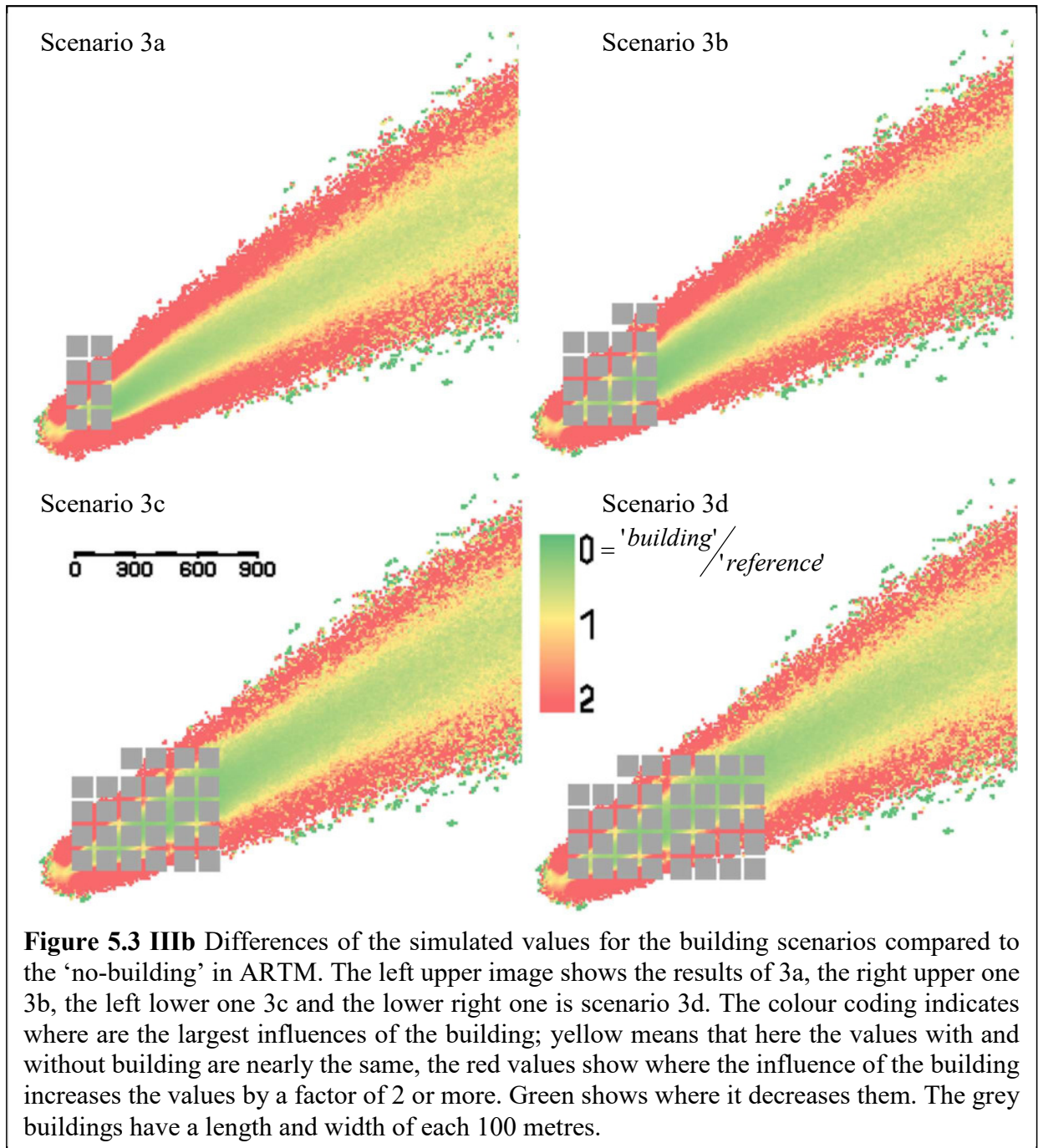




**Table 5.3** Differences in the results of LASAIR and ARTM at the monitoring points. Here the 20 monitoring points and the source point are listed. The values for the scenarios 3a to 3d show the factors of the ratio LASAIR/ARTM. The deviations arise from the ensemble simulation in ARTM and are the statistical error for each value.

Monitoring Point	Scenario 3a		Scenario 3b		Scenario 3c		Scenario 3d	
	mean value	deviation	mean value	deviation	mean value	deviation	mean value	deviation
Source Q	0.84	0.16	0.81	0.01	1.58	0.01	1.58	0.00
P1	1.95	0.46	1.80	0.07	1.74	0.06	1.84	0.00
P2	2.61	0.45	1.30	0.12	1.27	0.21	1.22	0.01
P3	2.52	0.40	3.00	0.37	2.72	0.25	2.72	0.01
P4	2.16	0.48	2.47	0.44	1.31	0.21	1.20	0.04
P5	2.16	0.51	2.53	0.35	2.38	0.41	1.17	0.09
P6	2.01	0.28	2.08	0.38	2.50	0.37	2.15	0.08
P7	1.89	0.44	2.19	0.37	2.56	0.63	2.26	0.13
P8	1.88	0.30	2.14	0.35	2.25	0.41	2.08	0.09
P9	1.67	0.44	1.61	0.13	0.80	0.07	0.83	0.02
P10	1.41	0.09	1.35	0.08	0.59	0.04	0.60	0.00
P11	3.22	4.37	5.15	2.07	40.14	10.45	5.50	367.52
P12	2.43	0.63	1.86	0.66	3.51	1.07	3.07	2.80
P13	7.76	6.97	3.93	2.43	4.43	3.99	4.69	0.16
P14	3.92	10.51	2.05	1.09	6.60	3.39	12.02	271.59
P15	3.60	1.33	3.02	0.64	3.61	1.73	3.74	1.73
P16	3.98	4.37	4.04	1.22	3.56	1.00	3.59	0.01
P17	51.18	35.46	17.81	9.65	22.69	10.35	12.11	0.17
P18	3.60	1.49	4.62	1.46	4.89	3.87	3.49	4.12
P19	3.38	1.76	3.68	1.24	3.53	1.60	1.72	0.03
P20	55.89	45.89	51.65	25.39	13.12	16.38	11.53	0.19





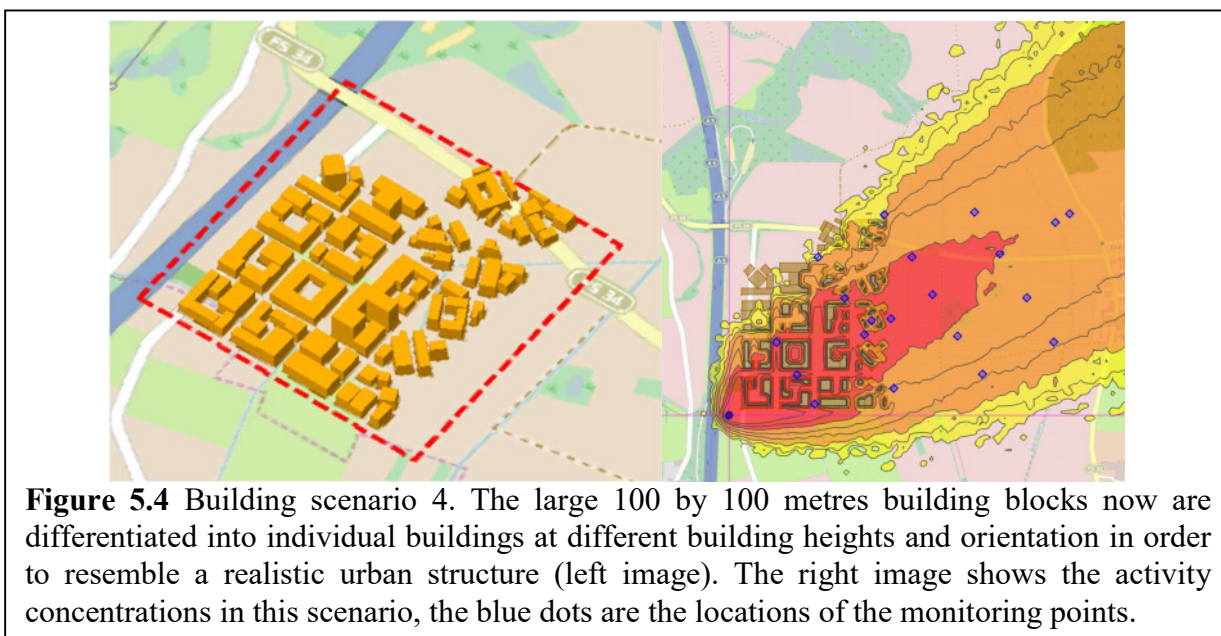
## 5.4 Realistic urban scenario and its approximation – building scenario 4, 3b and 3b-a

The last scenario, building scenario 4, was set-up to resemble a realistic urban building scenario with more differentiated building structures (see figure 5.4) and positions than the 100 by 100 metre square blocks. The altitudes were chosen to be more individual and varying, as they would be in a real city quarter, ranging from 10 metres as it would appear in a more residential area up to 50 metres to simulate office buildings.

This scenario could only be simulated with LASAIR, as in ARTM the complex building structure was not able to be handled properly within the model and produced an error during the simulation.

Therefore the aims of this scenario were to

- a) study how the cloud disperses within a complex urban structure and to
- b) study how well this structure could be approximated by using only rough buildings structures, such as the above named building blocks.



### 5.4.1 Dispersion in complex urban structures

In order to visualise the dispersion, the lowest, in LASAIR possible, temporal resolution of 5 minutes was chosen for the simulation time steps. Figure 5.4.1 shows the first 20 of these 5 minute intervals in a sequence.

In the first four images, resembling the first 20 minutes after the start of the release, the urban structure slowly gets filled with the polluted air. Remarkable here is that some inner courtyards, even near the emission source, stay unpolluted or less polluted than the streets around this building block for up to 15 minutes longer.

Then these courtyards fill up as well with high concentrations of the emitted radionuclide and for the following 40 minutes they contain nearly constant activity concentrations similar to those that can be found in the surrounding street valleys. After 60 minutes, the release has stopped, but for the next 10 minutes the concentrations still remain without any significant decline in the streets or in the courtyards. One time interval further, the streets get blown free of the contaminated air, while now the inner courtyards conserve the polluted air and show in



some cases even more than 30 minutes longer much higher concentration values than in the surrounding streets.

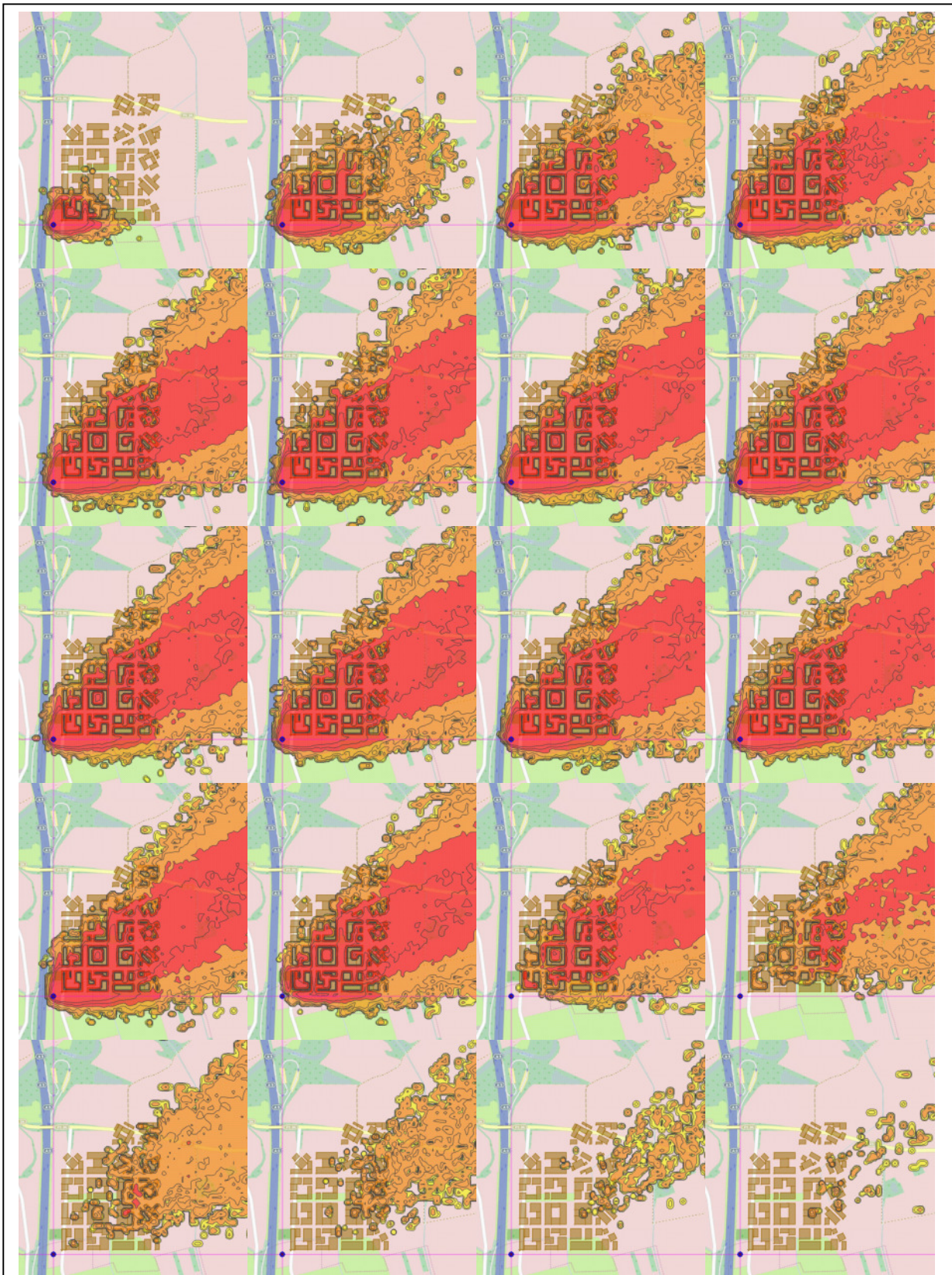


**Figure 5.4.1** LASAIR sequence of 5-minute time intervals. The first 100 minutes of the urban building scenario 4 show, in 5-minute intervals, how the cloud emerges, propagates and disappears again after the emission stopped.

Nevertheless, not all of the courtyards share the above described phenomenon. As it can be seen from closer observations of the images in figure 5.4.1, if the entrances to the yard lie in the luv side, they fill instantaneously with pollutant. If the entrance is not directly towards the wind direction, the concentrations inside depend on the height and location of the building structure within the main plume. One example for a courtyard that fills latest is the one in the building block that is in the third column and the forth row. Here, as visualised in figure 5.4 the luv side of the courtyard is shielded by high office buildings and the only entrance is a small gap on the lee side. It builds an island of relatively low concentration (shown in orange) in the third image of the sequence, while already the surrounding areas are in red, which means have factor 10 and higher concentrations.

In the latter images, this courtyard is on the other side also the one that preserves the high concentrations the longest, while the rest of the structures are already almost clean again.

### 5.4.2 Approximation of complex urban structures

Building structures as complex as the one shown in figure 5.4 are time-intense to develop, even with a graphical tool such as provided in LASAIR.

If the aim of a simulation is just to perform a scientific study, the time used to prepare the exact details of a city suburb is a minor factor. However, the main purpose of LASAIR, as described in chapter 1.2.2, is to provide a quick operational support in case of an emergency. Therefore, a suitable building model needs to be ready and operational within a couple of minutes. This can hardly be done manually by inserting detailed structures, even if all the buildings sizes, positions and heights are known, which in emergency cases will not be the case. So here a reliable approximation for the buildings needs to be found, since, as shown in previous chapters, buildings can have significant influence on the dispersion.

The easiest solution to approximate the scenario 4 would be to raise squared building blocks with dimensions of 100m times 100m and to estimate the average building height, for example to be 20 metres, such as shown in building scenario 3b.

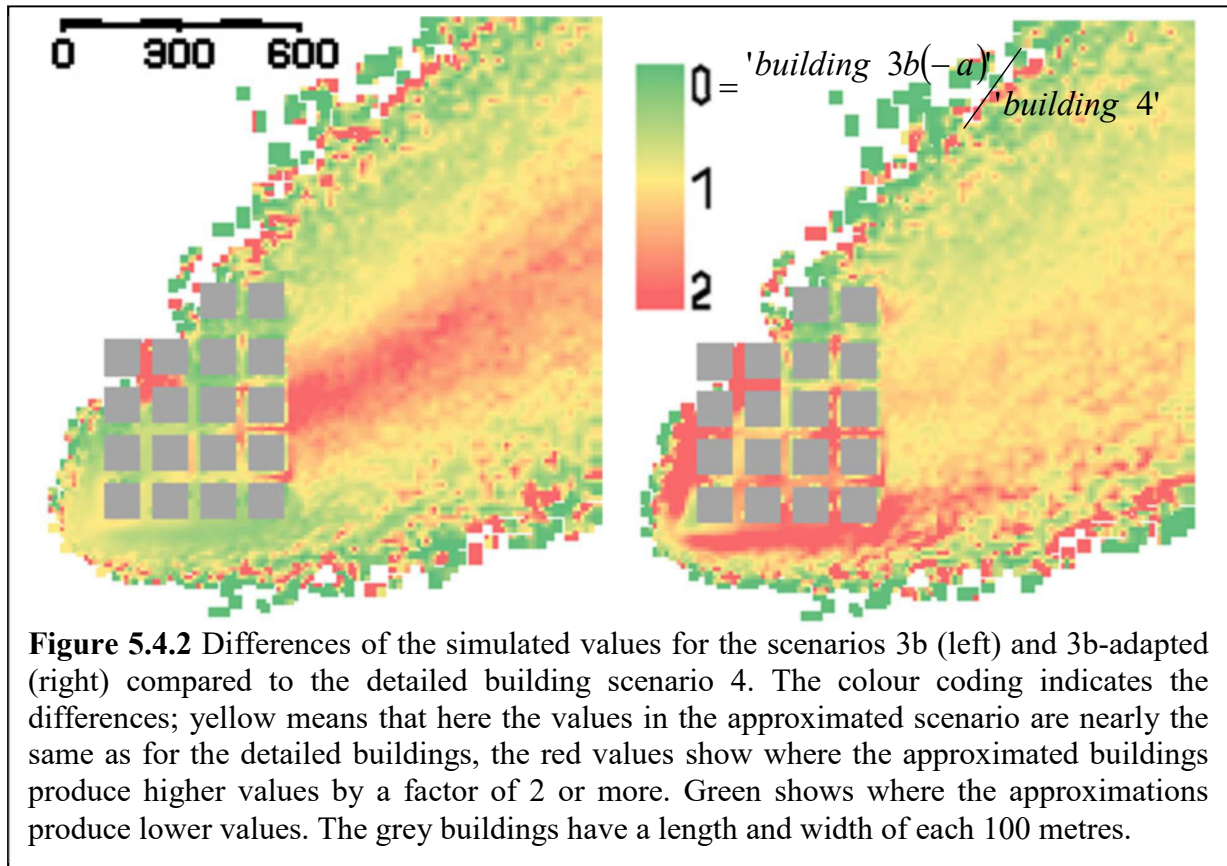
If now the result of this scenario is compared with the result for the detailed scenario 4 as shown in the left image of figure 5.4.2, one can see that in-between the buildings the factor is lower than 1, indicating that the concentration in the approximated case is lower than in the real scenario. Further in the plume direction after the last row of buildings though, the approximated case produced higher values than the detailed scenario leading to factors 2 in difference.

If this approximation would be a sufficient one, most of the area would light up in yellow or maximum orange. In fact, only small areas close to the source and in the trailing plume appear in yellow, while the majority of the plume over-or underestimates the real values.

Now since freely choosing the building heights is not necessarily based on the realistic circumstances, a much more realistic method would be to use the known or estimated building heights for each building block.

This has been done in the scenario 3b-adapted; here the same horizontal building structure as in scenario 3b has been used, but instead of keeping all heights the same, always the height of the largest building in scenario 4 for each building block was chosen (see chapter 1.4.4). The results of this simulation in comparison to the realistic building structure scenario are shown in the right image of figure 5.4.2 and what can be seen here is, that the red area of the previous image does not appear. Instead there is a large area of yellow and slightly orange cells. In-between the buildings, the previously green areas are now in orange or even red, and green areas appear only in the border region of the plume and further away to the north-eastern corner of the shown simulation area.

This means now, that the scenario 3b-adapted, despite not being a perfect match to scenario 4, shows a much better congruency than the scenario 3b. The fact that the green areas between the building blocks became red now is not a good match either from a scientific point of, but has some advantages in operational use of the simulation programme. For these use cases, it is better to have more conservative, i.e. overestimating, predictions rather than underestimating ones. At the same time the evacuation areas need to be kept as small as possible and as large as necessary. In case 3b some of the green areas might not be evacuated if only the values are seen, but instead some of the red ones, when in fact it should be the other way round. Therefore, more yellow and orange areas are favourable to green areas.



## 5.5 Conclusion of the urban building scenario

The difficulty to properly compare ARTM and LASAIR results is the fact that both models count the cells in a different way, leaving only half a grid cell in x-direction and half a grid cell in y-direction, i.e. only one quarter cell, in overlap. This can lead to some of the differences between the two models, yet the images reveal a rather homogeneous distribution with little to no differences between two neighbouring cells in the central plume area.

Also what comes out in some of the images is that obviously ARTM reacts more sensitive to buildings in some cases, compared to LASAIR, while for complex building structures LASAIR provides more stable simulations, and some cases, such as the scenario 4 cannot even be handled in ARTM.

To summarise the main results of this urban building scenario:

- 1) Despite being based on the same mathematical algorithm (see appendix A) the two models ARTM and LASAIR produce different results for the same input parameters,



even more if there are additionally buildings involved. In this building scenario it is shown that LASAIR results in the central area of the plume are between 1.2 to 3 times larger than the corresponding ARTM results, and also the plume tends to be wider in LASAIR than in ARTM. Which ones are more accurate cannot be determined without conducting a measurement campaign to obtain real data to compare the simulation results.

- 2) The time sequence of the LASAIR simulation for the detailed building case reveals how the urban structures fill and empty with contaminated air. This can help for decision making and giving better advice to the population in areas affected by a release accident.
- 3) For the modelling in time-critical situations, an approximation of the building structures might be faster than inserting detailed structures. Here the correct height of the building blocks is the most important parameter to generate a good prediction.

Of course, there are still many more things to study concerning these scenarios and to improve the results, for example in providing proper approximations. Most of all, a measurement campaign in an urban area, or in a mock-up would be helpful to determine how well both models are doing with their simulation results.

## 6. Conclusion

The main goal of this work was to verify and validate the atmospheric dispersion model ARTM using fictive and real emission scenarios.

For the verification of the ARTM algorithms, a sensitivity study was conducted to examine the behaviour of the simulation results in dependency of the input parameter.

Here it turns out that ARTM in large parts behaves as theoretically to expect. The results of the simulations with changing external input parameters are all plausible and can be explained with the underlying mathematical and physical model.

The only two exceptions found were with the starting random numbers and the error reduction with the increase in particle amount.

For the starting random numbers the differences between different choices sometimes appear overly large and create a high standard deviation. This phenomenon has been observed not only in the sensitivity analysis, but also in pre-cursor simulations to the simulations on Šoštanj. Since it appears in short-term as well as in long-term simulations, it suggests to be a general issue rather than scenario-specific. Since the impacts of this can be almost extinguished by increasing the amount of simulations and creating an average or by simple rising the particle amount of the simulation, further investigations on this might not have a high priority.

On the contrary is the reduction of the statistical error. Here the expected values of error reduction as given in the programme handbook could not be entirely reached. While for the first three duplications of the initial particle amount the error reduction is in the range of the theoretical value, if the standard deviation is considered, the last stage of increasing the particle amount does not result in the almost 94% of error reduction as the theory suggests. This result was gained from both, short-term and long-term simulation of the two entirely different scenarios La Hague and Neckarwestheim, suggesting that here the programme does not perform according to the mathematical background. In order to better understand this effect, it is therefore recommended to conduct a more detailed and extensive study here and to assess proper methods to investigate the cause of this deviation.

The main result of the sensitivity analysis was the evaluation of different input parameters, external and internal ones, on the simulation results. Here it was found that the external ones make the largest impact on the simulation results and especially the dispersion category can make or break a simulation. At the same time this is also the most difficult parameter to properly determine. Several different methods exist and can lead to entirely different classifications greatly impacting the simulation result.

The internal parameters have a smaller effect than the external ones in comparison, but here the user can freely choose which parameter he takes. So the deviation is not due to measurement errors of input data, but also of the user choice. The principle is to minimise the known error sources, which in case of user defined parameters such as starting random number or particle quality can be pretty much extinguished by chosen the highest particle quality and conducting an ensemble of simulations.

The choice of the grid size is another issue, as it partially is connected with the scenario conditions and the pre-defined orography. The observed difference in values for different grid sizes seems logical, as ARTM always integrates over the particles in each grid cell. However, this effect so far has only been studied in short-term dispersion simulations here. Further investigations can possibly rule out this issue for long-term simulations, or better determine the effects that lead to high deviations with the aim to minimise them for future short-term simulations.

The validation of ARTM was performed using the La Hague and the Šoštanj scenario. The data obtained from these two data sets were used to run the simulation in ARTM and to compare the

results with the actual measurement results. It shows that despite some situations being well projected in the simulation, these two scenarios bear specific thermal effects such as land wind – sea wind systems or mountain-valley wind systems which cannot be handled by the current version of ARTM (see appendix B.1).

A proper data set from a suitable measurement campaign, preferably a more long term study, would help a lot to improve and extend the validation of ARTM for various locations and situations.

It was also shown that buildings have an influence on the dispersion simulation. Results have been different with the involvement of nearby facility buildings or urban structures than simulating the same situation without them. However, some cases as the realistic building scenario 4 or the Šoštanj case 2 do not work to be simulated with buildings yet, as here the programme creates an error. So there is some development from the programming side recommended to produce a more stable building involvement as it is the case for the LASAIR software, which was used as a comparison to ARTM. Also, further studies on the building influence in ARTM can help to better quantify the effects occurring and probably to give an estimation for the amount and distance of buildings to the source that are necessary to provide reasonably correct simulation results.

What was also shown here in this study, that ARTM and LASAIR both have very specific designs that serve their specific purposes; ARTM as a regulatory long term simulation software and LASAIR as a short term decision making support tool for emergencies have different applicability. Therefore, not all data sets can be used in both programmes as shown for the Šoštanj scenario, which was border-lining the applicability of LASAIR. Both programmes possess their limitations and this study has shown where some of them are settled, where and where not each of the programmes can be used and how it can be done.

When compared with real measurement data in the Šoštanj scenario, both programmes produced nearly equally good or equally bad conformity.

New insights were gained during the direct comparison of both simulation softwares during the urban building scenario. Here it seems that LASAIR produces different and mostly larger values than ARTM, despite both being based on the same mathematical algorithm.

Another interesting fact was shown already during the sensitivity analysis with ARTM and also during the urban building scenario 4 in LASAIR; not the 2-dimensional extension of the source or the buildings make the great difference in the simulation results, but it is the source height and building heights. So if running a simulation the lateral extension can be estimated roughly as long as the heights are inserted correctly. Here it shows that a city suburb can be well represented by building blocks, if these are inserted into the simulation with the according building heights.

This study has dug deep into the applicability of the two dispersion models and especially ARTM has been studied in its performance in detail. Here it was found that while the model can already represent a lot of situations, there is still room for further improvements on the modelling side, such as making the algorithm more applicable in complex terrain. Mountainous regions like in the Šoštanj scenario still can cause error due to too steep inclines in the altitudes. Also thermal effects like mentioned above and complex building structures are not yet properly included in ARTM and should be included to extend the applicability of the model.

Although this work could answer some of the questions and backgrounds of the model, there is still more work to be done to investigate in detail certain aspects and scenarios handled throughout this work.

A big surplus for a better validation of ARTM would be the application of more data sets including measurement data to use for comparison with the simulation results. As there are not many long-term measurement campaign data available, which actually would be useful for validation purposes, it is suggested to plan and prepare such a measurement campaign in a suitable location specific for the validation of long-term dispersion models such as ARTM.

## 7. References

Arakawa, A.; Lamb, V.R., 1977, *Computational design of the basic dynamical processes of the UCLA general circulation model*, Methods of Computational Physics 17, New York: Academic Press, pp. 173–265.

AUSTAL2000, 2002-2016, AUSTAL2000 programme homepage, <http://www.austal2000.de/de/home.html> (viewed 12<sup>th</sup> April 2016).

AVV, 2012, *Allgemeine Verwaltungsvorschrift zu § 47 der Strahlenschutzverordnung (Ermittlung der Strahlenexposition durch die Ableitung radioaktiver Stoffe aus Anlagen oder Einrichtungen)*, BAnz AT 05.09.2012 B1. (German only)

Berliner Wetterkarte, 2009a, *Jahrgang 58 Nummer 40 (year 58 No.40)*, Berliner Wetterkarte e.V., ISSN 0177-3984. (German only)

Berliner Wetterkarte, 2009b, *Jahrgang 58 Nummer 41 (year 58 No.41)*, Berliner Wetterkarte e.V., ISSN 0177-3984. (German only)

BfS (Bundesamt für Strahlenschutz), 2016, *Nuclear Safety – legal bases*, BfS-homepage: [www.bfs.de/EN/topics/ns/safety/law/law.html](http://www.bfs.de/EN/topics/ns/safety/law/law.html), retrieved: 10<sup>th</sup> January 2017.

Bossard, M., Feranc, J., Otahel, J., 2000, *CORINE land cover technical guide – Addendum 2000*, European Environmental Agency, Copenhagen, 2000.

BMU (Bundesministerium für Umwelt, Naturschutz und Reaktorsicherheit), 2002, *Erste Allgemeine Verwaltungsvorschrift zum Bundes-Immissionsschutzgesetz (Technische Anleitung zur Reinhaltung der Luft – TA Luft)*, Gemeinsames Ministerialblatt 2002, Vol. 25-29, pp. 511-605, Carl Heymanns Verlag KG, Cologne, 2002-07-24. (German only)

BMU (Bundesministerium für Umwelt, Naturschutz und Reaktorsicherheit, Germany), 2010, *Umweltradioaktivität und Strahlenbelastung – Jahresbericht 2009*. (mainly in German)

BMU (Bundesministerium für Umwelt, Naturschutz, Bau und Reaktorsicherheit, Germany), 2014, *Bekanntmachung einer Empfehlung der Strahlenschutzkommission (Ermittlung der Strahlenexposition vom 12. September 2013)*, BMUB-RSII2-17027/2. (German only)

BMWFJ (Bundesministerium für Wirtschaft, Familie und Jugend, Austria), 2010, *Technische Grundlage zur Berechnung und Beurteilung von Immissionen im Nahbereich kleiner Quellen (Technische Grundlage Ausbreitungsrechnung)*, [www.bmwfj.gv.at](http://www.bmwfj.gv.at), viewed: 20<sup>th</sup> December 2016. (German only)

Brugger, R.M., 1969, *A Note on Unbiased Estimation of the Standard Deviation*, The American Statistician (23) 4 p. 32, DOI:10.1080/00031305.1969.10481865.

Buchroithner, M. F., Pfahlbusch, R., 2016, *Geodetic grids in authoritative maps–new findings about the origin of the UTM Grid*, Cartography and Geographic Information Science.

Connan, O., Smith, K., Organo, C., Solier, L., Maro, D., Hebert, D., 2013, *Comparison of RIMPUFF, HYSPLIT, ADMS atmospheric dispersion model outputs, using emergency*

*response procedures, with <sup>85</sup>Kr measurements made in the vicinity of a nuclear reprocessing plant*, Journal of Environmental Radioactivity 124, 266-277.

DIN EN ISO 9000, 2015, *Qualitätsmanagementsysteme – Grundlagen und Begriffe (ISO 9000:2015)*, edition of November 2015.

Eckert, M., 2006, *The Dawn of Fluid Dynamics: A Discipline Between Science and Technology*, John Wiley & Sons, 2006, ISBN 3527405135.

Elisei, G., Bistacche, S., Bocchiola, G., Brusasca, G., Macarri, P., Marzorati, A., Morseli, M.G., Tinarelli, G., Catenacci, G., Coris, V., Paina, G., Era, A., Finardi, S., Foggi, G., Nagri, A., Piazza, G., Villa, R., Lesjak, M., Božnar, M.Z., Mlakar, P., Slavic F., 1992, *Experimental Campaign for the Environmental Impact Evaluation of Šoštanj Thermal Power Plant – Progress Report*, ENEL, C.I.S.E. Tecnologie innovative, Josef Stephan Institute Ljubljana.

GRS, 2015, *History-Datei zu GO-ARTM / ARTM / TALDIA*, included in the ARTM programme package, <https://www.bfs.de/SharedDocs/Downloads/BfS/DE/fachinfo/ion/artm-download.html>, viewed on 12<sup>th</sup> April 2016. (German only)

Grašič, B., Božnar, M.Z, Mlakar, P., 2007, *Re-evaluation of the Lagrangian particle modelling system on an experimental campaign in complex terrain*, Il Nuovo Cimento, Vol. 30, No. 6, DOI 10.1393/ncc/i2007-10257-3.

Hanna, S.R., 1982, *Turbulent Diffusion: Chimneys and cooling towers*, Engineering meteorology, E. Plate (editor), Elsevier Scientific Publishing Company, ISBN 0-444-41972-1.

IAEA, 2017 (expected), *MODARIA - Report of Working Group 2 - 'Assessment of Radioactive Contamination and Effectiveness of Remedial Measures in Urban Environments'*, in preparation for publication.

Janicke Consulting, 2001-2013, *LASAIR Version 4.0.4 (2013-08-17)*, Programme-internal documentation.

Janicke Consulting, 2008, *Dispersion Model LASAT Reference Book for Version 3.0*.

Janicke Consulting, 2011, *AUSTAL2000 Program Documentation of Version 2.5*, ibj: austal2000/2.5/doc/austal2000 — 2011-08-01.

Janicke Consulting, 2014, *AUSTAL2000 Program Documentation of Version 2.6*, ibj: austal2000/2.6/doc/austal2000 — 2014-06-26.

Janicke, U., Janicke, L., 2007, *Lagrangian particle modeling for regulatory purposes; A survey of recent developments in Germany*, Proceedings of the 11th International Conference on Harmonisation within Atmospheric Dispersion Modelling for Regulatory Purposes, Cambridge, England, view [http://www.harmonio.org/Conferences/Proceedings/\\_Cambridge/Cambridge\\_proceedings.asp](http://www.harmonio.org/Conferences/Proceedings/_Cambridge/Cambridge_proceedings.asp) (viewed 22<sup>nd</sup> June 2016)

Jensen, N.O. & Busch, N.E, 1982, *Atmospheric Turbulence*, E. Plate (editor), Elsevier Scientific Publishing Company, ISBN 0-444-41972-1.

KTA (Kerntechnischer Ausschuss), 2006, *KTA 1508 – Bekanntmachung von sicherheitstechnischen Regeln des Kerntechnischen Ausschusses – Instrumentierung zur Ermittlung der Ausbreitung radioaktiver Stoffe in der Atmosphäre*, Bundes-Anzeiger BAnz Nr. 245b S. 5 (German only).

LfU (Bayerisches Landesamt für Umwelt), 2016, *Strahlenhygienischer Jahresbericht 2015 – Allgemeine Umweltradioaktivität und Umgebungsüberwachung der kerntechnischen Anlagen in Bayern*, Bayerisches Landesamt für Umwelt (German only).

Lochte, A., 2011, *Ausbreitungsrechnungen für luftgetragene radioaktive Stoffe mittels eines Lagrange-Partikelmodells – Einfluss des Verfahrens zur Bestimmung der Diffusionskategorie auf die Modellprognose*, Master Thesis, University of Rostock, ZQS – Fernstudium Umweltschutz. (German only)

Lutman, E.R., Jones, S.R., Hill, R.A., McDonald, P., Lambers, B., 2004, *Comparison between the prediction of a Gaussian plume model and a Lagrangian particle dispersion model for annual average calculations of long-range dispersion of radionuclides*, Journal of Environmental Radioactivity 75 (2004) 339-355, DOI: 10.1016/j.jenvrad.2003.11.013.

Martens, R., Janicke, L., Thielen, H., 2007, *Entwicklung, Validierung und Bereitstellung eines atmosphärischen Ausbreitungsmodells für luftgetragene radioaktive Stoffe auf der Basis des Ausbreitungsmodells AUSTAL2000 der neuen TA Luft*, Gesellschaft für Anlagen- und Reaktorsicherheit (GRS) mbH, GRS-A-3386. (German only)

Mayall, A., 2003, *Modelling the dispersion of radionuclides in the atmosphere*, Modelling radioactivity in the environment, Volume 4, E. Marian Scott (Editor), Elsevier Science 2003, ISBN 9780080436630.

Mlakar, P., Božnar, M.Z., Grašič, B., Brusasca, G., Tinarelli, G., Finardi, S., 2015, *Air pollution dispersion models validation dataset from complex terrain in Šoštanj*, International Journal of Environment and Pollution, ISSN 0957-4352 (in press).

Panofsky, H.A., 1982, *The Atmosphere*, Engineering meteorology, E. Plate (editor), Elsevier Scientific Publishing Company, ISBN 0-444-41972-1.

Richter, C., Sogalla, M., Thielen, H., Martens, R., 2013a, *Atmosphärisches Radionuklid-Transport-Modell mit Radon Postprozessor und SBG-Modul Modellbeschreibung zu Version 2.7.2*, Gesellschaft für Anlagen- und Reaktorsicherheit, 2013-11-25. (German only)

Richter, C., Sogalla, M., Thielen, H., Martens, R., 2013b, *Atmosphärisches Radionuklid-Transport-Modell mit der graphischen Benutzeroberfläche GO-ARTM Programmbeschreibung zu Version 2.7.2 (GO-ARTM Version 2.0)*, Gesellschaft für Anlagen- und Reaktorsicherheit, 2013-12-16. (German only)

Richter, C., Thielen, H., Sogalla, M., 2015, *Ergänzende Untersuchungen zur Validierung des Atmosphärischen Radionuklid-Transport-Modells (ARTM)*, Gesellschaft für Anlagen- und Reaktorsicherheit, GRS-A-3809. (German Only)

Rödel, W., 1992, *Physik unserer Umwelt – Die Atmosphäre*, Springer-Verlag Berlin Heidelberg, ISBN 3-540-54285-X.



Rotach, M.W., 2001, *Simulation of urban-scale dispersion using a Lagrangian stochastic dispersion model*, Boundary-Layer meteorology 99, 379-400,2001.

Seidel, H., 2006, *Die Mathematik der Gauß-Krüger-Abbildung*, <http://henrik-seidel.gmxhome.de/gausskrueger.pdf> (viewed 3<sup>rd</sup> October 2016). (German only)

SSK (Strahlenschutzkommission), 1995a, *Veröffentlichungen der Strahlenschutzkommission – Band 13 – Leitfaden für den Fachberater Strahlenschutz der Katastrophenschutzleitung bei kerntechnischen Notfällen*, 2. Überarbeitete Ausgabe, Gustav Fischer Verlag, ISBN 3-437-11639-8.

StrlSchV (Strahlenschutzverordnung), 2001, *Verordnung über den Schutz vor Schäden durch ionisierende Strahlen*, Version of 20<sup>th</sup> July 2001, last edits done on 26<sup>th</sup> July 2016.

Vapnyarskii, I.B., 2001, *Lagrange multipliers*, in Hazewinkel, Michiel, *Encyclopaedia of Mathematics*, Springer, ISBN 978-1-55608-010-4.

VDI 3782 Part 3, 1985, *Dispersion of Air Pollutants in the Atmosphere – Determination of Plume Rise*, VDI-Richtlinien, VDI-Verlag, Düsseldorf 1985.

VDI 3783 Part 8, 2002, *Environmental meteorology – Turbulence parameters for dispersion models supported by measurement data*, VDI-Richtlinien, VDI-Verlag, Düsseldorf 2002.

VDI 3945 Part 3, 2000, *Environmental meteorology – Atmospheric dispersion models – Particle model*, VDI-Richtlinien, VDI-Verlag, Düsseldorf 2000.

Vogl, K., 1994, *Aerosol particle losses in the sampling tubes of nuclear facilities: assessment and experimental determination*, Journal of Aerosol Science, Volume 25, Suppl. 1, pp. S265-S266.

Walter, H., Heinrich, G., 2016, *Effects from urban structures to atmospheric dispersion models in decision support systems for nuclear emergencies*, Proceedings of the 17<sup>th</sup> International Conference on Harmonisation within Atmospheric Dispersion Modelling for Regulatory Purposes 9-12 May 2016, pp.593-597.

# APPENDIX

## A. Wind Field Models

### A.1 TALdia

The following descriptions and information about TALdia were taken from the Program Documentation of AUSTAL2000 versions 2.5 and 2.6 by Janicke Consulting (2011 & 2014) and the model description and final report of the ARTM research project [Richter et al., 2013a; Richter et al., 2015]. They summarise the calculation process of the wind field with TALdia. More detailed information can be directly viewed in the above mentioned documents.

TALdia is a diagnostic wind field model based on the Technical Instructions on Air Quality Control (TA Luft) [Janicke Consulting, 2011; 2014]. It calculates divergence-free wind fields and creates a library for all different meteorological situations using the information on orography, land use and buildings [Janicke Consulting, 2011; 2014].

This is performed by

- creating a nearly homogeneous incoming wind field for the simulation area,
- adjusting the wind field to the orography, if orography is provided, by taking into consideration the stability and calculating it to be divergence free,
- considering the logarithmical parts of wind profile of a Prandtl-layer,
- and calculating the field divergence free again to receive the diagnostic wind field [Janicke Consulting, 2011; 2014].

If there are no buildings involved, the wind field calculation process ends here, otherwise the calculation now continues with

- cutting out the volume of the buildings, mapped as raster cells, from the wind field,
- adjusting the boundary conditions to prevent singularities,
- placing recirculation zones on the lee side of the buildings,
- and finally performing another calculation to ensure the wind field is free of any divergences [Janicke Consulting, 2011; 2014].

TALdia undergoes certain limitations, which, if not considered, can cause an abortion of the wind field calculation. One is the limitation of vertical wind speed components larger than  $50\text{ m/s}$  which can occur during the wind field calculation [Janicke Consulting, 2011; 2014]. A second one is directly linked to the input meteorology; if values below  $0.5\text{ m/s}$  for the horizontal wind speeds occur, TALdia cannot handle them [Janicke Consulting, 2011; 2014].

This issue is solved by ARTM through a pre-processing of the input meteorological data [Richter et al., 2013a; Richter et al., 2015]. It ensures that always the minimum wind speed of  $0.5\text{ m/s}$  is applied by changing smaller values accordingly [Richter et al., 2013a; Richter et al., 2015]. If a calm occurs for a short time period of 1 to 2 hours, the wind direction will be determined via interpolation of the wind directions before and after the calm [Richter et al., 2013a; Richter et al., 2015]. For calm periods longer than that, the wind directions will be assigned randomly according to a standard distribution for low wind speeds [Richter et al., 2013a; Richter et al., 2015].

## Mathematical Background

First of all the orographical altitudes have to be defined in Cartesian coordinates which results in (A.1 i) [Janicke Consulting, 2011; 2014].

$$z = b(x, y) \quad (\text{A.1 i})$$

The distance from the ground is given with  $h$  in dependency of  $z$  and  $b$  [Janicke Consulting, 2011; 2014].

$$h = z - b \quad (\text{A.1 ii})$$

The calculation area is limited by (A.1 iii), where the vertical component  $z$  is substituted with  $s$  [Janicke Consulting, 2011; 2014].

$$z = \hat{z} \quad (\text{A.1 iii})$$

This coordinate  $s$  is proportional to  $h$  which leads to (A.1 iv) and (A.1 v) [Janicke Consulting, 2011; 2014].

$$s = \hat{s} \frac{z - b(x, y)}{\hat{z} - b(x, y)} \quad (\text{A.1 iv})$$

$$z = b(x, y) + \frac{s}{\hat{s}} [\hat{z} - b(x, y)] \quad (\text{A.1 v})$$

Since TALdia only processes the special cases where  $\hat{z}$  and  $\hat{s}$  go towards  $\infty$ , the ratio between them goes towards 1, and so follows that  $s \equiv h$  [Janicke Consulting, 2011; 2014].

The grid cells are structured according to an Arakawa-C grid [Janicke Consulting, 2011; 2014]. Figure A.1 I shows a graphical sketch of this grid, and the distribution of the variables over that grid [Arakawa & Lamb, 1977].  $u$  and  $v$  are the wind speed components in  $x$  and  $y$  direction, while  $h$  here is for the height of the grid layer, indicating a 3-dimensional purpose of the model [Arakawa & Lamb, 1977].

For a fluid passing through this grid, the individual change with time can be generally given by (A.1 vi) [Arakawa & Lamb, 1977].

$$\frac{d}{dt} \equiv \frac{\partial}{\partial t} + u \frac{\partial}{\partial x} + v \frac{\partial}{\partial y} \quad (\text{A.1 vi})$$

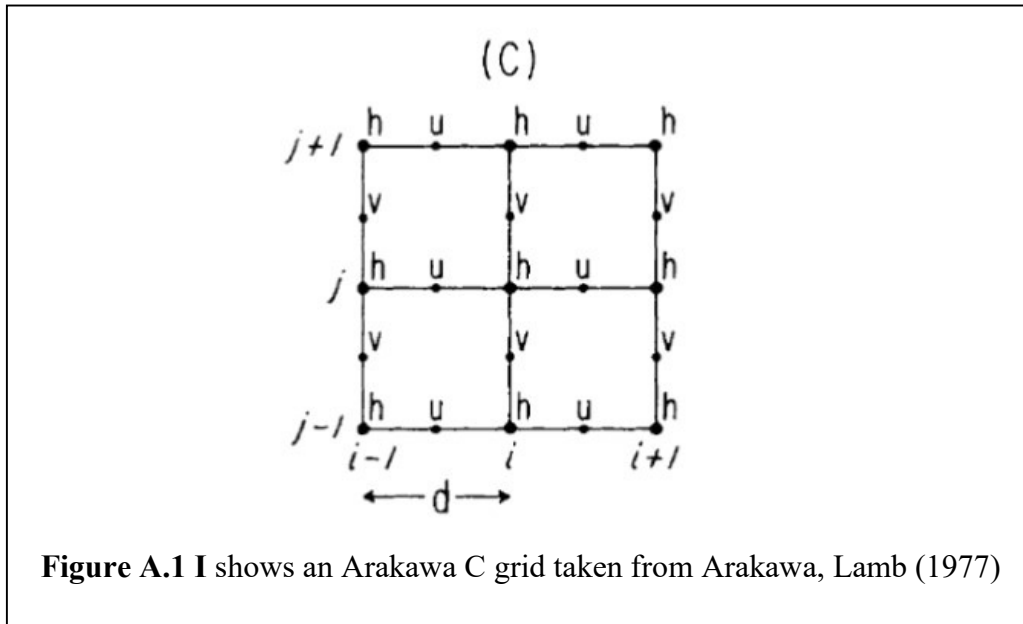
Derived from this formula, the vertical wind component in TALdia is given by (A.1 vii) [Janicke Consulting, 2011; 2014].

$$v_z = \left(1 - \frac{s}{\hat{s}}\right) \frac{\partial b}{\partial x} v_x + \left(1 - \frac{s}{\hat{s}}\right) \frac{\partial b}{\partial y} v_y + \frac{\hat{z} - b(x, y)}{\hat{s}} v_s \quad (\text{A.1 vii})$$

With

$$v_s = \frac{ds}{dt} \quad (\text{A.1 viii})$$

If the values for  $v_s$  and  $s$  are chosen to be equal to 0, the wind flows are parallel to the orography surface [Janicke Consulting, 2011; 2014].



Based on the Arakawa-C grid, the divergence can be computed via the net flux through a grid cell divided by its volume [Janicke Consulting, 2011; 2014]. More details on the divergence calculation can be found in Janicke Consulting, (2011; 2014), pp. 90 to 92.

Here the main focus is on the principle of creating the wind field. This is done in TALdia by starting with a terrain profile (A.1 i) and the initial wind field  $\vec{u}(\vec{r})$  to create a field  $\vec{v}(\vec{r})$  considering the conditions defined by (A.1 ix) and (A.1 x) [Janicke Consulting, 2011; 2014].

$$\vec{\nabla} \cdot \vec{v} = 0 \quad (\text{A.1 ix})$$

$$\int \frac{1}{2} (a_h (v_x - u_x)^2 + a_h (v_y - u_y)^2 + a_v (v_z - u_z)^2) d^3 \vec{r} = \min! \quad (\text{A.1 x})$$

(A.1 ix) ensures that the divergence of  $\vec{v}(\vec{r})$  is kept at 0 [Janicke Consulting, 2011; 2014]. The parameters  $a_h$  and  $a_v$  are for weighting the horizontal and vertical wind speed components [Janicke Consulting, 2011; 2014].

Here the relation

$$a_h = \frac{1}{a_v} \quad (\text{A.1 xi})$$

is applied [Janicke Consulting, 2011; 2014]. Special cases for  $a_v$  are for example, if  $\vec{u}(\vec{r})$  is a horizontal homogenous wind field, then  $a_v = 1$  is a potential flow, or if  $a_v \gg 1$  is chosen, the resulting wind field circum-streams orographic obstacles such as it would be typical for a stable atmospheric layering [Janicke Consulting, 2011; 2014].

In order to find this minima, applying Lagrangian multipliers  $\lambda$  is a viable solution method [Vapnyarskii, 2001]. Applying the Lagrange parameter  $\lambda(\vec{r})$  to (A.1 ix) and (A.1 x) results in (A.1 xii) [Janicke Consulting, 2011; 2014].

$$\delta \left\{ \int \frac{1}{2} (a_h (v_x - u_x)^2 + a_h (v_y - u_y)^2 + a_v (v_z - u_z)^2) d^3 \vec{r} + \int \lambda(\vec{r}) \vec{\nabla} \cdot \vec{v} d^3 \vec{r} \right\} = 0 \quad (\text{A.1 xii})$$

The velocity vector  $\vec{v}(\vec{r})$  can be split up in its components

$$\begin{aligned} v_x &= u_x + \frac{1}{a_h} \frac{\partial \lambda}{\partial x} \\ v_y &= u_y + \frac{1}{a_h} \frac{\partial \lambda}{\partial y} \\ v_z &= u_z + \frac{1}{a_v} \frac{\partial \lambda}{\partial z} \end{aligned} \quad (\text{A.1 xiii})$$

under the condition that

$$\oint \lambda \delta \vec{v} \cdot d\vec{f} = 0 \quad (\text{A.1 xiv})$$

which means basically that at all border surfaces of a grid cell  $\lambda$  must be 0, because here the normal component of  $\vec{v}(\vec{r})$  is not defined [Janicke Consulting, 2011; 2014]. The freedom of divergence is ensured if the flux through the entire surface of each grid cell goes to 0 [Janicke Consulting, 2011; 2014].

Now in the next step the orography will be considered in the calculation. This is done by first including the boundary conditions and then the Prandtl layers into the wind field [Janicke Consulting, 2011; 2014]. TALdia uses the alternate directions implicit method (ADI) due to its better performance for complex orography than the common successive overrelaxation method (SOR) [Janicke Consulting, 2011; 2014].

Therefore parameter  $a_v$  can be written in dependence of the Strouhal number  $S_r$  in (A.1 xv) which can be expressed by the Brunt-Väisälä frequency  $N_{BV}$  (A.1 xvi) [Janicke Consulting, 2011; 2014].

$$a_v = \sqrt{\frac{a_v}{a_h}} = \frac{1}{2} S_r^2 + \sqrt{1 + \frac{1}{4} S_r^4} \quad (\text{A.1 xv})$$

$$S_r = N_{BV} t_c \quad (\text{A.1 xvi})$$

With  $t_c$  being the characteristic time which is given by the characteristic length  $L_c$  and the characteristic velocity  $v_c$ , and  $N_{BV}$  being dependent on the potential temperature  $\vartheta$ , its vertical gradient  $\vartheta'$  and the mean terrestrial gravitational acceleration at surface level of  $g = 9.81 \text{ m/s}^2$  (A.1 xviii) [Janicke Consulting, 2011; 2014]. This model only considers neutral and stable atmospheric layering, where  $\vartheta' \geq 0$  [Janicke Consulting, 2011; 2014]. For unstable layering TALdia uses the same approach as for the neutral layering using  $a_v = a_h = 1$  [personal communication with Dr. U. Janicke from 3<sup>rd</sup> August 2016].

$$t_c = \frac{L_c}{v_c} \quad (\text{A.1 xvii})$$

$$N_{BV} = \sqrt{\frac{g \vartheta}{\vartheta'}} \quad (\text{A.1 xviii})$$

Also the length  $L_c$  which was defined as a geometrical average of the characteristic terrain height  $h_c$  and its horizontal size  $l_c$  (A.1 xix) [Janicke Consulting, 2011; 2014].

$$L_c = \sqrt{l_c h_c} \quad (\text{A.1 xix})$$

The characteristic velocity  $v_c(z)$  is applied for non-disturbed 1-dimensional wind profile [Janicke Consulting, 2011; 2014]. From (A.1 xvii) and (A.1 xix) follows the dependence of  $v_c(z)$  from the characteristic height  $h_c$  and length  $l_c$ . These again have their dependencies in the variance of the orographic height  $b(x, y)$  and the orographic slope  $\gamma(x, y)$ , respectively, as defined in the equations (A.1 xx) to (A.1 xxiv) [Janicke Consulting, 2011; 2014].

$$h_c = 4\sqrt{\int (b(x, y) - \bar{b})^2 dx dy / F} \quad (\text{A.1 xx})$$

$$\text{with } F = \int dx dy = (x_{\max} - x_{\min})(y_{\max} - y_{\min}) \quad (\text{A.1 xxi})$$

$$\text{with } \bar{b} = \int b(x, y) dx dy / F \quad (\text{A.1 xxii})$$

$$l_c = \frac{h_c}{2\gamma} \quad (\text{A.1 xxiii})$$

$$\gamma^2 = \int \left( \left( \frac{\partial b}{\partial x} \right)^2 + \left( \frac{\partial b}{\partial y} \right)^2 \right) dx dy / F \quad (\text{A.1 xxiv})$$

If  $a_v = a_h = 1$ , applying the substitution  $a_v v_z \rightarrow v_z$ ,  $a_v z \rightarrow z$  and if  $u_z \equiv 0$ , then (A.1 ix) and (A.1 x) can be reproduced [Janicke Consulting, 2011; 2014]. For  $\bar{u}$  defined as being constant,  $a_v$  provokes the calculation of a potential flow for an up-scaled orography and consecutive down-scaling to the original orography [Janicke Consulting, 2011; 2014]. Here the limits of this model become obvious, if even high  $a_v$  does not prevent the overflowing of a hill, only makes it more difficult to occur, which is different to the real situations for the case of stable atmospheric layering [Janicke Consulting, 2011; 2014].

Now the Prandtl layers, which describe the behaviour at the boundaries of the fluid (here the air) and solid obstacles that are circum-streamed, are implemented [Eckert, M., 2006, Janicke Consulting, 2011; 2014]. Figure A.1 II shows the effects at the borderline between solid and fluid bodies. Prandtl explained this effect of induced rotational motion in the fluid and the separation of the flow from the wall, already in 1904 [Eckert, M., 2006]. The rotation is caused by the wind shear, which means the increasing wind speed with increased altitude above the ground [Janicke Consulting, 2011; 2014].

TALdia accounts for the preservation of the rotation in these Prandtl boundary layers [Janicke Consulting, 2011; 2014].

Buildings can be implemented in two different ways; by parameterising them as roughness length in the dispersion model, or via directly resolving the building structures as boundaries within the simulation area in the wind field model [Rotach, 2001].



The latter one is implemented in TALdia by taking the previously calculated wind field, introducing the building and its boundary conditions, adding also the lee-sided recirculation and the building-enhanced turbulences, and finally applying the Prandtl layers also to the buildings, before extinguishing the divergence [Janicke Consulting, 2011; 2014].

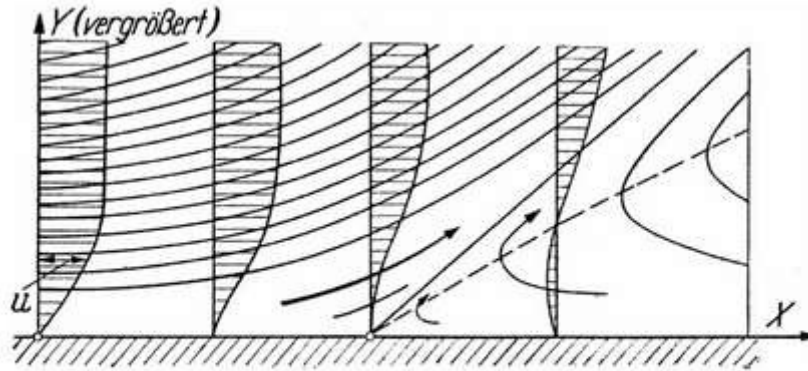


**Fig. 2.3** Velocity profile of the boundary layer, indicating the site where the flow separates from the wall. (The X-axis indicates the distance along the wall, the Y-axis the distance perpendicular from the wall).

**Figure A.1 II** shows the boundary between fluid and solid body, taken from Eckert (2006).

The recirculation is realised in imitation of an electrostatic field [Janicke Consulting, 2011; 2014]. It therefore assumes homogeneous surface charges on the lee-sided wall of the building, and can be expressed with the electrical field  $\vec{E}$  (A.1 xxv) [Janicke Consulting, 2011; 2014].

$$\vec{E}(\vec{r}) = \sum_i \frac{\rho_i}{4\pi} \int_{A_i} \frac{\vec{r} - \vec{a}}{|\vec{r} - \vec{a}|^3} d^2a \quad (\text{A.1 xxv})$$

Here,  $\rho_i$  is the surface charge density and  $\vec{a}$  stands for all points on the partial surface  $A_i$  [Janicke Consulting, 2011; 2014].

Further details to the mathematical description of this approach can be found in the AUSTAL2000 Program Documentation of Version 2.6 by Janicke Consulting, 2014 in Appendix D 2.1.

In figures Figure A.1 IIIa to Figure A.1 IIIc shown are three different wind field situations for different atmospheric layerings, calculated with TALdia and displayed in GO-ARTM. The initial wind speed and wind field was chosen at  $4 \text{ m/s}$  and at  $270^\circ$  for a scenario that includes orography as well as building structures.

What can be seen very well in the comparison of these three examples is that for the stable layering, the hills, which appear in the north and south-west of the building complex, are circum-streamed. In the case for neutral and unstable layering, these hills do not change much in the direction of the arrows that indicate the wind field. Therefore it can be assumed that here the hills are mostly over-streamed, as the model explained above is supposed to do for this case. Also the similarity between the very unstable and the neutral case due to the fact that the model applies the neutral case for the unstable one.

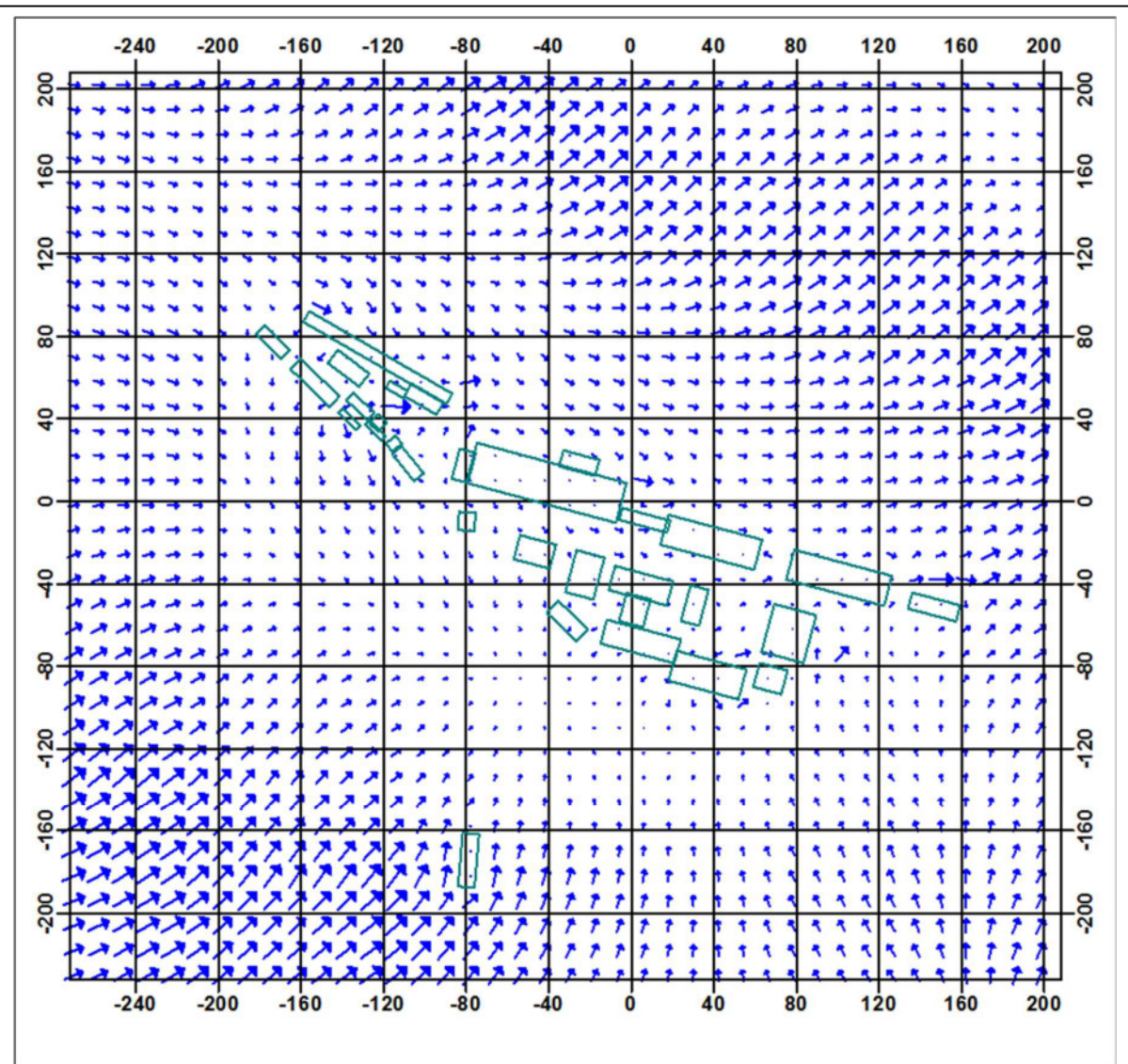


**Figure A.1 IIIa** shows the wind field for a very stable atmospheric layering

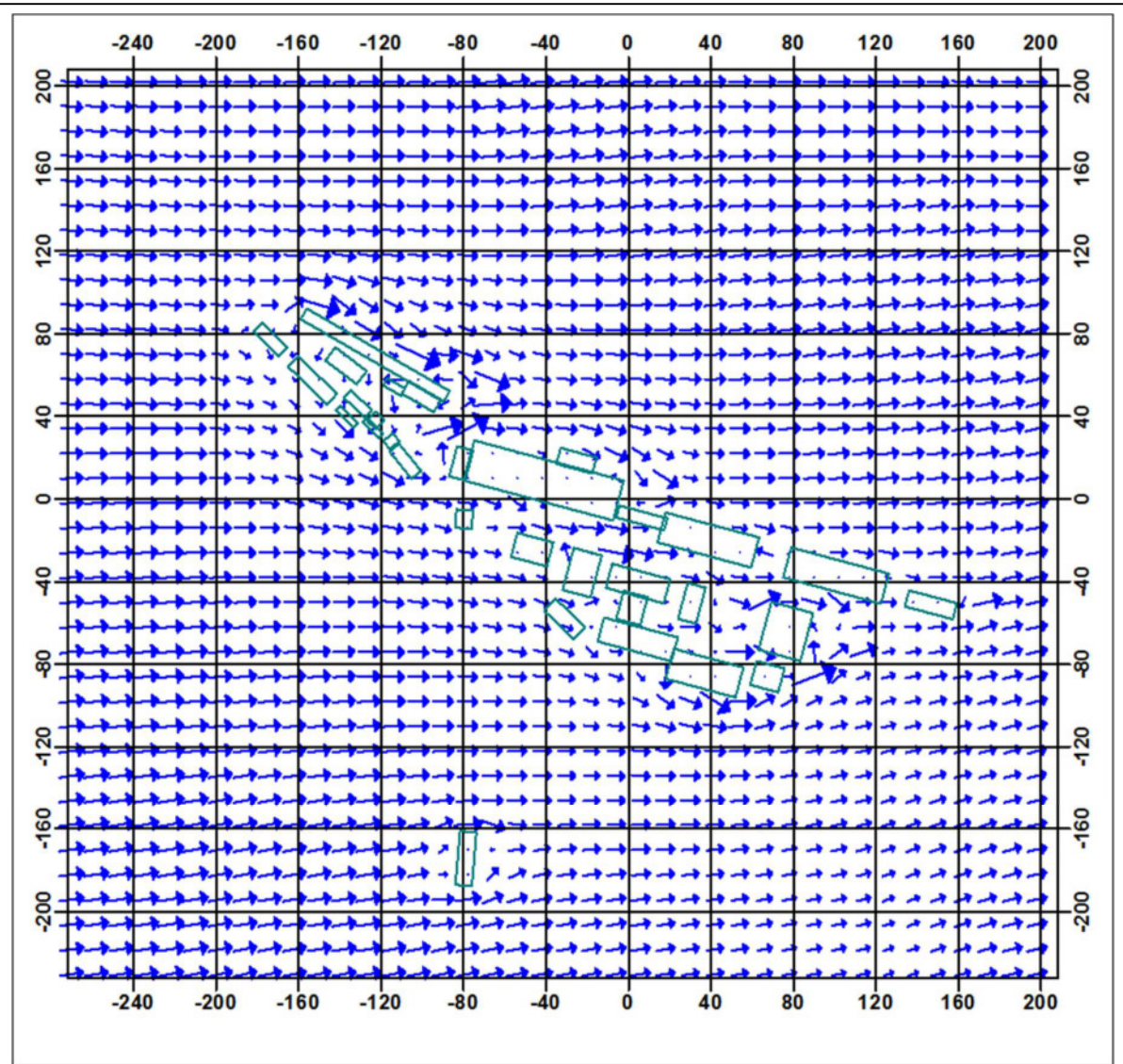
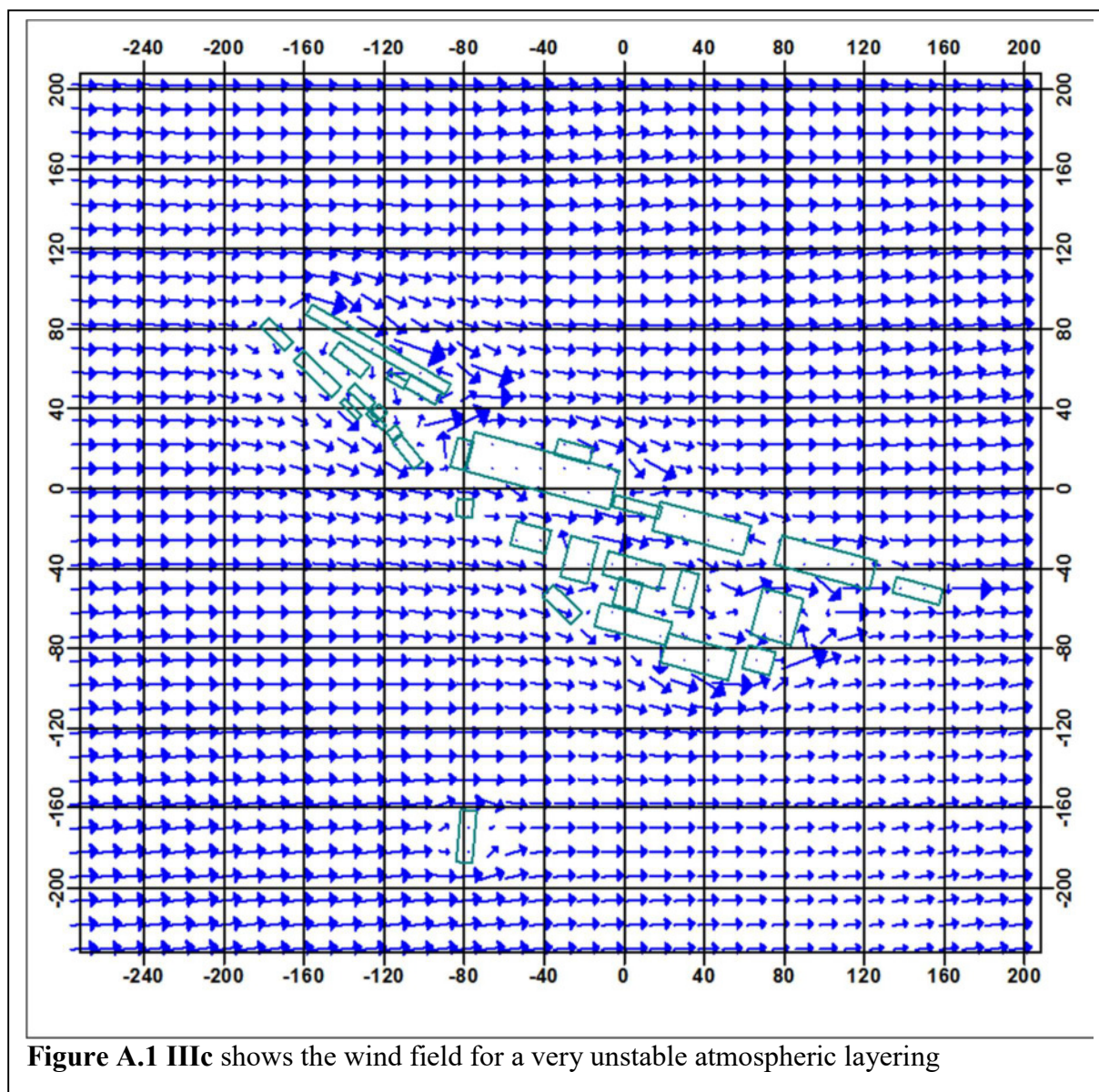


**Figure A.1 IIIb** shows the wind field for a neutral atmospheric layering





## A.2 Lprwnd

LASAIR uses the Lprwnd wind field model, which was originally developed for the use in AUSTAL 2000 (Ausbreitungsrechnung nach TA-Luft, [BMBFJ, 2010]) as a more accurate wind field model than the previous LASAT (Lagrange Simulation of Aerosol-Transport) approach [Janicke Consulting, 2008]. It based on the same mathematical algorithm and parameters as TALdia (see chapter above) according to the LASAT reference book (2008). As the basics are the same, details about its mathematical operations can be viewed in appendix A.1.

The differences between TALdia and Lprwnd are that, despite having the same origin, the developments of ARTM and LASAIR have been done independently over the last years. Therefore, implementations since then have been made to adapt the wind field models to their specific purposes within ARTM and LASAIR.

## B. Version Information

### B.1 ARTM

For this work the ARTM version 2.7.2 with integrated wind field model TALDIA 2.6.0 (released on 25<sup>th</sup> November 2014) will be used in the graphical user interface GO-ARTM 2.0 (<http://www.grs.de/content/ausbreitungsmodellierung>, viewed on 1<sup>st</sup> December 2014) [GRS, 2015].

During the process of the here presented studies, a more recent version, ARTM 2.8.0 (including TALDIA 2.7.0), was released on 15<sup>th</sup> April 2015 and can be downloaded from the BfS Homepage under <https://www.bfs.de/SharedDocs/Downloads/BfS/DE/fachinfo/ion/artm-download.html>, (viewed on 12<sup>th</sup> April 2016) [GRS, 2015].

Simulations conducted before 1<sup>st</sup> December 2014 used ARTM 2.6.4 including TALDIA 2.5.2 (released on 17<sup>th</sup> November 2011) [GRS, 2015].

Between ARTM 2.6.4 and ARTM 2.7.2 only minor changes appeared in the interface, according to the history file [GRS 2015], which did not affect the results of the earlier simulations as several performed verification runs of simulations performed also under the ARTM 2.7.2 version showed. The majority of the simulations whose results are evaluated and described in this work, were performed after updating to version 2.7.2.

As described in the history file, ARTM 2.8.0 contains some further developments in the model towards ARTM 2.7.2, for example the implementation of UTM coordinates, and the geographical adaptation of the Coriolis-parameter, which increases the global applicability [GRS, 2015].

By the time of this release, most simulations had already been performed using the 2.7.2 version. As a test of re-calculating an older simulation in the 2.8.0 version, it showed no differences in the results, when the same parameter and the Gauss-Krüger (GK) coordinates were kept the same. As described in CHAPTER 1.5, the GK-coordinates had to be artificially introduced and do not describe the real location. In order to simulate the dispersion including the real Coriolis parameter, all previous simulations would have had to be changed in its coordinates from GK to UTM coordinates, considering that the in this work used emission sources all lie within 45° - 50° northern latitude, where the Coriolis parameter of ARTM 2.7.2 applies as a good approximation.

So, in order to keep the simulations consistent, after the release of the new version 2.8.0, all further simulations were still continuously conducted using the 2.7.2 version, and all specifications about ARTM, its limitations and results are based on the simulations conducted with ARTM 2.7.2.

### B.2 LASAIR

For this work solely the LASAIR version 4.0.4, released on 17<sup>th</sup> August 2013, was used. This distribution is based on the LASAT version 3.3, released in July 2013.

## C. Coordinate Systems

In this work different coordinate systems are mentioned, namely the Gauss-Krüger Coordinates, Universal Trans-Mercator Coordinates and the usual geographic coordinates (geo coordinates).

Many German cartographic material is described in GK-coordinates, which is why the earlier versions of ARTM were based on this system.

### C.1 Gauss-Krüger Coordinates

The Gauss-Krüger coordinate system (GK-coordinates), introduced in the early 20<sup>th</sup> century, is a coordinate system that was used by German cartographers until recently.

Even though the Gauss-Krüger projection is the basis for most modern trans-mercator projections [Seidel, 2006], the explicit GK- coordinate system is rarely used outside the German-speaking countries in Europe. It follows a cylindrical projection (see figure C.1 I), where every 3 degrees a new main meridian is defined and is a new zone. The entire world therefore has 120 of those zones, making 120 stripes which generate a patchwork of flat coordinates (see figure C.1 II).

The coordinates consist of a northing and an easting value. While the northing just notes the distance to the equator in metres, the easting value is a bit more complex: it consists of the number of the stripe (0 to 119) and the distance to the main meridian in metres. In order to avoid negative values, the value 500,000 is added. So for example the easting value of the meridian of the 3 stripe would be 3,500,000. If a location is further west, this number will get smaller, to the east it will grow larger. A full mathematical description of this coordinate system is described by Dr. Hendrik Seidel (2006) in “Die Mathematik der Gauß-Krüger-Abbildung”, found on <http://henrik-seidel.gmxhome.de/gausskrueger.pdf> (viewed 3<sup>rd</sup> October 2016).



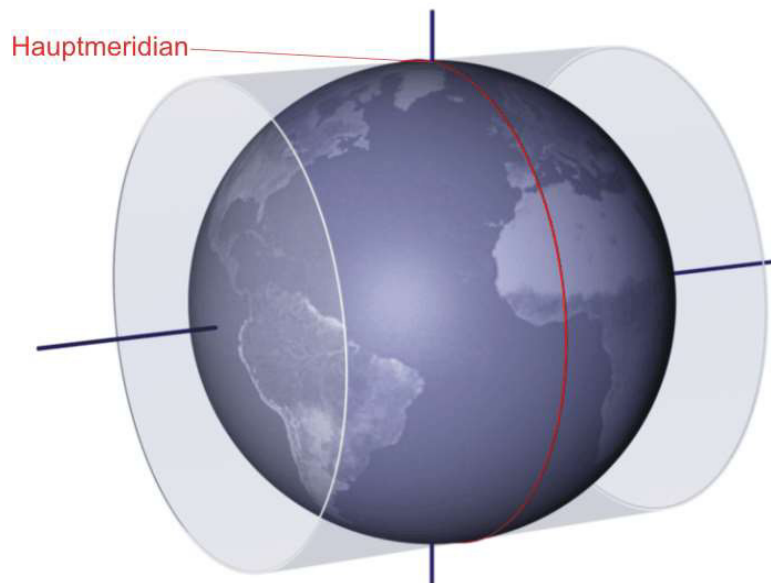


**Figure C.1 I** shows how the main meridian is projected from the sphere onto the cylinder. The areas near the meridian are flat enough to be approximated on the sphere. Further away areas would cause larger deviations, which is why the globe inside the cylinder is rotated by  $3^\circ$ , so that a new meridian falls exactly on the cylinder, leading to a second projection stripe. This way the Earth can be projected onto a flat surface.

(Graphic taken from <http://www.geoinformatik-os.de/index.php/koordinaten/gauss-krueger-koordinaten> (viewed on 3<sup>rd</sup> October 2016))

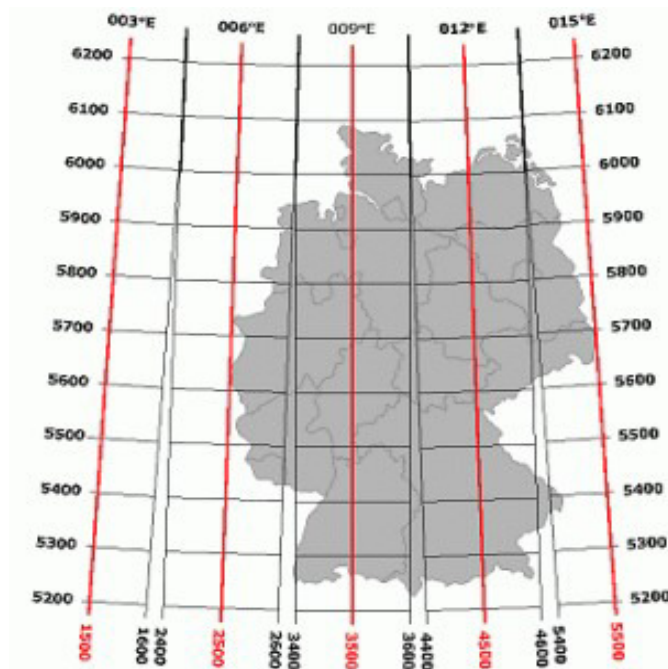


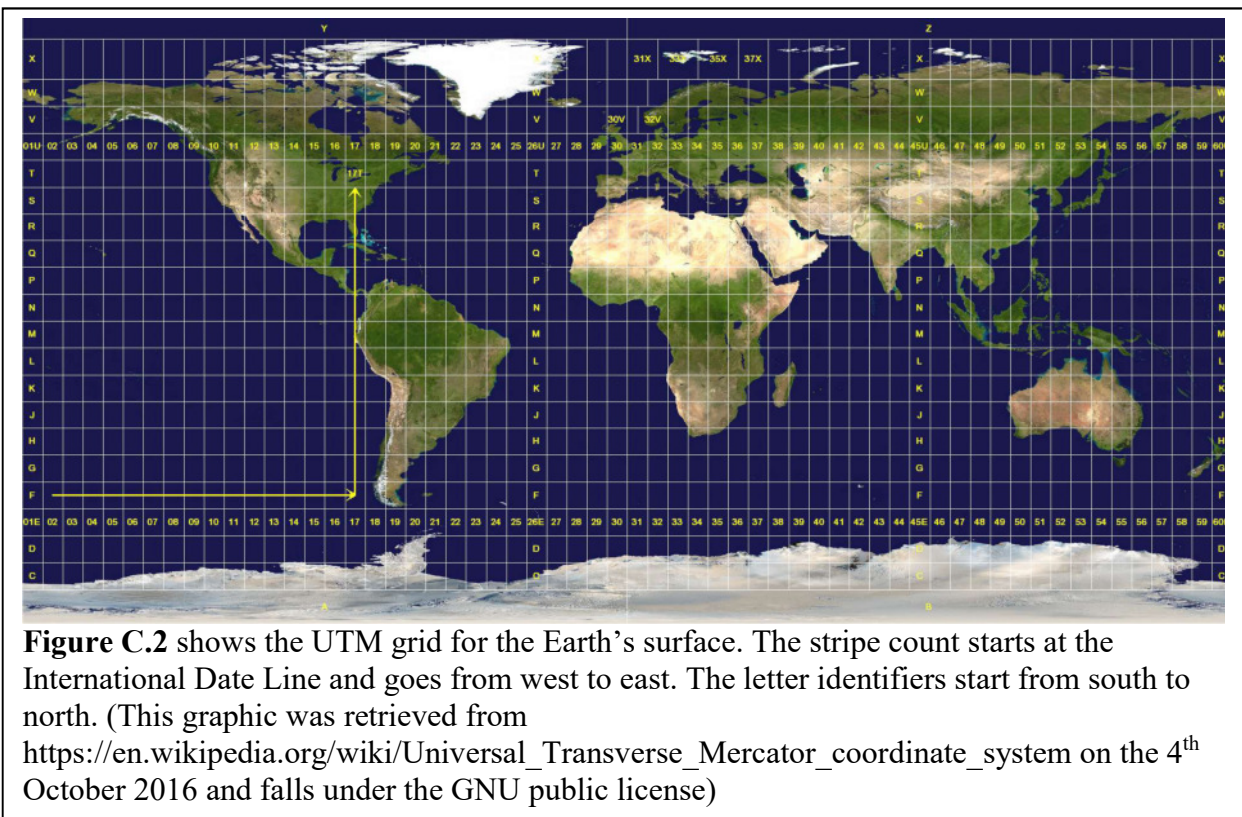
**Figure C.1 IT** shows the different stripes of the GK-coordinate system for Germany. In red are the main meridians, in black the according stripe boundaries. The small areas in between can be described by either of the two neighbouring stripe coordinates.

(Graphic taken from [http://www.gerhard-tropp.de/Troppe/gauss\\_krueger.html](http://www.gerhard-tropp.de/Troppe/gauss_krueger.html) (viewed on 3<sup>rd</sup> October 2016))

## C.2 UTM coordinates

Universal Trans-Mercator coordinates are similar to the GK-coordinates and based on the same Gauss-Krüger projection of the sphere onto a cylinder.

Different to the GK-coordinate system, the UTM system divides the total Earth surface not into 3° stripes, but into 6° ones, which are inter-divided into rectangular areas, so-called UTM zones (INCLUDE IMAGE). A location in the UTM system is defined by 3 different values, the number of the UTM zones (in total they range from 01 to 60 from west to east and from A to Z from south to north), a northing and an easting value, which are the distance in metres to the equator and the main meridian. This is done similar as for the GK-coordinates (as well an addition of 500,000 to the easting) but with the multiplication of 0.9996 to account for the small deviations due to the Earth's curvature [Buchroithner & Pfahlbusch, 2016].



## C.3 Geographic Coordinates

Geographic Coordinates are the well-known coordinates that determine a location by degrees in latitude and longitude. They do not draw equidistant or even just rectangular grids, but trapezoidal ones (see section 1.3.1.1). For the use in there here studied ARTM, the orographic maps need to be in an equidistant coordinate system, otherwise the simulation results will greatly differ due to wrong distances. Therefore all datasets including geo-coordinates need to be translated first into GK-coordinates or UTM- coordinates (for the most recent version, as described in Appendix B.1) before they can be used within ARTM.

## D. Synoptical Estimation of Dispersion Categories

For data sets where there is no data provided that can be used for the determination of the dispersion categories in accordance to the KTA 1508, such as vertical wind profile, solar radiation, or temperature profile, a synoptical observation can be used to estimate the dispersion category.

The principle is to view the combination of cloud coverage (e.g. from satellite images) and the wind speeds resulting from weather observations.

The cloud coverage provides a good understanding on the thermal situation. No, or little cloud coverage means, that sunlight can reach and warm the underground which usually leads towards more air mixtures and therefore to more instable dispersion categories.

The weather charts show both the horizontal wind directions and wind speeds.

The SSK volume 13 offers a method to estimate the dispersion category by using horizontal wind speed in an altitude of 10 metres above the disturbance level and cloud coverage/solar radiation estimates [SSK, 1995a]. Table D I shows the determination of the dispersion categories from synoptical observations as described by the SSK [SSK, 1995a].

However it has to be said, that this method is not an exact determination method and the values used in the following assumption are not exact values either.

**Table D I**, determination of dispersion categories based on synoptical observations. Table translated into English from SSK volume 13 p 24 [SSK, 1995a].

Wind speed $m \cdot s^{-1}$	Day			Night	
	Solar radiation			weak	strong
	strong	medium	weak	Back-ward radiation	
				$> \frac{3}{8}$	$\leq \frac{3}{8}$
				Cloud coverage	
$\bar{u} < 2$	A	A-B	B	(E-F)	(F)
$2 \leq \bar{u} < 3$	A-B	B	C	E	F
$3 \leq \bar{u} < 5$	B	B-C	C	D	E
$5 \leq \bar{u} < 6$	C	C-D	D	D	D
$6 \leq \bar{u}$	C	D	D	D	D

In this work, the in chapter 1.4.1 presented La Hague scenario is one of these data sets that provides no information on the dispersion categories after Klug-Manier (see chapter 2.1.1.4) in the published paper, which was used as a basis to extract the data.

From the weather charts (see figures D I to D VI) wind speeds (in a resolution of  $5kn \equiv 2.57m \cdot s^{-1}$ ) and wind directions not only of the anemometer location (as given in the meteorology file for this scenario, see Appendix E.1), but also of the surrounding area can be gathered.

On 26<sup>th</sup> February at 01:00 the wind speed and direction over ground (i.e. in 10 metres altitude) was  $5kn \equiv 2.57m \cdot s^{-1}$  and  $270^\circ$  in the La Hague and surrounding area, as can be seen in figure D I.

The meteorological measurements in 100 metres altitude at the La Hague site, that were taken during the night suggest wind speeds that are around  $4 \text{ m} \cdot \text{s}^{-1}$  (see Appendix E.1) [Connan et al., 2013].

Since for the determination of the dispersion category, the wind speed of 10 metres above the disturbance level is necessary, according to the SSK volume 13 (1995a), which is estimated to be in this case between 25 and 45 metres, these wind speeds were linearly interpolated (see figure D IX). Despite wind profiles being logarithmic in this altitude, here only the target zone of 25 to 45 metres is of interest, which is why the linear estimation in this case was considered sufficient enough. In the graphic the vertical orange field shows this target area, while the horizontal ones represent the different wind speed intervals to simplify the read out.

In the 850hPa pressure regime which correlates to an altitude of around 1500 metres, figure D II shows a wind of  $10 \text{ kn} \equiv 15.29 \text{ m} \cdot \text{s}^{-1}$  and around  $290^\circ$  in this area.

Together with the distribution of the high pressure area over ground above the Atlantic Ocean and the low pressure area over southern Scandinavia, it creates an inversion situation in this area. Inversion areas cause highly stable atmospheric layering and can entirely prevent the vertical mixture [Rödel, 1992].

The infrared image (figure D VII) for around this time suggests little to no cloud coverage, but definitely lower than  $\frac{3}{8}$ , therefore the radiation balance is negative (i.e. there is more infra-red radiation emitted into the sky than there is radiation input from the sky).

Applying now table D I, as taken from SSK volume 13, the estimated dispersion category is the stable E category. The cloud coverage is low and the wind speed above the disturbance level (see figure D IX) is around  $3 \text{ m} \cdot \text{s}^{-1}$ . As the tendency shows an increase (at 01:00 already  $5.5 \text{ m} \cdot \text{s}^{-1}$ ) in the wind speed, it is save to assume that the category tends more to be E than F.

During the day of the 26<sup>th</sup> February, the degree of cloud coverage remains the same with low to no clouds. Due to the season time (low solar zenith angle) the solar radiation is estimated with low to medium.

The ‘Berliner Wetterkarte’ (year 58, No. 40) contains a chart for central Europe at 13:00 (figure D III). In order to estimate the ground wind speed, the closest measurements were considered and their correlation with the isobar lines can be extrapolated towards the La Hague area. The closest measurement are in Rouen, where it shows  $10 \text{ kn} \equiv 5.14 \text{ m} \cdot \text{s}^{-1}$ , and Paris with 3 and  $4 \text{ m} \cdot \text{s}^{-1}$ . The extrapolation of the isobar lines towards La Hague suggests similar values. Therefore there is reasonable to assume the ground wind speed being between 5 and 10 knots. In figure D IX, there are two resulting interpolation lines, which show the borders of possible values. Taking the average value of both, the wind speed for the disturbance level lies within a range of 5 and  $6 \text{ m} \cdot \text{s}^{-1}$ .

Together with the medium to low solar radiation, the dispersion category D can be expected.

The situation for 27<sup>th</sup> February looks quite similar.

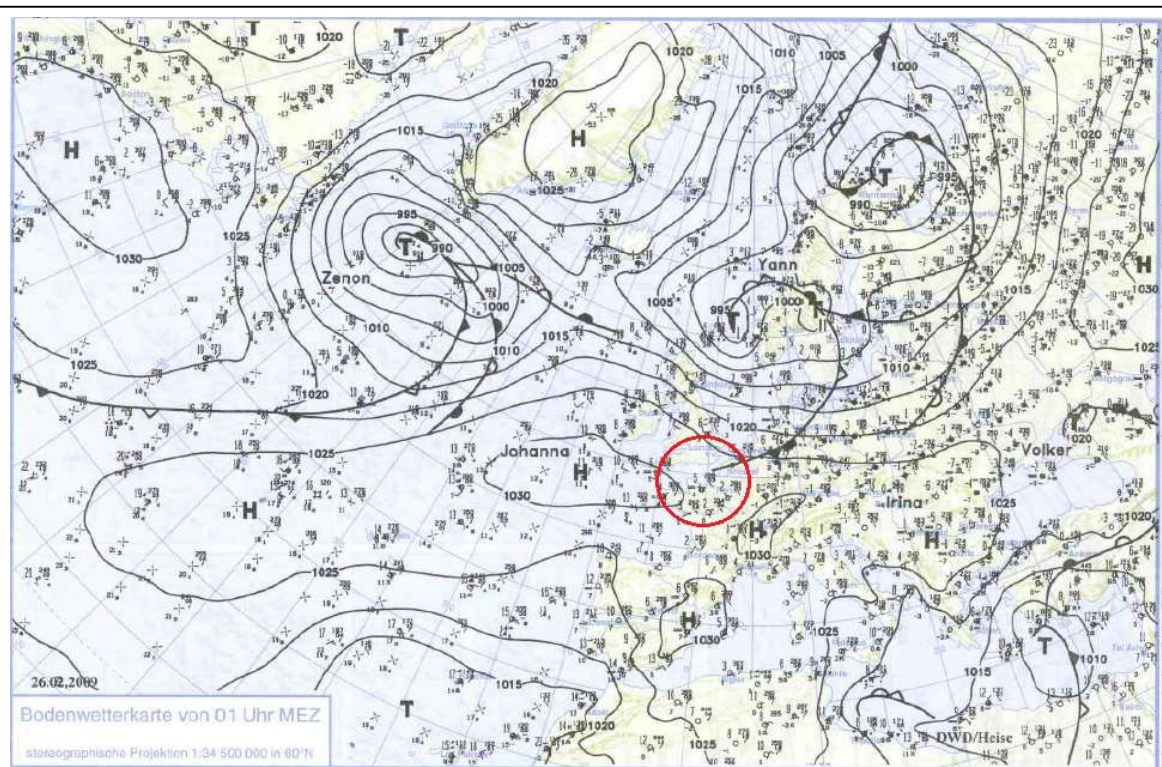
During the night wind speeds from 5 to 10 knots from western directions are dominant in the over ground measurements of the area around La Hague (figure D IV). Observations of the conditions at 850 hPa show there a wind speed of 20 knots ( $10.29 \text{ m} \cdot \text{s}^{-1}$ ) from north-west (figure D V). The anemometer measurements (taken from Connan et al. (2013)) shows at 100 metres  $5.5 \text{ m} \cdot \text{s}^{-1}$ . Therefore it suggests a low shear wind profile, if now the middle of the two lines is taken, then the wind speed at 25 to 45 metres is between 4 and  $5 \text{ m} \cdot \text{s}^{-1}$ , together with the cloud coverage this would make an E like on the day before.

For the day time, the wind speeds appear at 5 knots for the ground level and at only  $3 \text{ m} \cdot \text{s}^{-1}$  for the anemometer altitude. According to the graphic in figure D IX and the table D I, this would result in a C category. However, taking a look into the satellite image of the day (figure D X) suggests that on this day there was a high cloud coverage far above the  $\frac{3}{8}$  and definitely high enough to disable the solar radiation. For this case, the SSK volume 13 (1995a) suggests the application of category D.

**Table D II** summarises the results of the synoptical determination of the dispersion categories for the days 26<sup>th</sup> and 27<sup>th</sup> February

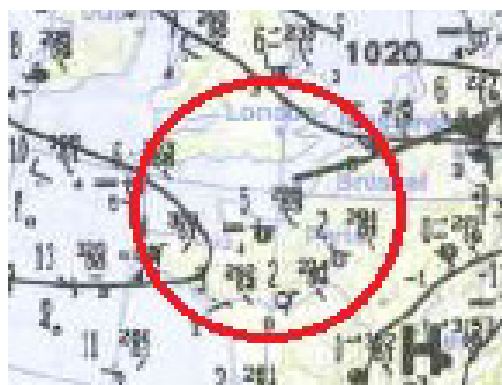
Day	Determined dispersion category	Reasoning
26 <sup>th</sup> February - Night	E	Low cloud coverage, wind speeds around $3 \text{ m} \cdot \text{s}^{-1}$ with tendency to increase
26 <sup>th</sup> February - Day	D	Low to medium solar radiation, wind speeds between 5 and $6 \text{ m} \cdot \text{s}^{-1}$
27 <sup>th</sup> February - Night	E	Low cloud coverage, wind speeds between 4 and $5 \text{ m} \cdot \text{s}^{-1}$
27 <sup>th</sup> February - Day	D	High cloud coverage



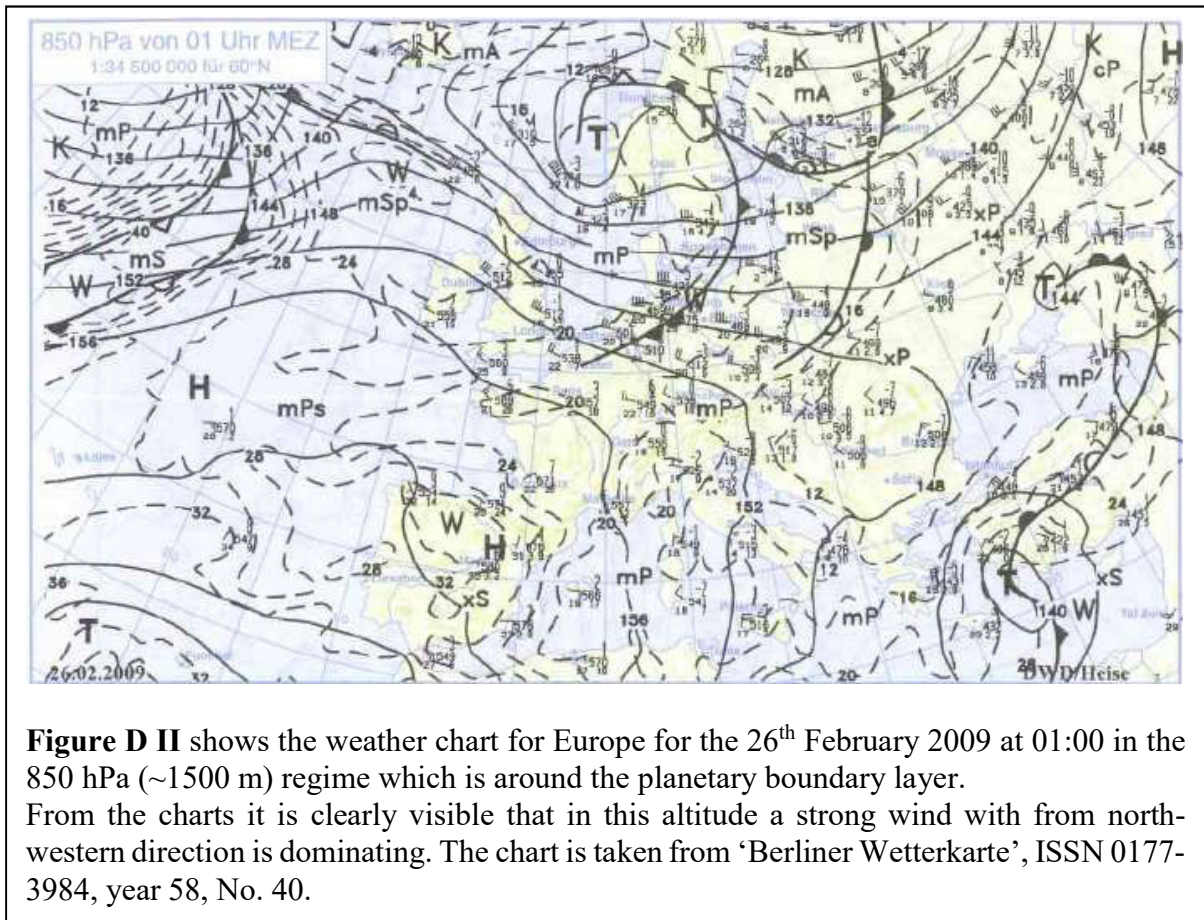


**Figure D I** shows the weather chart for Europe for the 26<sup>th</sup> February 2009 at 01:00 over ground.

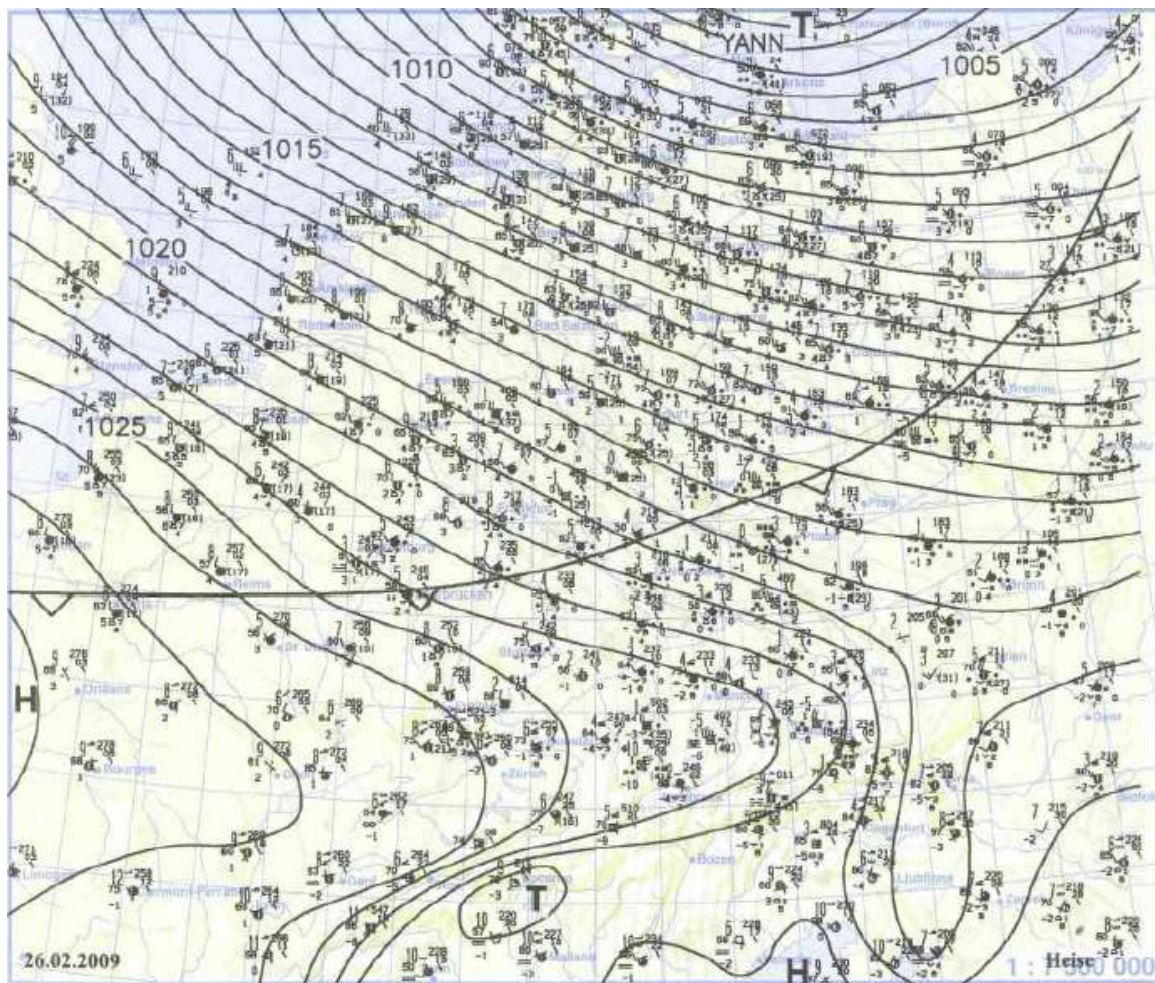
The red circle marks the area round La Hague (to the right). From the charts it is clearly visible that here a slow wind with from western direction is present. The chart is taken from 'Berliner Wetterkarte', ISSN 0177-3984, year 58, No. 40.





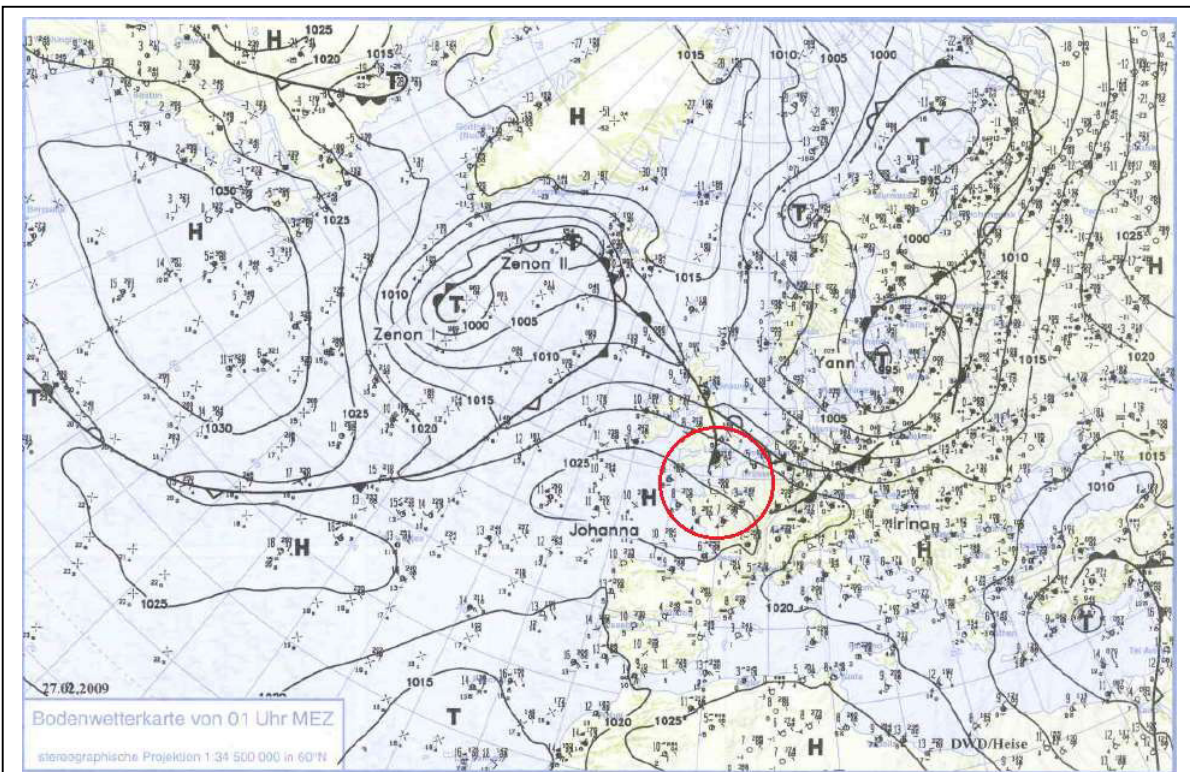


**Figure D II** shows the weather chart for Europe for the 26<sup>th</sup> February 2009 at 01:00 in the 850 hPa (~1500 m) regime which is around the planetary boundary layer. From the charts it is clearly visible that in this altitude a strong wind with from north-western direction is dominating. The chart is taken from 'Berliner Wetterkarte', ISSN 0177-3984, year 58, No. 40.



**Figure D III** shows the weather chart for Central Europe for the 26<sup>th</sup> February 2009 at 13:00 over ground. The chart is taken from 'Berliner Wetterkarte', ISSN 0177-3984, year 58, No. 40.

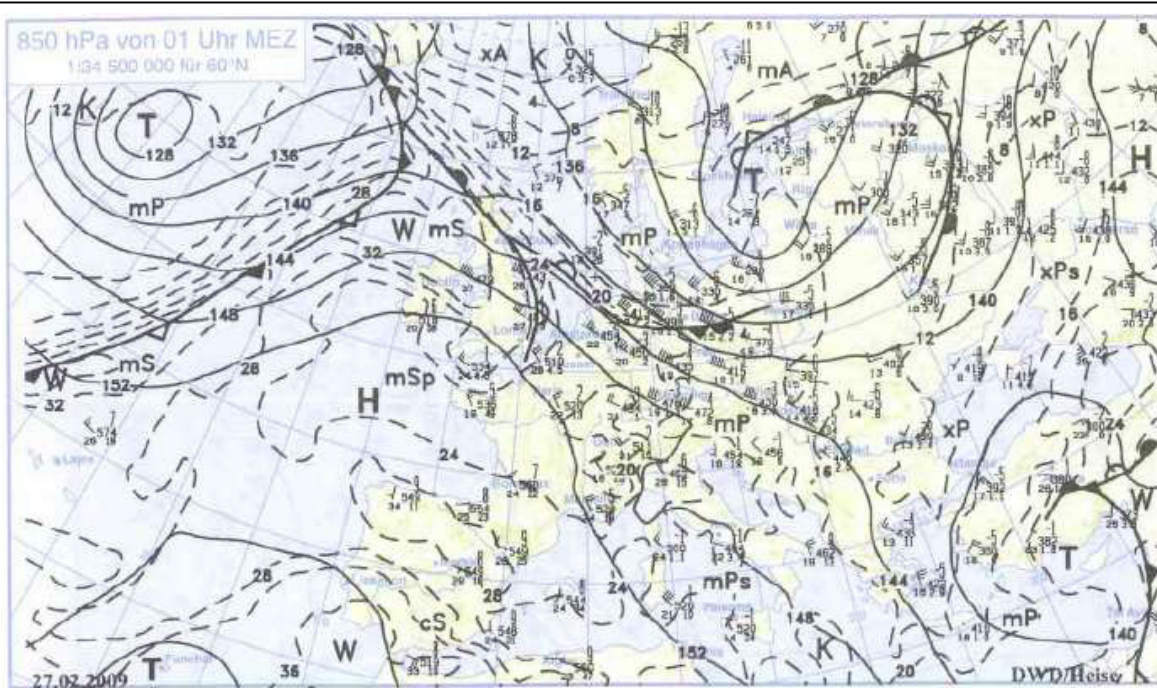




**Figure D IV** shows the weather chart for Europe for the 27<sup>th</sup> February 2009 at 01:00 over ground.

The red circle marks the area round La Hague (to the right). From the charts it is clearly visible that here a slow wind with  $10 \text{ kn} \approx 5.14 \text{ m} \cdot \text{s}^{-1}$  from western direction is present. The chart is taken from 'Berliner Wetterkarte', ISSN 0177-3984, year 58, No. 41.

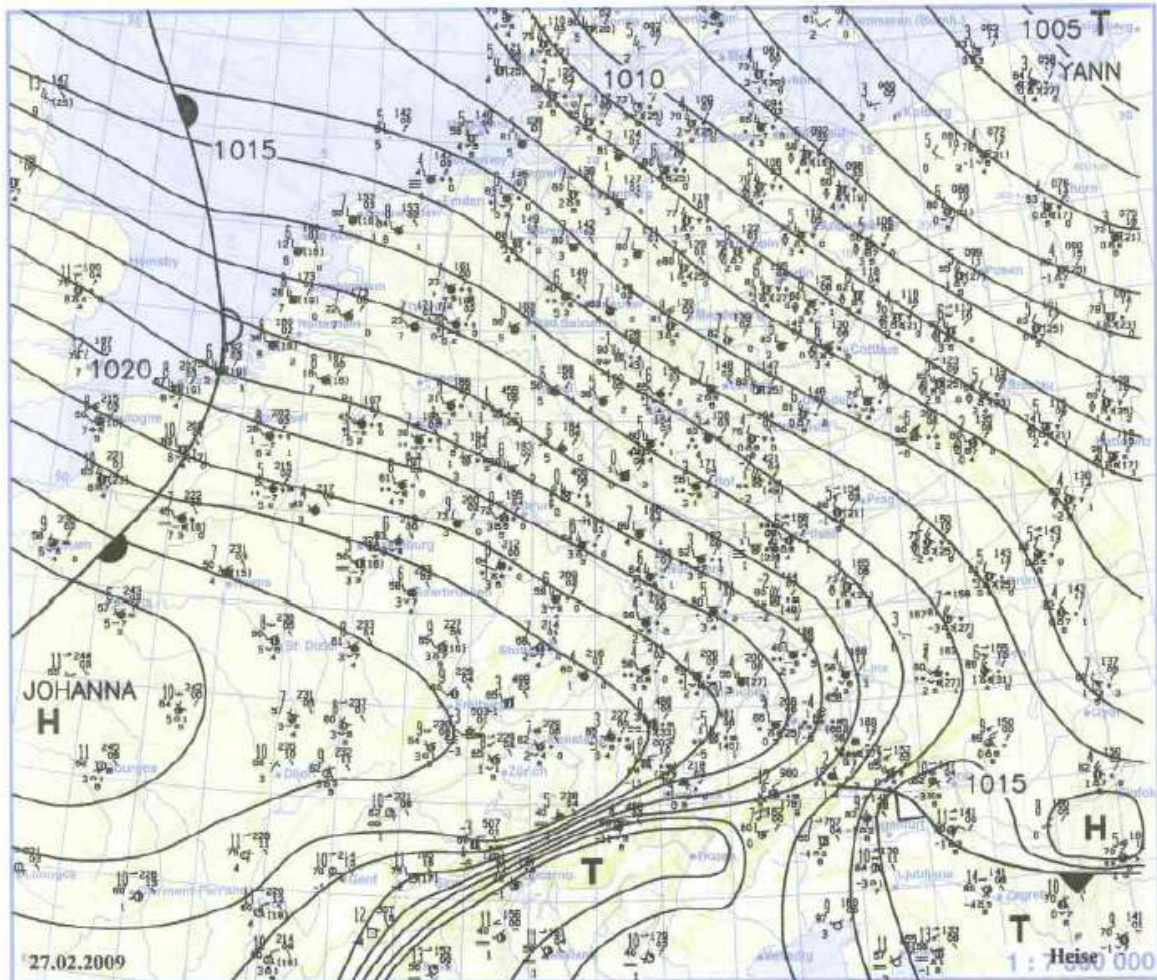




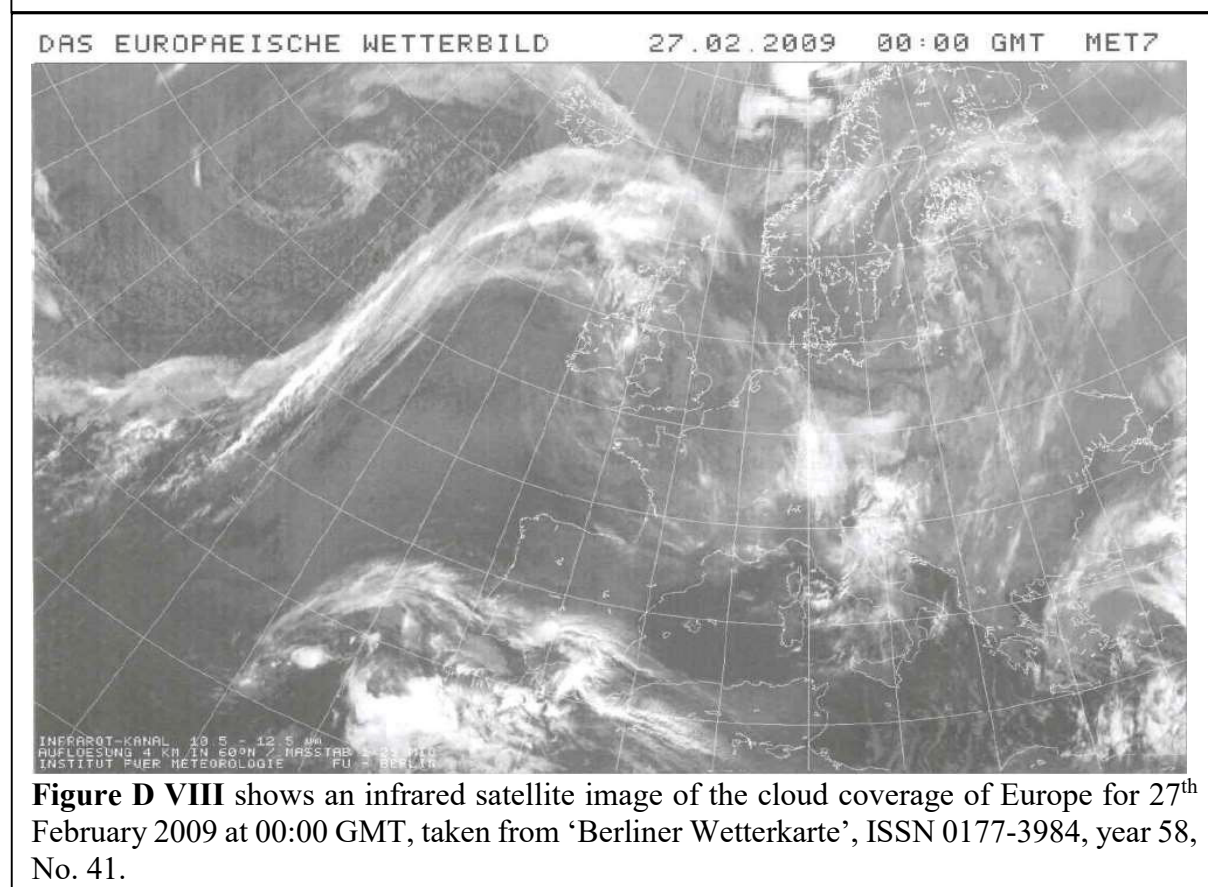
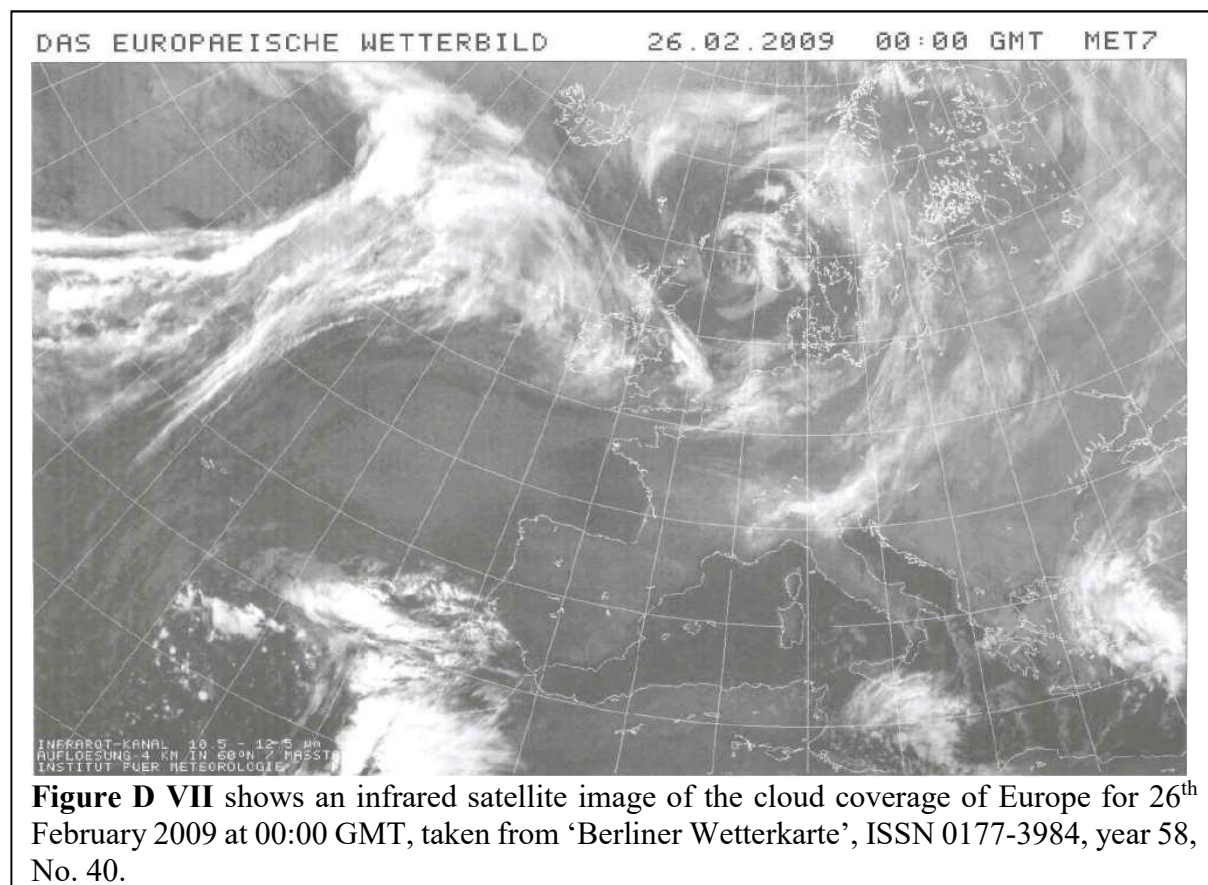
**Figure D V** shows the weather chart for Europe for the 27<sup>th</sup> February 2009 at 01:00 in the 850 hPa (~1500 m) regime.

From the chart it is clearly visible that in this altitude at the La Hague area a wind with from north-west is present. The chart is taken from 'Berliner Wetterkarte', ISSN 0177-3984, year 58, No. 41.





**Figure D VI** shows the weather chart for Central Europe for the 27<sup>th</sup> February 2009 at 13:00 over ground. The chart is taken from 'Berliner Wetterkarte', ISSN 0177-3984, year 58, No. 41.





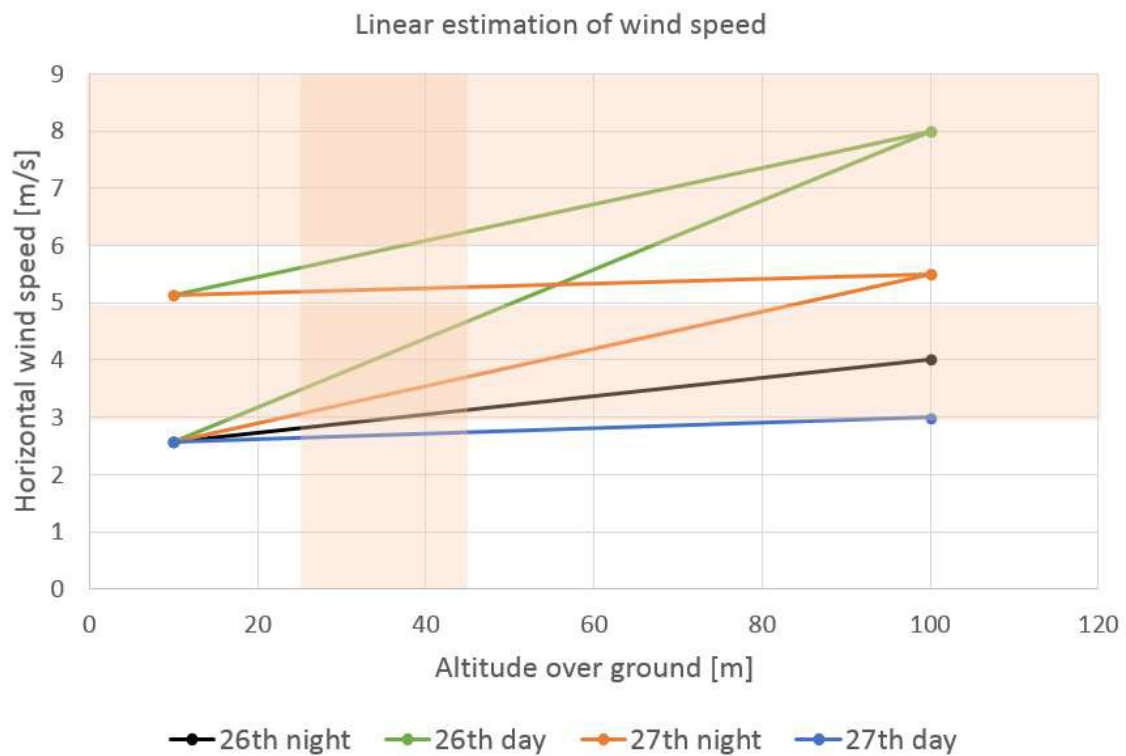


**Figure D IX** provides a linear estimation of the wind speeds above the disturbance level, shown as vertical zone. The horizontal zones distinguish wind speed intervals that lead to different dispersion categories if the suggestions of SSK volume 13 (1995a) are applied.

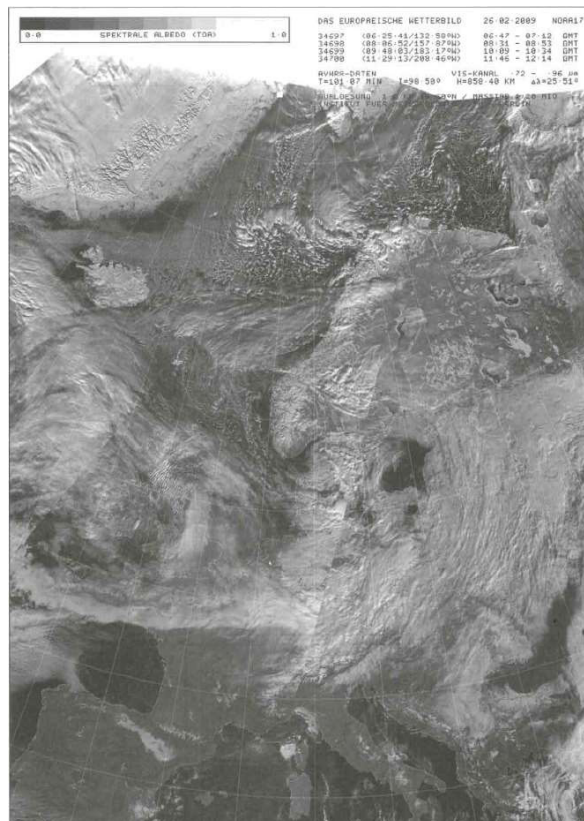


**Figure D X** shows the cloud cover (visual image) over Europe for morning until noon of 27<sup>th</sup> February 2009 taken from 'Berliner Wetterkarte', ISSN 0177-3984, year 58, No. 41.

## E. Meteorological Data Files

Here all the original meteorological files for the in chapter 1.4 introduced data sets can be found, except the one for the Neckarwestheim scenario. This meteorological data file, since it contains the data of an entire year in hourly resolution, is too large to be listed in this work.

Variations of the original data files are not listed here, explanations of the changes and edits can be found in the appendix G and in the data set descriptions.

The data below are listed with:

ID / Station number / year / month / day / hour / zero / quality byte (wind direction) / quality byte (wind speed) / wind direction / wind speed / quality byte (value status) / dispersion category / quality byte (value status) / mixing layer altitude / quality byte (value status) / precipitation / quality byte (value status)

### E.1 La Hague Scenario

\* AKTERM-Zeitreihe mit Niederschlag La Hague

\* Zeitraum 02/2009 bis 02/2009

\* anonymisierte Daten Stand: 15.10.2013 QDD=2(Spalte27: gradgenaue WR)

+ Anemometerhoechen (0.1 m): 32 41 57 74 98 144 200 244 283

AK	10999	2009	2	26	0	0	2	1 295	40	1	2 1	-999 9 990	1
AK	10999	2009	2	26	1	0	2	1 325	55	1	2 1	-999 9 990	1
AK	10999	2009	2	26	2	0	2	1 300	40	1	2 1	-999 9 990	1
AK	10999	2009	2	26	3	0	2	1 315	50	1	2 1	-999 9 990	1
AK	10999	2009	2	26	4	0	2	1 300	50	1	2 1	-999 9 990	1
AK	10999	2009	2	26	5	0	2	1 250	25	1	2 1	-999 9 990	1
AK	10999	2009	2	26	6	0	2	1 280	75	1	2 1	-999 9 990	1
AK	10999	2009	2	26	7	0	2	1 290	60	1	2 1	-999 9 990	1
AK	10999	2009	2	26	8	0	2	1 275	60	1	2 1	-999 9 990	1
AK	10999	2009	2	26	9	0	2	1 280	75	1	3 1	-999 9 990	1
AK	10999	2009	2	26	10	0	2	1 265	65	1	3 1	-999 9 990	1
AK	10999	2009	2	26	11	0	2	1 270	110	1	3 1	-999 9 990	1
AK	10999	2009	2	26	12	0	2	1 260	85	1	3 1	-999 9 990	1
AK	10999	2009	2	26	13	0	2	1 295	80	1	3 1	-999 9 990	1
AK	10999	2009	2	26	14	0	2	1 280	50	1	3 1	-999 9 990	1
AK	10999	2009	2	26	15	0	2	1 290	65	1	3 1	-999 9 990	1
AK	10999	2009	2	26	16	0	2	1 285	75	1	3 1	-999 9 990	1
AK	10999	2009	2	26	17	0	2	1 265	60	1	3 1	-999 9 990	1
AK	10999	2009	2	26	18	0	2	1 270	80	1	3 1	-999 9 990	1
AK	10999	2009	2	26	19	0	2	1 270	70	1	3 1	-999 9 990	1
AK	10999	2009	2	26	20	0	2	1 275	80	1	2 1	-999 9 990	1
AK	10999	2009	2	26	21	0	2	1 285	60	1	2 1	-999 9 990	1
AK	10999	2009	2	26	22	0	2	1 305	70	1	2 1	-999 9 990	1
AK	10999	2009	2	26	23	0	2	1 290	75	1	2 1	-999 9 990	1
AK	10999	2009	2	27	0	0	2	1 310	95	1	2 1	-999 9 990	1
AK	10999	2009	2	27	1	0	2	1 300	55	1	2 1	-999 9 990	1
AK	10999	2009	2	27	2	0	2	1 305	100	1	2 1	-999 9 990	1
AK	10999	2009	2	27	3	0	2	1 305	115	1	2 1	-999 9 990	1
AK	10999	2009	2	27	4	0	2	1 315	90	1	2 1	-999 9 990	1
AK	10999	2009	2	27	5	0	2	1 315	25	1	2 1	-999 9 990	1

AK	10999	2009	2	27	6	0	2	1 300	80	1	2 1	-999 9 990 1
AK	10999	2009	2	27	7	0	2	1 280	60	1	2 1	-999 9 990 1
AK	10999	2009	2	27	8	0	2	1 285	75	1	2 1	-999 9 990 1
AK	10999	2009	2	27	9	0	2	1 290	65	1	3 1	-999 9 990 1
AK	10999	2009	2	27	10	0	2	1 280	50	1	3 1	-999 9 990 1
AK	10999	2009	2	27	11	0	2	1 275	40	1	3 1	-999 9 990 1
AK	10999	2009	2	27	12	0	2	1 260	45	1	3 1	-999 9 990 1
AK	10999	2009	2	27	13	0	2	1 270	30	1	3 1	-999 9 990 1
AK	10999	2009	2	27	14	0	2	1 295	50	1	3 1	-999 9 990 1
AK	10999	2009	2	27	15	0	2	1 290	75	1	3 1	-999 9 990 1
AK	10999	2009	2	27	16	0	2	1 300	50	1	3 1	-999 9 990 1
AK	10999	2009	2	27	17	0	2	1 305	40	1	3 1	-999 9 990 1
AK	10999	2009	2	27	18	0	2	1 300	20	1	3 1	-999 9 990 1
AK	10999	2009	2	27	19	0	2	1 285	30	1	3 1	-999 9 990 1
AK	10999	2009	2	27	20	0	2	1 295	50	1	2 1	-999 9 990 1
AK	10999	2009	2	27	21	0	2	1 355	15	1	2 1	-999 9 990 1
AK	10999	2009	2	27	22	0	2	1 10	5	1	2 1	-999 9 990 1
AK	10999	2009	2	27	23	0	2	1 20	10	1	2 1	-999 9 990 1

## E.2 Šoštanj Scenario

For the Šoštanj scenario four meteorology files taking at 104 metres above ground are listed here, the first two being a direct transcription of the values at each full hour, ignoring the half-hourly values, and the second two where the half-hourly values were considered. This was done using vector-addition of the half-hour and the full hour values resulting in a total value for the entire hour.

This is done using the following formulas (kindly provided by Primož Mlakar):

The wind speed  $v$  in  $ms^{-1}$  and the wind direction  $\delta$  in  $^{\circ}$  are given from the data file, and used to calculate the  $u$  and  $v$  - components for all values as shown in (E.2 i).

$$\begin{aligned} u &= v \cdot \cos\left(\pi \cdot \frac{270^{\circ} - \delta}{180^{\circ}}\right) \\ v &= v \cdot \sin\left(\pi \cdot \frac{270^{\circ} - \delta}{180^{\circ}}\right) \end{aligned} \quad (E.2 \text{ i})$$

Now always the half-hourly and the hourly  $u$  and  $v$  values have to be averaged by applying (E.2 ii).

$$\begin{aligned} u_{avg}(i) &= \frac{1}{2} \sum_i^{i+1} u_i \\ v_{avg}(i) &= \frac{1}{2} \sum_i^{i+1} v_i \end{aligned} \quad (E.2 \text{ ii})$$

In order to now gain the average hourly values for the wind speed and wind direction, (E.2 iii) can be applied, leading to the final  $v_{avg}(i)$  and  $\delta_{avg}(i)$  results.

Attention: in case  $\delta_{avg}(i) > 360^{\circ}$ , these  $360^{\circ}$  have to be subtracted from the total  $\delta_{avg}(i)$ .

$$v_{avg}(i) = \sqrt{u_{avg}^2(i) + v_{avg}^2(i)}$$

$$\delta_{avg}(i) = 270^\circ - \arctan^2\left(\frac{u_{avg}(i)}{v_{avg}(i)}\right) \cdot \frac{180^\circ}{\pi} \quad (\text{E.2 iii})$$

The in chapter 4 described other variations of the meteorological data, are not listed here.

### i) Meteorology for 30<sup>th</sup> March 1991 without considering half-hour values

\* AKTERM-Zeitreihe mit Niederschlag Sostanj

\* Zeitraum 03/1991 bis 03/1991

\* anonymisierte Daten Stand: Tue Feb 25 13:32:37 2014

+ Anemometerhoehen (0.1 m): 32 41 57 74 98 144 200 244 283

AK	10000	1991	3	30	0	0	9	9	-99	-99	9	9	9	-999	9	990	9
AK	10000	1991	3	30	1	0	2	1	347	35	1	5	1	-999	9	990	1
AK	10000	1991	3	30	2	0	2	1	356	34	1	4	1	-999	9	990	1
AK	10000	1991	3	30	3	0	2	1	350	44	1	4	1	-999	9	990	1
AK	10000	1991	3	30	4	0	2	1	5	34	1	3	1	-999	9	990	1
AK	10000	1991	3	30	5	0	2	1	23	34	1	3	1	-999	9	990	1
AK	10000	1991	3	30	6	0	2	1	42	24	1	3	1	-999	9	990	1
AK	10000	1991	3	30	7	0	2	1	14	29	1	3	1	-999	9	990	1
AK	10000	1991	3	30	8	0	2	1	168	3	1	4	1	-999	9	990	1
AK	10000	1991	3	30	9	0	2	1	347	13	1	5	1	-999	9	990	1
AK	10000	1991	3	30	10	0	2	1	12	31	1	5	1	-999	9	990	1
AK	10000	1991	3	30	11	0	2	1	19	38	1	6	1	-999	9	990	1
AK	10000	1991	3	30	12	0	2	1	9	47	1	5	1	-999	9	990	1
AK	10000	1991	3	30	13	0	2	1	354	43	1	5	1	-999	9	990	1
AK	10000	1991	3	30	14	0	2	1	349	38	1	4	1	-999	9	990	1
AK	10000	1991	3	30	15	0	2	1	336	52	1	4	1	-999	9	990	1
AK	10000	1991	3	30	16	0	2	1	351	33	1	5	1	-999	9	990	1
AK	10000	1991	3	30	17	0	2	1	337	34	1	4	1	-999	9	990	1
AK	10000	1991	3	30	18	0	2	1	343	38	1	4	1	-999	9	990	1
AK	10000	1991	3	30	19	0	2	1	3	37	1	4	1	-999	9	990	1
AK	10000	1991	3	30	20	0	2	1	357	41	1	4	1	-999	9	990	1
AK	10000	1991	3	30	21	0	2	1	4	36	1	4	1	-999	9	990	1
AK	10000	1991	3	30	22	0	2	1	8	30	1	3	1	-999	9	990	1
AK	10000	1991	3	30	23	0	2	1	85	17	1	5	1	-999	9	990	1
AK	10000	1991	3	31	0	0	2	1	7	19	1	4	1	-999	9	990	1

### ii) Meteorology for 1<sup>st</sup> and 2<sup>nd</sup> of April 1991 without considering half-hour values

\* AKTERM-Zeitreihe mit Niederschlag Sostanj

\* Zeitraum 04/1991 bis 04/1991

\* anonymisierte Daten Stand: Tue Feb 25 13:51:54 2014

+ Anemometerhoehen (0.1 m): 32 41 57 74 98 144 200 244 283

AK	10000	1991	4	1	0	0	2	1	141	6	1	3	1	-999	9	990	1
AK	10000	1991	4	1	1	0	2	1	290	5	1	3	1	-999	9	990	1
AK	10000	1991	4	1	2	0	2	1	343	7	1	3	1	-999	9	990	1
AK	10000	1991	4	1	3	0	2	1	41	6	1	3	1	-999	9	990	1

AK	10000	1991	4	1	4	0	2	1349	5	1	31-99999901
AK	10000	1991	4	1	5	0	2	133	7	1	21-99999901
AK	10000	1991	4	1	6	0	2	1358	5	1	21-99999901
AK	10000	1991	4	1	7	0	2	1321	7	1	21-99999901
AK	10000	1991	4	1	8	0	2	115	4	1	51-99999901
AK	10000	1991	4	1	9	0	2	116	9	1	31-99999901
AK	10000	1991	4	1	10	0	2	193	16	1	51-99999901
AK	10000	1991	4	1	11	0	2	197	28	1	61-99999901
AK	10000	1991	4	1	12	0	2	199	26	1	61-99999901
AK	10000	1991	4	1	13	0	2	1118	19	1	51-99999901
AK	10000	1991	4	1	14	0	2	1176	10	1	51-99999901
AK	10000	1991	4	1	15	0	2	1114	46	1	51-99999901
AK	10000	1991	4	1	16	0	2	1114	37	1	51-99999901
AK	10000	1991	4	1	17	0	2	1123	16	1	41-99999901
AK	10000	1991	4	1	18	0	2	1117	38	1	41-99999901
AK	10000	1991	4	1	19	0	2	1102	40	1	31-99999901
AK	10000	1991	4	1	20	0	2	1330	8	1	31-99999901
AK	10000	1991	4	1	21	0	2	1324	8	1	41-99999901
AK	10000	1991	4	1	22	0	2	1299	3	1	31-99999901
AK	10000	1991	4	1	23	0	2	150	16	1	31-99999901
AK	10000	1991	4	2	0	0	2	1305	8	1	21-99999901
AK	10000	1991	4	2	1	0	2	1290	6	1	21-99999901
AK	10000	1991	4	2	2	0	2	1326	4	1	21-99999901
AK	10000	1991	4	2	3	0	2	1295	7	1	21-99999901
AK	10000	1991	4	2	4	0	2	1286	12	1	21-99999901
AK	10000	1991	4	2	5	0	2	1304	8	1	21-99999901
AK	10000	1991	4	2	6	0	2	1290	9	1	21-99999901
AK	10000	1991	4	2	7	0	2	1324	11	1	41-99999901
AK	10000	1991	4	2	8	0	2	1342	16	1	31-99999901
AK	10000	1991	4	2	9	0	2	117	20	1	31-99999901
AK	10000	1991	4	2	10	0	2	1271	4	1	41-99999901
AK	10000	1991	4	2	11	0	2	1341	0	1	61-99999901
AK	10000	1991	4	2	12	0	2	193	24	1	51-99999901
AK	10000	1991	4	2	13	0	2	1149	23	1	61-99999901
AK	10000	1991	4	2	14	0	2	1123	26	1	61-99999901
AK	10000	1991	4	2	15	0	2	1108	36	1	51-99999901
AK	10000	1991	4	2	16	0	2	1155	27	1	61-99999901
AK	10000	1991	4	2	17	0	2	1110	43	1	31-99999901
AK	10000	1991	4	2	18	0	2	1108	36	1	31-99999901
AK	10000	1991	4	2	19	0	2	1121	24	1	31-99999901
AK	10000	1991	4	2	20	0	2	1186	2	1	31-99999901
AK	10000	1991	4	2	21	0	2	1318	8	1	31-99999901
AK	10000	1991	4	2	22	0	2	1348	5	1	21-99999901
AK	10000	1991	4	2	23	0	2	128	6	1	41-99999901
AK	10000	1991	4	3	0	0	2	167	10	1	21-99999901

### iii) Meteorology for 30<sup>th</sup> March 1991 considering half-hour values

\* AKTERM-Zeitreihe mit Niederschlag Sostanj

\* Zeitraum 03/1991 bis 03/1991

\* anonymisierte Daten Stand: Tue Feb 25 13:32:37 2014

+ Anemometerhoehen (0.1 m): 32 41 57 74 98 144 200 244 283

AK	10000	1991	3	30	0	0	2	1	347	35	1	9	1	-999	9	990	9
AK	10000	1991	3	30	1	0	2	1	349	32	1	5	1	-999	9	990	1
AK	10000	1991	3	30	2	0	2	1	353	36	1	4	1	-999	9	990	1
AK	10000	1991	3	30	3	0	2	1	350	42	1	4	1	-999	9	990	1
AK	10000	1991	3	30	4	0	2	1	358	33	1	3	1	-999	9	990	1
AK	10000	1991	3	30	5	0	2	1	18	37	1	3	1	-999	9	990	1
AK	10000	1991	3	30	6	0	2	1	33	31	1	3	1	-999	9	990	1
AK	10000	1991	3	30	7	0	2	1	24	30	1	3	1	-999	9	990	1
AK	10000	1991	3	30	8	0	2	1	344	7	1	4	1	-999	9	990	1
AK	10000	1991	3	30	9	0	2	1	356	5	1	5	1	-999	9	990	1
AK	10000	1991	3	30	10	0	2	1	15	29	1	5	1	-999	9	990	1
AK	10000	1991	3	30	11	0	2	1	18	31	1	6	1	-999	9	990	1
AK	10000	1991	3	30	12	0	2	1	12	45	1	5	1	-999	9	990	1
AK	10000	1991	3	30	13	0	2	1	356	42	1	5	1	-999	9	990	1
AK	10000	1991	3	30	14	0	2	1	356	40	1	4	1	-999	9	990	1
AK	10000	1991	3	30	15	0	2	1	335	42	1	4	1	-999	9	990	1
AK	10000	1991	3	30	16	0	2	1	352	29	1	5	1	-999	9	990	1
AK	10000	1991	3	30	17	0	2	1	341	33	1	4	1	-999	9	990	1
AK	10000	1991	3	30	18	0	2	1	348	41	1	4	1	-999	9	990	1
AK	10000	1991	3	30	19	0	2	1	2	32	1	4	1	-999	9	990	1
AK	10000	1991	3	30	20	0	2	1	358	38	1	4	1	-999	9	990	1
AK	10000	1991	3	30	21	0	2	1	2	38	1	4	1	-999	9	990	1
AK	10000	1991	3	30	22	0	2	1	1	32	1	3	1	-999	9	990	1
AK	10000	1991	3	30	23	0	2	1	50	17	1	5	1	-999	9	990	1
AK	10000	1991	3	31	0	0	2	1	19	20	1	4	1	-999	9	990	1

### iv) Meteorology for 1<sup>st</sup> and 2<sup>nd</sup> of April 1991 considering half-hour values

\* AKTERM-Zeitreihe mit Niederschlag Sostanj

\* Zeitraum 04/1991 bis 04/1991

\* anonymisierte Daten Stand: Tue Feb 25 13:51:54 2014

+ Anemometerhoehen (0.1 m): 32 41 57 74 98 144 200 244 283

AK	10000	1991	4	1	0	0	2	1	141	6	1	3	1	-999	9	990	1
AK	10000	1991	4	1	1	0	2	1	92	2	1	3	1	-999	9	990	1
AK	10000	1991	4	1	2	0	2	1	332	10	1	3	1	-999	9	990	1
AK	10000	1991	4	1	3	0	2	1	51	7	1	3	1	-999	9	990	1
AK	10000	1991	4	1	4	0	2	1	3	7	1	3	1	-999	9	990	1
AK	10000	1991	4	1	5	0	2	1	39	7	1	2	1	-999	9	990	1
AK	10000	1991	4	1	6	0	2	1	343	7	1	2	1	-999	9	990	1
AK	10000	1991	4	1	7	0	2	1	339	4	1	2	1	-999	9	990	1
AK	10000	1991	4	1	8	0	2	1	352	4	1	5	1	-999	9	990	1
AK	10000	1991	4	1	9	0	2	1	26	9	1	3	1	-999	9	990	1
AK	10000	1991	4	1	10	0	2	1	100	16	1	5	1	-999	9	990	1
AK	10000	1991	4	1	11	0	2	1	91	23	1	6	1	-999	9	990	1



AK	10000	1991	4	1	12	0	2	1	101	29	1	6	1	-999	9	990	1
AK	10000	1991	4	1	13	0	2	1	102	22	1	5	1	-999	9	990	1
AK	10000	1991	4	1	14	0	2	1	144	10	1	5	1	-999	9	990	1
AK	10000	1991	4	1	15	0	2	1	122	31	1	5	1	-999	9	990	1
AK	10000	1991	4	1	16	0	2	1	111	37	1	5	1	-999	9	990	1
AK	10000	1991	4	1	17	0	2	1	131	21	1	4	1	-999	9	990	1
AK	10000	1991	4	1	18	0	2	1	116	29	1	4	1	-999	9	990	1
AK	10000	1991	4	1	19	0	2	1	110	50	1	3	1	-999	9	990	1
AK	10000	1991	4	1	20	0	2	1	42	5	1	3	1	-999	9	990	1
AK	10000	1991	4	1	21	0	2	1	330	9	1	4	1	-999	9	990	1
AK	10000	1991	4	1	22	0	2	1	348	3	1	3	1	-999	9	990	1
AK	10000	1991	4	1	23	0	2	1	43	10	1	3	1	-999	9	990	1
AK	10000	1991	4	2	0	0	2	1	9	4	1	2	1	-999	9	990	1
AK	10000	1991	4	2	1	0	2	1	293	6	1	2	1	-999	9	990	1
AK	10000	1991	4	2	2	0	2	1	298	4	1	2	1	-999	9	990	1
AK	10000	1991	4	2	3	0	2	1	307	5	1	2	1	-999	9	990	1
AK	10000	1991	4	2	4	0	2	1	289	9	1	2	1	-999	9	990	1
AK	10000	1991	4	2	5	0	2	1	312	7	1	2	1	-999	9	990	1
AK	10000	1991	4	2	6	0	2	1	286	9	1	2	1	-999	9	990	1
AK	10000	1991	4	2	7	0	2	1	318	9	1	4	1	-999	9	990	1
AK	10000	1991	4	2	8	0	2	1	330	11	1	3	1	-999	9	990	1
AK	10000	1991	4	2	9	0	2	1	23	25	1	3	1	-999	9	990	1
AK	10000	1991	4	2	10	0	2	1	349	10	1	4	1	-999	9	990	1
AK	10000	1991	4	2	11	0	2	1	295	6	1	6	1	-999	9	990	1
AK	10000	1991	4	2	12	0	2	1	103	15	1	5	1	-999	9	990	1
AK	10000	1991	4	2	13	0	2	1	141	22	1	6	1	-999	9	990	1
AK	10000	1991	4	2	14	0	2	1	130	22	1	6	1	-999	9	990	1
AK	10000	1991	4	2	15	0	2	1	116	31	1	5	1	-999	9	990	1
AK	10000	1991	4	2	16	0	2	1	151	29	1	6	1	-999	9	990	1
AK	10000	1991	4	2	17	0	2	1	111	36	1	3	1	-999	9	990	1
AK	10000	1991	4	2	18	0	2	1	112	36	1	3	1	-999	9	990	1
AK	10000	1991	4	2	19	0	2	1	121	29	1	3	1	-999	9	990	1
AK	10000	1991	4	2	20	0	2	1	162	3	1	3	1	-999	9	990	1
AK	10000	1991	4	2	21	0	2	1	321	7	1	3	1	-999	9	990	1
AK	10000	1991	4	2	22	0	2	1	323	6	1	2	1	-999	9	990	1
AK	10000	1991	4	2	23	0	2	1	36	4	1	4	1	-999	9	990	1
AK	10000	1991	4	3	0	0	2	1	72	10	1	2	1	-999	9	990	1

## E.3 Urban Buildings Scenario

\* AKTERM-Zeitreihe mit Niederschlag, Building  
Scenario

\* Zeitraum 08/2015 bis 08/2015

\* anonymisierte Daten Stand: 03.08.2015, QDD=2(Spalte27: gradgenaue WR)

+ Anemometerhoehen (0.1 m): 32 41 57 74 98 144 200 244 283

AK	10999	2015	8	3	0	0	2	1	240	10	1	4	1	-999	9	990	1
AK	10999	2015	8	3	1	0	2	1	240	10	1	4	1	-999	9	990	1
AK	10999	2015	8	3	2	0	2	1	240	10	1	4	1	-999	9	990	1
AK	10999	2015	8	3	3	0	2	1	240	10	1	4	1	-999	9	990	1

## F. Šoštanj TPP Buildings

For the buildings of the Šoštanj thermal power plant (TPP) facility no explicit data were available within the data set regarding position and size. In order to simulate the building influence for the Šoštanj scenario, as described in chapter 4, for ARTM and LASAIR, the locations and dimensions had to be measured and estimated. Basis for these were an overview map and an aerial image (figures F I and F II) of the 1991 configuration of the TPP Šoštanj, kindly provided by Marija Zlata Boznar and Primož Mlakar.

The map was used to measure the positions of the buildings. This had to be done for ARTM and LASAIR depending on their reference system:

- For ARTM the coordinate origin was in the south western corner of the simulation area.
- For LASAIR the coordinate origin was in the centre of the simulation area.

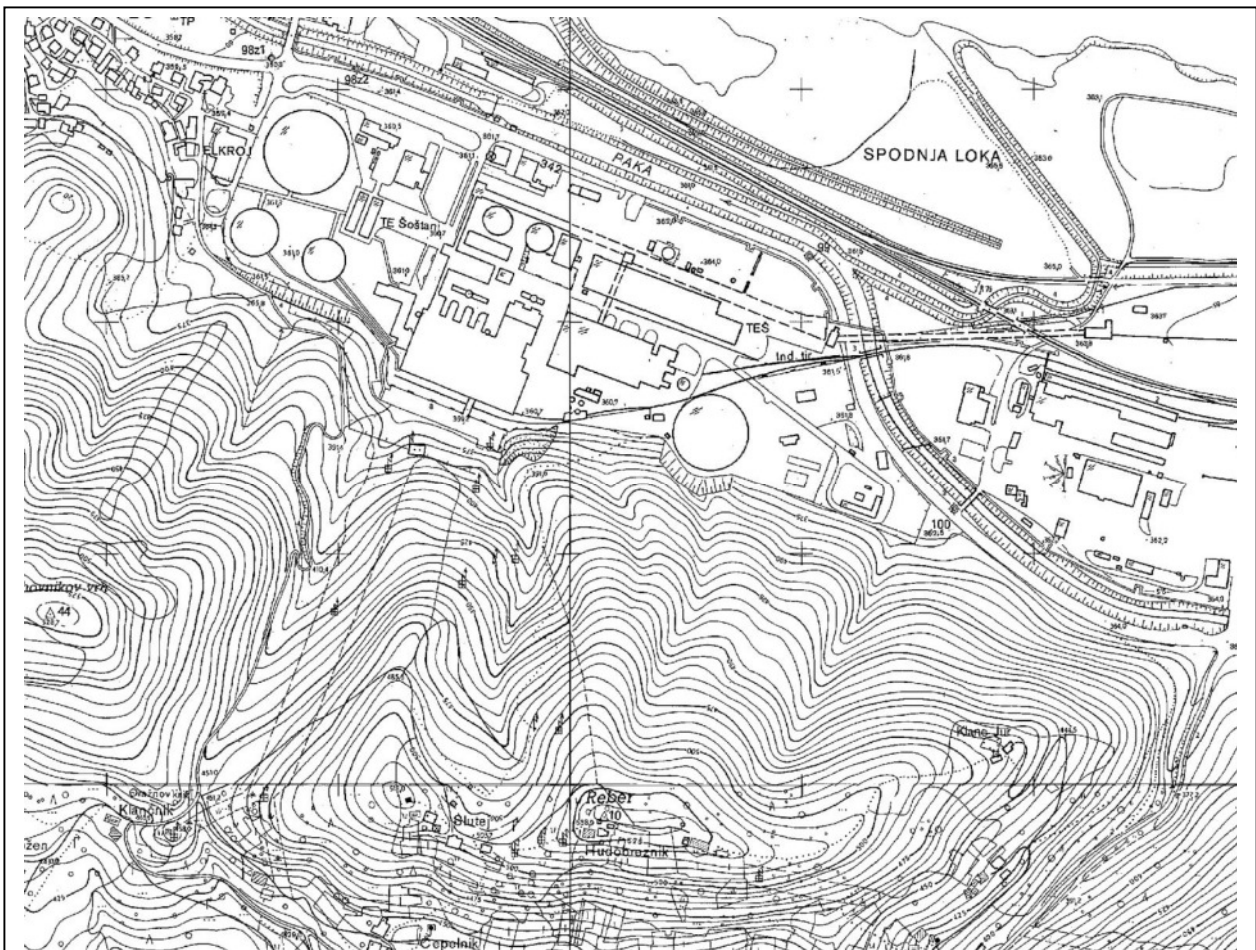


**Figure F I** Map of the 1991 configuration of the thermal power plant Soštanj (Image courtesy by Marija Zlata Boznar and Primoz Mlakar)

For the read-out a fixed reference point was taken, such as the centre of the large north-western cooling tower. In both models the building location were defined by one corner (in ARTM the south-western corner) for rectangular (or polygonal) buildings, and by the central point for cylindrical buildings such as cooling towers.

The horizontal extensions and the angle of the buildings towards the north direction were measured manually from the overview map.



**Figure F II** Aerial image of the 1991 configuration of the thermal power plant Šoštanj (Image courtesy by Marija Zlata Boznar and Primož Mlakar)

The building height was more challenging to obtain. The only known altitudes were those of the three stacks ‘Blok-1-2-3’ with 100 metres, ‘Blok-5’ with 230 metres and the cooling towers as shown in figure F III, kindly provided by Marija Zlata Boznar and Primož Mlakar. In the aerial image of figure F II the shadow of the stacks and the facility buildings are clearly distinguishable. So the method used to estimate the building heights was to scale the shadows of the stacks and cooling towers to their respective heights and to transfer this to the other buildings, i.e. to conclude on the height by measuring the length of the shadows. This estimation was additionally supported by an old, yet a little younger image of the plant (see figure F IV). Despite already having several new buildings, most of the old configuration is still present or can be assumed.

This method is not very accurate and a conservative estimation would be to allow for a deviation of 3 to 5 metres. However, the final product seems to be reasonable and delivers realistic results.





**Figure F III** Known heights of the Cooling towers for the Šoštanj TPP (Image courtesy by Marija Zlata Boznar and Primoz Mlakar)



**Figure F IV** Image of the TTP Šoštanj in a later configuration. (Image courtesy by Marija Zlata Boznar and Primoz Mlakar)

The implementation into ARTM and LASAIR worked a bit different in each of the models:

- For ARTM, the buildings had to be defined by the locations of the south-western corner, length, width, height and angle for the rectangular buildings and central point location, radius and height for cylindrical ones. Table F shows the used building configurations in ARTM. The used ARTM version (see appendix B1) does not provide a 3d-view of the buildings and the 2d-view is available only after running the simulation.
- LASAIR provides a GUI tool to define buildings. Here the correct shape and size has to be inserted first before turning the building in order to obtain the correct angle. The height had to be inserted by the number. Figure F V shows the resulting 2d and 3d images created by the tool.

**Table F** Šoštanj building data input for ARTM. Xb and yb are the coordinates, ab and bb length and width, cb the height and wb the angle. For cylindrical building the length and angle are 0 and the width is the diameter. The minus signalises that a cylindrical building was chosen.

	Build. 1	Build. 2	Build. 3	Build. 4	Build. 5	Build. 6	Build. 7	Build. 8	Build. 9
xb	11530.7	11476.7	11536.7	11581.7	11599.4	11635.7	11620.7	11607.4	12006.4
yb	12873	12768	12747	12710	12666	12679	12636	12649	12541
ab	0	0	0	30	10	75	75	15	25
bb	-80	-40	-40	15	50	25	45	30	25
cb	94	60	60	10	10	35	40	10	45
wb	0	0	0	340	340	340	340	340	340
	Build. 10	Build. 11	Build. 12	Build. 13	Build. 14	Build. 15	Build. 16	Build. 17	Build. 18
xb	11614.7	11716.4	11706.7	11726.4	11735.4	11690.4	11665.4	11742.4	11766.4
yb	12839	12649	12652	12676	12641	12609	12743	12749	12741
ab	30	20	10	20	10	60	60	25	25
bb	30	30	50	20	50	45	30	25	25
cb	15	93	50	50	50	45	8	50	25
wb	342	340	340	340	340	340	340	340	340
	Build. 19	Build. 20	Build. 21	Build. 22	Build. 23	Build. 24	Build. 25	Build. 26	
xb	11684.4	11719.4	11753.4	11652.4	11789.4	11827.4	11839.4	11864.4	
yb	12778	12802	12791	12706	12642	12643	12640	12632	
ab	50	0	0	60	35	10	25	30	
bb	15	-30	-30	15	65	50	50	5	
cb	10	8	8	20	40	45	50	50	
wb	340	0	0	340	340	340	340	340	

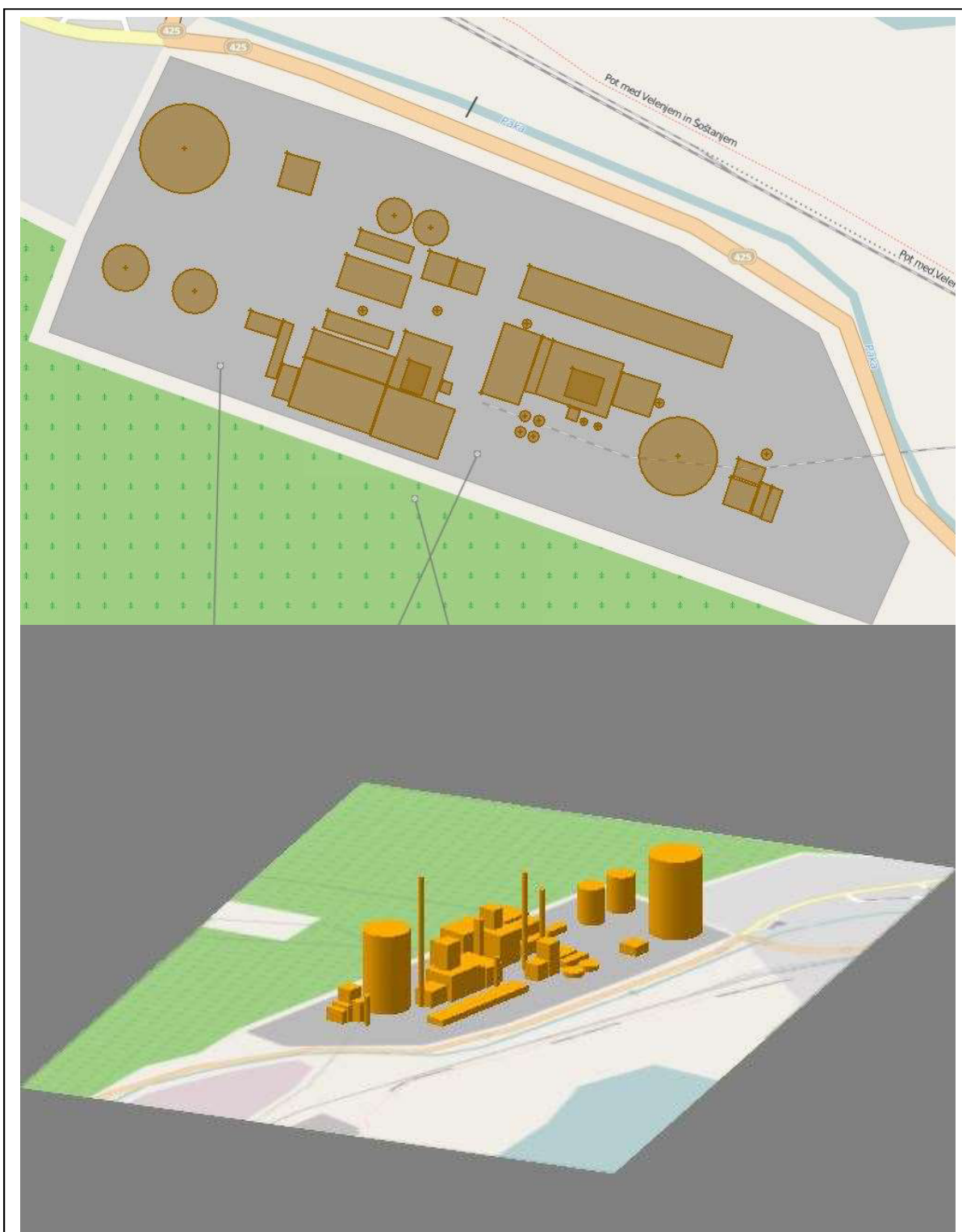


**Figure F V** Model of the Šoštanj TPP in 2d and 3d produced with LASAIR.



## G. ARTM Input Parameter

In this section all the input parameters used for successful simulations with ARTM are given, structured by sections. The with \*, \*\* or \*\*\* marked parameters are varying throughout the scenario-set. Their values or variations are always given below the table with the kept-constant ones.

The footnotes <sup>(1)</sup> to <sup>(8)</sup> are listed and explained here:

<sup>(1)</sup>For simulations with locations outside the defined Gauss-Krüger-Coordinate system (GK), i.e. outside of Germany, a fictive value from within the defined GK area is assumed in order to allow the simulation with ARTM 2.7.2. This coordinate has no influence on the simulation result

<sup>(2)</sup>For user-defined calculation grids ARTM asks the location of the origin of the coordinate system. This is usually half the chosen grid size in x- and y-direction.

<sup>(3)</sup>The number of rows and columns refers the input orographical grid. The number of rows and columns are given in the header of the orography file. However for the correct input, nx and ny have to be 1 smaller than in the orography file.

<sup>(4)</sup>The roughness length is defined for a circular area around the source location with the radius being the 10-fold of the source altitude above ground [Richter et al., 2013a]. Does this area contain parts with different surface roughness, the arithmetic mean value should be determined and rounded to the closest value according to table 2.1.1.3 in chapter 2.1.1.3 [Richter et al., 2013a].

<sup>(5)</sup>The displacement layer altitude defines how much the meteorological profiles are shifted in vertical direction depending on vegetation or constructions [Richter et al., 2013a]. This value need to be at least 6-times the value for the roughness length or for dense urban structures 0.8-times the average construction height [Richter et al., 2013a].

<sup>(6)</sup>Reference point is the coordinate origin, the x-value (distance in m) increases in east direction and the y-value (distance in m) in north direction.

<sup>(7)</sup>Angles refer counter-clockwise starting from the north direction.

<sup>(8)</sup>Multiple emission sources, monitoring points or building structures get accounted for in the same lines following a space character.

## G.1 Section 2.1.1.1 Emission Strength

Parameter Name	ID	Value
General calculation parameters		
Meteorology file	az	LaHague20090226-27-KM3a-D.akterm
Orography file	gh	N49_W02_eq_500-big_grid
Starting random number	sd	2476
Particle quality	qs	0
Definition of the calculation grid		
Lower left coordinate in GK coordinate system <sup>(1)</sup>	gx	3426000
	gy	5319000
Location of coordinate origin in x and y <sup>(2)</sup>	x0	250
	y0	250
Grid size	dd	500
Number of columns <sup>(3)</sup>	nx	141
Number of rows <sup>(3)</sup>	ny	221
Roughness length <sup>(4)</sup>	z0	0.1
Displacement layer altitude <sup>(5)</sup>	d0	5
Definition of source geometries		
x-coordinate of source <sup>(6)</sup> [m]	xq	10000
y-coordinate of source <sup>(6)</sup> [m]	yq	75000
Source altitude above ground [m]	hq	100
Geometry of source in length (aq), width (bq) and height (cq) [m]	aq	10
	bq	10
	cq	10
Angle of source <sup>(7)</sup> [°]	wq	10
Definition of emission strength		
Nuclide type and emission <sup>(8)</sup> [Bq/s]	KR85E	*
Definition of the anemometer		
Anemometer altitude above ground [m]	ha	100
x-coordinate of anemometer <sup>(6)</sup> [m]	xa	10000
y-coordinate of anemometer <sup>(6)</sup> [m]	ya	75000
Definition of monitoring points		
x-coordinate of monitoring point <sup>(6) (8)</sup> [m]	xp	27000
y-coordinate of monitoring point <sup>(6) (8)</sup> [m]	yp	70000
Altitude above ground [m]	hp	1.5
Definition of buildings		
x-coordinate of building <sup>(6) (8)</sup> [m]	xb	-
y-coordinate of building <sup>(6) (8)</sup> [m]	yb	-
Geometry of building in length (aq), width (bq) and height (cq) <sup>(8)</sup> [m]	ab	-
	bb	-
	cb	-
Angle of building <sup>(7) (8)</sup> [°]	wb	-

\* Emission strength variation [Bq/s]: 1051630438, 2103260876, 4206521752, 8413043504, 10516304380, 105163043800, 1051630438000, 10516304380000, 1051630438000000

## G.2 Section 2.1.1.2 Source Geometry

Parameter Name	ID	Value
General calculation parameters		
Meteorology file	az	LaHague20090226-27-KM3a-D.akterm
Orography file	gh	N49_W02_eq_500-big_grid
Starting random number	sd	2476
Particle quality	qs	*
Definition of the calculation grid		
Lower left coordinate in GK coordinate system <sup>(1)</sup>	gx	3426000
	gy	5319000
Location of coordinate origin in x and y <sup>(2)</sup>	x0	250
	y0	250
Grid size	dd	500
Number of columns <sup>(3)</sup>	nx	141
Number of rows <sup>(3)</sup>	ny	221
Roughness length <sup>(4)</sup>	z0	0.1
Displacement layer altitude <sup>(5)</sup>	d0	5
Definition of source geometries		
x-coordinate of source <sup>(6)</sup> [m]	xq	10000
y-coordinate of source <sup>(6)</sup> [m]	yq	75000
Source altitude above ground [m]	hq	100
Geometry of source in length (aq), width (bq) and height (cq) [m]	aq	** ** ** *
	bq	** ** ** *
	cq	0, 0, ****
Angle of source <sup>(7)</sup> [°]	wq	10
Definition of emission strength		
Nuclide type and emission <sup>(8)</sup> [Bq/s]	KR85E	8413043500
Definition of the anemometer		
Anemometer altitude above ground [m]	ha	100
x-coordinate of anemometer <sup>(6)</sup> [m]	xa	10000
y-coordinate of anemometer <sup>(6)</sup> [m]	ya	75000
Definition of monitoring points		
x-coordinate of monitoring point <sup>(6) (8)</sup> [m]	xp	27000
y-coordinate of monitoring point <sup>(6) (8)</sup> [m]	yp	70000
Altitude above ground [m]	hp	1.5
Definition of buildings		
x-coordinate of building <sup>(6) (8)</sup> [m]	xb	-
y-coordinate of building <sup>(6) (8)</sup> [m]	yb	-
Geometry of building in length (aq), width (bq) and height (cq) <sup>(8)</sup> [m]	ab	-
	bb	-
	cb	-
Angle of building <sup>(7) (8)</sup> [°]	wb	-

\* The particle qualities used were: 0 and 4

\*\* Linear source variation (aq/bq) in [m]: 1, 2, 3, 4, 5, 6, 7, 8, 9, 10

\*\*\* Square source variation (aq/bq) in [m]: 1/1, 2/2, 3/3, 4/4, 5/5, 6/6, 7/7, 8/8, 9/9, 10/10

\*\*\*\* Cubic source variation (aq/bq/cq) in [m]: 1/1/1, 2/2/2, 3/3/3, 4/4/4, 5/5/5, 6/6/6, 7/7/7, 8/8/8, 9/9/9, 10/10/10

### G.3 Section 2.1.1.3 Terrain Roughness

Parameter Name	ID	Value
General calculation parameters		
Meteorology file	az	LaHague20090226-27-KM3a-D.akterm
Orography file	gh	N49_W02_eq_500-big_grid
Starting random number	sd	*
Particle quality	qs	4
Definition of the calculation grid		
Lower left coordinate in GK coordinate system <sup>(1)</sup>	gx	3426000
	gy	5319000
Location of coordinate origin in x and y <sup>(2)</sup>	x0	250
	y0	250
Grid size	dd	500
Number of columns <sup>(3)</sup>	nx	141
Number of rows <sup>(3)</sup>	ny	221
Roughness length <sup>(4)</sup>	z0	**
Displacement layer altitude <sup>(5)</sup>	d0	5
Definition of source geometries		
x-coordinate of source <sup>(6)</sup> [m]	xq	10000
y-coordinate of source <sup>(6)</sup> [m]	yq	75000
Source altitude above ground [m]	hq	100
Geometry of source in length (aq), width (bq) and height (cq) [m]	aq	10
	bq	10
	cq	10
Angle of source <sup>(7)</sup> [°]	wq	10
Definition of emission strength		
Nuclide type and emission <sup>(8)</sup> [Bq/s]	KR85E	8413043500
Definition of the anemometer		
Anemometer altitude above ground [m]	ha	100
x-coordinate of anemometer <sup>(6)</sup> [m]	xa	10000
y-coordinate of anemometer <sup>(6)</sup> [m]	ya	75000
Definition of monitoring points		
x-coordinate of monitoring point <sup>(6) (8)</sup> [m]	xp	27000
y-coordinate of monitoring point <sup>(6) (8)</sup> [m]	yp	70000
Altitude above ground [m]	hp	1.5
Definition of buildings		
x-coordinate of building <sup>(6) (8)</sup> [m]	xb	-
y-coordinate of building <sup>(6) (8)</sup> [m]	yb	-
Geometry of building in length (ab), width (bq) and height (cq) <sup>(8)</sup> [m]	ab	-
	bb	-
	cb	-
Angle of building <sup>(7) (8)</sup> [°]	wb	-

\* The random starting numbers used were 1, 10, 100, 1000, 10000, 2476, 2475, 2477, 2466, 2486, 2376, 2576, 1476, 3476, 12476, and 22476

\*\* The roughness length values used were: 0.01, 0.02, 0.05, 0.1, 0.2, 0.5, 1.0, 1.5 and 2.0

## G.4 Section 2.1.1.4 Dispersion Categories

Parameter Name	ID	Value
General calculation parameters		
Meteorology file	az	**
Orography file	gh	N49_W02_eq_500-big_grid
Starting random number	sd	*
Particle quality	qs	4
Definition of the calculation grid		
Lower left coordinate in GK coordinate system <sup>(1)</sup>	gx	3426000
	gy	5319000
Location of coordinate origin in x and y <sup>(2)</sup>	x0	250
	y0	250
Grid size	dd	500
Number of columns <sup>(3)</sup>	nx	141
Number of rows <sup>(3)</sup>	ny	221
Roughness length <sup>(4)</sup>	z0	1
Displacement layer altitude <sup>(5)</sup>	d0	5
Definition of source geometries		
x-coordinate of source <sup>(6)</sup> [m]	xq	10000
y-coordinate of source <sup>(6)</sup> [m]	yq	75000
Source altitude above ground [m]	hq	100
Geometry of source in length (aq), width (bq) and height (cq) [m]	aq	10
	bq	10
	cq	10
Angle of source <sup>(7)</sup> [°]	wq	10
Definition of emission strength		
Nuclide type and emission <sup>(8)</sup> [Bq/s]	KR85E	8413043500
Definition of the anemometer		
Anemometer altitude above ground [m]	ha	100
x-coordinate of anemometer <sup>(6)</sup> [m]	xa	10000
y-coordinate of anemometer <sup>(6)</sup> [m]	ya	75000
Definition of monitoring points		
x-coordinate of monitoring point <sup>(6) (8)</sup> [m]	xp	27000
y-coordinate of monitoring point <sup>(6) (8)</sup> [m]	yp	70000
Altitude above ground [m]	hp	1.5
Definition of buildings		
x-coordinate of building <sup>(6) (8)</sup> [m]	xb	-
y-coordinate of building <sup>(6) (8)</sup> [m]	yb	-
Geometry of building in length (aq), width (bq) and height (cq) <sup>(8)</sup> [m]	ab	-
	bb	-
	cb	-
Angle of building <sup>(7) (8)</sup> [°]	wb	-

\* The random starting numbers used were 1, 10, 100, 1000, 10000, 2476, 2475, 2477, 2466, 2486, 2376, 2576, 1476, 3476, 12476, and 22476

\*\* The meteorology files used differed only in the dispersion categories:  
 LaHague20090226-27-KM1-F.akterm, LaHague20090226-27- KM2-E.akterm,  
 LaHague20090226-27-KM3a-D.akterm, LaHague20090226-27-KM3b-C.akterm,  
 LaHague20090226-27-KM4-B.akterm, LaHague20090226-27-KM5-A.akterm

## G.5 Section 2.1.2.1 Starting Random Numbers and section 2.1.2.2 Particle Quality

Parameter Name	ID	Value
General calculation parameters		
Meteorology file	az	LaHague20090226-27.akterm
Orography file	gh	N49_W02_eq_500-big.grid
Starting random number	sd	*
Particle quality	qs	**
Definition of the calculation grid		
Lower left coordinate in GK coordinate system <sup>(1)</sup>	gx	3426000
	gy	5319000
Location of coordinate origin in x and y <sup>(2)</sup>	x0	250
	y0	250
Grid size	dd	500
Number of columns <sup>(3)</sup>	nx	141
Number of rows <sup>(3)</sup>	ny	221
Roughness length <sup>(4)</sup>	z0	1
Displacement layer altitude <sup>(5)</sup>	d0	5
Definition of source geometries		
x-coordinate of source <sup>(6)</sup> [m]	xq	10000
y-coordinate of source <sup>(6)</sup> [m]	yq	75000
Source altitude above ground [m]	hq	100
Geometry of source in length (aq), width (bq) and height (cq) [m]	aq	10
	bq	10
	cq	10
Angle of source <sup>(7)</sup> [°]	wq	10
Definition of emission strength		
Nuclide type and emission <sup>(8)</sup> [Bq/s]	KR85E	8413043500
Definition of the anemometer		
Anemometer altitude above ground [m]	ha	100
x-coordinate of anemometer <sup>(6)</sup> [m]	xa	10000
y-coordinate of anemometer <sup>(6)</sup> [m]	ya	75000
Definition of monitoring points		
x-coordinate of monitoring point <sup>(6) (8)</sup> [m]	xp	27000
y-coordinate of monitoring point <sup>(6) (8)</sup> [m]	yp	70000
Altitude above ground [m]	hp	1.5
Definition of buildings		
x-coordinate of building <sup>(6) (8)</sup> [m]	xb	-
y-coordinate of building <sup>(6) (8)</sup> [m]	yb	-
Geometry of building in length (aq), width (bq) and height (cq) <sup>(8)</sup> [m]	ab	-
	bb	-
	cb	-
Angle of building <sup>(7) (8)</sup> [°]	wb	-

\* The random starting numbers used were 1, 10, 100, 1000, 10000, 2476, 2475, 2477, 2466, 2486, 2376, 2576, 1476, 3476, 12476, and 22476

\*\* The particle quality was varied between 0, 1, 2, 3, and 4 for the qs value.



## G.6 Section 2.1.2.3 Grid Size and Orography

Parameter Name	ID	Value
General calculation parameters		
Meteorology file	az	LaHague20090226-27-KM3a-D.akterm
Orography file	gh	***
Starting random number	sd	*
Particle quality	qs	**
Definition of the calculation grid		
Lower left coordinate in GK coordinate system <sup>(1)</sup>	gx	3426000
	gy	5319000
Location of coordinate origin in x and y <sup>(2)</sup>	x0	****
	y0	****
Grid size	dd	****
Number of columns <sup>(3)</sup>	nx	****
Number of rows <sup>(3)</sup>	ny	****
Roughness length <sup>(4)</sup>	z0	0.1
Displacement layer altitude <sup>(5)</sup>	d0	5
Definition of source geometries		
x-coordinate of source <sup>(6)</sup> [m]	xq	5331
y-coordinate of source <sup>(6)</sup> [m]	yq	30883.5
Source altitude above ground [m]	hq	100
Geometry of source in length (aq), width (bq) and height (cq) [m]	aq	1
	bq	1
	cq	1
Angle of source <sup>(7)</sup> [°]	wq	0
Definition of emission strength		
Nuclide type and emission <sup>(8)</sup> [Bq/s]	KR85E	?
Definition of the anemometer		
Anemometer altitude above ground [m]	ha	100
x-coordinate of anemometer <sup>(6)</sup> [m]	xa	5331
y-coordinate of anemometer <sup>(6)</sup> [m]	ya	30883.5
Definition of monitoring points		
x-coordinate of monitoring point <sup>(6) (8)</sup> [m]	xp	8148 5264 3316 6560 10743 22000 9228 13589 18381 12816 20673 16461
y-coordinate of monitoring point <sup>(6) (8)</sup> [m]	yp	29220 29776 31445 33220 30553 26109 23716 26607 29426 21732 21638 24721
Altitude above ground [m]	hp	1.5 1.5 1.5 1.5 1.5 1.5 1.5 1.5 1.5 1.5
Definition of buildings		
x-coordinate of building <sup>(6) (8)</sup> [m]	xb	-
y-coordinate of building <sup>(6) (8)</sup> [m]	yb	-
Geometry of building in length (ab), width (bb) and height (cb) <sup>(8)</sup> [m]	ab	-
	bb	-
	cb	-
Angle of building <sup>(7) (8)</sup> [°]	wb	-

\* The random starting numbers used were 1, 10, 100, 1000, 10000, 2476, 2475, 2477, 2466, 2486, 2376, 2576, 1476, 3476, 12476, and 22476

\*\* The particle quality was varied between 0, 1, 2, 3, and 4 for the qs value.

\*\*\* The used orography files were: NONE, and N49\_W02\_eq\_150.grid, N49\_W02\_eq\_200.grid,

N49\_W02\_eq\_250.grid, N49\_W02\_eq\_300.grid, N49\_W02\_eq\_350.grid,  
N49\_W02\_eq\_400.grid, N49\_W02\_eq\_450.grid, N49\_W02\_eq\_500.grid  
\*\*\*\* Depending on the chosen grid size and on the orography file the following sets has to be inserted  
(x0/y0/dd/nx/ny): 150m (75/75/150/156/250), 200m (100/100/200/117/187),  
250m (125/125/250/93/149), 300m (150/150/300/77/124), 350m (175/175/350/66/106),  
400m (200/200/400/57/92), 450m (225/225/450/50/82), 500m (250/250/500/45/73)  
? The emission was variable with time

## G.7 Section 2.2 Neckarwestheim Scenario

Parameter Name	ID	Value
General calculation parameters		
Meteorology file	az	NEC-2009.akterm
Orography file	gh	NeuNeckar.grid
Starting random number	sd	*
Particle quality	qs	**
Definition of the calculation grid		
Lower left coordinate in GK coordinate system <sup>(1)</sup>	gx	3512740
	gy	5433623
Location of coordinate origin in x and y <sup>(2)</sup>	x0	-7000
	y0	-7000
Grid size	dd	50
Number of columns <sup>(3)</sup>	nx	300
Number of rows <sup>(3)</sup>	ny	300
Roughness length <sup>(4)</sup>	z0	0.3
Displacement layer altitude <sup>(5)</sup>	d0	-
Definition of source geometries		
x-coordinate of source <sup>(6)</sup> [m]	xq	0
y-coordinate of source <sup>(6)</sup> [m]	yq	0
Source altitude above ground [m]	hq	160
Geometry of source in length (aq), width (bq) and height (cq) [m]	aq	-
	bq	-
	cq	-
Angle of source <sup>(7)</sup> [°]	wq	-
Definition of emission strength		
Nuclide type and emission <sup>(8)</sup> [Bq/s]	H3W	2442
	C14GB	3805
	C14R	2505
	AR41E	2600
	CO60A-2	0.00019
	KR85E	6342
	KR87E	3.8
	KR88E	2.4
	I131R	0.002
	XE131ME	1300
	XE133ME	2.76
	XE133E	1.14
	XE135ME	2.1
	XE135E	1.9
	XE137E	28.2
Definition of the anemometer		

Anemometer altitude above ground [m]	ha	160
x-coordinate of anemometer <sup>(6)</sup> [m]	xa	1
y-coordinate of anemometer <sup>(6)</sup> [m]	ya	1
Definition of monitoring points		
x-coordinate of monitoring point <sup>(6) (8)</sup> [m]	xp	-
y-coordinate of monitoring point <sup>(6) (8)</sup> [m]	yp	-
Altitude above ground [m]	hp	-
Definition of buildings		
x-coordinate of building <sup>(6) (8)</sup> [m]	xb	-
y-coordinate of building <sup>(6) (8)</sup> [m]	yb	-
Geometry of building in length (aq), width (bq) and height (cq) <sup>(8)</sup> [m]	ab	-
	bb	-
	cb	-
Angle of building <sup>(7) (8)</sup> [°]	wb	-

\* The random starting numbers used were 1, 10, 100, 1000, 10000, 2476, 2475, 2477, 2466, 2486, 2376, 2576, 1476, 3476, 12476, and 22476

\*\* The particle quality was varied between 0, 1, 2, 3, and 4 for the qs value.

## G.8 Section 3 La Hague Scenario

Parameter Name	ID	Value
General calculation parameters		
Meteorology file	az	LaHague20090226-27.akterm
Orography file	gh	N49 W02_eq_500-big.grid
Starting random number	sd	*
Particle quality	qs	4
Definition of the calculation grid		
Lower left coordinate in GK coordinate system <sup>(1)</sup>	gx	3426000
	gy	5319000
Location of coordinate origin in x and y <sup>(2)</sup>	x0	250
	y0	250
Grid size	dd	500
Number of columns <sup>(3)</sup>	nx	141
Number of rows <sup>(3)</sup>	ny	221
Roughness length <sup>(4)</sup>	z0	0.1
Displacement layer altitude <sup>(5)</sup>	d0	5
Definition of source geometries		
x-coordinate of source <sup>(6)</sup> [m]	xq	**
y-coordinate of source <sup>(6)</sup> [m]	yq	**
Source altitude above ground [m]	hq	100
Geometry of source in length (aq), width (bq) and height (cq) [m]	aq	**
	bq	**
	cq	-
Angle of source <sup>(7)</sup> [°]	wq	0
Definition of emission strength		
Nuclide type and emission <sup>(8)</sup> [Bq/s]	KR85E	?
Definition of the anemometer		
Anemometer altitude above ground [m]	ha	100

x-coordinate of anemometer <sup>(6)</sup> [m]	xa	8729
y-coordinate of anemometer <sup>(6)</sup> [m]	ya	75224
Definition of monitoring points		
x-coordinate of monitoring point <sup>(6)</sup> <sup>(8)</sup> [m]	xp	24712 25212 25712 26212 26712 24712 25212 25712 26212 26712 24712 25212 25712 26212 26712 24712 25212 25712 26212 26712 24712 25212 25712 26212 26712 47206 47706 48206 47206 47706 48206 47206 47706 48206 31323 31823 32323 31323 31823 32323 31323 31823 32323
y-coordinate of monitoring point <sup>(6)</sup> <sup>(8)</sup> [m]	yp	71552 71552 71552 71552 71552 71052 71052 71052 71052 71052 70552 70552 70552 70552 70552 70052 70052 70052 70052 70052 69552 69552 69552 69552 69552 43276 43276 43276 42776 42776 42776 42276 42276 42276 36276 36276 36276 35776 35776 35776 35276 35276 35276
Altitude above ground [m]	hp	1.5 1.5
Definition of buildings		
x-coordinate of building <sup>(6)</sup> <sup>(8)</sup> [m]	xb	-
y-coordinate of building <sup>(6)</sup> <sup>(8)</sup> [m]	yb	-
Geometry of building in length (aq), width (bq) and height (cq) <sup>(8)</sup> [m]	ab	-
	bb	-
	cb	-
Angle of building <sup>(7)</sup> <sup>(8)</sup> [°]	wb	-

\* The random starting numbers used were 1, 10, 100, 1000, 10000, 2476, 2475, 2477, 2466, 2486, 2376, 2576, 1476, 3476, 12476, and 22476

\*\* The source geometries (xq/yq/aq/bq) are: UP2 (8729/75224/5/5), UP3 (8972/75326/3/3) and both Together

? The emission was variable with time

## G.9 Section 4 Šoštanj Scenario

Parameter Name	ID	Value
General calculation parameters		
Meteorology file	az	**
Orography file	gh	N46_E14_eq_150.grid
Starting random number	sd	*
Particle quality	qs	4
Definition of the calculation grid		
Lower left coordinate in GK coordinate system <sup>(1)</sup>	gx	3426000
	gy	5319000
Location of coordinate origin in x and y <sup>(2)</sup>	x0	75
	y0	75
Grid size	dd	150
Number of columns <sup>(3)</sup>	nx	175
Number of rows <sup>(3)</sup>	ny	182
Roughness length <sup>(4)</sup>	z0	0.74



		12643 12640 12632 12659 12621 12636 12631 12618 12646 12581 12731 12564 12534 12529)
Geometry of building in length (aq), width (bq) and height (cq) <sup>(8)</sup> [m]	ab	- (0 0 0 30 10 75 75 15 25 30 20 10 20 10 60 60 25 25 50 0 0 60 35 10 25 30 30 10 30 35 10 10 0 190 25 10 15)
	bb	- (-80 -40 -40 15 50 25 45 30 25 30 30 50 20 50 45 30 25 25 15 -30 -30 15 65 50 50 5 20 50 25 30 10 10 -70 30 15 30 30)
	cb	- (94 60 60 10 10 35 40 10 45 15 93 50 50 50 45 8 50 25 10 8 8 20 40 45 50 50 50 50 93 30 80 80 94 10 30 25 20)
Angle of building <sup>(7)</sup> <sup>(8)</sup> [°]	wb	- (0 0 0 340 340 340 340 340 340 342 340 340 340 340 340 340 340 340 340 340 0 340 340 340 340 340 340 340 340 340 340 340 340 0 340 340 340 340)

- \* The random starting numbers used were 1, 10, 100, 1000, 10000, 2476, 2475, 2477, 2466, 2486, 2376, 2576, 1476, 3476, 12476, and 22476
- \*\* The meteorology data files used are: Sostanj-104-1991-3-30-avg.akterm, Sostanj-104-1991-3-30.akterm, Sostanj-104-1991-3-30-avg-newcat.akterm, Sostanj-104-1991-3-30-newcat.akterm, Sostanj-104-1991-4-1-avg.akterm, Sostanj-104-1991-4-1.akterm
- \*\*\* The data for the additional stack (in brackets; xq/yq/hq/aq/bq) are (11948.4/12626.1/230/6.2/6.2) and for the case with 2 stacks the exhaust temperatures are (168.8 170)
- ( ) The scenario was simulated with and without the buildings given in brackets
- ? The emission, heat exhaust and exhaust velocity was variable with time

## G.10 Section 5 Urban Building Scenario

Parameter Name	ID	Value
General calculation parameters		
Meteorology file	az	Building-scenario.akterm
Orography file	gh	-
Starting random number	sd	*
Particle quality	qs	4
No-standard option	os	NOSTANDARD;NODAY;NOGAM
Definition of the calculation grid		
Lower left coordinate in GK coordinate system <sup>(1)</sup>	gx	4605175
	gy	5402175
Location of coordinate origin in x and y <sup>(2)</sup>	x0	-200 -200
	y0	-200 -200
Grid size	dd	5 10
Number of columns <sup>(3)</sup>	nx	300 300
Number of rows <sup>(3)</sup>	ny	300 300
Roughness length <sup>(4)</sup>	z0	0.5
Displacement layer altitude <sup>(5)</sup>	d0	7
Definition of source geometries		
x-coordinate of source <sup>(6)</sup> [m]	xq	1
y-coordinate of source <sup>(6)</sup> [m]	yq	1
Source altitude above ground [m]	hq	5
Geometry of source in length (aq), width (bq) and height (cq) [m]	aq	-
	bq	-
	cq	-



Angle of source <sup>(7)</sup> [°]	wq	-
Definition of emission strength		
Nuclide type and emission <sup>(8)</sup> [Bq/s]	I131A-1	?
Definition of the anemometer		
Anemometer altitude above ground [m]	ha	5
x-coordinate of anemometer <sup>(6)</sup> [m]	xa	-150
y-coordinate of anemometer <sup>(6)</sup> [m]	ya	-150
Definition of monitoring points		
x-coordinate of monitoring point <sup>(6) (8)</sup> [m]	xp	214 428 512 644 772 856 1030 1074 150 270 282 364 520 490 578 722 800 776 940 1024
y-coordinate of monitoring point <sup>(6) (8)</sup> [m]	yp	128 256 306 382 458 510 614 640 230 34 500 370 84 638 500 250 130 646 372 232
Altitude above ground [m]	hp	1.5 1.5 1.5 1.5 1.5 1.5 1.5 1.5 1.5 1.5 1.5 1.5 1.5 1.5 1.5 1.5 1.5 1.5 1.5
Definition of buildings		
x-coordinate of building <sup>(6) (8)</sup> [m]	xb	**
y-coordinate of building <sup>(6) (8)</sup> [m]	yb	**
Geometry of building in length (aq), width (bq) and height (cq) <sup>(8)</sup> [m]	ab	**
	bb	**
	cb	**
Angle of building <sup>(7) (8)</sup> [°]	wb	**

- \* The random starting numbers used were 1, 10, 100, 1000, 10000, 2476, 2475, 2477, 2466, 2486, 2376, 2576, 1476, 3476, 12476, and 22476
- \*\* The scenario was simulated using none of the buildings or increasing the amount. The ‘&’ separates the different steps:  
xb: 40 & 40 40 40 160 160 160 160 & 280 280 280 280 280 400 400 400 400 400 & 540 540 540 540 540  
660 660 660 660 660 & 780 780 780 780 780 900 900 900 900 900  
yb: 20 & 140 260 380 20 140 260 380 & 20 140 260 380 520 20 140 260 380 520 & 20 140 260 380 520  
20 140 260 380 520 & 20 140 260 380 520 20 140 260 380 520  
ab and bb are 100 for all buildings, cb is 20 and wb is 0 for all buildings
- ? The emission was variable with time

